Molecular Origins of the Thermophysical Properties of Polymers and Modeling of Polymer Permeation by Large Molecules

Thesis by

Michael Paul Belmares

In Partial Fulfillment of the Requirements
for the Degree of
Doctor of Philosophy

California Institute of Technology
Pasadena, California
(Submitted May 28, 1998)

Acknowledgements

During my stay at Caltech, I enjoyed discussing science with Professor Goddard, a highly competent individual. I felt comfortable discussing new ideas in science with him and I could always expect a smart suggestion or idea for my research. Finally, I thank Bill for helping me with my future career plans, and also for the times he invited me to dinner with his family.

I would especially like to thank my wife, Helen, for being very supportive of me, which made my final year at Caltech much more bearable. Also, I would like to thank Helen for spending time with me editing my thesis.

I would also especially like to thank my parents and sisters for advice and encouragement during my stay at Caltech.

While at the MSC, I had several good friends I could count on. So, I would like to thank Ben Ramirez, Jim Gerdy, Mario Blanco, and Tahir Cagin for their encouragement and friendship. I also thank other members of the MSC who helped me out when I had science questions.

Last but not least, I would like to thank Jesus for guiding my life throughout all of these years at Caltech.

Sincerely,

Michael P. Belmares

Chapter 1

Abstract

The molecular origins of the phase transitions of polymers have not been completely understood. The molecular level understanding of polymer behavior is of great technological and scientific value. For example, the melt to glass transition of a polymer (T_g) is perhaps its most useful quantity describing it. A low T_g polymer will be a useful elastomer and a high T_g polymer will serve for structural purposes. Additionally, sub-glass relaxations are related to polymer aging.

Based on a simple poly (ethylene) model, the intramolecular and intermolecular factors governing polymer melting, the glass transition and sub-glass transitions were investigated through a careful and systematic variation of the torsional potential as well as the cohesive energy of the polymer. The model polymers were studied using constant pressure canonical (Gibbs) dynamics of a system of four polymer chains with one hundred and fifty beads per chain. The advantage of varying systematically the torsional potential is that the morphology of the polymer is controlled, ranging from highly amorphous to highly crystalline, depending on the *gauche-trans* conformational energy differences. The effect of cohesive energy on the various transitions may also be studied by changing the Van der Waals well depth of each bead in the polymer chain.

The first study presented in this chapter is a semi-crystalline case where the *gauche* energy was +1.14 kcal/mol more stable than the *trans* energy, and the *trans-gauche* barrier was 3.01 kcal/mol. A melting point, a glass transition and a tentatively assigned gamma relaxation were characterized.

In a second study, the effect of the *trans-gauche* barrier on the phase transitions of a semi-crystalline polymer (*gauche energy*=+1.14 kcal/mol) was investigated.

In a third study, the effect of the torsional barrier on the glass transition of amorphous polymers (*gauche* energy=*trans* energy) was investigated.

In a fourth study, the effects of crystallinity on the phase transitions of polymers was investigated by varying the *trans-gauche* energy differences while maintaining the *trans-gauche* barrier constant at 4.03 kcal/mol.

In the fifth and final study, the effect of the cohesive energy on the polymer phase transitions was investigated by changing the Lennard Jones well depth of each bead while maintaining the torsional potential fixed with a *gauche* energy of 1.14 kcal/mol relative to the *trans* energy, and a trans-gauche barrier of 4.03 kcal/mol.

Based on these studies, new insights on the general thermo-physical properties of polymers were obtained. A summary of the molecular interpretations of the melting point, glass transition, and sub-glass transitions is provided at the conclusion of this study.

Therefore, the strength of this study is its ability to produce numerous phase transitions within a single structural polymer model by a systematic variation of the intermolecular and intramolecular forcefield parameters. This allows an effective comparison of the thermodynamics, the kinetics and morphology of each of the polymer cases.

Molecular Origins of the Various Phase Transitions of Polymers

The glass transition of a polymer (T_g) perhaps is the most useful quantity describing it. Thus, a low T_g polymer will be useful as an elastomer, and high T_g polymer will serve for structural purposes. Numerous approaches exist for predicting glass transitions from phenomenological group additivity values, such as the Van Krevelen approach.[1] The group additivity method relies on a databank of information containing the glass transition of numerous polymers to predict the T_g of novel polymers. However, it would be of scientific and technological interest to understand how intra-molecular and intermolecular factors affect material properties such as the T_g, compressibility, heat capacity and expansivity of polymers. Additionally, sub-glass relaxations are related to polymer aging. Therefore, the intra-molecular and intermolecular effects on the properties of a polyethylene-like model were investigated through molecular dynamics simulations, since its structure is very simple. In addition, the origins of various phase transitions of polyethylene have been a subject of controversy, and this study may address some of those issues.

General Overview of Experimental and Theoretical Studies on The various Phase Transitions and Relaxations in Polymers

There have been numerous modeling efforts on the study of the glass transition of polymers through the molecular dynamics simulations method for various specific polymer cases. Early computational and theoretical studies of lattice polymer systems through a Monte Carlo approach were done by Skolnick.[2] In this study, it was

estimated that the glass transition occurs at 8% of the free volume of the system where local four-bond transitions were frozen into place. The insight that came out this study is that density fluctuations that occur below the glass temperature do not create enough free volume to allow configurational transitions. In another theoretical study, Allegra and co-workers investigated the glass transition with a non-lattice model.[3] According to Gibbs and DiMarzio theory, the configurational entropy of polymer chains vanishes to zero below T_g and the chains are frozen into place. Based on the Gibbs and DiMarzio definition of the glass transition, Allegra estimated that at T_g there is a discontinuous change in the amplitude of the backbone rotational oscillations for various polymers, and a "universal" root-mean-square angle of oscillation of ~8^0 was calculated. The polymers studied were polyethylene, iso- and syndiotactic polypropylene, atactic poly (styrene), cis-1, 4-polybutadiene, and cis-1, 4-polyisoprene.

With the increase in computational power detailed studies of the glass transition with fully atomistic polymer models has been made possible. For example, the volumetric glass transition of polyethylene, polypropylene and polystyrene has been studied through the use of molecular dynamics simulations, but the atomistic details on its origin were not carefully investigated.[4] However, the calculated glass transitions were comparable to experimental values. Cagin has investigated the local chain dynamics at the glass transition of Poly (carbonate).[5] Cooperative motions of the backbone rings were found below the T_g and good agreement with NMR correlation times was found as well. In an *ab initio* study of poly (ester carbonates), Bicerano and Clark qualitatively related the intramolecular torsional potential energy surfaces of

small polymer fragments to some of its mechanical relaxations.[6] For example, the δ relaxation is attributed to methyl group rotations, the γ relaxation is attributed to phenyl ring rotations, and the origin of the β relaxation was ambiguously described as the displacement of two to four main chain monomers. It should be pointed out that the atomistic origin of the relaxations varies from polymer to polymer. However, the general observation that the motions of low temperature relaxations are more localized than the motions of high temperature relaxations holds true for all polymers, and as the temperature increases, the higher temperature relaxations are excited. For example, experimental 2D exchange NMR experiments on Poly (methyl methacrylate) revealed that the β-process involves a $180^0 \pm 10^0$ flip of the ester unit accompanied by a restricted backbone rearrangement of a $\pm 20^0$ amplitude, while the α-process is related to the backbone mobility.[7] Another interesting polymer case is poly (vinyl chloride), where the sub-T_g β-relaxation is attributed to the movement of small segments of the main chain, and the restrictions to reorientation are believed to be intramolecular in nature.[8] The α-relaxation in PVC is associated with its T_g.

Finally, several atomistic studies of polymer chain collapse and melting have been reported in the literature. Suter studied a polyethylene model above and below its melting point with a Monte Carlo technique and a single chain under periodic boundary conditions.[9] A melting point between 100-150 ^{0}C was obtained based on the radial distribution function and the torsional occupations of the trans and gauche-states. Properties of the system were investigated every 50^0C around the melting point. Therefore, the results in this study were very qualitative since the gradual process of

crystallization was not studied. In another atomistic study, the process of crystalline lamella formation of a united atom polymer model on a surface was studied with a molecular dynamics technique.[10] The process was described by, first, a local straightening of chain segments, clustering of these chain segments followed by coalescence of clusters to lamellae, and a final collapse into a single lamella.

A brief review of the vast field of the molecular origins of the polymer phase transitions was presented. Fundamental questions still remain regarding the origin of the sub-glass transitions, glass transitions and melting point of polymers in general. Therefore, the purpose of this work was to try to shed further insights into the atomistic origins of the thermo-physical properties of polymers using a simple poly (ethylene) like polymer model. Before proceeding with the results of this study, a special literature review on the phase transitions and relaxations of polyethylene is presented in detail.

Discussion of Experimental Phase transitions of Poly (ethylene)

The temperature and assignment of the phase transitions of poly (ethylene) other than melting have been a matter of controversy. The latest quote for the glass transition of poly (ethylene) which is believed to be amorphous in origin is 237 K, which corresponds to the temperature of half vitrification according to Wunderlich and co-workers.[11] The change in heat capacity at Tg was reported as ΔC_p=10.5 J/Kmol. The previous T_g value cited by Wunderlich was 252 K. The best equilibrium melting point

of poly (ethylene) also determined by Wunderlich was 414.6 (±0.50 K) with a ΔH of fusion of 4.1 (±0.2) kjoul/mol of CH_2.[12] A melting point of 394.2 K was obtained for paraffins of 140 methylene units. The origins of lower temperature transitions/relaxations has been reviewed by Boyd.[13] In this review, the relaxations are categorized in various groups. A high temperature process (α) is associated with the crystal fraction in a semicrystalline polymer. The β process is related to the glass transition occurring mainly in the amorphous fraction, and its origin comes from the glass-rubber relaxation. It is believed that the low temperature process (γ) is associated with the amorphous fraction, but many groups suggest that the crystal part plays an important role as well. Thus, polymers with low crystallinity will show a clear β process while high crystallinity polymers will have both α and β processes. All of the types of media from crystalline to amorphous will have a low temperature γ process (known as β when α is absent). Furthermore, the β glass-rubber process is very broadened in semi-crystalline materials. In polyethylene, the γ relaxation is believed to be amorphous in origin. The process by which the origins of the various polyethylene relaxations were determined was reviewed systematically by Boyd as well[13b] and a summary based on this reference is provided below for each process.

Experimental Mechanical, Thermal, and Spectroscopic Experiments on Various Poly(ethylene) Samples

α process

Torsional pendulum mechanical studies have been carried out as a function of crystallinities for various linear polyethylene (LPE) samples. Dynamic shear responses were measured in the form of tanδ (known as the loss factor, G"/G', G' = storage modulus, G" = loss modulus). The peaks and valleys of tanδ were assigned to the γ, β, and α transitions. All experiments revealed that the crystal phase is involved in the α process. In another mechanical study, it was shown that the γ process disappears entirely in 100 % crystalline LPE. One of the conclusions by Boyd is that the origin of the mechanical α, β an γ relaxations is from the amorphous regions.[14] Additionally, the results of a series of mechanical dynamical relaxation experiments by Alberola suggested that the alpha relaxation was due to the diffusion of defects in the lamellar regions as well as compensating relaxation in the amorphous interfacial regions.

Dielectric Relaxation and NMR Studies on Poly (ethylene)

Since poly (ethylene) does not have any polar groups, usually it is functionalized chemically with a small concentration of carbonyl groups. Then dielectric relaxation studies are carried out. NMR studies are able to detect different kinds of motion occurring in a polymer. Using these techniques for the α process study, it was concluded that the dielectric and NMR experiments measure processes associated with reorientational motions within the crystalline phase. However, the mechanical α

process measures relaxations in the amorphous phase that requires the presence of the crystal phase.

β *process*

NMR studies reveal that molecular motions become especially unrestricted in the amorphous region as the glass transition is approached. Specimens quenched rapidly show a much more pronounced mechanical β-relaxation due to a higher amorphous fraction. In another mechanical relaxation experiment, the crystallinity portion of a polyethylene sample was eliminated through co-polymerization and the β process was traced to the amorphous fraction.

In another study, pure amorphous LPE was produced by fast quenching of thin samples, and mechanical relaxation studies (torsion pendulum) were carried out. A γ process at 150 K was observed, as well as relaxation processes at 190 K, 260 K and 370 K. The relaxation at 190 K was explained as the glass-rubber relaxation of "unconstrained amorphous PE. The process at 260 K was interpreted as the glass-rubber relaxation of the "crystal-constrained" amorphous fraction. The 370 K relaxation was assigned to the α process. When the temperature scan was repeated several times, a broad β process centered at 230 K was observed between the γ and α peaks. Furthermore, in a careful analysis of experimental dynamic shear modulus data as a function of crystallinity, Boyd concluded that the β process is insensitive to crystallinity.[14]

γ process

The γ process is amorphous in origin according to mechanical relaxation data, dielectric relaxation, and NMR relaxation (broad-line proton resonance) measurements. Several studied have been done to rule out the crystalline phase as the origin of the γ process. One example of a careful study was by Passaglia[15] who studied a macroscopic single crystal of n-Eicosane (20 carbons) and found no mechanical relaxation at the γ region. In another study by Crissman, the complex tensile moduli of poly-crystalline n-$C_{94}H_{190}$ were determined and no relaxations were found around the γ region. In contrast, completely amorphous branched polyethylene (also partially chlorinated) clearly showed a γ relaxation from shear modulus studies.[13c] Furthermore, NMR measurements have revealed a local crankshaft motion (three bond) occurring at this region.

In a further study, Laredo et. al. studied the relaxations of linear low density polyethylene by thermally stimulated depolarization currents.[16] The basic procedure is to place the polyethylene sample functionalized with diethyl maleate polar groups between two capacitor plates at a given temperature, apply a high voltage, quench the sample, to a low temperature, and then gradually heat up the sample at a fixed rate. The relaxation temperatures are detected by the current generated around the relaxing regions. With this technique, a sub-γ relaxation at 116 K and a γ relaxation at 134 K were detected, as well as a β relaxation at 232 K. The conclusion was that the γ and β relaxations represented two glass transition temperatures and the sub-γ relaxation

corresponded to a sub-glass process. Furthermore, NMR measurements have revealed a local crankshaft motion (three bonds).

Theretore, although some controversy exists about the origin and number of γ processes, it is generally agreed that the γ relaxation is amorphous in origin.

Heat Capacities

Experimentally, the α, β and γ regions have small and poorly resolved increases in heat capacities in semicrystalline polymers relative to the extrapolated heat capacity of a pure crystalline polymer as shown in **Figure 1a.**

Conclusion on Experimental Evidence for the Various Phase Transitions and Relaxations in Polyethylene

Experimental evidence from the literature was presented revealing the nature of the various phase transitions and relaxations in polyethylene. The melting point (T_m=414.6 K) is a well defined first order thermodynamics process. The α relaxation process occurs in the amorphous fraction of a PE, but requires the presence of the crystalline phase. Additionally, the α-relaxation occurs at a (temperature range 300-400) temperature somewhat lower than T_m. but certainly higher than T_g.[17] Second, the glass transition (rubber-glass) is a pseudo-second order phase transition with an associated β relaxation. The latest value of T_g is 237 K for pure amorphous materials, although it may be shifted toward higher values for semi-crystalline polymers. Third, the γ-relaxation occurs exclusively in the amorphous phase and does not require the

presence of the crystalline phase. There are a range of Tγ temperatures in the literature among them 153, 159,175 K for LDPE, 152 and 153 K for HDPE and 149 K for LLDPE.[17]

Atomistic Model Study of a Semi-Crystalline Poly (ethylene) System

(gauche energy=1.14 kcal/mol, trans-gauche barrier=3.01 kcal/mol)

A review of the experimental studies of the bulk phase transitions of poly (ethylene) has been presented to allow a comparison with the properties of the polyethylene system in this study. Mechanical properties (tensile modulus), storage and loss modulus, differential scanning calorimetry and volumetric properties as well as molecular motional correlation times (NMR) are valuable experimental tools in understanding the thermo-physical properties of poly (ethylene) as well as other polymers. However the detailed atomistic origin of the phase transitions of polymers is not completely understood. As a result, the phase transitions of a system of linear chains resembling poly (ethylene) under periodic boundary conditions was studied using molecular dynamics techniques. The advantage of fully atomistic simulations is that virtually all information is measurable from atomic vibrations to collective chain motions. The details of the procedure used in a study of a semi-crystalline polymer model are presented, followed by a detailed analysis of the results.

Procedure

Four united atom chains, each one hundred of 150 beads each were constructed into an initial amorphous bulk system with the use of a Cerius2 amorphous builder at a density of 0.92 g/cc. Then the system was minimized to a root mean square force of 0.50 kcal/mol/Å and relaxed for 20 ps with fixed volume canonical (TVN) dynamics at 550 K. A time step of 3 femto-seconds (fs) was used in all simulations. Then the volume was allowed to equilibrate for 700 ps at 550 K using the canonical "constant pressure" (TPN) dynamics with a piston mass of 0.10. After equilibration, the last snapshot and velocities of the 700 ps @550 K trajectory was extracted and a new 200 ps trajectory at a temperature of 550K was created and measurements were taken from this run. Snapshots were written to the trajectory every 0.297 ps. Then velocities were extracted from the end of the 200 ps 550 K trajectory to start a new 525 K trajectory, and this process was repeated down to 50 K. This process will be referred to "quench 1" run. Then a second "quench2" run was created by extracting the final snapshot of the 550 K "quench 1" run and the dynamics was run at 550 K for 200 ps. Then a new temperature ramp from 550 K to 50 K was created and this is referred to as "quench2." The previous process was repeated six times (quench 1-6) and the results presented here are ensemble averages of the six runs which are closely related. In most cases studied, standard deviations were not calculated since the samples were not truly independent measurements.

Force Field Parameters

The forcefields used in this chapter used simple non-bonded and valence parameters that approximately reproduced the experimental cohesive energy and bulk modulus of the orthorhombic of crystalline polyethylene. (Ref Naoki)[18]

a) Nonbond

A simple united atom representation of the methylene (CH_2) unit was used where nonbonded interactions were of the Lennard Jones form,

$$E_{VDW}= D_0\{ [R_0/R]^{12} -2[R_0/R]^6 \} \quad (1)$$

where D_0 is the well depth with value of 0.1411 kcal/mol, and the equilibrium distance is R_0 with a value of 4.483 Å. A spline cut off of 8.00 Å (turned off at 8.50 Å) was used for computational expediency.

Torsional Potential

The torsional energy was in the Fourier series form of

$$V(\phi)=V_0 + V_1\cos(\phi) + V_2\cos(2\phi) +V_3\cos(3\phi) +V_4\cos(4\phi) +V_5\cos(5\phi) +V_6\cos(6\phi) \quad (2)$$

where V_0=2.5722 kcal/mol, V_1=1.6383 kcal/mol, V_2=0.7565 kcal/mol, V_3= 1.6771 kcal/mol, V_4= 0.0384 kcal/mol, V_5=0.0417 kcal/mol and V_6= -0.0034 kcal/mol. This leads to a trans 180° energy minimum relative to the gauche local minima at ± 69.20° with an energy of 1.1417 kcal/mol, local maxima at ±119.76° with an energy of 3.0073 kcal/mol an a global maximum at 0° with an energy of 6.7142 kcal/mol. The *trans-gauche* barrier is 3.007 kcal/mol. The relative gauche energy of 1.14 kcal/mol originated from an ab initio Hartree Fock study of n-pentane with the 6-31G** basis set.

Valence Parameters

A simple harmonic potential of the form

$E_B = (1/2)K_B(R-R_0)^2$ (3)

was used for the bond term, where the bond force constant was set to 800 kcal/molÅ^2 and the equilibrium distance R_0 was set to 1.531 Å.

A simple harmonic potential of the form

$E_\theta = (1/2)K_\theta(\theta-\theta_0)^2$ (4)

was used where the force constant was set to 70.0 kcal/molrad^2 and the equilibrium angle θ_0 was set to 112.13^0.

Orthorhombic Crystalline Poly (ethylene) Properties

The forcefield values of various properties of the orthorhombic crystal structure of poly (ethylene) are compared to the experimental values in **Table 1**. The properties of crystal poly (ethylene) predicted by the forcefield are in reasonable agreement with the experimental values. Some of the lattice parameters are not reproduced with very high accuracy due to the united atom representation of the methylene unit. The forcefield calculated bulk modulus and binding energy per methylene unit of 0.0815 GPa^{-1} and 2.14 kcal/mol respectively are in reasonable agreement with the corresponding experimental values of 0.0937 GPa^{-1} and 2.049 kcal/mol.

Analysis of Results

VOLUMETRIC(Tg)

The volume versus temperature curve averaged over the six "quench runs" is given in **Figure 1** as well as the "SMOOTH" Stineman curve fit for the data points.[19] "Smooth" fitting is found in the *Kaleidagraf* software.[20] At temperatures above the glass transition, the volume uncertainties are relatively small, but in the glassy temperature region, the volume uncertainties are considerably large (it must be pointed out that the six "quench" runs are not strictly independent from each other, and therefore caution must be taken in interpreting the standard deviation). The interpretation of this result is that around the glass transition, samples collapse in a variety of ways depending on the configurations in the melt. Therefore, at temperatures below the glass temperature, the system is very heterogeneous. Experimentally, one would see heterogeneous micro-configurations in bulk polyethylene below the T_g, while a more homogeneous behavior for the melt above T_g. The calculated glass transition temperature from the "volume intersection method" is 286.11 K and is shown in **Figure 2** and summarized in **Table 2.**

Specific Thermal expansivity (alpha, units 1/K)

The thermal expansivity is defined by

$$\alpha=(dV/dT)/V \quad (5)$$

where V is the volume. The value α may be calculated from numerical derivatives of the "Stineman" curve and is shown in **Figure 3.** The tentative assignment of the main

thermal transitions are a melting point (T_m) at 441 K, two tentative a relaxations at 309 K ($\alpha 1$) and 358 K ($\alpha 2$), a possible relaxation at 229 K which is assigned at $\beta 1$ and a low temperature relaxation at 165 K which is assigned as a γ transition.

Thermal Characterization

The enthalpy (sum of Kinetic and Potential energy) versus temperature curve averaged over the six "quench runs" and the associated uncertainties are given in **Figure 4**. Enthalpy uncertainties are much smaller than volume uncertainties. The enthalpy "intersection" method was used to calculate a T_g of 286.11 K as shown in **Figure 5**. The statistics for the fit are given in **Table 3**.

Additionally, a "SMOOTH" Stineman fit interpolation was carried out for the enthalpy points. The heat capacity curve in **Figure 6** may be calculated numerically from the derivative of the "SMOOTH" enthalpy curve as defined by

$C_v=(dH/dt)$ (6)

The tentative assignments for the phase transitions are a melting point (T_m) at 434 K, and a gamma relaxation (γ_1) at 161 K, in agreement with the observed T_m and γ transition temperatures determined from the α-curve. Other transitions/relaxations are not observable.

In order to determine the relevance of the intra-molecular torsional energy and the nonbond van der Waals energy to the heat capacity, the derivatives of both energies with respect to temperature were calculated and are shown in **Figure 7**. The torsional contribution to the heat capacity appears to be great at the melting point (Tm=433 K) with a tentative T_g (inflection) at 301 K and very subtle γ (159 K) and β points (203K).

On the other hand, the Van der Waals energy derivative has a T_m of 437 K and a clearer glass transition (inflection point) at 301 K. A clearer Van der Waals γ at 164 K and β at 231 K has been assigned.

Mechanical Characterization

The compressibility (β_C) of a bulk system may be calculated from the volume fluctuations over a given molecular dynamics trajectory where R is the molar Boltzmann constant and T is the temperature:

$$\beta_c = (\langle V^2 \rangle - \langle V \rangle^2)/(VRT) \quad (7)$$

In this study, the compressibility was calculated by averaging six compressibilities obtained from each individual run for a given temperature. The temperature dependence of β_c is shown in **Figure 8**. The "mechanical" T_g of 296.92 K was calculated by the intersection of two linear fits of a lower set of temperatures (125 K to 225 K, R=0.96993) and an upper linear curve fit (325 K to 425 K, R=0.99546). The "mechanical" T_g agrees well with the "volumetric" T_g. Additionally, the mechanical T_g is a measure of the overall softening point of the bulk polymer. Another interesting derived quantity is the derivative of the compressibility with respect to temperature shown in **Figure 9** that was calculated numerically from a Stineman fit (not including anomalous point at 550 K). The "mechanical" melting point of 440 K agrees well with the volumetric and thermal values. Although the derivative curve appears to have many features at temperatures below the melting point, it is interesting to note that the last and well defined high temperature peak occurs at 289 K which is very similar to the previously

calculated glass transition by the enthalpy and volume intersection methods. The low temperature compressibility values are not reliable because Equation 7 diverges as the temperature approaches zero.

Molecular Structure Analysis for the Various Phase Transitions

The crystalline content of a polymeric material such as poly (ethylene) may be analyzed by calculating its order parameter, which is defined as

$$OP = (1/2)(3\langle\cos^2\theta\rangle - 1) \quad (8)$$

where θ is the angle between two vectors defined by the structure of the polymer. In this study, three distinct types of order parameters were calculated.

Temperature Dependence of the Intra Chain Order Parameter and Angular Distribution

The first kind of order parameter, the intra-chain order parameter, is a measure of the average curvature of a given chain in the polymer. If the chain adopts the all *trans* conformation, Equation 8 would approach 1.0. The intra chain vectors were generated from the position of one atom in the chain to another, and the "stride" length was chosen as four. Thus, in a chain with methylene units numbered 1 to 150, the first vector would range from atom 1 to atom 5 (1-5), the second vector would be atom 2 to atom 6, and the last vector would be formed between atoms 146 to 150. The midpoint of the vector was chosen to define the vector "position." A cutoff distance of 6.50 Å between vector midpoints was used to measure the short-range intra chain order parameter. The average intra chain order parameter is given in **Figure 10**. Several features stand out. First, a rapid increase in the order parameter is noticeable around

the melting point, and a leveling off to a value of 0.60 is reached just above the glass temperature region (300 K). The angular distribution of the short-range intra chain vector orientations was calculated from 0^0 to 90^0 in which 0^0 corresponds to both parallel and anti-parallel vectors. **Figures 11 through 20** contain intra chain vector angular distributions for temperatures spaced 50 K apart for comparison purposes. The distribution bins are 5^0. For example, **Figure 11** contains the intra chain angular vector distribution for the temperatures 50 K and 100 K.

Analysis of the Intra Chain Vector Angular Distribution As a Function of Key Phase Transition or Relaxation Temperatures

γ transition or relaxation

No remarkable change occurs for the intra chain vector angular distribution around the γ point as shown in **Figure 13** (150 K to 200 K).

β point or relaxation

As with the γ point, no remarkable change occurs in the distribution around the β point as shown in **Figure 14** (200 K to 250 K).

T_g (glass transition)

There is a small but noticeable change at the $0\text{-}5^0$ bin occupation around the glass temperature as shown in **Figure 15**. This is interpreted as the beginnings of intra-molecular mobility.

T_m (melting point)

The bimodal distribution changes noticeably around the melting point (400 K to 450 K) as shown in **Figure 18.** The angular population peaks shift from nearly equality at 450 K to larger occupation for the 5-10 degree bin (as opposed to the 25-30° bin population) at 400 K.

Temperature Dependence of the Inter Chain Plane Order Parameter and Angular Distribution

Each set of three poly (ethylene) atoms in a chain define a plane, which is defined as the cross product of the two centrally connected vectors. Therefore, a set of "plane" vectors were calculated for each set of three atoms in each chain, and the "position" of each vector was defined as the central atom. Therefore, in a chain of 150 beads, there are 148 "plane" vectors, whose origin is located at atoms 2-149. Then the "planar" order parameter was calculated with two restrictions: First, no two vectors between the same chain were considered unless their carbon atom separation was greater or equal to 6. So, for example, in a given chain, the angle between the vector with origin at atom 1 and atom 7 was considered but not between atoms 1 and 6. The reason is that a "stride" of 6 is possibly long enough to avoid intra-chain planar calculations but short enough to allow the possibility for the chain to wind around, becoming an "external" nearest neighbor.

The resulting average planar order parameter as a function of temperature is given in **Figure 21.** Note again the leveling off of the order parameter around the glass temperature, and the rapid increase just below the melting point. No special

observations can be made around the γ or β point for the average planar order parameter. The planar angle vector distribution was calculated for the pure orthorhombic crystal (**Figure 22**) and for various temperatures for the semi-crystalline system as was done for the intra chain order parameters. Note that the crystal distribution has two spikes, the first one corresponds to the same plane orientation, and the second one corresponds to the crystal inter-layer orientation. The inter-planar vector angle distribution is given in **Figures 23-32** for the semi-crystalline case.

Analysis of the Inter Planar Vector Angular Distribution As a Function of Key Phase Transition or Relaxation Temperatures

γ point

Minor shifts in the distribution occur between 150-200 K (**Figure 25**)

β point

Minor shifts in the distribution occur between 200-250 K (**Figure 26**)

T_g (glass transition)

Small but widespread changes in the distribution occur between 250 K to 300 K (**Figure 27**).

T_m (melting point)

The distribution "inverts"about the 45-degree value at the melting point (**Figure30**).

Temperature Dependènce of the Inter Chain Axis Order Parameter and Angular Distribution

In this study, the vectors were defined in the same way as the intrachain order parameter study, except, this time the angle between the vectors within the same chain were not considered unless their index difference was six or greater. For example, the angle between the first and seventh vectors was calculated but not the angle between the first and sixth vector. The purpose of this procedure was to minimize the short range intrachain order parameter contribution to the inter chain axis order parameter, while still including intrachain folding effects such as occurs in lamellae, in which the external nearest neighbor is from the same chain. The resulting average inter chain axis order parameter is shown in **Figure 33**. Note a rapid increase in the order parameter around the melting point region, while a slowing down at the glass temperature. The inter-axial order parameter curve was spline fitted and the first derivative was taken analytically as shown in **Figure 34**. The minimum at 431.32 K corresponds to the largest rate of order parameter change with respect to temperature at the melting point and levels off around the glass temperature. The corresponding inter chain vector angular distributions are shown in **Figures 35-44**.

Analysis of the Inter Chain Axis Vector Angular Distribution As a Function of Key Phase Transition or Relaxation Temperatures

γ *point*

Noticeable sharpening at low angles of the distribution occurs between 150-200 K (**Figure 37**)

β *relaxation*

The position of the distribution peak shifts between 200-250 K (**Figure 38**)

T_g (glass transition)

Small but widespread changes in the distribution occur between 250 K to 300 K (**Figure 39**).

T_m (melting point)

A relatively large shift of the distribution towards lower inter chain axis angles is observed at the melting point as the temperature is increased (**Figure 42**).

Analysis of the Temperature Dependence of the Torsional State Occupations, Transition Cooperativity and Torsional Transition Kinetics

The temperature dependence of the occupation of the *trans* and *gauche* torsional states is shown in **Figure 45**. The highest increase in the percent *trans* population occurs approximately around the melting point region (400-450 K) and levels off at around 350 K.

Spiess and co-workers have studied the molecular motions of linear polyethylene with deuterium quadrupole resonance NMR techniques.[21] The C-D bond reorientation data around the γ point could be explained as a local three-bond crankshaft motion. However, at higher temperatures such as β the relaxation region, the data was consistent with longer bond re-orientations. However, even at higher temperatures, there were considerable constraints on bond reorientation.

In this study, the average torsional transition correlation was measured as a function of temperatures from 550K to 275 K where numerous transitions occurred to obtain a statistically meaningful result. The procedure for calculating the transition

correlation value for a given chain is defined as $<\phi_i\phi_{i+j}>$, where ϕ=1 if a transition occurs at a given snapshot, and ϕ=0 if it does not. Therefore, if a transition at torsion *i* occurs at the same time (within the same snapshot) as torsion *i+j*, then $\phi_i\phi_{i+j}$ is 1, otherwise it is zero. The transition correlation value is measured over all possible torsions and times for a given chain and the average value $<\phi_i\phi_{i+j}>$ is obtained. Then, the correlation value for the scenario of non correlated transitions (random) was calculated ($<\phi_i\phi_{i+j}>_{rand}$) and the percent correlation deviation from random (CDEV) is given by

$$CDEV=100*(<\phi_i\phi_{i+j}>-<\phi_i\phi_{i+j}>_{rand})/<\phi_i\phi_{i+j}>_{rand} \quad (9)$$

The procedure is repeated for the other three chains, and an average percent correlation over the four chains was calculated for a given quench run. Finally, a *grand* average percent deviation correlation was calculated over the six quench runs as presented in **Figure 45b**. From this study, it appears that the transitions occurring between torsions i and i+2 are strongly correlated, while transitions i, i+1, i, i+3 and i, i+4 are weakly correlated and occur almost as random processes (also very infrequent). Additionally, the i+2 torsion coupling mechanism dominates at all temperatures, and becomes more important at lower temperatures. However, at lower temperatures, transitions begin to occur more like isolated events. These results are in agreement with the molecular dynamics studies of bulk polyethylene by Boyd.[22]

Torsional Transition Kinetics

The torsional transition rate for the poly (ethylene) bulk system was measured as a function of temperature and the resulting curve is shown in **Figure 46**. The effective

"bulk" torsional barrier was determined from an Arrhenius plot of the conformational rate as a function of temperature shown in **Figure 47**. The statistics for the fits are summarized in **Table 4**. It is interesting to note that the "effective" barrier at temperatures above the glass transition (4.94 kcal/ml) is higher than the effective barrier below the glass transition (2.418 kcal/mol). Additionally, the intercept for the Arrhenius plot at higher temperatures is much higher than the intercept for the lower temperatures, which means that at higher temperatures the entropy of activation is less unfavorable upon a torsional transition relative to the entropy change below the glass temperature. This is reasonable since below T_g, there is a greater torsional cooperativity because of the lower free volume available. Additionally, greater cooperativity implies a lower "transition energy" barrier at the cost of unfavorable entropy changes. An additional observation is that the intersection temperature between the lines corresponding to fit number one and fit number two is 311.08 K which is close the T_g calculated using the volume (286.11 K) and enthalpy (289.97 K) methods previously described. Finally, the intersection temperatures between the lines corresponding to fit number two and fit number three is 194.59 K which is similar to the tentative gamma transition temperature assignment of 165 K using the "SMOOTH" volume derivative method and 161 K using the "SMOOTH" enthalpy derivative method. Therefore, the molecular environment in the liquid state above the T_g has a characteristic effect on the effective torsional barrier and entropy of activation and the same observation applies to the glassy temperature region and the sub-glass (below the gamma point) temperature region. Specifically, there is a halving in the effective torsional barrier when going from

the liquid to the glass state, and a further halving in the apparent torsional barrier when going from the glass state to the sub-gamma state. The seemingly counter-intuitive barrier effects are compensated by an approximate halving in the ln (pre-exponential factor) related to the entropy of activation when going from the liquid to glass and glass to sub-gamma phase, which means that torsional rearrangements become much more cooperative as the system becomes more compact and rigid.

Finally, let us define the thermal ratio at the glass transition (TR) as

$$TR = E_a / k_B T_g \qquad (10)$$

where E_a is the Arrhenius activation energy of torsional transition in the liquid phase above T_g and k_B is Boltzmann's constant. This definition will be useful in determining whether the glass transition is a kinetic phenomenon or not. **Table 5** contains a listing of the thermal ratio at the glass transition and the gamma transition for the semi-crystalline system. In terms of the effective barrier, a thermal ratio of 8.634 was calculated for T_g and a thermal ratio of 7.465 was calculated for T_γ.

Conclusion

Tentative assignments and characterizations of the various phase transitions of the poly (ethylene) semi-crystalline model were given. The results partially agreed with the experimental physical characterization of polyethylene found in the literature. The general phenomena of partial crystallization was captured in this model with a calculated melting point T_m of 434 K while the experimental value is 414.6 K. The evidence supporting the melting point transition in this model was presented trough various structural order parameters, torsional state occupation as well as volumetric

and enthalpic data. However, the melting point of the model presented was very broad, which is possibly a consequence of a high cooling rate (200ps/25 K) which promotes non-equilibrium conditions. The glass transition (T_g) was determined from enthalpic and volumetric data using graphical intersection techniques. The calculated T_g for the volumetric data is 286.11 K, which compares well with the enthalpy intersection method (289.97 K). Additionally, there was evidence for sub-glass relaxations, which are tentatively called γ and β based mainly on the heat capacity curve and specific thermal expansivity curves and the changes in the inter-axial and the intra-axial order parameters. Based on the heat capacity curve the tentative T_γ temperature is around 160 K while the T_β relaxation is around 230 K. The γ and β transitions also show up in the Van der Waals and torsion energy derivatives with respect to temperature shown in **Figure 7.** Finally, a simplified model resembling polyethylene was thoroughly studied and the atomistic origins of some phase transitions were explained. Next, the influence on the *trans-gauche* torsional barrier on the glass transition of a semi-crystalline polyethylene model will be discussed.

Dependence of T_g on the Intramolecular Torsional Barrier for Medium Crystalline Polymers: *Gauche* energy=1.14 kcal/mol

The factors influencing the glass transition have not been clearly understood at the molecular level due to a lack of a systematic de-coupling of intermolecular and intra-molecular effects. Therefore, the effect of the *trans-gauche* barrier height on the phase transition was investigated for the simplified polyethylene model with a fixed

trans-gauche energy difference of 1.14 kcal/mol. The four torsional barriers were 1.99 kcal/mol, 3.01 kcal/mol (previously described), 4.03 kcal/mol and 6.07 kcal/mol.

Thermal and Volumetric Glass Transitions: The intersection Method

The thermal and volumetric glass transitions of the four cases studied were determined through linear fits of the lower and upper temperature regions. The volume and enthalpy intersection method results are summarized in **Table 6** as well as the corresponding figure numbers. From **Table 6**, it is apparent that only a marginal increase in T_g of approximately 30 K occurs when the trans-gauche barrier changes from 1.99 kcal/mol to 3.01 kcal/mol. However, as the barrier increases further, the glass transition appears to decrease very slowly. A possible explanation is that for a given cooling rate, the efficiency of intermolecular packing in a semi-crystalline system decreases as the barrier is increased, with a resulting greater fraction of free volume which may account for the counterintuitive results of the simulation experiment. To illustrate this point, the compressibilities for the four cases studied are shown in **Figure 54**. Note that the compressibilities for the 6.07 kcal/mol barrier case are considerably smaller than all of the other quench runs, which is interpreted as a larger free volume. Finally, there seems to be a cancellation of effects for the different barrier cases due to a decreasing density at a given temperature with an increasing torsional barrier. For example, as shown in Table 6, the case with the 3.01 kcal/mol torsional barrier has an average density at 300 K of 0.919 g/cc (actual T_g = 288.04 K) and a (forcefield torsional) barrier to $k_B T_g$ ratio of 5.26. In contrast, the case with the 4.03 kcal/mol torsional barrier has an average density at 300 K of 0.895 g/cc (actual T_g of 288.46 K) and a barrier to $k_B T_g$

ratio of 7.03. One would expect the case with the 4.03 kcal/mol barrier to have a higher T_g than the 3.01 kcal/mol case, but the lower density of the 4.03 kcal/mol (more free volume) apparently cancels this effect and the result is a nearly identical T_g for both cases. The calculated lower density for the higher barrier case is probably due to a less efficient search to form compact crystal structures, which means that for a given cooling rate, the higher barrier will pack less efficiently than a lower barrier case for systems where there is a driving force to pack in a semi-crystalline fashion. Finally, the linear coefficient of expansion below and above T_g is listed in **Table 7** as a function of barrier height. Similarly, the heat capacity below and above T_g is given in **Table 8**.

The torsional barrier dependent studies were analyzed in terms of the heat capacity and thermal expansivity. The thermal expansivity and heat capacity curves for the 1.99 kcal/mol *trans-gauche* barrier are shown in **Figures 55** and **56** respectively. The respective thermal expansivity and heat capacity curves for the 3.01 kcal/mol *trans-gauche* barrier original case are shown in **Figures 3** and **6** respectively. The respective thermal expansivity and heat capacity curves for the 4.03 kcal/mol *trans-gauche* barrier are shown in **Figures 57** and **58** respectively. The respective thermal expansivity and heat capacity curves for the 6.07 kcal/mol *trans-gauche* barrier are shown in **Figures 59** and **60** respectively. The tentative assignments for various transitions are summarized in **Table 9**. However, little or no supporting evidence is given to justify the proposed assignments.

Discussion of Alpha and Heat Capacity Curves for the Barrier Study

The *trans-gauche* barrier cases ranging from 1.99 to 4.03 kcal/mol all show consistently a gamma (T_γ) around 160 K and a melting point (T_m) transition at around 430-440 K. Other intermediate transitions such as the tentatively assigned beta (T_γ) and alpha (T_α) transitions occur at various temperatures, depending on the barrier height as shown in **Table 9**. For example, the barrier cases ranging from 1.99-3.01 kcal/mol all have (alpha or heat capacity) a beta relaxation around 230 K (assigned as $T\beta$) while the 4.01 kcal/mol barrier case has higher temperature beta temperature (286 K in alpha curve, and 250 K in heat capacity curve). The barrier cases ranging from 1.99 to 4.03 kcal/mol also have what are assigned as alpha relaxations ($T\alpha$) at higher temperatures (280 K to 360 K). The lowest barrier case (1.99 kcal/mol) clearly has the lowest temperature (282K for the alpha curve, 301 K for the heat capacity curve) "alpha" shoulder next to the melting point. However, clear trends in the $T\alpha$ temperatures are not observed as a function of barrier height. As mentioned before, with the exception of the melting point and gamma point, all other temperature assignments are speculative for the barrier case study on the semi-crystalline system.

The *trans-gauche* barrier study of 6.07 kcal/mol is very different from the rest of the lower barrier cases. The only clear result is that a polymer collapse or melting point occurs around 514-516 K. Two other transitions at 238 K and 338 K of unknown origin occur in the (alpha curve) and a transition at 338 K shows up in the heat capacity curve.

The results for the specific expansivity and heat capacity dependence on the barrier height are summarized in **Figures 61** and **62** respectively. A clear trend is that as

the barrier increases, the melting point peak height decreases and the speculated "polymer collapse" transition around 500 K becomes better resolved in both the alpha and heat capacity curves. Therefore at a fixed cooling rate, the barrier height does not affect the melting point temperature but it decreases its strength. However, at the barrier height of 6.07 kcal/mol, the melting point becomes a mere shoulder region of the high temperature collapse point.

Purely Amorphous Glass Transition Barrier Dependence Study

In order to complement the studies of the glass transition dependence on barrier, several studies were done where the *trans* and *gauche* energy levels were set equal to each other to favor a bulk amorphous system. The first case was a system with no torsional energy term, which means that the polymer was virtually a free rotor. The average volume and enthalpy curves for six quench runs were fitted to a straight line for the whole temperature range (**Figures 63** and **64** respectively), since there was no clear T_g throughout the whole temperature range. It is possible that a glass transition exists between 0 to 50 K but this was not explored further.

Next, "quench" runs with different barriers but equal *gauche* and *trans* energies were simulated. The torsional energies for the various states are summarized in **Table 10**. The thermal and volumetric glass transitions of the four cases studied were determined through linear fits of lower and upper temperature regions. The volume and enthalpy intersection results are summarized in **Table 11**. Finally, the linear coefficient of expansion below and above T_g is listed in **Table 12** as a function of barrier

height for the amorphous cases. Similarly, the heat capacity below and above T_g is given in **Table 13** as a function of barrier height for the amorphous cases.

Discussion of the Effects of the *Forcefield* Torsional Barrier on the Glass Transition of Amorphous Polymers

The glass transition for various torsional barriers was studied for a system in which the *gauche* conformational energy was equivalent to the *trans* conformational energy. The case where all the torsional states were equivalent in energy (no barrier) resulted in an unobservable glass transitions down to 50 K. It is possible that below 50 K there exists a glass transition but this was not determined. Therefore, the glass transition was assigned as 0.00 K. In contrast, the case with a 2.88 kcal/mol barrier had a T_g of 173.26 K as shown in Table 11. The ratio of the barrier energy over the characteristic thermal energy (k_BT_g) at the glass temperature was 8.36 for this case with a relative rate of 2.33E-4. The thermal ratio is important because it is a measure of the kinetic effects at the glass transition as shown in the Arrhenius expression for the reaction rate is given by

$$K=Ae^{-(E_a/k_BT)} \qquad (11)$$

where A is the pre-exponential factor. The case with the 4.03 kcal/mol barrier resulted in a T_g of 247.93 K, a thermal ratio of 8.18 and a relative rate of 2.803E-4. Finally, the case with the 5.04 kcal/mol barrier resulted in a T_g of 292.50 K, a thermal ratio of 8.67 and a relative rate of 1.72E-4. The glass transition definitely has a positive correlation with the conformational barrier, but the thermal ratio for the various "molecular"

conformational barriers is not exactly the same. In terms of the Arrhenius rate constant, if the pre-exponential factor "*A*" is the same for the three barrier cases, then the glass transition is proportional to the *forcefield* barrier. In order to verify this hypothesis it is necessary to calculate the glass transition for a higher barrier (6.0 kcal/mol for example) and a lower barrier (1.0 cal/mol). An additional remark is that the calculated density near the glass transition decreases as the conformational barrier increases. This may lead to an effective lower barrier for the 5.04-kcal/mol conformational case, and a higher effective barrier for the 2.88 and 4.03 kcal/mol conformational barrier cases. The densities for all four-barrier cases are compared in **Figure 71**. Similarly, the compressibilities for the four barrier cases are shown in **Figure 72**. One interesting feature is that the 5.04 kcal/mol barrier case has a significantly lower compressibility at temperatures ranging from 275 K to 550 K than the other barrier cases. However, at lower temperatures, the compressibility of the higher barrier case is relatively higher than the other barrier cases due to less efficient packing.

The question remains of why the glass transition is relatively sensitive to the *gauche-trans* barrier when the *gauche* energy is equal to the *trans* energy, compared to the case where the *trans* conformation was 1.14 kcal/mol more stable than the *gauche* states. There is clearly a driving force to go to the *trans* state in the first case studied where the *trans* conformation is more stable than the *gauche* conformation by 1.14 kcal/mol. As the barrier is increased, it is harder for the polymer system to reach equilibrium and as a consequence, the density at all temperatures is generally lower because of less efficient packing. However, when the torsional barrier is decreased, the

system may find compact structures (all trans, semi-crystalline) more efficiently at a given temperature, but as it does this it conformationally traps itself. This may lead to a cancellation of effects leading to a weak T_g dependence on barrier for the case where the *gauche* energy is 1.14 kcal/mol more unstable than the *trans* energy.

In contrast, the case where the *gauche* and *trans* energy levels are equal, there is a relatively strong T_g dependence on the conformational barrier. Although, the crystalline phase is favored at very low temperatures due to better intermolecular packing, at higher temperatures the entropy term dominates leading to an equal population of the *trans* and two *gauche* conformations. Therefore, for temperatures significantly above 0 K, there is a relatively weak driving force to form the compact *trans* conformation. In the limit of no torsion, the glass transition has not appeared yet, even in the limit of 50 K. However, once a conformational barrier is placed on the system, the weak drive toward a compact state is stopped at given density and temperature.

Finally, the specific expansivity (alpha) and heat capacity (C_p) were calculated based on numerical derivatives of the "Stineman" smooth curve fit of the volume and enthalpy curves respectively. The specific expansivity curves in **Figure 73** are quite noisy, but a general displacement of the curves toward higher temperatures may be noted. However the heat capacity curves in **Figure 74** clearly have a general displacement toward higher temperatures as a function of barrier and are in qualitative agreement with the calculated glass transitions using the intersection method.

Molecular Structure Analysis as a Function of Temperature for Purely Amorphous Polymers with Different Torsional Barriers Where the Gauche Energy=Trans Energy

Intra-chain Order Parameter and Bond Vector Orientational Distribution as a Function of Torsional Barrier: The amorphous case

As mentioned previously the Intra-chain order parameter is a measure of the average curvature of a given chain in the polymer. A numerical value of one means that the chain is in an all-*trans* conformation.

The intra-chain order parameters for the 2.88 kcal/mol, 4.03 kcal/mol and 5.04 kcal/mol barrier cases are shown in **Figures 75,76 and 77** respectively. There is no clear or dramatic change in the intra-chain axis order parameter throughout a very wide temperature range. For example, the order parameter range for the 2.88 kcal/mol case is 0.27 to 0.29, 0.24 to 0.30 for the 4.03 kcal/mol barrier and 0.24 to 0.28 for the 5.04 kcal/mol range. However, the scatter in the intra-chain order parameter values tends to decrease as the temperature is lowered for all cases. The major conclusion is that the local intra-chain conformations are amorphous in nature since a purely random order parameter value would correspond to a value of zero.

The temperature dependence of the intra-chain angle distribution for the 2.88 kcal/mol barrier case is shown in **Figures 78-89**. The temperature dependence of the intra-chain angle distribution for the 4.03 kcal/mol barrier case is shown in **Figures 90-99**. Finally, the temperature dependence of the intra-chain angle distribution for the 5.04 kcal/mol barrier case is shown in **Figures 100-109**. The major observed features as a function of temperature is the broadening of the peak centered at a vector-vector

angle of 30° as the temperature is increased. There is no outstanding change in the distribution around the glass transition for all barrier cases.

Inter-chain Order Parameter and Bond Vector Orientational Distribution as a Function of Torsional Barrier: The amorphous case

The temperature dependence for the inter-chain order parameters for the 2.88 kcal/mol, 4.03 kcal/mol and 5.04 kcal/mol torsional barriers are shown in **Figures 110, 111** and **112** respectively. The order parameter values range from 0.07 to 0.11 for all cases, indicating that the structures are highly amorphous at all temperatures. However, it is interesting to note that the scatter in the order parameter decreases considerably at and below the glass transition for all of the cases studied which means that there are no major structural fluctuations and rearrangements below the glass transition temperature.

The temperature dependence of the inter-chain angle distribution for the 2.88 kcal/mol barrier case is shown in **Figures 113-122**. The temperature dependence of the inter-chain angle distribution for the 4.03 kcal/mol barrier case is shown in **Figures 123-132**. Finally, the temperature dependence of the inter-chain angle distribution for the 5.04 kcal/mol barrier case is shown in **Figures 133-142**. The overall order parameter is featureless at all temperatures and for all torsional barriers. The shape of the order parameter distribution is a function that starts at nearly zero population at 0°, increases gradually and levels off at 90°. There are no major characteristic changes around the glass transition temperatures for all the barrier cases studied, implying that the overall intermolecular topology has not changed significantly between 50 K to 550 K.

Inter-Planar Order Parameter and Bond Vector Orientational Distribution as a Function of Torsional Barrier: The amorphous case

The temperature dependence of the inter-planar order parameters for the 2.88 kcal/mol, 4.03 kcal/mol and 5.04 kcal/mol torsional barriers are shown in **Figures 143, 144** and **145** respectively. The order parameter values range from 0.01 to 0.03 for all cases, indicating that all the structures are highly amorphous at all temperatures. However, it is interesting to note that the scatter in the order parameter decreases considerably at temperatures below 200 K.

The temperature dependence of the inter-planar angle distribution for the 2.88 kcal/mol barrier case is shown in **Figures 146-155**. The temperature dependence of the inter-planar angle distribution for the 4.03 kcal/mol barrier case is shown in **Figures 156-165**. Finally, the inter-planar angle distribution as a function of temperature for the 5.04 kcal/mol barrier case is shown in **Figures 166-175**. The overall order parameter is featureless at all temperatures and for all torsional barriers. The shape of the order parameter distribution is a function that starts at nearly zero population at 0^0, increases gradually and levels off at 90^0. There are no major characteristic changes around the glass transition temperatures for all the barrier cases studied, implying that the overall intermolecular topology has not changed significantly between 50 K to 550 K.

Torsional Conformation Behavior and Transition Kinetics for Equal *Trans* and *Gauche* Energy Levels: The Amorphous Case

The temperature dependence of the torsional state populations for the model system with torsional barriers of 2.88 kcal/mol, 4.03 kcal/mol and 5.04 kcal/mol are shown in **Figures 176 to 178.** The percent *trans* population ranges from 50 % at higher temperatures (i.e. 550 K) to 60 % at lower temperatures (i. e. 50 K) regardless of barrier. The *gauche* population has an even weaker temperature dependence, which means that the moderate increase in the *trans* population as the temperature is lowered is primarily due to the decrease in population in transition state conformations. From this observation it may be concluded that it is necessary to have an intra-molecular low *trans* energy with respect to the *gauche* conformation in order to see a strong temperature dependence on the *trans* population. As an example, the semi-crystalline case previously described where the *trans* conformation was 1.14 kcal/mol more stable than the *gauche* conformation led to a strong dependence of the *trans* conformation occupation as shown in **Figure 45.** Finally, a complementary observation is that as the torsional barrier is raised, the fractional occupation of the torsional transition states is decreased at a given temperature as shown in **Figure 179.**

The temperature dependence of the torsional conformational rate (transitions per nanosecond per torsion) was measured in the bulk for the barriers 2.88, 4.03 and 5.04 kcal/mol as shown in **Figures 180, 181** and **182** respectively. For a given temperature, the calculated transition rate decreased as the barrier height is increased as expected. The degree of cooperativity of the transitions was measured as a function of

temperatures for the barrier heights 2.88, 4.03 and 5.04 kcal/mol as shown in **Figures 183, 184** and **185** respectively. All barrier cases clearly showed a dramatic increase in cooperativity in the 1-3 torsional coupling as the temperature in the bulk is lowered which is consistent with the commonly accepted "crankshaft" mechanism. The average percent deviation from random of correlated pair transitions for the 1-2, 1-4 and 1-5-torsion couplings were negligible compared to the 1-3 torsional coupling.

The effective torsional barriers of the three torsional cases studied were extracted from Arrhenius plots of ln (torsional rate) versus the inverse temperature and barriers were extracted from the slope. The Arrhenius plots for the 2.88 kcal/mol, 4.03 kcal/mol and 5.04 kcal/mol torsional barrier cases are shown in **Figures 186-188**. The statistics for the linear fits are shown in **Table 14**. The effective barrier in the liquid state (above T_g) is clearly higher than the effective barrier in the glassy state. For example, for the 2.88 kcal/mol forcefield barrier case, the effective barrier in the liquid state is 3.308 kcal/mol while the effective barrier for the glassy state is 1.372 kcal/mol. The intercept of the Arrhenius plot is the "natural logarithm" of the preexponential factor, which is a measure of the entropy of activation. Just for clarification, higher entropy of activation would favor the reaction rate. For all barrier cases studied, the entropy of activation is higher for the liquid state relative to the glassy state. For example, the 2.88 kcal/mol forcefield barrier case resulted in an Arrhenius plot intercept of 8.297 in the liquid state and 3.793 for the glassy state. This implies that a torsional transition in the glassy state must involve more cooperative motions with

respect to the liquid state which is consistent with the remarkable increase in 1-3 torsional coupling shown in **Figures 183, 184 and 185.**

An additional value reported in **Table 15** is the "Arrhenius" T_g defined as the intersection of the liquid and glassy linear fits of the Arrhenius plot. An interpretation of the "Arrhenius" T_g is the temperature at which the cooperative motions involved in conformational rearrangements change significantly. The "thermal" ratio of the effective barrier over the Boltzmann constant weighted glass transition (Effective Barrier/k_BT_g) was calculated for the three amorphous cases studied.
The thermal ratios for the "real" T_g are 8.365 for the 2.88 kcal/mol forcefield barrier, 8.180 for the 4.03 kcal/mol forcefield barrier and 8.671 for the 5.04 kcal/mol forcefield barrier. The effective torsional barrier results discussed next refer to the actual torsional barrier for the bulk system. The thermal ratios for the "real" T_g are 9.608 for the 3.308 kcal/mol effective barrier, 8.460 for the 4.168 kcal/mol effective barrier and 9.108 for the 5.294 kcal/mol effective barrier. Although not identical, the thermal ratios for different barriers are very similar in size. Simplistically one would expect for all the thermal ratios to be equal. However, further computer experiments with completely independent starting polymer configurations may be needed to calculate a more accurate thermal ratio. As mentioned earlier, the results presented basically originate from one random bulk polymer configuration with four chains. Additionally, polymer systems with forcefield barriers of 2.00 kcal/mol and 6.00 kcal/mol would be needed to clearly see if there is an approximately constant thermal ratio for the higher and lower torsional barrier ranges. Another question that could be answered is how the thermal

ratio changes as the torsional barrier approaches zero. Results presented earlier showed that there is no apparent glass transition for the case where there is no barrier, implying an "undefined" thermal ratio.

Conclusion of the Glass Transition in Amorphous Systems: The *Trans* equals *Gauche* Energy Case

Approximately constant thermal ratios of torsional barrier with respect to $k_B T_g$ were found for systems where the *trans* conformational energy was equal to the *gauche* conformational energy. Clearly, the glass transition increases with respect to the torsional barrier and disappears when the torsion barrier is removed. The cooperativity in torsional transitions changes dramatically when the polymer is quenched from the liquid to the glass. The evidence is in the dramatic increase in cooperativity of torsional transitions in form of the 1-3 torsional coupling and in the change in the intercept of the Arrhenius plot as the system is cooled from the melt to the glass. This means that the entropy of activation decreases dramatically at temperatures below T_g.

For amorphous systems, there is no obvious structural reorganization or change at T_g as demonstrated with the various order parameters studied. Therefore, the glass transition may be interpreted as the temperature where the bulk surroundings perturb the torsional transition state populations, causing a high degree of structural rearrangement cooperativity, and this occurs at a thermal ratio of 8.2 to 8.7 in terms of the forcefield barrier, and 8.5 to 9.6 for the "effective" bulk barrier. Another way of looking at the glass transition is the "falling" of torsional transition state conformations into the potential energy torsional minima catalyzed by the increasing pressure of the

bulk as the temperature is lowered. An indirect support of this observation is the absence of a glass transition for the polymer case that had a flat torsional potential (zero barriers). For comparison, Rigby and Roe calculated a finite but low value of T_g for a study where the torsional potential was turned off.[23] Additionally, they obtained a glass temperature for polyethylene of 230 K, in agreement with the experimental value.

Crystal Effects: The Glass Transition as a Function of the *Trans-Gauche* Conformational Energy Differences

In order to understand the effects of crystallinity on T_g, a series of polyethylene polymers were studied with different gauche-*trans* energy differences summarized in **Table 16**. The first case with equal *gauche* and *trans* energy levels and a barrier of 4.03 kcal/mol was previously discussed. Then, the *trans-gauche* energy difference was increased to 0.49 kcal/mol, with the torsional energies listed in **Table 16**, as well as other relevant cases. Some of the cases are reintroduced from the previous sections of this chapter. Additional cases are the ones with the *trans-gauche* energy difference of 1.50 kcal/mol but with different barriers. The temperature dependence of the volume and enthalpy for the 0.49 kcal/mol *gauche* energy and *trans-gauche* barrier of 4.03 kcal/mol is shown in **Figures 189** and **190** respectively. A glass transition for the two curves was calculated using the linear intersection method and the results are summarized in **Table 17** as well as the other barrier cases. Additionally, the expansivities and heat capacities below and above T_g were calculated with the linear intersection method as a function of the *gauche* energy (*trans-gauche* barrier fixed at 4.03

kcal/mol) and the results are summarized in **Tables 18** and **19** respectively. The thermal expansivity and heat capacity curves for the 0.49 kcal/mol *gauche* energy and *trans-gauche* barrier of 4.03 kcal/mol case are given in **Figures 191** and **192** respectively. An assignment of various transitions was made, although the values are useful only for qualitative purposes (**Table 20**).

Glass transitions were calculated for the case where the *gauche* energy was 1.50 kcal/mol and the trans-gauche barrier was 4.03 kcal/mol based on the intersection method for the volume (**Figure 193**) and enthalpy (**Figure 194**). The glass transitions were also calculated for the case where the gauche energy was 1.50 kcal/mol and the *trans-gauche* barrier was 4.39 kcal/mol based on the volume (**Figure 195**) and enthalpy (**Figure 196**). Additionally, the compressibility and density for the two barrier cases with an identical *gauche* energy of 1.50 kcal/mol are shown in **Figures 197** and **198** respectively. The calculated thermal expansivity and heat capacity curves are show in **Figures 199** and **200** respectively for both barrier cases with a fixed *gauche* energy of 1.50 kcal/mol. An apparent melting point of 526 K for the 4.03 kcal/mol barrier case and an apparent melting point of 514 K for the 4.39 kcal/mol barrier case was determined from the expansivity (**Figure 199**). An apparent melting point of 519 K and 515 K was determined for the 4.03 and 4.39 kcal/mol barrier cases respectively based on the heat capacity (**Figure 200**).

In order to study the effect of having a *gauche* state more stable relative to the *trans* state, a special torsional forcefield was constructed with the parameters shown in **Table 16**. This time the *gauche* state was -1.16 kcal/mol more stable than the *trans* state.

Also, the barrier refers to the *gauche-trans* torsional barrier, since it is the largest barrier the system will encounter. The calculated thermal expansivity and heat capacity curves are given in **Figures 201** and **202** respectively. The lowest observable transition appears to be first order since there is a peak in the expansivity at 238 K and a peak at 242 K in the heat capacity curve. However, the origin of this peak is not clear. Other two transitions of unclear origin occur at 363 K and 514 K in the expansivity curve and at 369 K and 465 K for the heat capacity curve. The glass transition was determined from the volume and enthalpy curves as shown in **Figures 201b** and **202b**. An average T_g of 209.35.0 K was calculated based on the linear intersection method.

Finally a complete summary of the calculated glass transitions for the cases with varying *gauche* energy are shown in **Table 17**. Some of the data was imported from previous tables for the sake of clarity and convenience.

Discussion of the Effects of the Gauche Conformational energy on The Glass Transition of Polymers

A study was performed in which the *gauche* energy was varied from 0.00 to 1.50 kcal/mol while maintaining a fixed trans-gauche barrier of 4.03 kcal/mol and relative *trans* energy of 0.00 kcal/mol. A special case in which the *gauche* energy was -1.16 kcal/mol relative to the *trans* conformational energy was studied as well. The glass transition increased in a nonlinear fashion with increasing *gauche* energy. Additionally, the densities at a temperature near the glass transition were very similar for the various cases studied with the exception of the case where the gauche energy was 1.50 kcal/mol and the trans barrier was 4.03 kcal/mol. However, a different study of a case where the

gauche energy was 1.50 kcal/mol and a trans-gauche barrier of 4.39 kcal/mol yielded a density near T_g very similar to the other case studies (0.896 g/cc). Therefore, a high driving force to form a *trans* conformation promotes the formation of higher density structures compared to a low driving force at a given temperature. A tentative explanation for the observed trend in the glass transition temperatures is that the same fraction of free volume at T_g occurs at higher temperatures for the case where the *trans* energy is more stable as opposed to a case in which the *trans* conformation is less favorable. This is because *trans* conformations pack much more efficiently than *gauche* conformations. This is especially evident in the case where the *gauche* energies are -1.16 kcal/mol more stable than the *trans* energy which has the lowest glass transition of all of the semi-crystalline cases studied as shown in **Table 17**.

Detailed Analysis of the Phase Transitions in A Highly Crystalline System

In order to understand the phase transitions occurring in highly crystalline systems, the case where the *gauche* energy was set to 1.50 kcal/mol with *trans-gauche* barrier of 4.03 kcal/mol was analyzed in full detail. The determination of the glass transition from the volume and enthalpy curves was reconsidered and new fits were determined. Two high temperature linear fits were determined for the "high temperature" glass transition which will tentatively be referred to as the α-transition (T_α) and two low temperature linear fits were determined for what will be called the glass transition (T_g). The calculated temperatures for the glass transition and α-transition were 271.575 K and 391.377 K respectively as given in **Table 22**. This is in

contrast to the previously determined "averaged" T_g of 324.17 K reported in **Table 17**. It will become clear in the next discussion why the enthalpic and volumetric phase transitions were reanalyzed. As a further remark, the new assignment of T_g and T_α is tentative, and it is possible that the T_g assignment could correspond to a gamma transition, and T_α really corresponds to the glass transition. The approximate average melting point for this system was 522.5 K as reported in **Table 21**. This would yield a value T_α/T_m of 0.749, a value T_g/T_m of 0.520 and a value of T_g/T_α of 0.694. In contrast, the semi-crystalline sample (*gauche* energy=1.14 kcal/mol, *trans-gauche* barrier=3.01 kcal/mol) resulted in a value Tg/T_m of 0.658, a value T_γ/T_m of 0.373, and a value T_γ/T_g of 0.566. Therefore, it is possible that what is called T_α for the highly crystalline system is really T_g, and what is called T_g is really T_γ. Or perhaps, the transition at 272 K is the glass transition of an amorphous region uninfluenced by crystallinity and the phase transition at 391 K is the glass transition of a crystal-constrained amorphous fraction. Such a phenomenon for semi-crystalline polymers has been accepted in the literature.[24] Additionally, the rate of decrease in compressibility changes abruptly around 375 K but does not stabilize until about 250 K as shown in **Figure 197** (circles).

Molecular Structure Analysis as a Function of Temperature for the Highly Crystalline Polymer Case where the *Gauche* Energy is 1.50 kcal/mol and the *Trans-Gauche* Barrier is 4.03 kcal/mol

Intra-chain Order Parameter and Bond Vector Orientational Distribution: The Highly Crystalline Case

The intra-chain order parameter as a function of temperature is shown in **Figure 207**. Qualitatively, there is a dramatic increase in the intra-chain order parameter from 525 to 475 K within the melting point region, which implies the rapid growth of *trans* chain segments due to crystal formation. Second, there is sharp leveling off of the order parameter at round 400 K to a value of 0.6, which is very near the assigned T_α point. Third, there are small irregularities in the order parameter around 300 K, which is near the interpreted T_g temperature.

The temperature dependence of the intra-chain angle distribution is shown in **Figures 208-217**. At low temperatures (50-100 K) there is a large relative population of straight polymer segments with vector-vector angles of 0-5^0, and there is a smaller population peak at around 30^0 (peak of 9 %) which corresponds to the amorphous population as was shown in the previous study. From 150 K to 300 K there is a gradual decrease in the straight chain population and a very minor change in the "amorphous" peak at 30^0. Therefore, there is no clear interpretation of T_g based on these observations. From 300 to 350 K there is a clear decrease in the straight chain population (0-5^0) accompanied by a small but general increase in the amorphous population occupation. From 350-450 K the maximum in the 0-5^0 bin is shifted to the 5-10^0 bin, and a significant

decrease in the low angle vector population peak height is observed, with a corresponding gradual increase of the amorphous population. Finally, around the melting point region (500-550K) there is a final large decrease in the 5-10^0 population occupation with a corresponding noticeable increase in the amorphous population region.

Inter-chain Order Parameter and Bond Vector Orientational Distribution: The Highly Crystalline Case

The temperature dependence of the inter-chain order parameter is shown in **Figure 218**. As with the intra-chain axis distribution, there is rapid increase in the order parameter around the melting point between 475-550 K. The order parameter levels off to a value of about 0.45 at about 400 K which is near the assigned T_α. Small irregularities in the inter-chain order parameter occur around 300 K which is near the assigned T_g region.

The temperature dependence of the inter-chain vector distribution is shown in **Figures 219-228**. The low temperature distribution from 50-100 K in **Figure 219** resembles a decaying exponential function with the largest values for the 0-5^0 vector population. The next noticeable change in the distribution occurs from 150-200 K (**Figure 221**) where there is a noticeable peak formation in the 5-10^0 vector population. Next, there is a general but subtle increase in the 20-30^0 vector population accompanied by a small decrease in the 5-10^0 vector population (**Figure 223**). Between 350K to 450 K there is a significant decrease in the 5-10^0 vector population and a general increase in the larger angle vector population (**Figures 225-226**). Between 450-500 K there is a

significant decrease and broadening of the low angle (0-20°) vector population as shown in **Figure 227**, which is interpreted as the beginning of a general crystal disordering. Finally, there is a dramatic shift in the inter-chain angle distribution from a broadened peak centered at about 15° at 500 K to an almost completely amorphous distribution at 550 K (**Figure 228**). This is consistent with the calculated melting point at 522 K by means of the heat capacity and specific expansivity curves.

Inter-Planar Order Parameter and Bond Vector Orientational Distribution: The Highly Crystalline Case

The temperature dependence of the inter-planar order parameter is shown in **Figure 229**. The calculated inter-planar order parameter ranged from 0.06 at 550 K to 0.16 at 50 K, which indicates that it is not a very sensitive function of the structure of the system. Nevertheless, there is a qualitatively rapid increase of the inter-planar order parameter near the melting point.

The temperature dependence of the inter-planar angle distribution is shown in **Figures 230-239**. The shape of the population distribution is a gradually increasing function, which levels off to a converging value. The other observation is that the distribution gradually shifts toward higher values for the larger vector angles as the temperature is increased.

Torsional Conformation Behavior and Transition Kinetics for the Highly Crystalline Case: *Gauche* energy is 1.50 kcal/mol, *Trans-Gauche* Barrier is 4.03 kcal/mol

The temperature dependence of the torsional transition rate is shown in **Figure 240**. The torsional transition rate clearly has a dramatic decrease around 550 K. The degree of torsional transition cooperativity has a pronounced maximum at around 350 K for the 1-3 torsion coupling and decays at lower temperatures as shown in **Figure 241**. An Arrhenius plot of the torsional transition rate reveals that there are actually two different torsional processes occurring above 390 K and below 390 K as shown in **Figure 242** and summarized in the **Table 23**. The effective torsional barrier for the temperature range 400-550 K is 7.755 kcal/mol with an Arrhenius intercept of 11.68. This barrier corresponds to the liquid state prior to the first glass transition T_{α}. The effective torsional barrier of the high temperature liquid state is much higher than the average (torsional) forcefield barrier of 3.28 kcal/mol. This is most likely due to the inter-molecular constraining forces of the crystalline fraction. A similar observation was made for the semi-crystalline case where the effective barrier found was 4.94 kcal/mol while the average forcefield barrier was 2.418 kcal/mol. The intercept of the Arrhenius plot, related to the entropy, is remarkably high for the highly crystalline case compared to the amorphous studies reported previously. For example, the intercept corresponding to the liquid state for the Arrhenius plots of the three amorphous studies ranged from 8.3 to 8.6. However, the semi-crystalline polyethylene liquid case had an intercept of 10.0. Therefore, there is a positive correlation between the torsional driving

force to form the *trans* conformation and entropy of activation as well as the bulk torsional barrier.

The effective torsional barrier for the temperature range 250-350 K was 4.985 kcal/mol with an intercept of 8.103. This low temperature range corresponds to the condensed state between T_α and T_g and may be interpreted as a constrained amorphous phase. The evidence supporting this assertion is the value of 8.103 of the intercept of the Arrhenius plot, very similar to the values found for the amorphous cases. The effective barrier of 4.985 kcal/mol is definitely higher than the average forcefield torsional barrier of 2.418 kcal/mol, which is a sign that the amorphous fraction is being constrained by the crystalline fraction. Another feature worth mentioning is that the "thermal ratios" at T_α and T_g are 9.971 and 9.237 respectively, which are similar to the values calculated for the three amorphous test cases and also similar to the thermal ratio at the glass transition for the semi-crystalline case. These values are summarized in **Table 24**.

Effect of the Cohesive Energy on the Glass Transition Temperature of a Model Poly (ethylene) System

In a separate study, the effect of cohesive energy on the glass transition of a polyethylene model with a fixed torsional potential was determined by varying the Lennard Jones well (D_c). The torsional *gauche* energy was 1.14 kcal/mol, the energy at 0^0 was 6.72 kcal/mol, and the *trans* to *gauche* barrier was 4.03 kcal/mol. The calculated glass transitions are summarized in **Table 25** as well as the figure numbers for the

volume and enthalpy curves. The first column is the calculated binding energy per bead for the crystal structure at 0 K, not including zero point energy. The actual Lennard Jones well depth is given in the footnotes. A detailed summary of the volumetric and enthalpic glass transition statistics and slopes is given in **Tables 26** and **27** respectively.

Discussion of the effects of binding energy on the Calculated Glass Transition

The effect of cohesive energy on the glass transition is remarkably non-linear in this systematic model study. A crystal binding energy per bead of 1.6881 kcal/mol gives a glass transition of 212.32 K as shown in Table 25. However increasing the binding energy per bead to 2.14 kcal/mol results in a T_g of 288.46 K.

The thermal expansivity and heat capacity curves for the case with the 1.69 kcal/mol binding energy per bead are shown in **Figures 249** and **250** respectively. A clear observation is that the melting point has shifted to 362-363 K, which is significantly lower than the melting point of 430 K for the binding energy per bead of 2.14 kcal/mol (**Figures 57 and 58** for the expansivity and heat capacity respectively). The expansivity and heat capacity curves for the case with binding energy per bead of 2.596 kcal/mol are included in **Figures 251** and **252** respectively. The expansivity and heat capacity curves for the case with the binding energy per bead of 3.051 kcal/mol are shown in **Figures 253** and **254** respectively.

The compressibility of the polymer system as a function of the Lennard Jones well depth is shown in **Figure 255**. As expected, there is a clear increase in compressibility as the well depth is decreased.

A Direct Connection between Computer Modeling and Experiments: Qualitative Agreement of Calculated Heat Capacity Trends for Various Polymer Morphologies

In order to bring the results of this research into perspective, the calculated heat capacities of the purely amorphous polymer case (barrier = 4.03 kcal/mol), the semi-crystalline case (*gauche* energy=1.14 kcal/mol, *trans-gauche* barrier=4.03 kcal/mol), and the highly crystalline case (*gauche* energy=1.50 kcal/mol and *trans-gauche* barrier=4.03 kcal/mol) are presented in **Figure 256**. The experimentally extrapolated heat capacity curves for the pure amorphous and pure crystalline curves are shown in the bottom left of Figure **256**.[11] The agreement between experiment and theory in the shape of the heat capacity curves is excellent, and features such as the crossing of the pure amorphous with the highly crystalline heat capacity curves occur at 400 K both for the calculated and the experimental heat capacities. Finally, the pattern of the combined amorphous, semi-crystalline and highly crystalline heat capacities is in excellent agreement with the widely accepted qualitative behavior shown in the bottom right of **Figure 258**.[11]

Conclusion

The general thermo-physical behavior of polymers was explored through a simple united atom poly (ethylene) like model. Specifically, an attempt was made to provide insights into the molecular processes involved at various phase transitions ranging from the melting point, the glass transition and the gamma transition. Specific structural properties such as various short range order parameters were used to describe the ordering process at the molecular level as well as torsional transition kinetics which are the fundamental process by which polymers rearrange themselves. Summaries are presented expressing observations and possibly new insights into a variety of molecular processes in polymers occurring at various phase transitions, starting from high temperature processes to low temperature processes.

The Melting Point

First of all, in order for crystallization to occur, there must be a significant energy stabilization of the intra-molecular conformational energy of the *trans* or crystal forming conformation relative to the *gauche* or crystal destabilizing conformation. From these studies, it became apparent that a gauche energy of +0.50 kcal/mol is possibly the minimum energy difference required to see the beginnings of a melting point at 437 K with a heat capacity of 31.6 J/molK. Interestingly enough an associated gamma transition appears at 176 K, a feature not apparent for the analogous pure amorphous case where the melting point is not found either (**Figure 74**, barrier=4.03 kcal/mol). When the *gauche energy* is destabilized further to 1.14 kcal/mol relative to the *trans*

conformation, a quantity derived from *ab initio* studies, the heat capacity peak at the melting point (T_m=435 K) becomes more prominent with a value of 34.7 J/molK. The gamma transition is found at about 160 K as well. These values are in good agreement with the experimental melting point of poly (ethylene) of 414 K and the experimental gamma relaxation point of about 160 K for poly (ethylene) as well. However, as the *gauche* energy is destabilized even further to 1.50 kcal/mol, the melting point is shifted to 519 K and the heat capacity increases to over 41.8 J/molK as shown in **Figure 200** (barrier=4.03 kcal/mol). As a side remark, the gamma transition at 160 K disappears, in agreement with the experimental observation that the gamma transition does not show up in highly crystalline samples. A main conclusion from this discussion is that an intra-molecular torsional potential that clearly favors the *trans* conformation is required to *seed* the formation of crystalline regions in the polymer at a temperature *significantly* above its glass transition. Therefore, having the correct symmetry or molecular structure for crystal packing like poly (ethylene) is necessary but not sufficient for crystal formation. Having an intra-molecular torsional potential that energetically favors significantly the crystalline conformation is also a requirement.

In this work, the molecular structure of the polymer was studied by the temperature dependence of local order parameters. During the melting point there is a clear increase in the short-range intermolecular and intra-molecular order parameters, a reflection of the onset of crystallization. Additionally, there were clear changes in the order parameter distribution as the system was cooled around the melting point. For example, above the melting point, the inter-chain order parameter was similar to an

amorphous structure order parameter distribution, while at the melting point there was a clear formation of a peak at lower angle distributions, indicating the formation of parallel chains.

Finally, the study of the influence of the melting point dependence on the binding energy per bead was not very conclusive. One of the main results is that there is a definite increase in melting point when the binding energy is increased from 1.69 kcal/mol/bead (T_m=362 K) to a value of 2.14 kcal/mol (T_m= 435 K). However, as the binding energy per bead is increased to 2.60 kcal/mol/bead, an unambiguous assignment of the melting point temperature was not possible.

The Glass Transition

A clear positive correlation between the glass transition in pure amorphous polymers, the amorphous fraction in semicrystalline polymers, the amorphous fraction in highly crystalline polymers and the bulk torsional barrier was found. The control experiment was a case where there was no conformational barrier, and the result was the absence of a glass transition even down to temperatures of 50 K. The purely amorphous studies were carried out by setting the forcefield torsional *trans* conformational energy equal to the *gauche* conformational energy. Thermal ratios E_a/k_BT_g (E_a is effective barrier in the melt) were found to be very similar for the various barriers studied, ranging from 8.50 to 10.0. This implies that the glass transition is a kinetic phenomenon controlled by torsional barriers in amorphous polymers, provided packing effects are held constant. Additionally, a forcefield barrier of 4.03 kcal/mol

resulted in a T_g of 248 K, while the experimental amorphous T_g value is 237 K. The interpretation is that the bulk torsional barrier of real poly (ethylene) should be around 4.0 kcal/mol. Finally, the calculated "Arrhenius T_g" may be the temperature where the molecular process known as the β-relaxation is excited.

In the case of amorphous polymers, heat capacity curves corresponding to a pure glass transition were obtained which clearly shows that the glass transition phenomenon has been captured. In the case of the highly crystalline system where the gauche energy was 1.50 kcal/mol higher than the trans energy (barrier= 4.03 kcal/mol), two glass transitions were observed at 391.4 K and 271.6 K. The glass transition at 391.4 K probably corresponds to an amorphous fraction highly constrained by the crystal, while the glass transition at 271.6 K corresponds to an amorphous fraction that was much less constrained.

An additional study of the glass transition dependence on the barrier for a system in with the *gauche* energy was 1.14 kcal/mol higher than the *trans* energy was presented. A surprisingly weak dependence of the glass transition on the torsional barrier was observed in this case. A tentative explanation was that a higher barrier prevents efficient crystal formation, which in turn increases the amount of free volume in the system relative to a system with a lower barrier. Therefore, two counter-acting effects may cancel out each other. However, further studies may be needed to clarify these issues.

In terms of order parameters and order parameter distributions, there was no dramatic or clear change in structure at the glass transition as was observed for the

melting point. The evidence that no major structural changes in amorphous polymers occur at the glass transition suggests that torsional conformations that are caught at the transition state at T_g fall into the nearest local torsional minimum potential well (i.e. either *trans* or *gauche*).

Gamma Transition

The main evidence obtained for the gamma transition was in the form of slight but noticeable increases in the heat capacity curves of semi-crystalline polymers. For example the specific expansivity (**Figure 3**) and heat capacity curves (**Figure 6**) for a semi-crystalline case clearly shows that a minor phase transition is occurring around 160 K. The inter-chain axis order parameter change between 150-200 K in **Figure 37** shows a subtle change in the distribution at low angles which is interpreted as a slight and local adjustment of straight chain segments. In contrast, when the temperature is increased from 100 to 150 K, there is virtually no change in the inter-chain order parameter distribution as shown in **Figure 36.** Another important observation is that the gamma transition is not readily detected for the high crystalline case as shown in **Figures 199** and **200** that correspond to the specific expansivity and heat capacity of the highly crystalline cases. In the other extreme, the corresponding pure amorphous cases with barriers of 2.88 kcal/mol and 4.03 kcal/mol do not show a gamma transition as shown in **Figures 73** and **74** which correspond to the specific expansivity and heat capacity curves. However, the amorphous case with a barrier of 5.04 kcal/mol does show a feature in the heat capacity curve that appears around the gamma transition. Nevertheless, the general results of this study indicate that a semi-crystalline system is

required in order to observe the gamma transition, and this is in agreement with experimental observations. Therefore, a tentative molecular interpretation of the gamma transition is the short range intermolecular straightening of chains in the *trans* conformation possibly related to defective crystals.

Finally, the molecular nature of the physical and thermal properties of polymers was systematically investigated through a careful variation of the forcefield parameters of a model poly (ethylene) system. Valuable new insights of the behavior of polymers were gained which may eventually prove useful in understanding and prediction of the properties of more complex systems.

Table 1. Experimentàl and forcefield calculated properties of the orthorhombic form of crystalline poly (ethylene).

Crystal Property	Experimental	Calculated
Density, g/cc	1.060	1.070
Length *a*, Angstroms	7.202	7.800
Length *b*, Angstroms	2.546	2.532
Length *c*, Angstroms	4.795	4.410
Angle α, degrees	90.0	90.0
Angle β, degrees	90.0	90.0
Angle γ, degrees	90.0	90.0
Bulk modulus, 1/GPa	0.0937	0.0815
Energy/ methylene, kcal/mol	2.049	2.14

Table 2. Volume intersection statistics for the semi-crystalline polymer study.

Lower temperature linear fit statistics: 50 K-200 K, R value=0.9955549

Linear expansion coefficient (slope): 1.252 ±0.053 $cm^3/gK\ 10^{-4}$

Upper temperature linear fit statistics: 300K-400 K R value=0.997343

Linear expansion coefficient (slope): 4.392 ± 0.185 $cm^3/gK10^{-4}$

Calculated T_g (intersection): 286.11 K

Table 3. Enthalpy intersection statistics for the determination of T_g of the semi-crystalline system.

Lower temperature linear fit statistics: 50 K-200 K, R value=0.9999867

Heat capacity (slope): 24.6333 ± 0.057 joule/molK

upper temperature linear fit statistics: 300K-400 K, R value=0.9993914

Heat capacity (slope)= 31.116 ± 0.627 joule/molK

Calculated T_g (intersection): 289.97 K

Table 4. Conformational Arrhenius plot for the polymer study in which the gauche energy was 1.14 kcal/mol and the trans-gauche barrier was 3.01 kcal/mol. Three fits were determined for the regions above the glass temperature (325-475 K), between the glass temperature and the gamma transition (200-300K), and below the gamma transition (100-175 K).

Fit Number	Effective Barrier kcal/mol	Intercept	Temperature range fit,K	R value Linear fit	Intersection Of fits, K
1	4.942 ± 0.140	10.038 ± 0.178	325-475	-0.9980585	
2	2.418 ± 0.055	5.955 ± 0.115	200-300	-0.9992142	Fit 1, Fit2=311.08
3	1.134 ± 0.043	2.635 ± 0.168	100-175	-0.9985727	Fit 2, Fit3=194.59

Table 5. Thermal ratios at the glass transition (288.04 K) and at the gamma transition (163 K) for the case where the *gauche* energy is 1.14 kcal/mol and the *trans-gauche* barrier is 3.01 kcal/mol.

Effective Barrier Kcal/mol	Real T_g Kelvin	Thermal Ratio (Real T_g)	Arrhenius T_g Kelvin	Thermal Ratio (Arrhenius T_g)
4.942 ± 0.140	288.04	8.634	311.080	7.994
2.418 ± 0.055	163	7.465	194.590	6.253

Table 6. Glass transition summary for the four barrier cases studied.

Barrier, kcal/mol	Volume T_g	Enthalpy T_g	Figure #	Average T_g, K
1.99[1]	252.59 K	257.27 K	48, 49	254.93
3.01[2]	286.11 K	289.97 K	2, 5	288.04
4.03[2]	284.32 K	292.61 K	50, 51	288.46
6.07[4]	276.06 K	277.72 K	52, 53	276.89

(Table 6 continued next page)

Calculated Trans-gauche Barrier/k_BTg

Barrier, kcal/mol	Ratio	$e^{-(barrier/k_BT)}$ densities near T_g	
1.99	3.93	1.97E-2	0.929 g/cc at 300 K
3.01	5.26	5.20E-3	0.919 g/cc at 300 K
4.03	7.03	8.85E-3	0.895 g/cc at 300 K
6.07	11.03	1.62E-5	0.877 g/cc at 275 K

[1]Data corresponds to analysis of average volume and enthalpy curves of five different runs.
[2-4]Data corresponds to analysis of average volume and enthalpy curves of six different runs.

Table 7. Volumetric Glass transition statistics and slopes for linear fits of barrier study.

Part I

Barrier,kcal/mol	lower slope	upper slope	lower range	upper range
kcal/mol	$10^{-4}cm^3/gK$	$10^{-4}cm^3/gK$	(linear fit)	(linear fit)
1.99	1.19 +-0.04	3.52+-0.14	50-200 K	275-375 K
3.01	1.25 +-0.05	4.39+-0.19	50-200 K	300-400 K
4.03	1.35+-0.06	4.12+-0.18	50-200 K	325-400 K
6.07	1.52+-0.03	3.08+-0.12	50-200 K	325-425 K

Part II. Correlation coefficient values, R

Barrier, kcal/mol	lower range	Rvalue	Upper range	Rvalue
1.99	50-200 K	0.9966720	275-375 K	0.9976279
3.01	50-200 K	0.9955549	300-400 K	0.9973430
4.03	50-200 K	0.9943103	325-400 K	0.9980658
6.07	50-200 K	0.9991786	325-425 K	0.9975364

Table 8. Enthalpic Glass transition statistics and slopes for linear fits of barrier study.

Part I

Barrier,kcal/mol	lower slope	upper slope	lower range	upper range
kcal/mol	joules/molK	joules/molK	(linear fit)	(linear fit)
1.99	24.72±0.07	30.43±0.40	50-200 K	275-375 K
3.01	24.63±0.06	31.12±0.63	50-200 K	300-400 K
4.03	24.59±0.05	30.34±0.61	50-200 K	325-400 K
6.07	24.66±0.04	27.35±0.29	50-200 K	325-425 K

Part II. Correlation coefficient values, R

Barrier, kcal/mol	lower range	Rvalue	Upper range	Rvalue
1.99	50-200 K	0.9999787	275-375 K	0.9997459
3.01	50-200 K	0.9999867	300-400 K	0.9993914
4.03	50-200 K	0.9999897	325-400 K	0.9995939
6.07	50-200 K	0.9999951	325-425 K	0.9998260

Table 9. Tentative assignment of various peaks for the "semi-crystalline" barrier study where the *gauche* energy is 1.14 kcal/mol.

Trans to gauche barrier: 1.99 kcal/mol

*Alpha Curve: (**figure 55**)*

T_γ=160 K (shoulder, gamma relaxation interpretation)

T_β=237 K (shoulder, Sub T_g beta relaxation interpretation)

T_α=282 K (shoulder, alpha relaxation?)

T_m=437 K (peak, melting point)

T_X=519 K (peak, some kind of collapse)

*Heat Capacity Curve: (**figure 56**)*

T_γ=150 K (inflection, gamma transition), T_γ=155 K (shoulder)

$T\beta$=225 K (inflection, Sub-T_g beta relaxation), $T\beta$=228 K (shoulder)

$T\alpha$=301 K (inflection, alpha relaxation), $T\alpha$=309 K (shoulder)

T_m= 430 K (peak, melting point)

Trans to gauche barrier: 3.01 kcal/mol

*Alpha Curve: (**figure 3**)*

T_γ=165 K (peak, gamma relaxation interpretation)

T_β= 229 K (peak, Sub-Tg beta relaxation)

$T_{\alpha 1}$=309 K (shoulder, alpha relaxation)

$T_{\alpha 2}$=358 K (shoulder, alpha relaxation)

T_m=441 K (peak, melting point)

*Heat Capacity Curve:(**figure 6**)*

T_γ=161 K (gamma transition)

T_m=434 K (peak, melting point)

Trans to gauche barrier: 4.03 kcal/mol

*Alpha Curve(**figure 57**)*

T_γ=160 K (shoulder, gamma transition)

T_β=286 K (shoulder, beta relaxation or T_g)

T_m=442 K (peak, melting point)

T_x=512 K (peak, collapse)

Heat Capacity Curve: (**Figure 58**)

T_γ= 151 K (inflection, gamma transition), T_γ=160 K (shoulder)

T_β=250 K (inflection, Sub-T_g beta relaxation 250 K), T_β=258 K (shoulder)

T_α=325 K (inflection, alpha relaxation), T_α=331 K (shoulder, alpha relaxation)

T_m= 435 K (peak, melting point)

T_x=514 K (peak, collapse)

Trans to gauche barrier: 6.07 kcal/mol:

Alpha Curve: (**figure 59**)

T_{x1}=238 K (peak, unknown origin)

T_{x2}=338 K (peak, unknown origin)

T_m=516 K (peak, possible melting or polymer collapse)

*Heat Capacity Curve: (**figure 60**)*

T_{x2}= 338 K (peak, unknown origin)

T_m= 514 K (peak, possibly melting point)

Table 10. Summary of Torsional forcefields for the amorphous glass transition dependence on torsional barrier. The names of the different cases refer to the trans to gauche barriers. Energies are in kcal/mol

Case:	0° Energy	*gauche* energy	*trans* energy
No barrier	0.00	0.00	0.00
2.88 barrier	5.57	-0.01	0.00
4.03 barrier	6.72	-0.02	0.00
5.04 barrier	6.71	-0.01	0.00

Table 11. Amorphous glass transition summary for the four barrier cases studied.

Barrier, kcal/mol	Volume T_g	Enthalpy T_g	Figure #	Average T_g, K
0.00[1]	0.00 K	0.00 K	63,64	0.00
2.88[2]	171.94 K	174.59 K	65,66	173.26
4.03[3]	253.18 K	242.68 K	67,68	247.93
5.04[4]	295.33 K	289.68 K	69,70	292.50

(Table 11 continued next page)

Calculated Barrier/k_BTg

Barrier, kcal/mol	Ratio	$e^{-(barrier/k_BT)}$	densities near T_g
2.88	8.36	2.33E-4	0.926 g/cc at 175 K
4.03	8.18	2.80E-4	0.896 g/cc at 250 K
5.04	8.67	1.72E-4	0.876 g/cc at 300 K

[1]Data corresponds to analysis of average volume and enthalpy curves of six different runs.
[2-4]Data corresponds to analysis of average volume and enthalpy curves of five different runs.

Table 12. Amorphous volumetric glass transition statistics and slopes for linear fits of the barrier study.

Part I

Barrier,kcal/mol	lower slope	upper slope	lower range	upper range
kcal/mol	$10^{-4}cm^3/gK$	$10^{-4}cm^3/gK$	(linear fit)	(linear fit)
0.00	5.22 ±0.08	5.22 ±0.08	50-550 K	50-550 K
2.88	1.73 ±0.03	2.93 ±0.07	50-175 K	175-275 K
4.03	1.58 ±0.02	4.04 ±0.13	50-200 K	275-375 K
5.04	1.71 ±0.05	4.67 ±0.20	50-200 K	350-450 K

Part II. Correlation coefficient values, R

Barrier, kcal/mol	lower range	Rvalue	Upper range	Rvalue
0.00	50-550 K	0.9977663	50-550 K	0.9977664
2.88	50-175 K	0.9992589	175-275 K	0.9990565
4.03	50-200 K	0.9996796	275-375 K	0.9984244
5.04	50-200 K	0.9978482	350-450 K	0.9971942

Table 13. Amorphous enthalpic glass transition statistics and slopes for linear fits of the barrier study.

Part 1

Barrier,kcal/mol	lower slope	upper slope	lower range	upper range
kcal/mol	joules/molK	joules/molK	(linear fit)	(linear fit)
0.00	26.62±0.08	26.62±0.08	50-550 K	50-550 K
2.88	24.84±0.06	27.02±0.09	50-175 K	175-275 K
4.03	24.78±0.05	28.06±0.13	50-200 K	275-375 K
5.04	24.77±0.05	28.66±0.32	50-200 K	350-450 K

Part II. Correlation coefficient values, R

Barrier, kcal/mol	*lower range*	*Rvalue*	*Upper range*	*Rvalue*
0.00	50-550 K	0.9999313	50-550 K	0.9999313
2.88	50-175 K	0.9999889	175-275 K	0.9999835
4.03	50-200 K	0.9999894	275-375 K	0.9999675
5.04	50-200 K	0.9999908	350-450 K	0.9998170

Table 14. Effective barrier calculations for the liquid and glassy states of amorphous polymers with forcefield barriers of 2.88 kcal/mol (**Figure 186**), 4.03 kcal/mol (**Figure 187**), and 5.04 kcal/mol (**Figure 188**). The first calculated effective barrier in each case corresponds to the liquid phase, while the second number corresponds to the glassy phase.

Forcefield Barrier Kcal/mol	Effective Barrier Kcal/mol	Ln(Preexp)	Temperature Range fit,K	R value Linear fit	Intersection Of fits, K
2.88	3.308 ± 0.039	8.297 ± 0.054	550-225	-0.9992169	"Tg"=216.26
"	1.372 ± 0.068	3.793 ± 0.221	200-125	-0.9975425	
4.03	4.168 ± 0.0417	8.252 ± 0.055	550-275	-0.9994990	"Tg"=245.48
"	2.122 ± 0.070	4.059 ± 0.215	225-125	-0.9983619	
5.04	5.294 ± 0.042	8.578 ± 0.051	550-325	-0.9997441	"Tg"= 327.88
"	3.917 ± 0.267	6.465 ± 0.620	275-175	-0.9931170	

Table 15. Thermal ratios for the real glass transition temperature and the Arrhenius glass transition temperature. The definition used is (Torsional Barrier/$k_B T_g$) where k_B is the Boltzmann constant. The real glass transition is an average of the volumetric and enthalpic T_g.

Forcefield Barrier Kcal/mol	Real Tg Kelvin	Thermal Ratio (Real Tg)	Arrhenius Tg Kelvin	Thermal Ratio (Arrhenius Tg)
2.88	173.26	8.365	212.260	6.828
4.03	247.93	8.180	245.480	8.261
5.04	292.50	8.671	327.880	7.735

Effective Barrier Kcal/mol	Real Tg Kelvin	Thermal Ratio (Real Tg)	Arrhenius Tg Kelvin	Thermal Ratio (Arrhenius Tg)
3.308 ± 0.039	173.26	9.608	212.260	7.770
4.168 ± 0.0417	247.93	8.460	245.480	8.544
5.294 ± 0.042	292.50	9.108	327.880	8.125

Table 16. Summary of Torsional forcefields for the glass transition dependence on the *gauche -trans* energy difference. The names of the different cases refer to the *trans* to *gauche* barriers. Energies are in kcal/mol

Case:	0^0 Energy	*gauche* energy	*trans* energy
4.04 barrier*	5.56	-1.16	0.00
4.03 barrier	6.72	-0.02	0.00
4.03 barrier	6.71	0.49	0.00
4.03 barrier	6.72	1.14	0.00
4.03 barrier	6.72	1.50	0.00
4.39 barrier	7.08	1.50	0.00

*In this case the barrier refers to the *gauche* to *trans* energy barrier, since the *gauche* state is the most stable state.

Table 17. Glass transition dependence on the gauche energy level. The *trans-gauche* barrier was 4.03 kcal/mol unless otherwise indicated.

Energy kcal/mol	Volume Tg	Enthalpy Tg	Figure #	Average T_g,
-1.16	207.60 K	211.12 K	201b,202b	209.36**
0.00	253.18 K	242.68 K	67,68	247.93
0.49	254.47 K	254.20 K	189,190	254.34
1.14	284.32 K	292.61 K	50, 51	288.46
1.50	316.27 K	332.07 K	193,194	324.17
1.50*	315.94 K	319.40 K	195,196	317.67

Calculated Densities near T_g

Energy, kcal/mol	densities near T_g
-1.16[1]	0.910 g/cc at 200 K
0.00[2]	0.896 g/cc at 250 K
0.49[3]	0.899 g/cc at 250 K
1.14[4]	0.895 g/cc at 300 K
1.50[5]	0.916 g/cc at 325 K
1.50*,[6]	0.896 g/cc at 325 K

[1,3] Data corresponds to analysis of average volume and enthalpy curves of five different runs.

[2] Data corresponds to analysis of average volume and enthalpy curves of six different runs.

[4-6] Data corresponds to analysis of average volume and enthalpy curves of six different runs.

* Actual trans-gauche barrier is 4.39 kcal/mol.

** This lowest main transition was actually first order.

Table 18. Volumetric Glass transition statistics and slopes for linear fits of *gauche* energy study. All cases have a 4.03 kcal/mol trans-gauche barrier unless indicated.

Part I

Energy,kcal/mol	lower slope	upper slope	lower range	upper range
kcal/mol	$10^{-4}cm^3/gK$	$10^{-4}cm^3/gK$	(linear fit)	(linear fit)
-1.16	1.89±0/06	3.11±0.13	50-200 K	225-325 K
0.00	1.58 ±0.02	4.04±0.13	50-200 K	275-375 K
0.49	1.56 ±0.04	4.43±0.20	50-200 K	300-400 K
1.14	1.35±0.06	4.12±0.18	50-200 K	325-400 K
1.50	0.98±0.04	4.16±0.04	50-200 K	350-450 K
1.50*	1.26±0.04	4.45±0.16	50-200 K	350-450 K

Part II. Correlation coefficient values, R

Energy, kcal/mol	lower range	Rvalue	Upper range	Rvalue
-1.16	50-200 K	0.9976823	225-325 K	0.9974656
0.00	50-200 K	0.9996796	275-375 K	0.9984244
0.49	50-200 K	0.9987029	300-400 K	0.9969298
1.14	50-200 K	0.9943103	325-400 K	0.9980658
1.50	50-200 K	0.9965730	350-450 K	0.9895605
1.50*	50-200 K	0.9974610	350-450 K	0.9980417

*Actual *trans-gauche* barrier is 4.39 kcal/mol.

Table 19. Enthalpic Glass transition statistics and slopes for linear fits of *gauche* energy study. All cases have a 4.03 kcal/mol *trans-gauche* barrier unless indicated.

Part 1

Energy, kcal/mol	lower slope	upper slope	lower range	upper range
kcal/mol	joules/molK	joules/molK	(linear fit)	(linear fit)
-1.16	24.94±0.05	27.74±0.26	50-200 K	225-325 K
0.00	24.78±0.05	28.06±0.13	50-200 K	275-375 K
0.49	24.83±0.07	29.17±0.26	50-200 K	300-400 K
1.14	24.59±0.05	30.34±0.61	50-200 K	325-400 K
1.50	24.36±0.02	29.85±0.79	50-200 K	350-450 K
1.50*	24.58±0.04	30.61±0.42	50-200 K	350-450 K

Part II. Correlation coefficient values, R

Energy, kcal/mol	lower range	Rvalue	Upper range	Rvalue
-1.16	50-200 K	0.9999919	225-325 K	0.9998727
0.00	50-200 K	0.9999894	275-375 K	0.9999675
0.49	50-200 K	0.9999800	300-400 K	0.9998816
1.14	50-200 K	0.9999897	325-400 K	0.9995939
1.50	50-200 K	0.9999977	350-450 K	0.9989477
1.50*	50-200 K	0.9999933	350-450 K	0.9997238

*Actual *trans-gauche* barrier is 4.39 kcal/mol.

Table 20. Qualitative transition assignments obtained from the thermal expansivity and heat capacity curves of the case where the gauche energy is 0.49 kcal/mol.
*Thermal expansivity curve: (**Figure 191**)*
T_m=439 K (calculated)
T_g=261 K (from graph)
*Heat capacity curve: (**Figure 192**)*
T_m= 437 K (calculated)
T_g=247 K (from graph)
T_γ= 165 K (from graph, approximate half height)

Table 21. Qualitative transition assignments obtained from the thermal expansivity and heat capacity curves of the case where the gauche energy is 1.50 kcal/mol.
*Thermal expansivity curve: (**Figure 199**)*
Trans-Gauche barrier=4.03 kcal/mol
T_m = 526 K
Trans-Gauche barrier=4.39 kcal/mol
T_m = 514 K
*Heat Capacity Curve: (**Figure 200**)*
Trans-Gauche barrier=4.03 kcal/mol
T_m = 519 K
Trans-Gauche barrier=4.39 kcal/mol
T_m = 515 K

Table 22. Volumetric and enthalpic glass and alpha transitions determined by linear fits for the case where the *gauche* energy is 1.50 kcal/mol and the *trans-gauche* barrier is 4.03 kcal/mol. Statistics for the linear fits as well as an average T_g and T_α are reported.

Volumetric

Phase Transition Name	lower slope 10-4 cm3/gK	Upper slope 10-4 cm3/gK	Lower range fit (linear fit)	Upper range fit (linear fit)	Figure Number	Intersection
Glass Transition	0.975 ± 0.036	2.591 ± 0.068	50-200 K	300-375 K	203	268.720 K
Alpha Transition	2.591 ± 0.068	5.038 ± 0.064	300-375 K	400-475 K	204	388.564 K
Part II. R values	lower range fit	R value	Upper range fit	R value		
Glass Transition	50-200 K	0.99657300	300-375 K	0.9993020	203	
Alpha Transition	300-375 K	0.9993020	400-475 K	0.9998374	204	

Enthalpic

Phase Transition Name	lower slope joules/molK	Upper slope Joules/molK	Lower range fit (linear fit)	Upper range fit (linear fit)	Figure Number	Intersection
Glass Transition	24.36 ± 0.02	26.42 ± 0.18	50-200 K	300-375 K	205	274.43 K
Alpha Transition	26.42 ± 0.18	32.66 ± 0.21	300-375 K	400-475 K	206	394.19 K
Part II. R values	lower range fit	R value	Upper range fit	R value		
Glass Transition	50-200 K	0.99999770	300-375 K	0.99995577	205	
Alpha Transition	300-375 K	0.99995577	400-475 K	0.9999604	206	

Average T_g	271.575 K
Average T_α	391.377 K

Table 23. Arrhenius rate statistics for the torsional transitions for highly crystalline poly(ethylene) where the forcefield *gauche* energy is 1.50 kcal/mol and the *trans-gauche* barrier is 4.03 kcal/mol.

Fit Number	Effective Barrier kcal/mol	Intercept	Temperature range fit,K	R value Linear fit	Intersection of fits, K
1	7.755 ± 0.127	11.68 ± 0.14	400-550	-0.9993264	
2	4.985 ± 0.158	8.103 ± 0.271	250-350	-0.9984978	Fit 1, Fit2=389.91 K

Table 24. Thermal ratios at the glass transitions for highly crystalline poly(ethylene) where the forcefield gauche energy is 1.50 kcal/mol and the *trans-gauche* barrier is 4.03 kcal/mol.

Effective Barrier Kcal/mol	Real T_g Kelvin	Thermal Ratio (Real Tg)	Arrhenius T_g Kelvin	Thermal Ratio (Arrhenius T_g)
7.755 ± 0.127	391.377	9.971	389.910	10.009
4.985 ± 0.158	271.575	9.237	NA	NA

Table 25. Glass transition summary for the four cohesive energy cases studied.

Binding energy kcal/mol	Volume T_g	Enthalpy T_g	Figure #	Average T_g, K
1.6881[a,*]	205.07 K	219.56 K	243,244	212.32
2.1400[b,*]	284.32 K	292.61 K	50, 51	288.46
2.5960[c,*]	279.07 K	290.00 K	245,246	284.54
3.0510[d,*]	302.65 K	297.72 K	247,248	300.18

Part II. Calculated Thermal Binding Ratio

Binding energy kcal/mol	Binding energy/k_BT_g	$e^{-(\text{Binding energy}/k_BT_g)}$
1.6881	4.00	1.83E-2
2.1400	3.73	2.39E-2
2.5960	4.59	1.01E-2
3.0510	5.11	6.01E-3

[a]Actual Do=0.1115 kcal/mol. [b]Actual Do=0.1411 kcal/mol. [c]Actual Do=0.1710 kcal/mol. [d]Actual Do=0.2010 kcal/mol.

*Data corresponds to analysis of average volume and enthalpy curves of six different runs.

Table 26. *Volumetric glass transition statistics and slopes for linear fits of binding energy study.*

Part I

Binding energy kcal/mol	lower slope $10^{-4}cm^3/gK$	upper slope $10^{-4}cm^3/gK$	lower range (linear fit)	upper range (linear fit)
1.6881	1.60±0.06	3.65±0.12	50-175	225-325 K
2.1400	1.35±0.06	4.12±0.18	50-200 K	325-400 K
2.5960	1.09±0.03	3.07±0.15	50-200 K	325-425 K
3.0510	0.96±0.02	2.44±0.06	50-200 K	325-425 K

Part II. Correlation coefficient values, R

Binding energy kcal/mol	lower range	Rvalue	Upper range	Rvalue
1.6881	50-175	0.9973475	225-325 K	0.9982541
2.1400	50-200 K	0.9943103	325-400 K	0.9980658
2.5960	50-200 K	0.9977450	325-425 K	0.9965873
3.0510	50-200 K	0.9992346	325-425 K	0.9991247

Table 27. Enthalpic Glass transition statistics and slopes for linear fits of binding energy study.

Part 1

Binding energy kcal/mol	lower slope joules/molK	upper slope joules/molK	lower range (linear fit)	upper range (linear fit)
1.6881[a]	24.57±0.05	27.32±0.36	50-175 K	225-325 K
2.1400[b]	24.59±0.05	30.34±0.61	50-200 K	325-400 K
2.5960[c]	24.56±0.03	29.62±0.34	50-200 K	325-425 K
3.0510[d]	24.56±0.03	28.76±0.24	50-200 K	325-425 K

[a]Actual Do=0.1115 kcal/mol. [b]Actual Do=0.1411 kcal/mol. [c]Actual Do=0.1710 kcal/mol. [d]Actual Do=0.2010 kcal/mol.

Part II. Correlation coefficient values, R

Binding energy kcal/mol	lower range	Rvalue	Upper range	Rvalue
1.6881	50-175 K	0.9999924	225-325 K	0.9997342
2.1400	50-200 K	0.9999897	325-400 K	0.9995939
2.5960	50-200 K	0.9999959	325-425 K	0.9998048
3.0510	50-200 K	0.9999970	325-425 K	0.9998990

Figure 1a

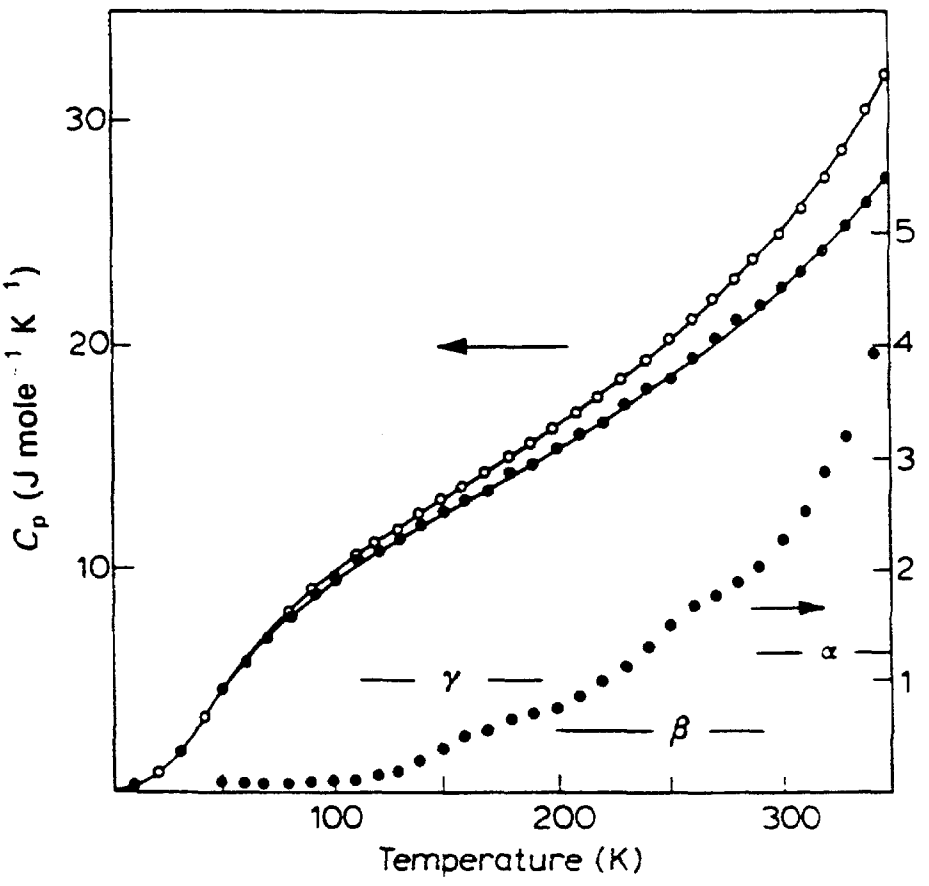

Figure 35 Heat capacity of LPE. Values for a 81% crystalline specimen (○) compared to extrapolated behaviour of 100% crystalline material; (●) (curves: left-hand ordinate scale). (Chang[93], Chang *et al.*[92]). A difference plot of these two curves is also shown (points only: right-hand ordinate scale). Approximate temperature ranges where mechanical relaxation occurs at low frequency (torsion pendulum) are indicated

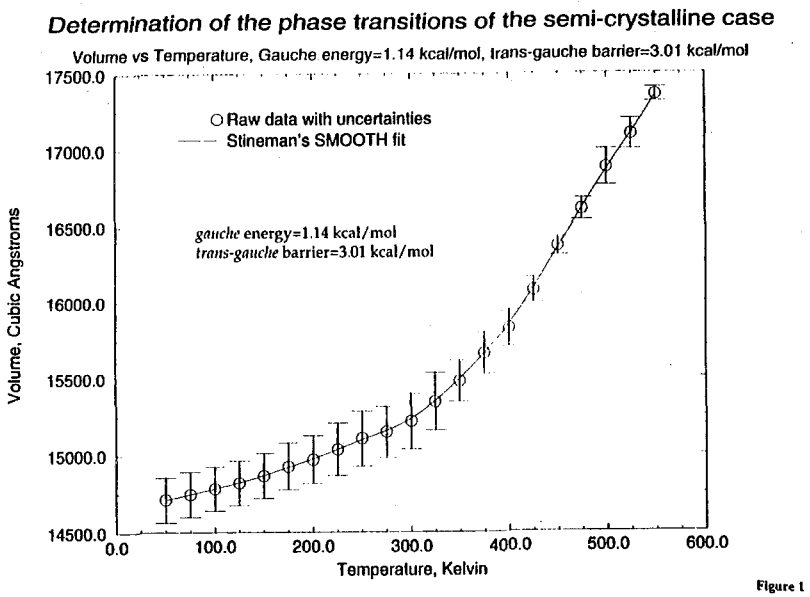

Figure 1

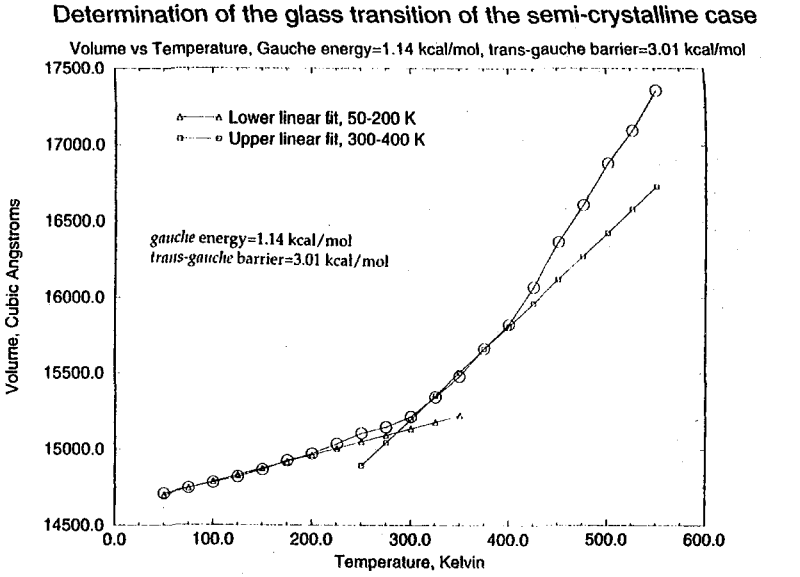

Figure 2

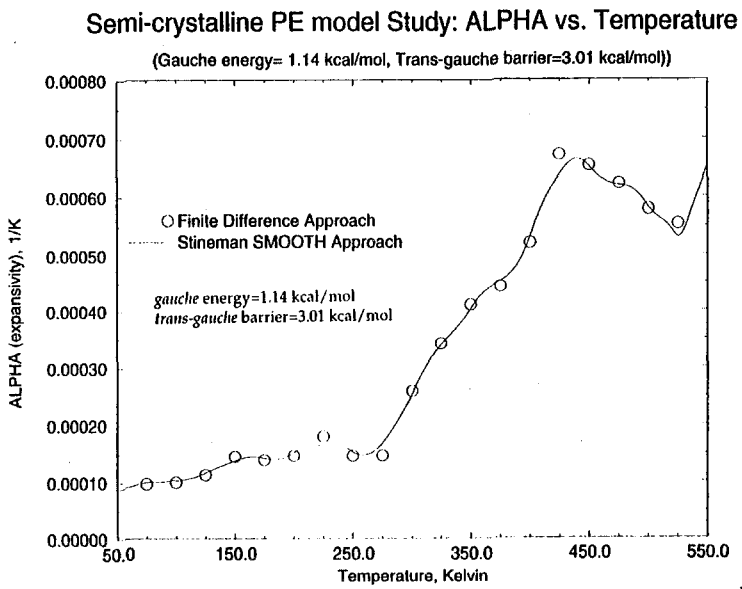

Figure 3

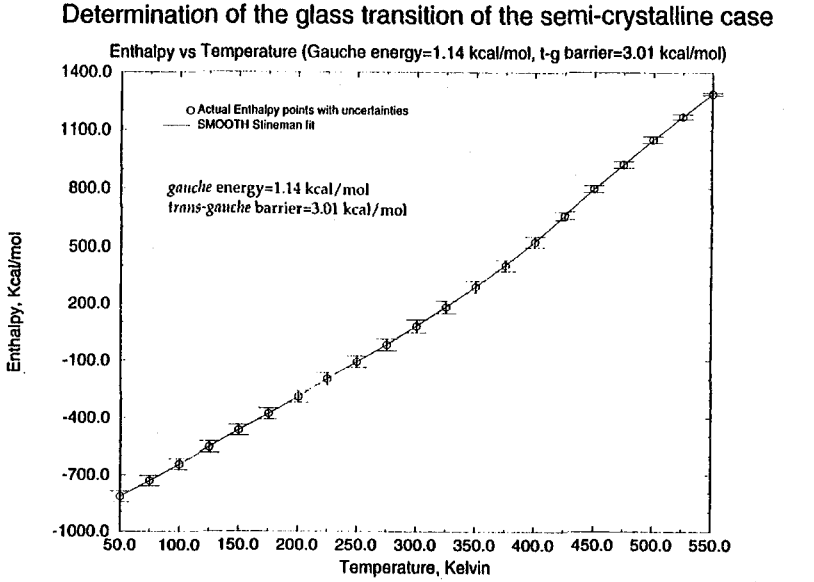

Figure 4

Determination of the Phase Transitions of the semi-crystalline case

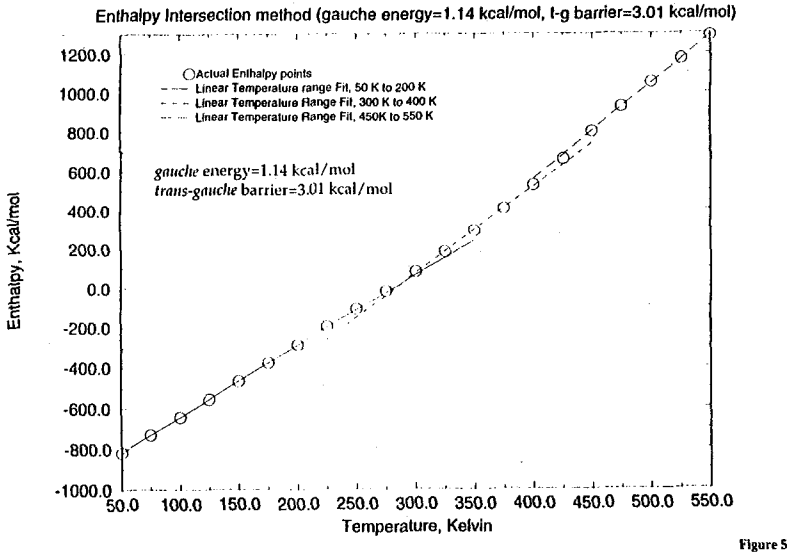

Figure 5

Semi-crystalline PE model study: Heat Capacity vs. Temperature

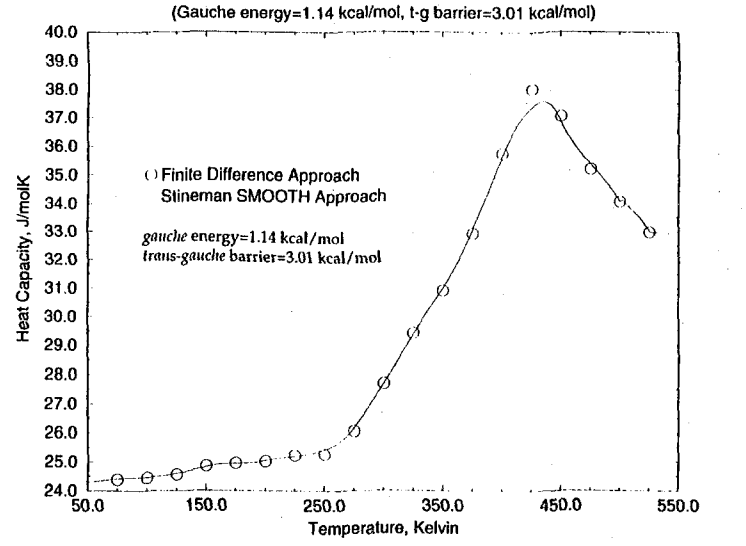

Figure 6

Determination of the phase transitions of the semi-crystalline case

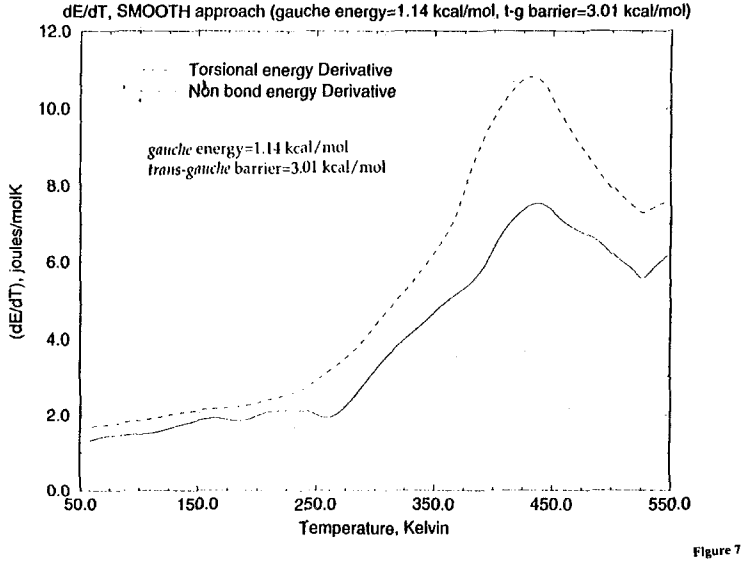

Figure 7

Semi-crystalline PE model Study

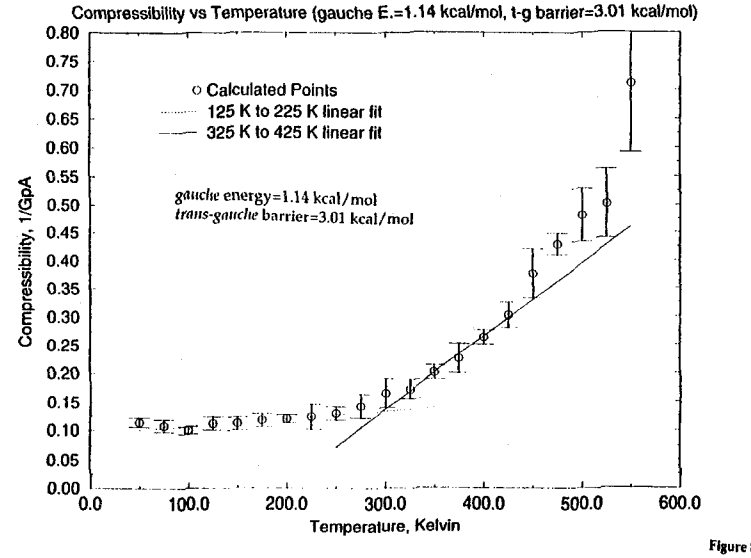

Figure 8

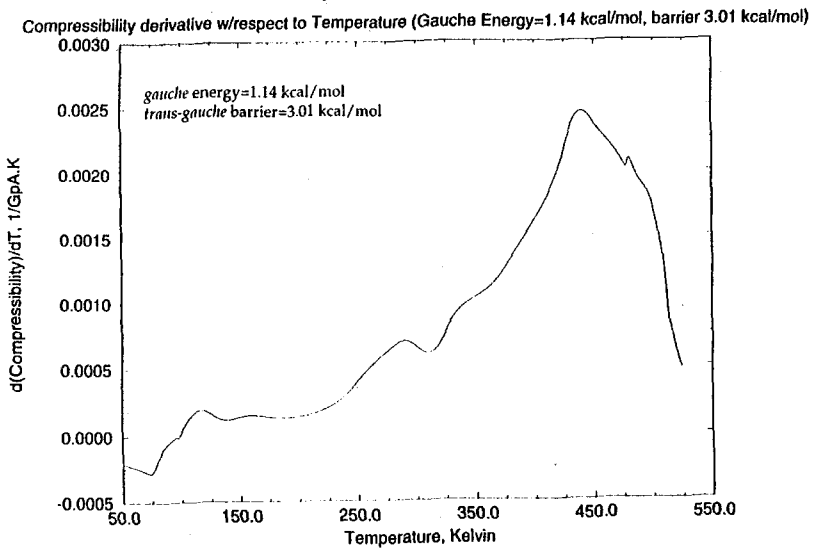

Figure 9

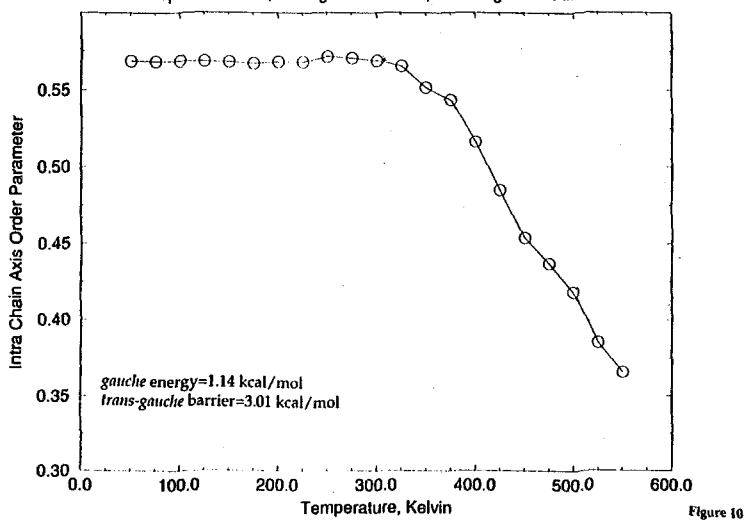

Figure 10

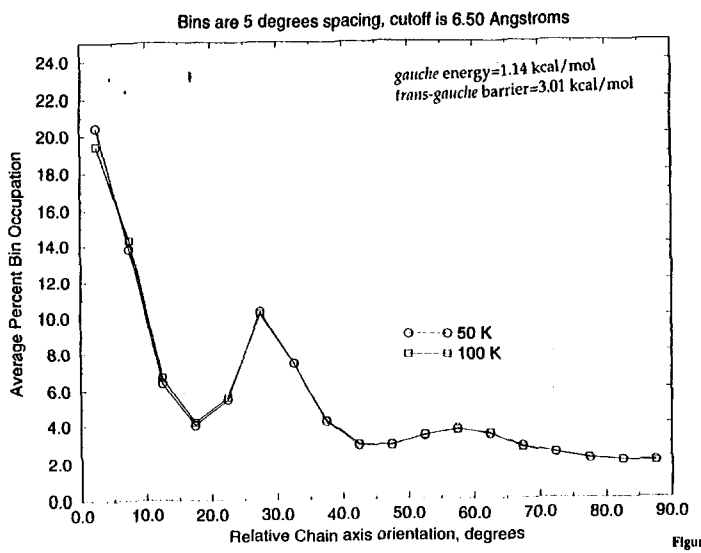

Figure 11

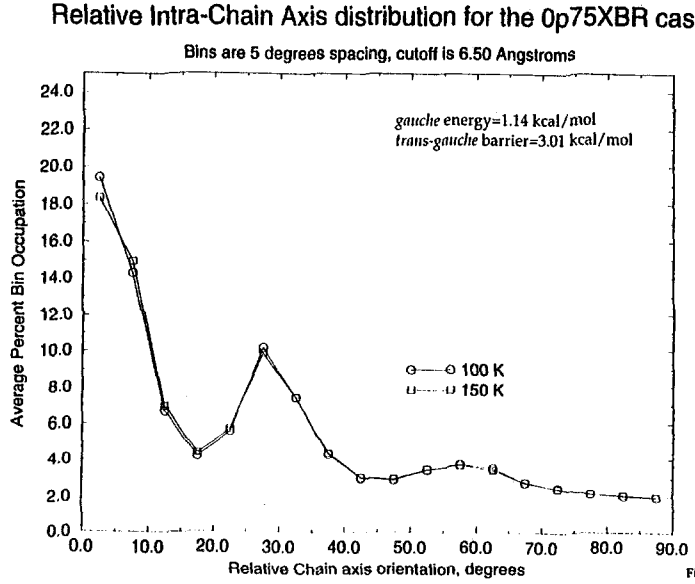

Figure 12

Relative Intra-Chain Axis distribution for the 0p75XBR case

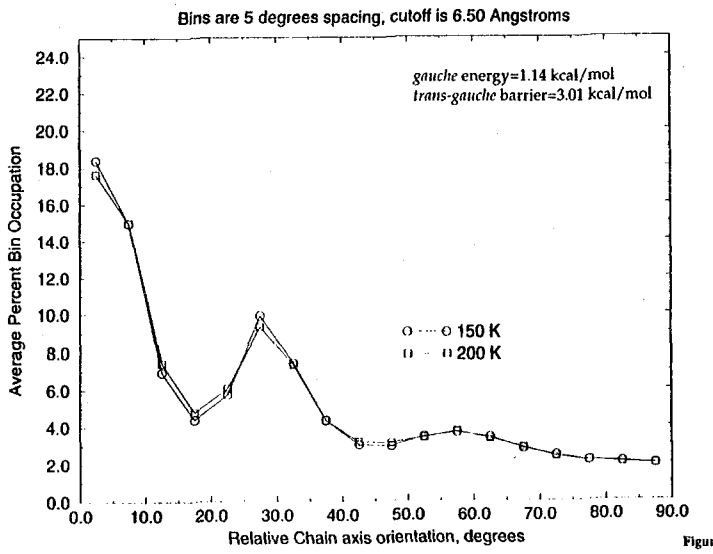

Figure 13

Relative Intra-Chain Axis distribution for the 0p75XBR case

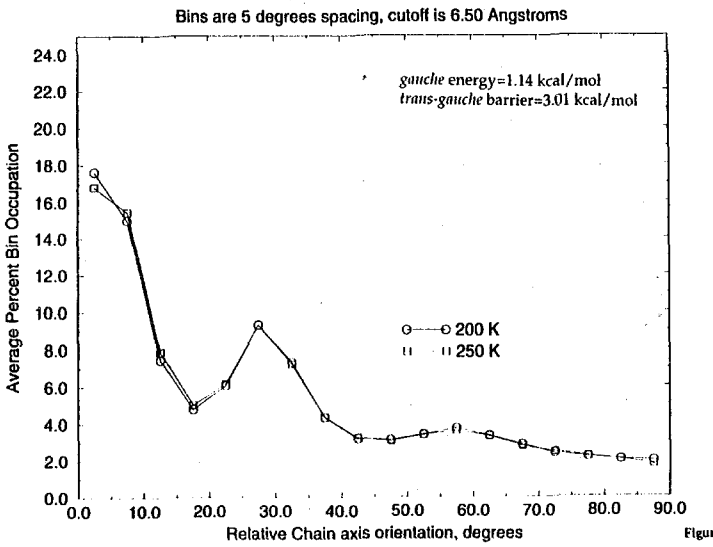

Figure 14

Relative Intra-Chain Axis distribution for the 0p75XBR case

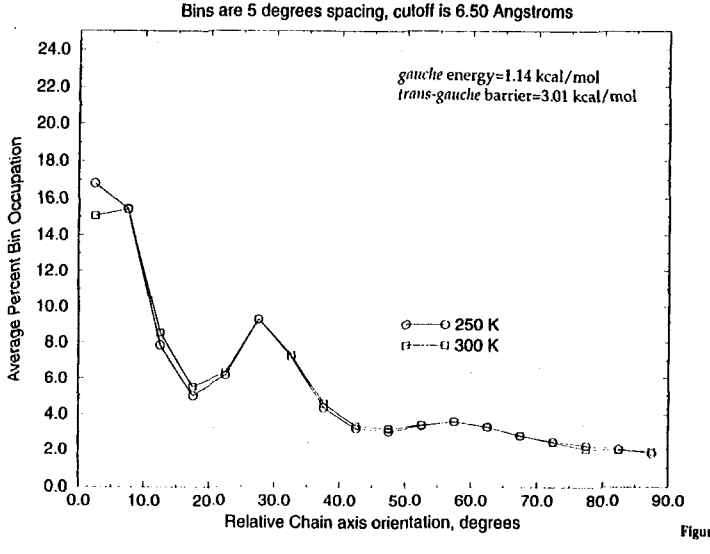

Figure 15

Relative Intra-Chain Axis distribution for the 0p75XBR case

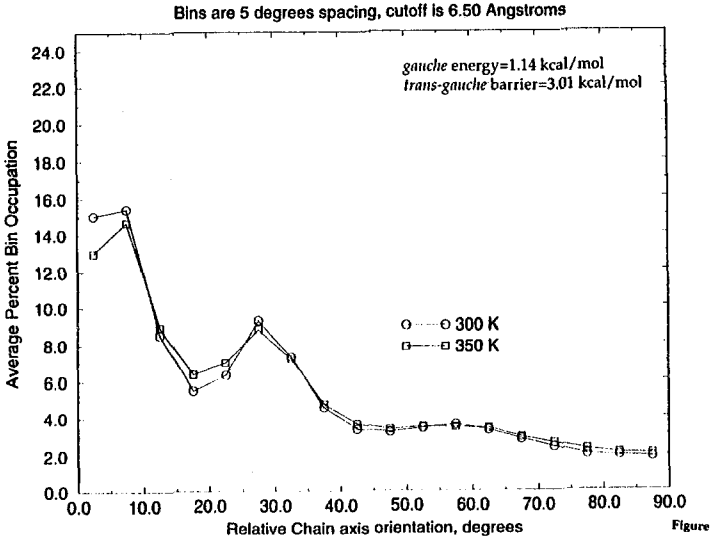

Figure 16

Relative Intra-Chain Axis distribution for the 0p75XBR case

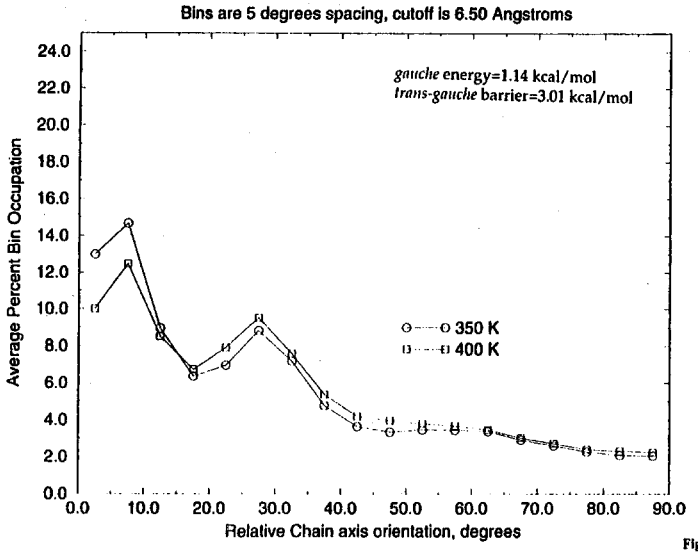

Figure 17

Relative Intra-Chain Axis distribution for the 0p75XBR case

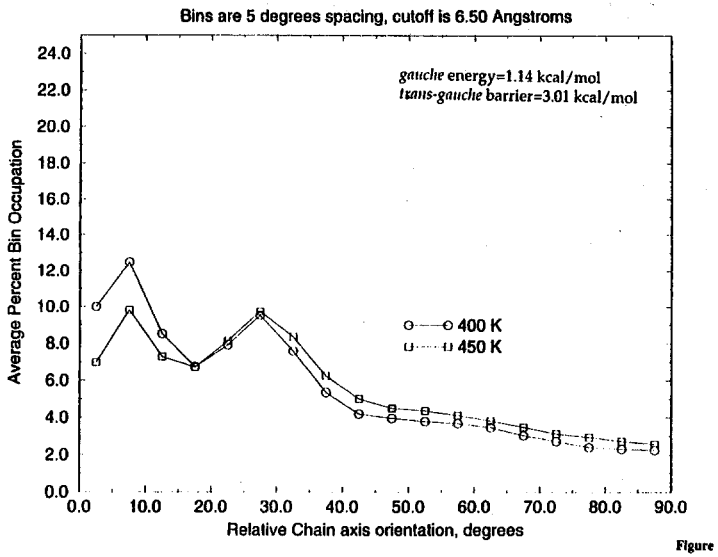

Figure 18

Relative Intra-Chain Axis distribution for the 0p75XBR case

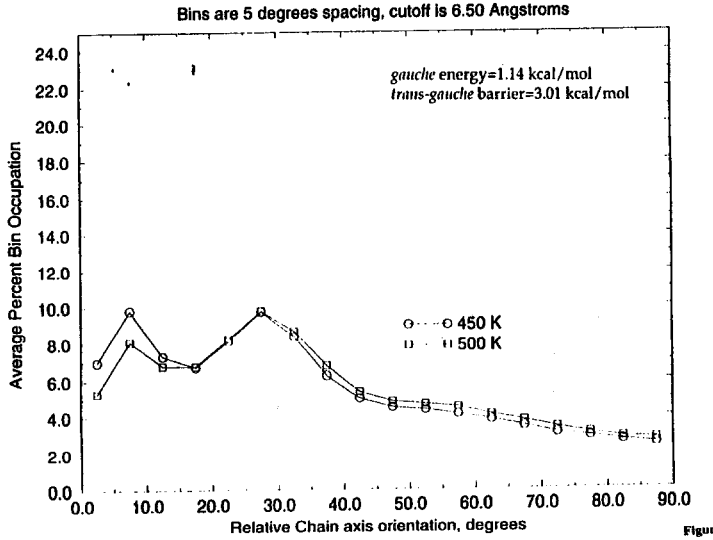

Figure 19

Relative Intra-Chain Axis distribution for the 0p75XBR case

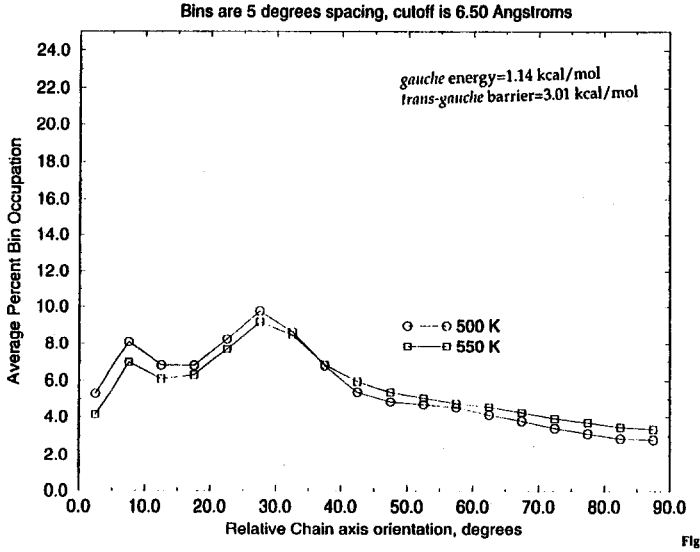

Figure 20

Average Inter Planar order Parameter, 0p75xBR case

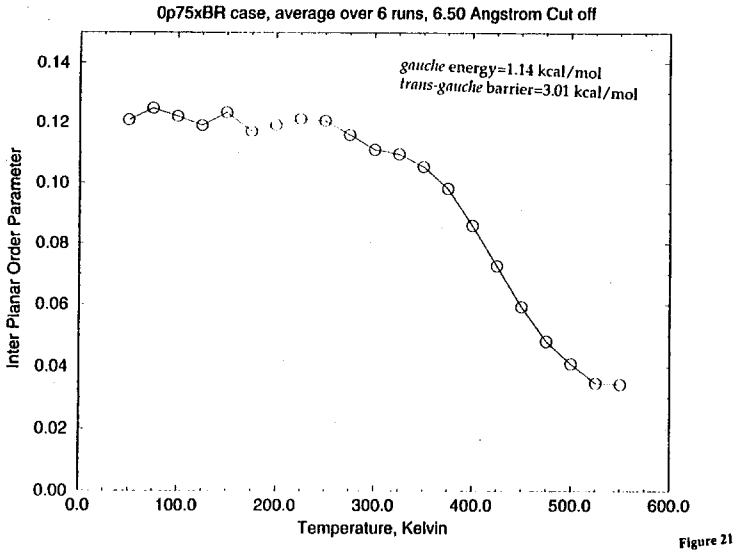

Figure 21

Relative Inter-Chain Plane distribution for the 0p75XBR case

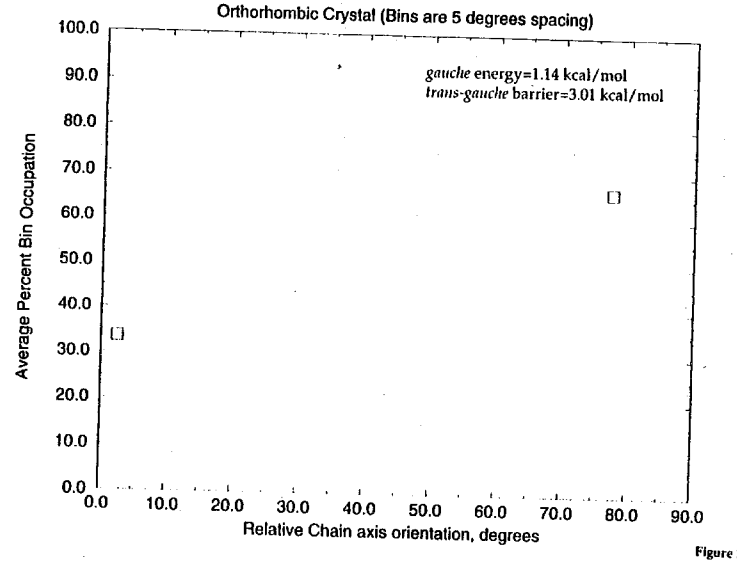

Figure 22

Relative Inter-chain Plane distribution for the 0p75XBR case

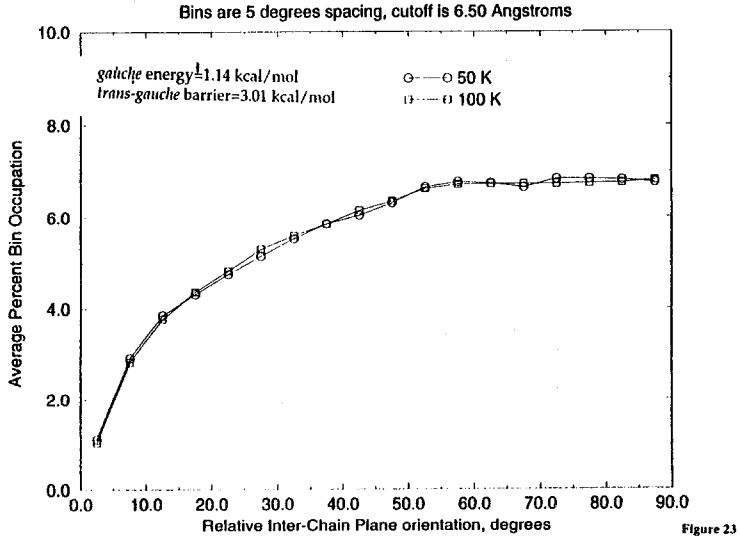

Figure 23

Relative Inter-chain Plane distribution for the 0p75XBR case

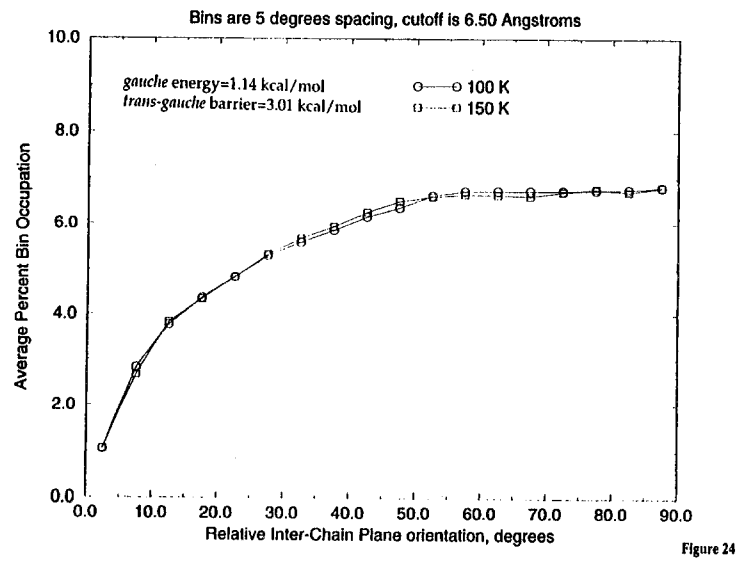

Figure 24

Relative Inter-chain Plane distribution for the 0p75XBR case

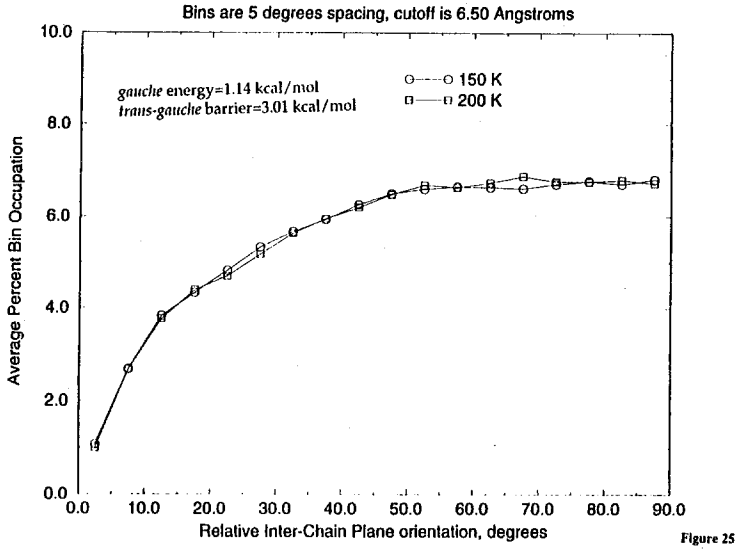

Figure 25

Relative Inter-chain Plane distribution for the 0p75XBR case

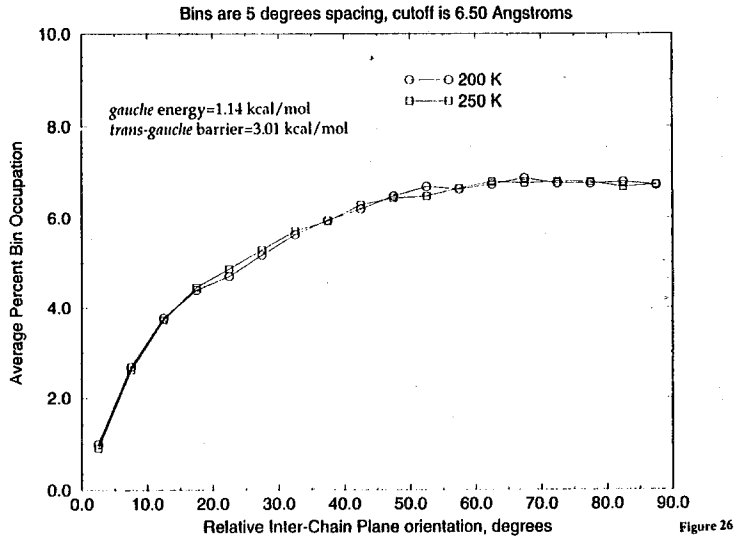

Figure 26

Relative Inter-chain Plane distribution for the 0p75XBR case

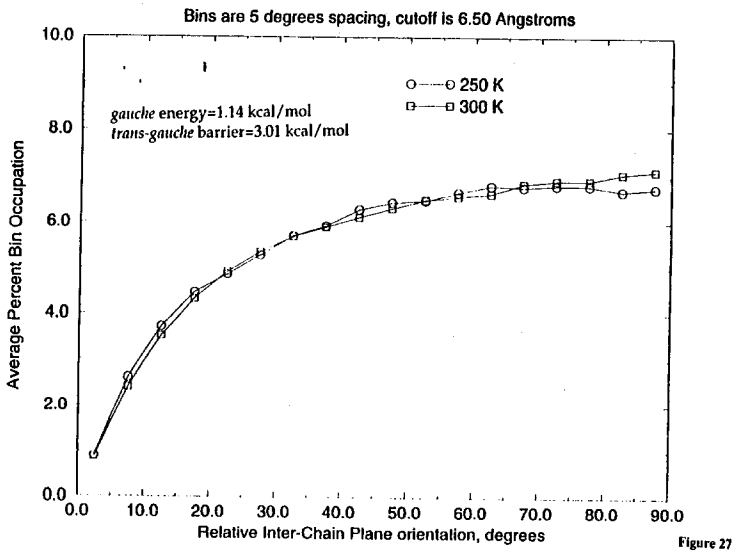

Figure 27

Relative Inter-chain Plane distribution for the 0p75XBR case

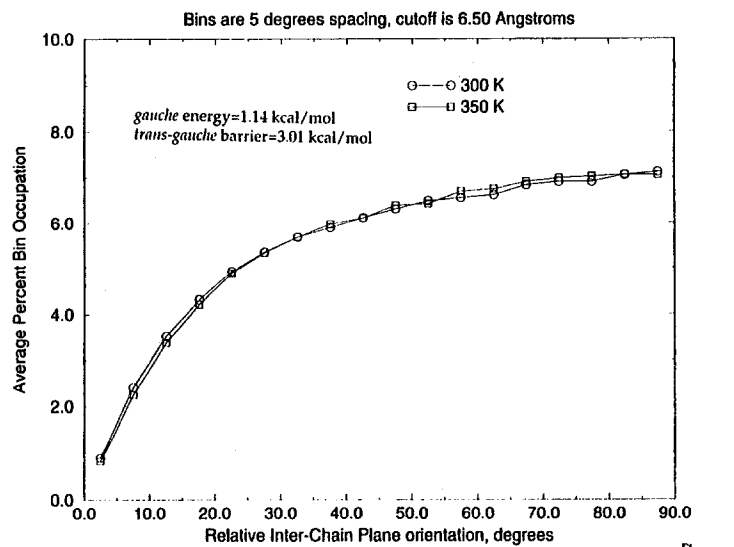

Figure 28

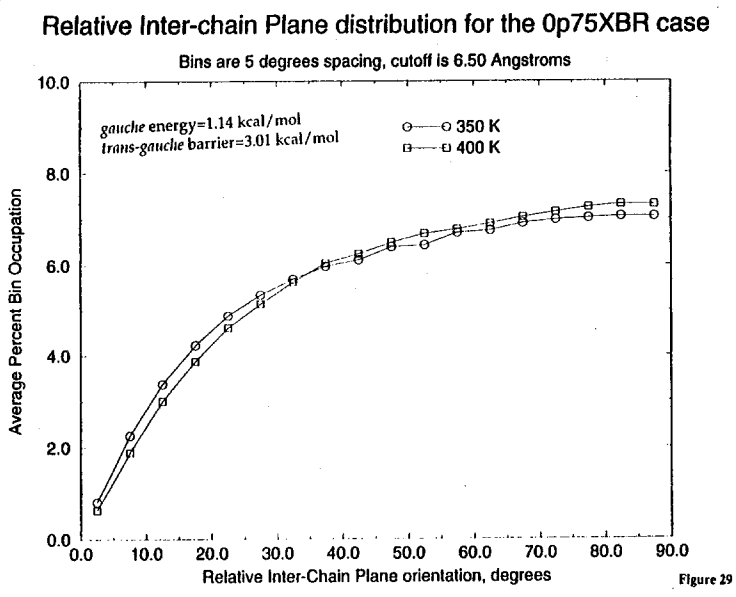

Figure 29

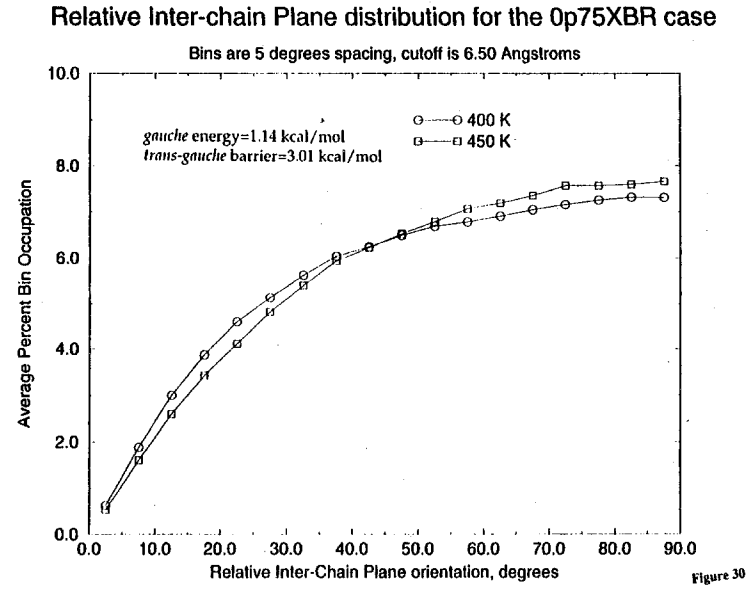

Figure 30

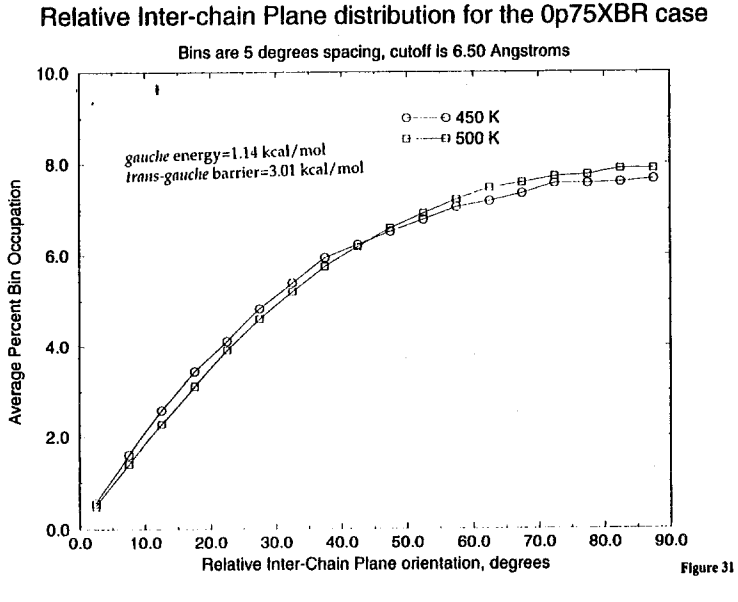

Figure 31

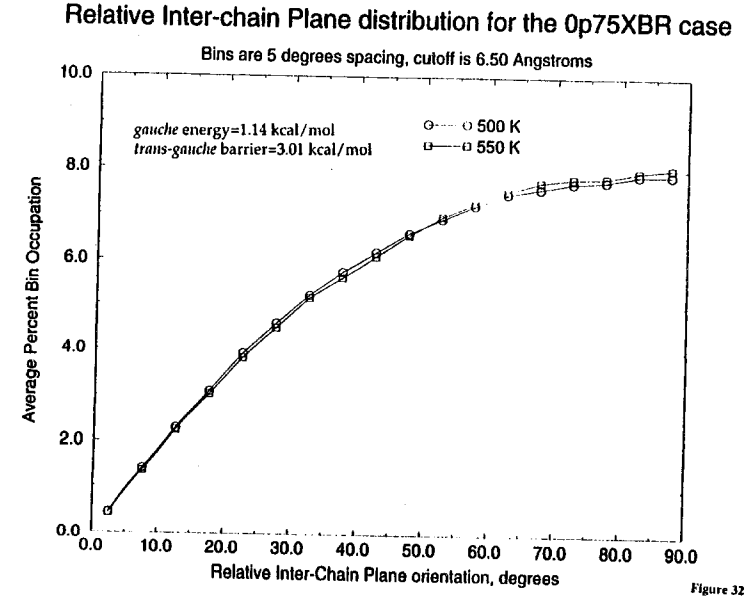

Figure 32

Average Inter Chain axis order Parameter, 0p75xBR case

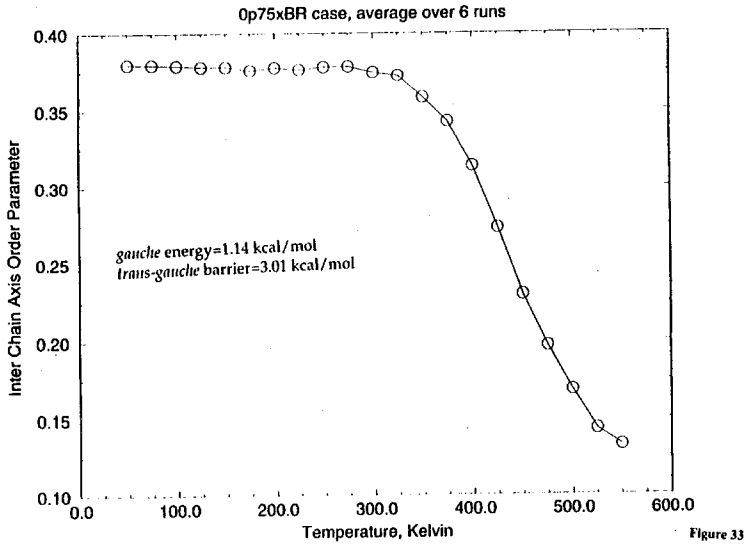

Figure 33

Inter-Chain order parameter derivative w/r T for the 0p75XBR case

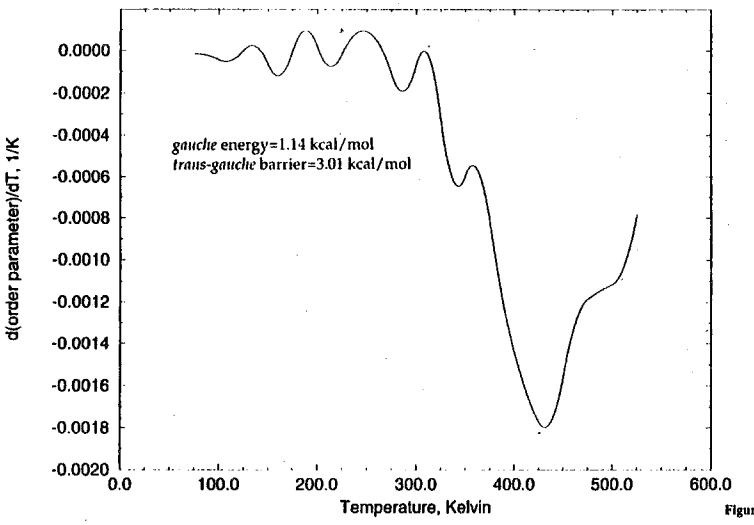

Figure 34

Relative Inter-Chain Axis distribution for the 0p75XBR case

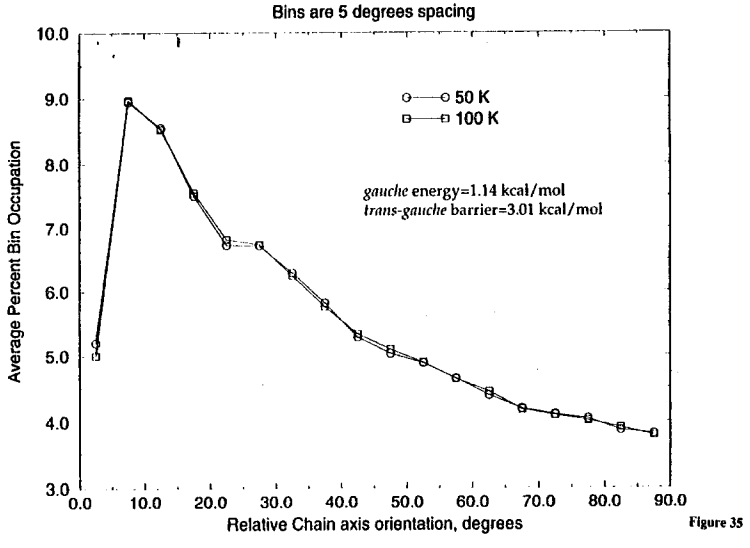

Figure 35

Relative Inter-Chain Axis distribution for the 0p75XBR case

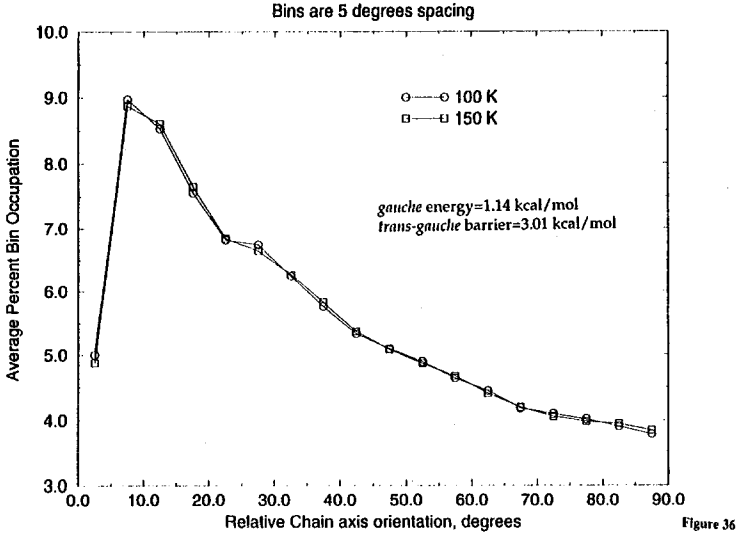

Figure 36

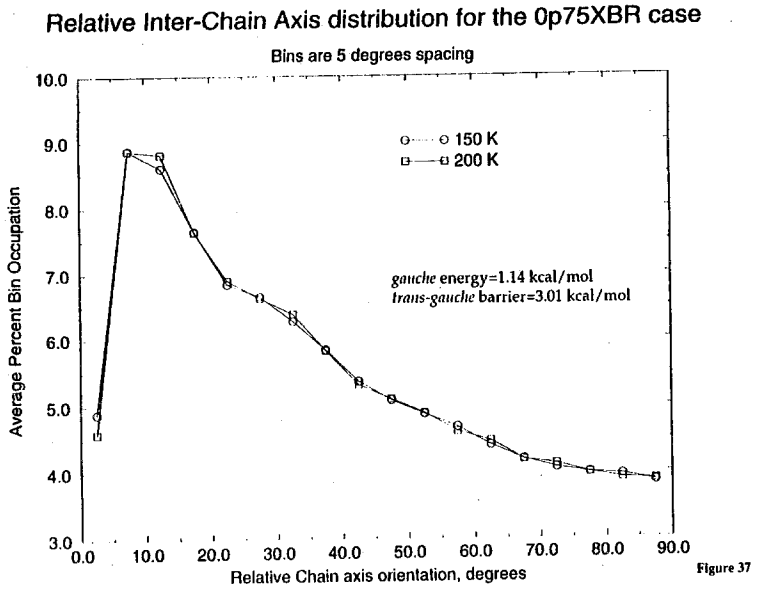

Figure 37

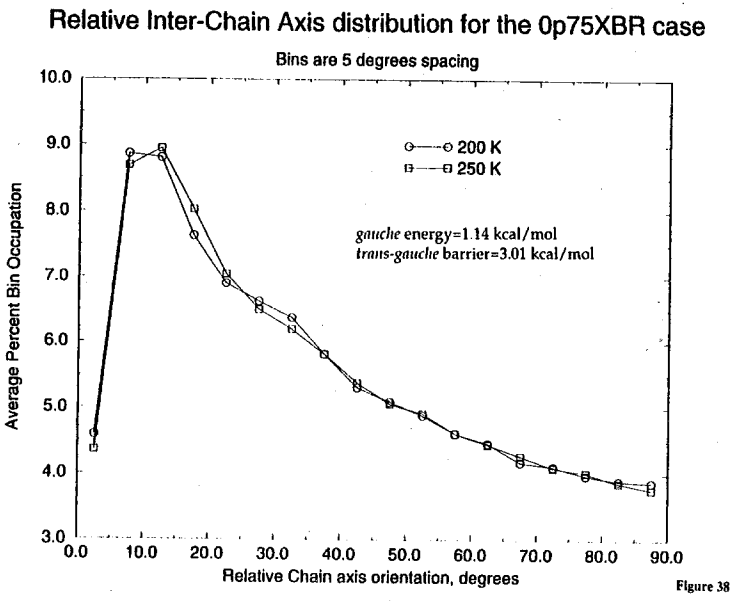

Figure 38

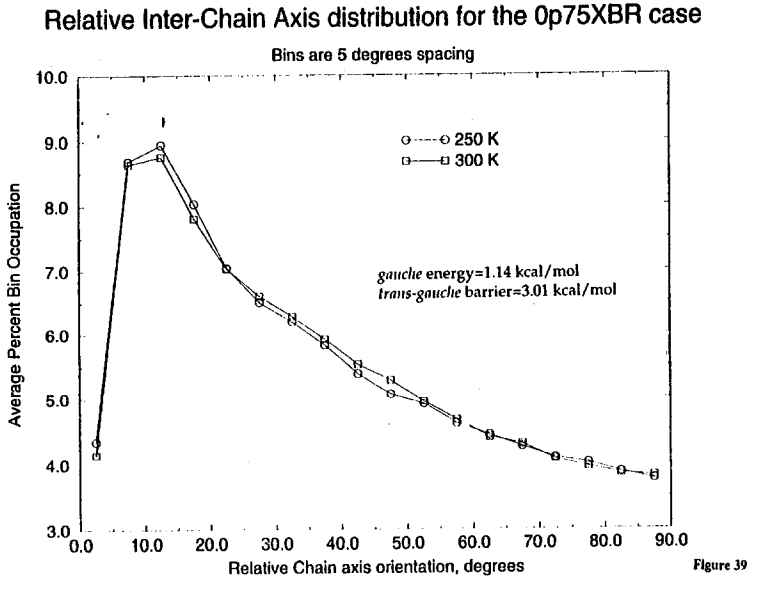

Figure 39

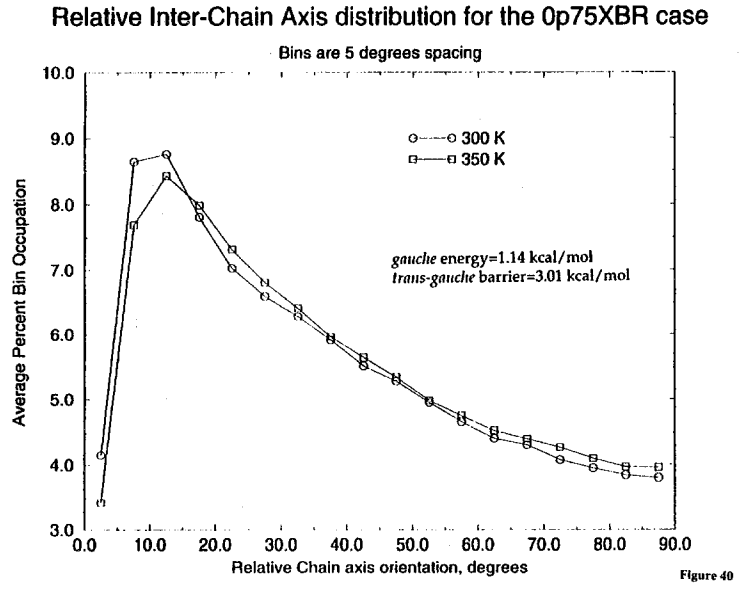

Figure 40

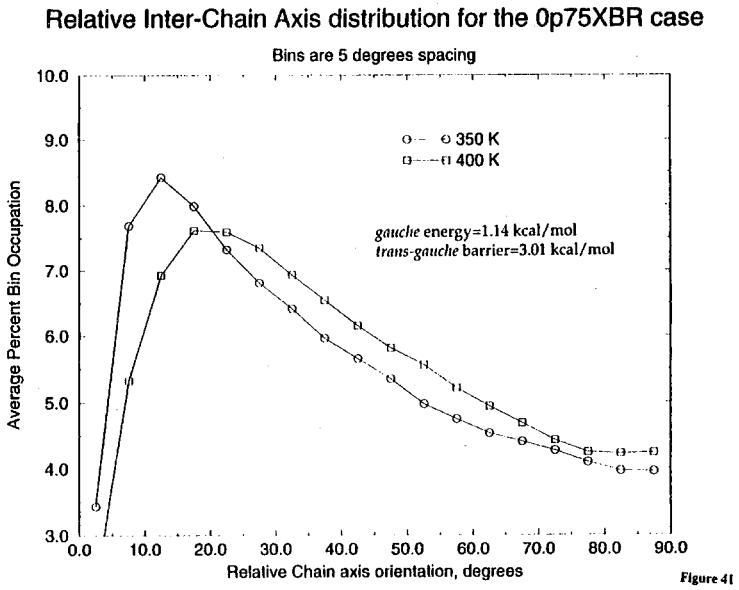

Figure 41

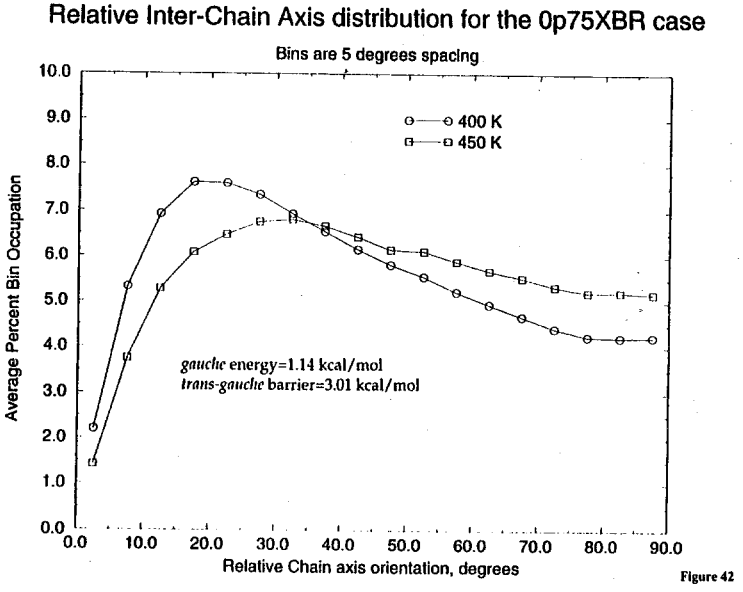

Figure 42

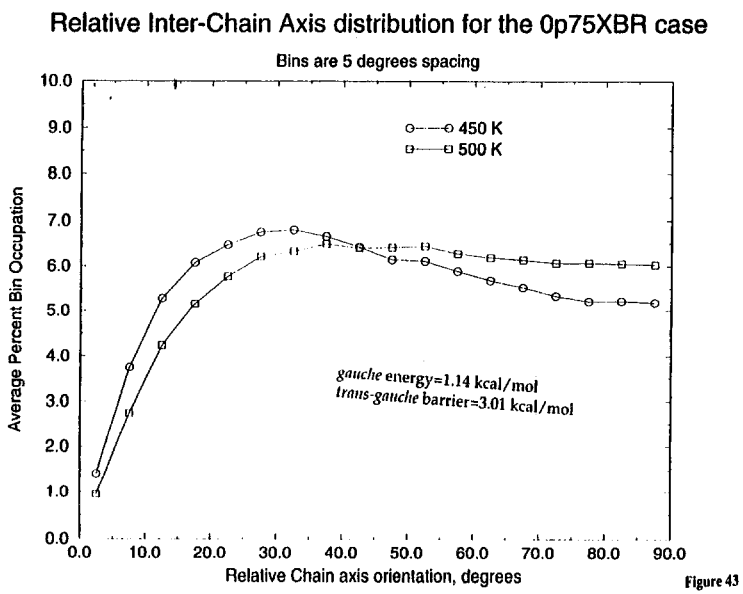

Figure 43

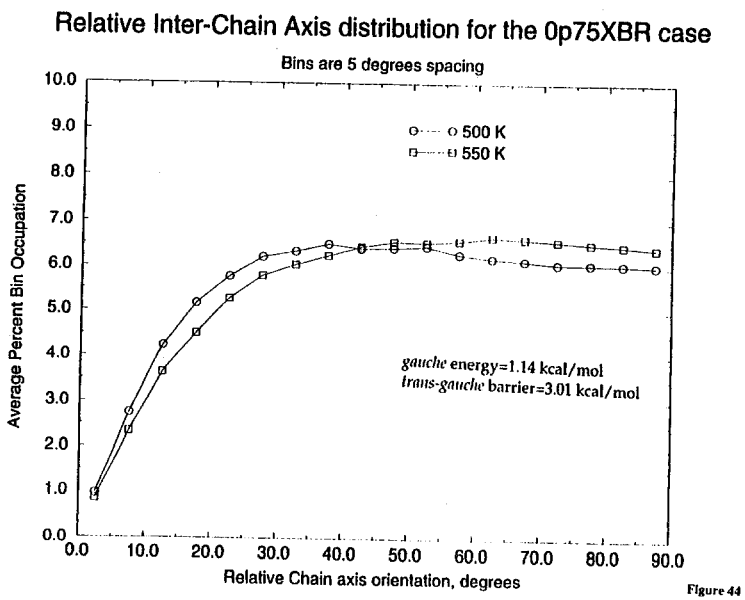

Figure 44

PE model Study: Percent States vs. Temperature

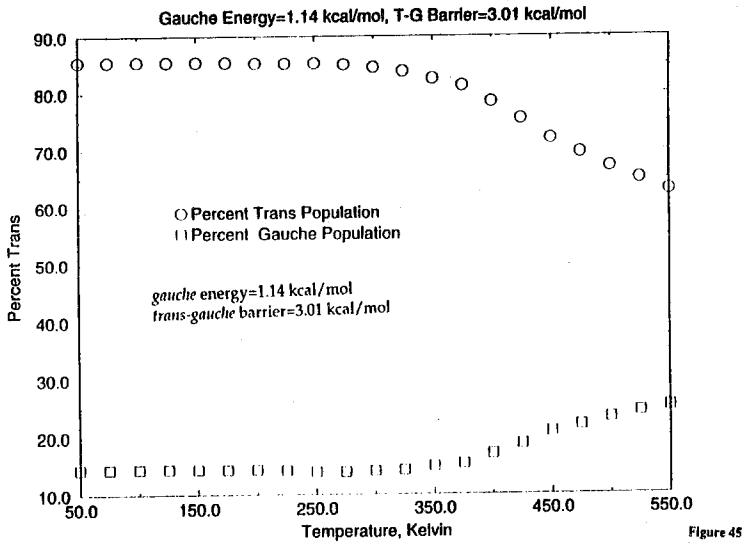

Figure 45

Average Percent deviation from random of correlated pair transitions

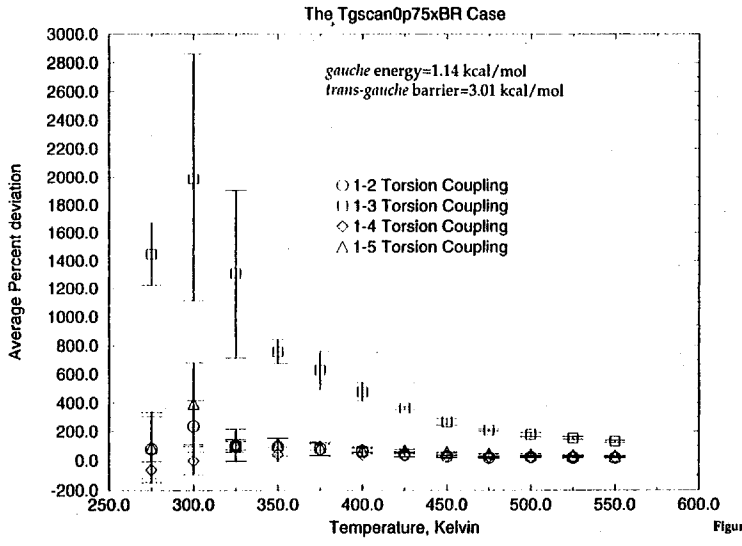

Figure 45 B

Torsional Transition Rate of PE Model vs Temperature

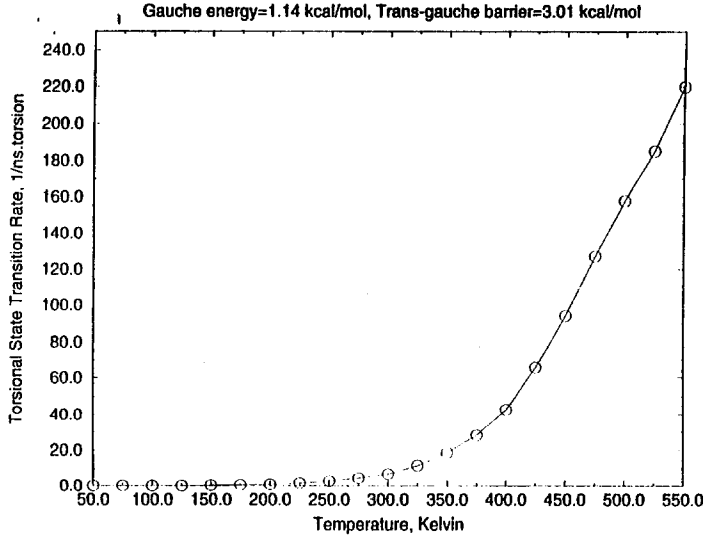

Figure 46

Conformational Arrhenius Plot: ln(Rate) vs. 1/T

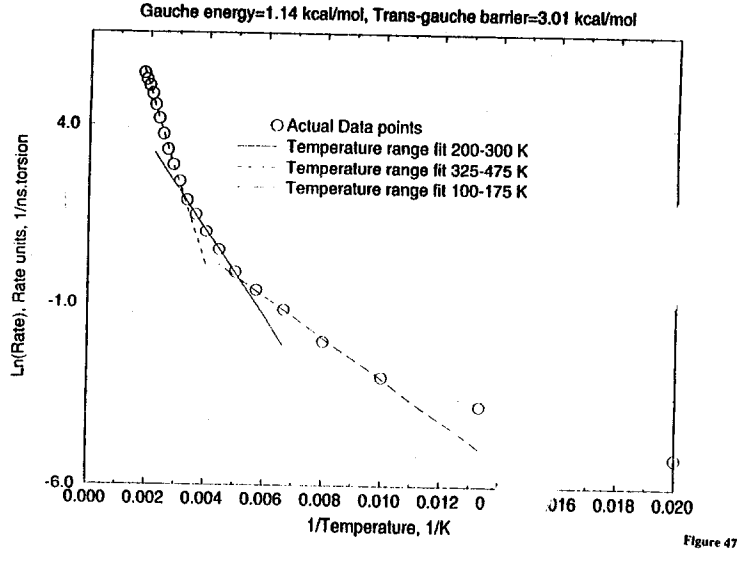

Figure 47

Determination of the Glass Transition of 0p5XBR case

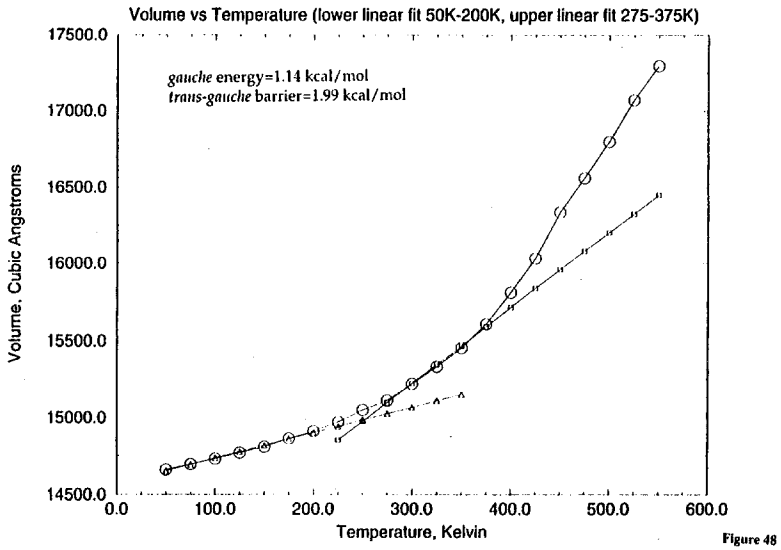

Figure 48

Determination of the Phase Transitions of 0p5XBR case

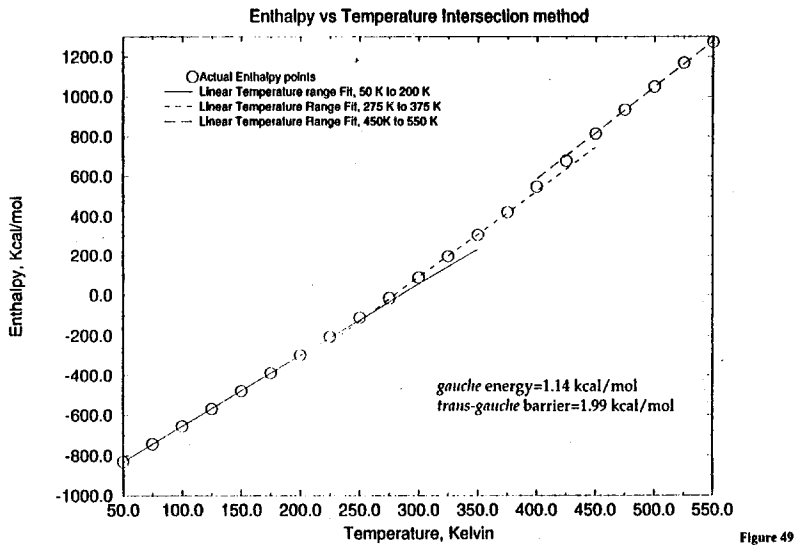

Figure 49

Determination of the Glass Transition of 1p0XBR case

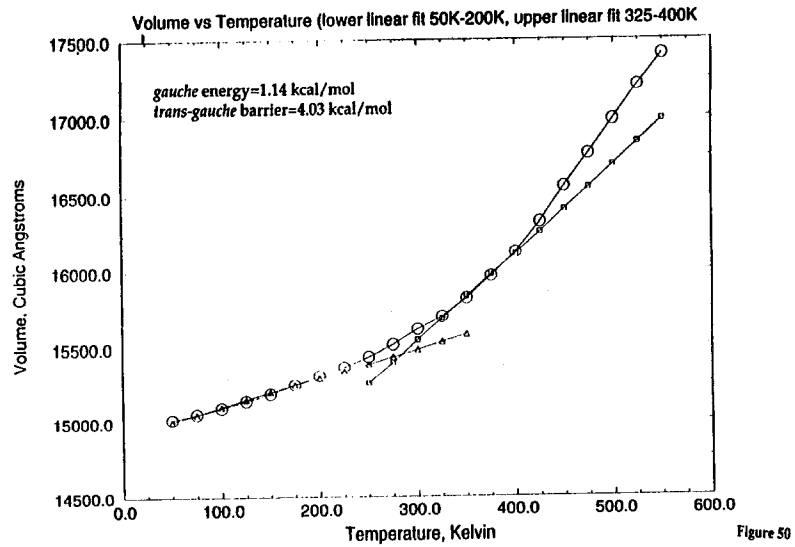

Figure 50

Determination of the Phase Transitions of 1p0XBR case

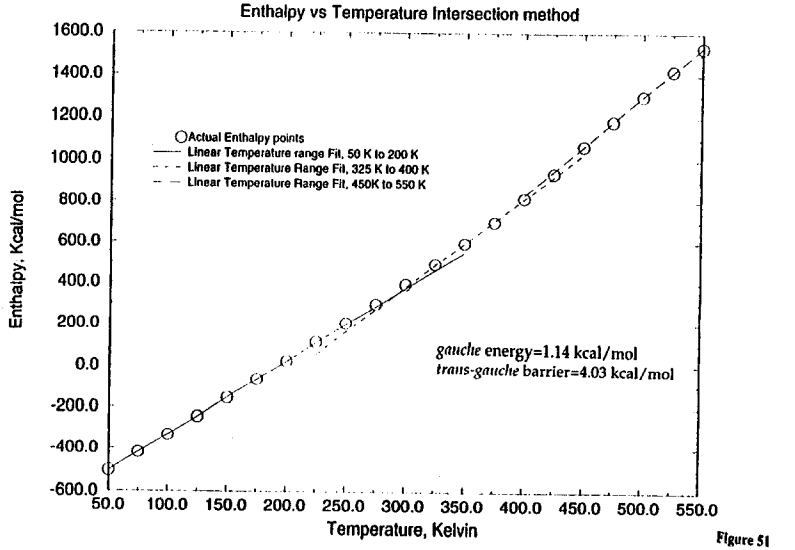

Figure 51

Determination of the Glass Transition of 1p5XBR case

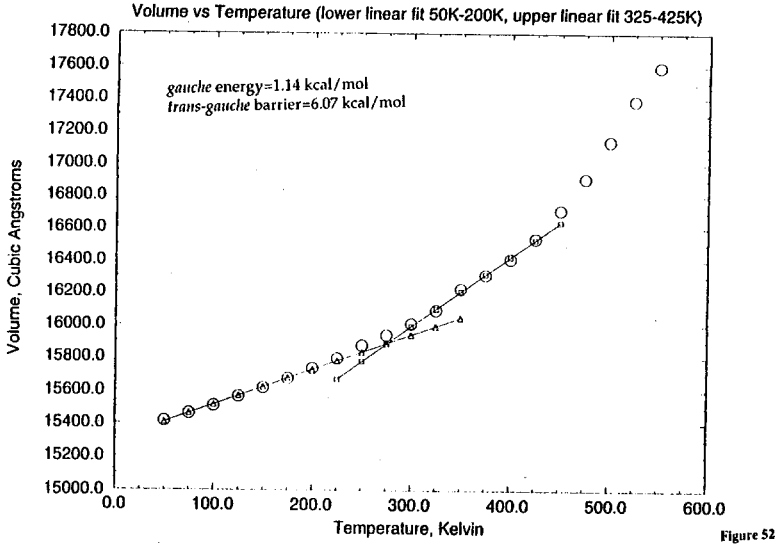

Figure 52

Determination of the Phase Transitions of 1p5XBR case

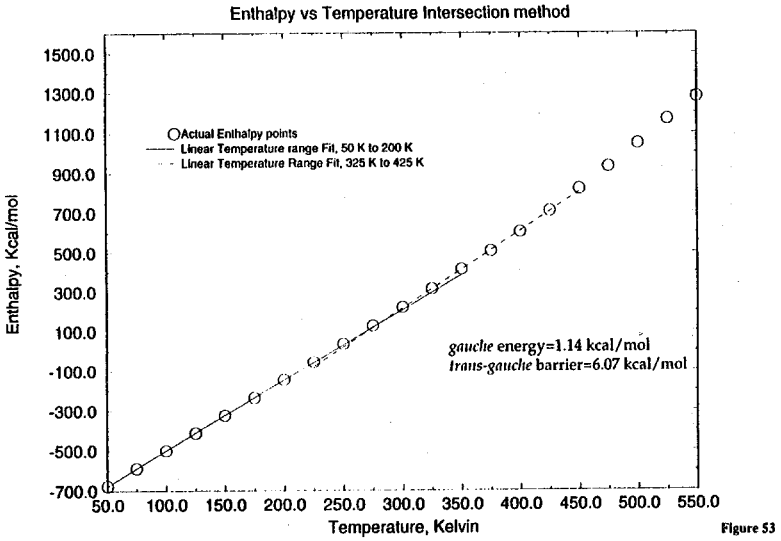

Figure 53

Torsional Barrier Effect on Compressiblity: PE model Study

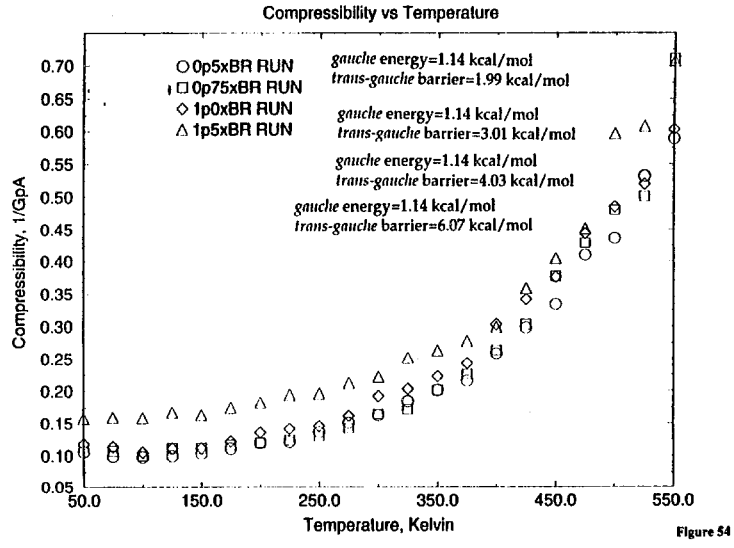

Figure 54

0p5XBR PE model Study: ALPHA vs. Temperature

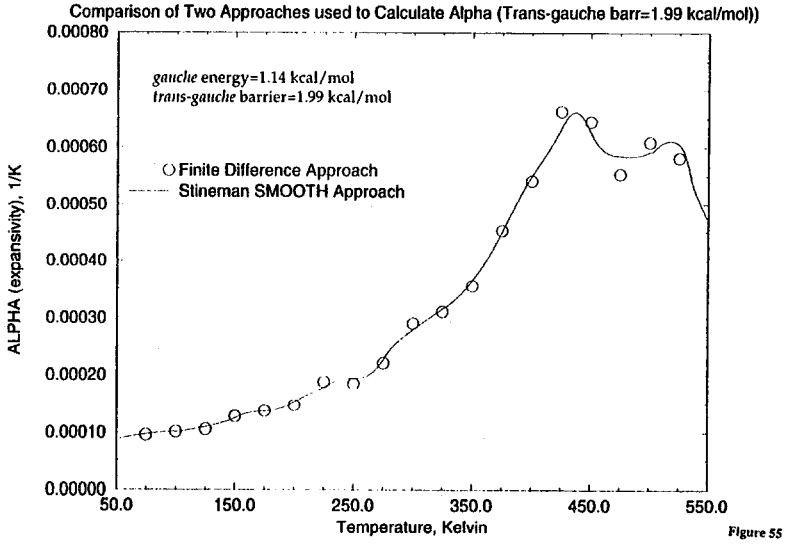

Figure 55

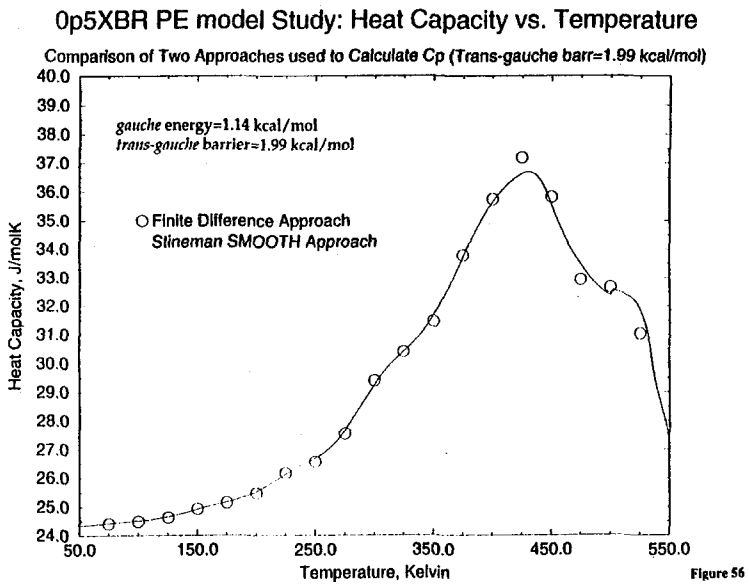

Figure 56

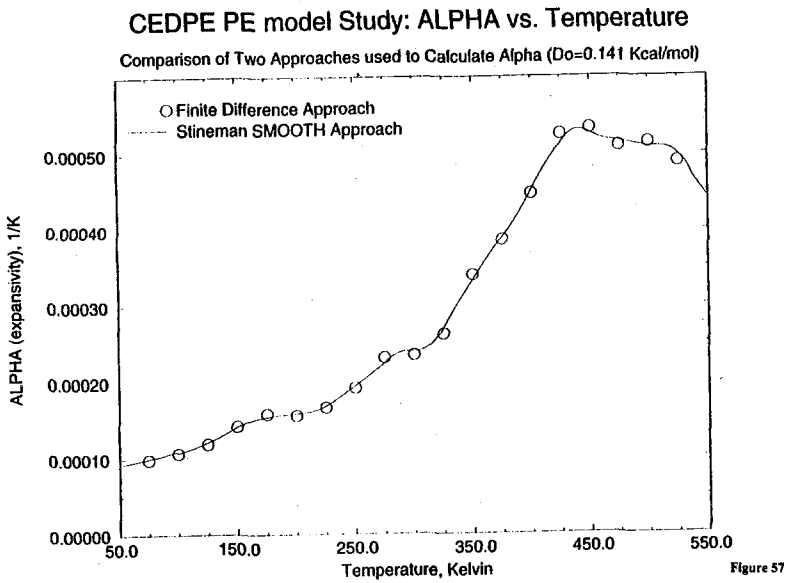

Figure 57

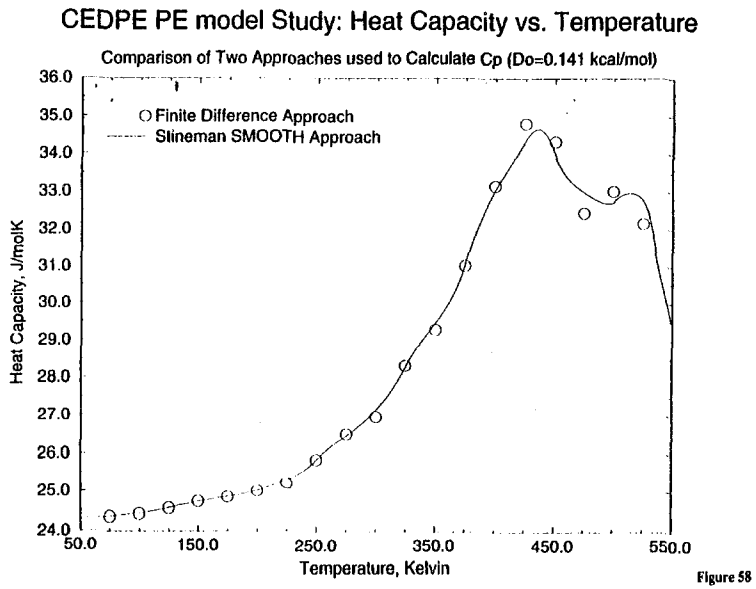

Figure 58

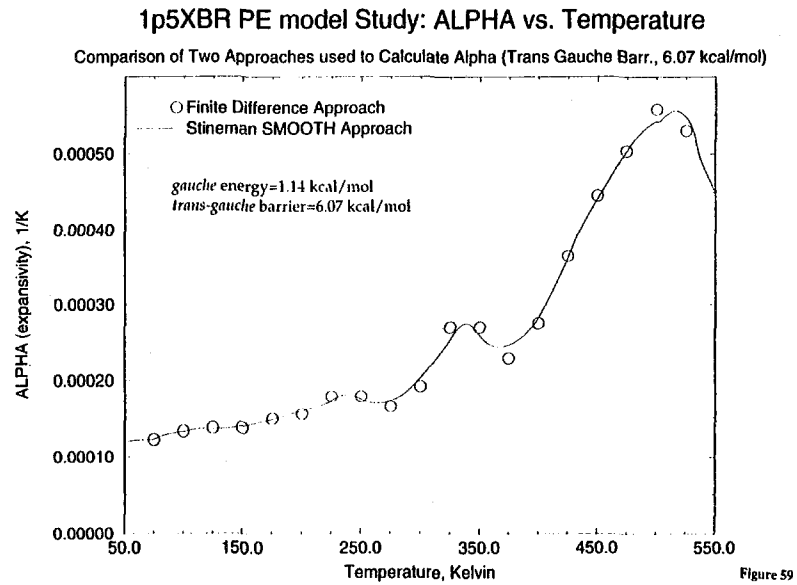

Figure 59

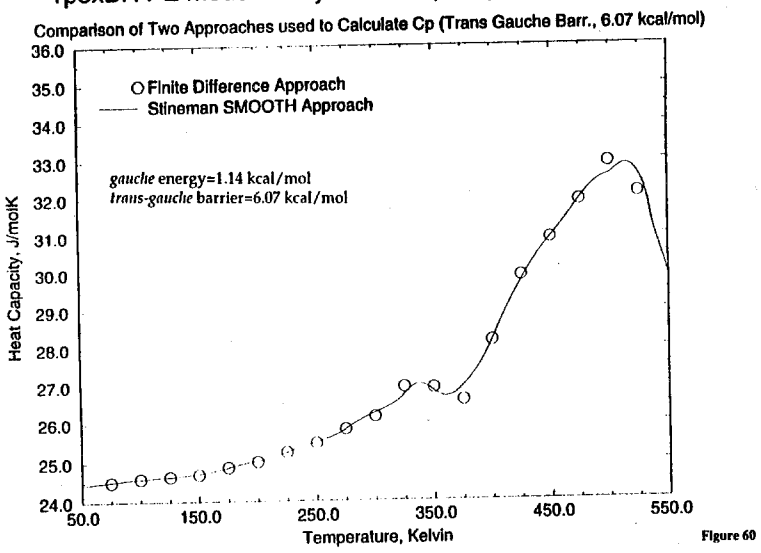

Figure 60

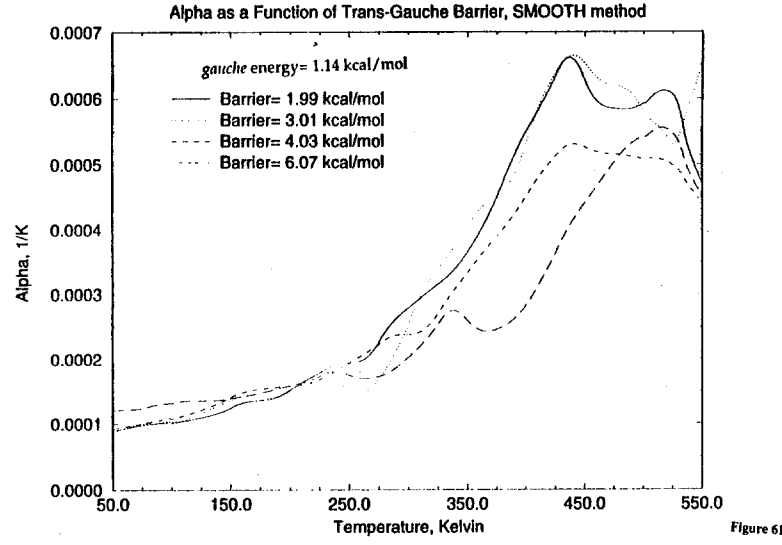

Figure 61

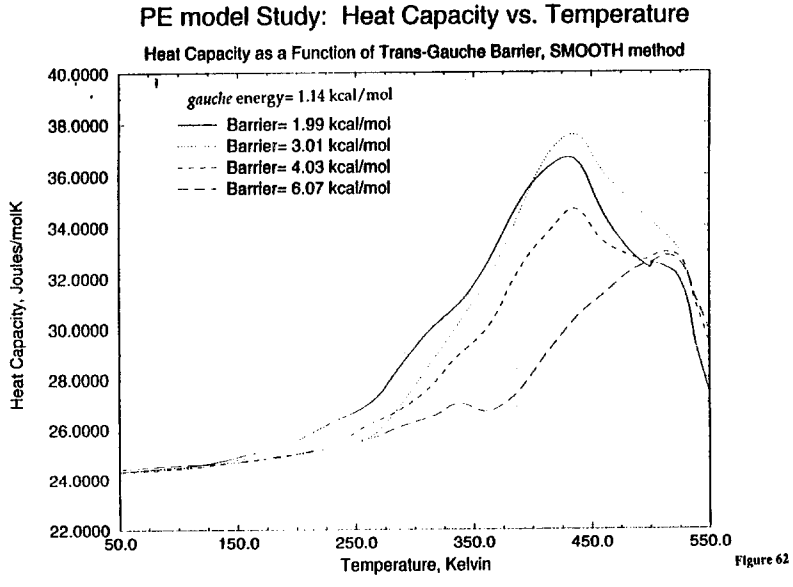

Figure 62

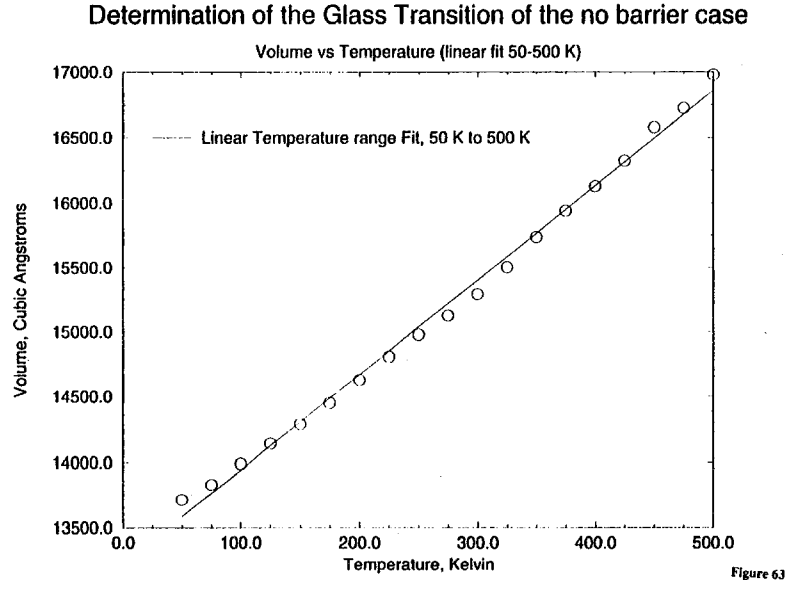

Figure 63

Determination of the Phase Transitions of the no barrier case

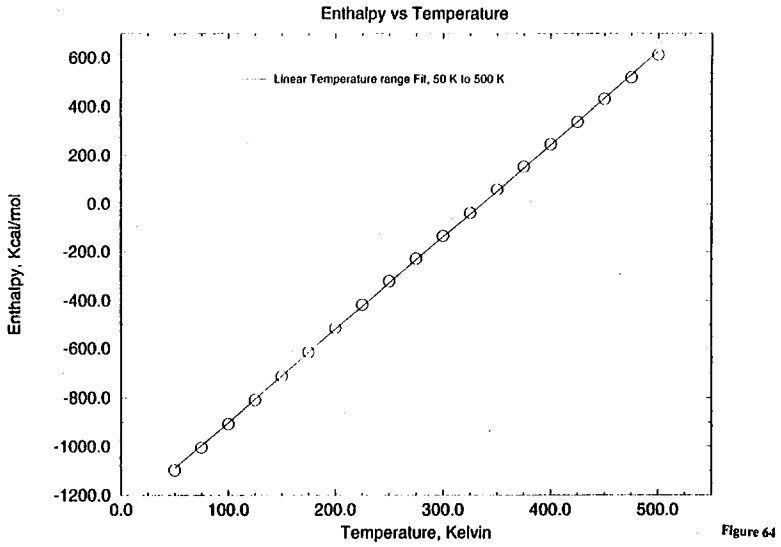

Figure 64

Determination of the Glass Transition of tgscan0p002 case

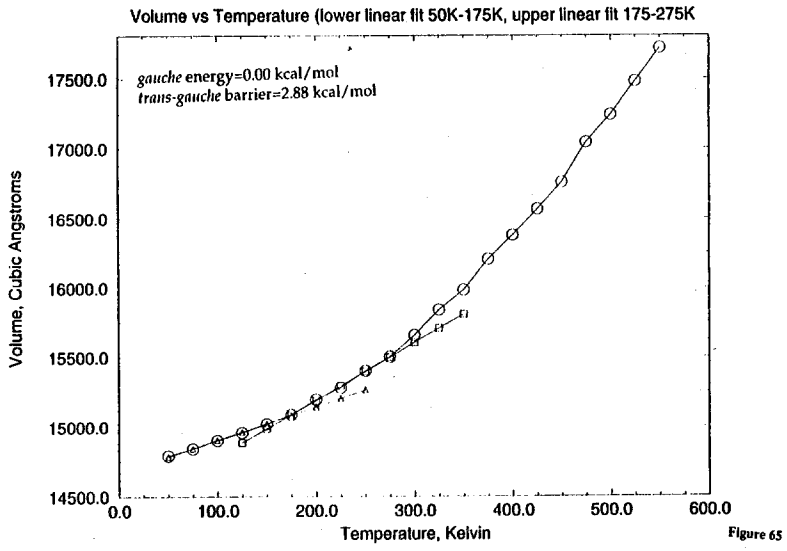

Figure 65

Determination of the Phase Transitions of 0p002 case (low barrier)

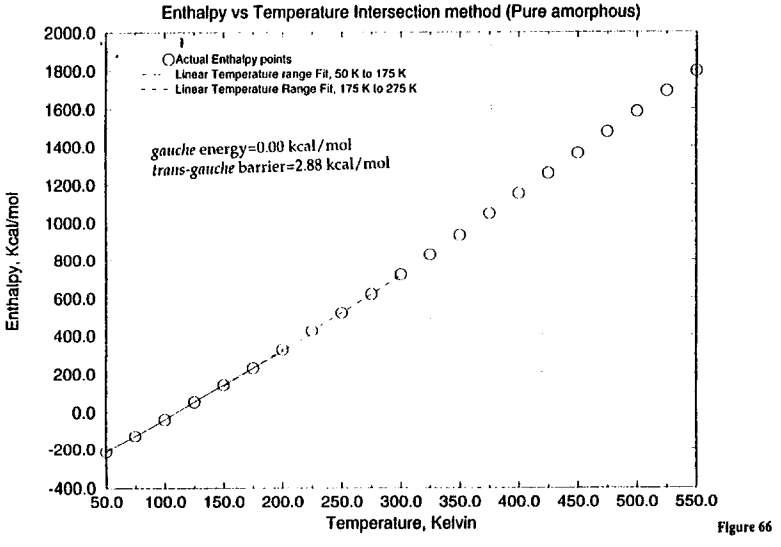

Figure 66

Determination of the Glass Transition of 0p00 case (high barrier)

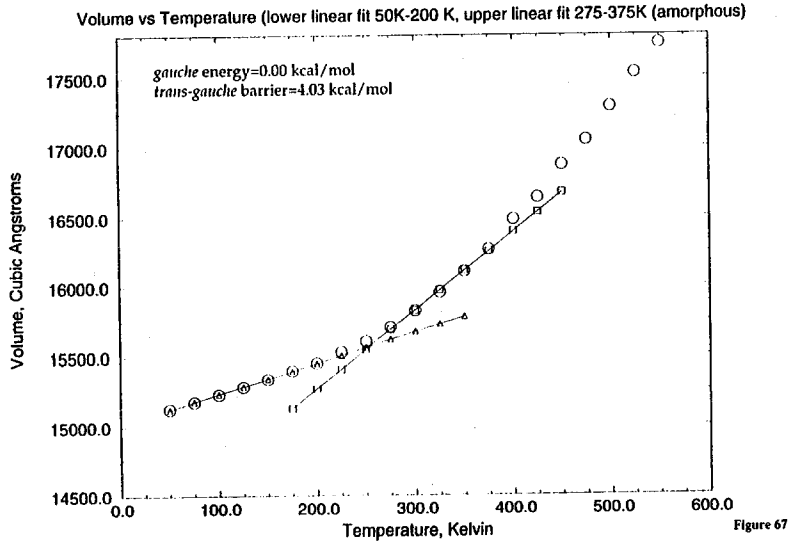

Figure 67

Determination of the Phase Transitions of 0p00 case (high barrier)

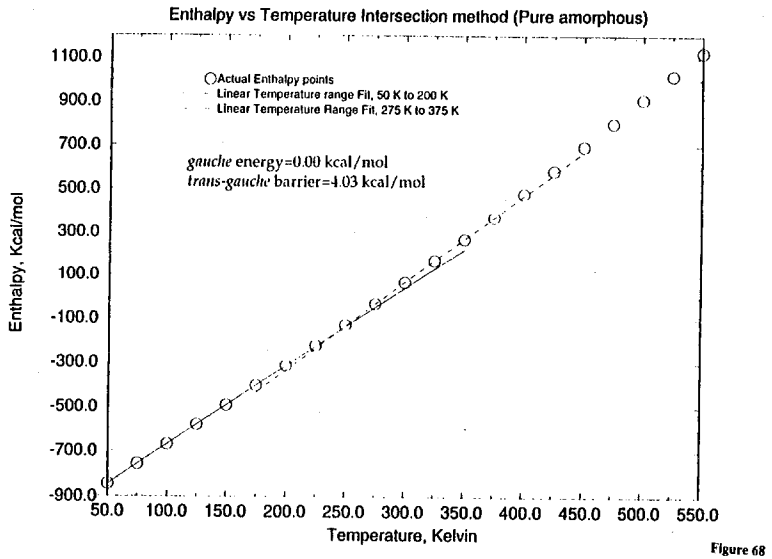

Figure 68

Determination of the Glass Transition of 0p003 case (highest barrier)

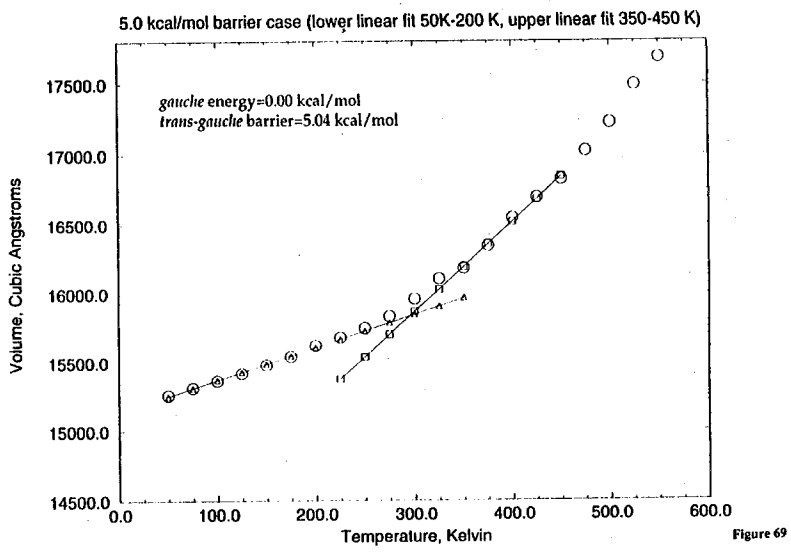

Figure 69

Determination of the Phase Transitions of 0p003 case (highest barrier)

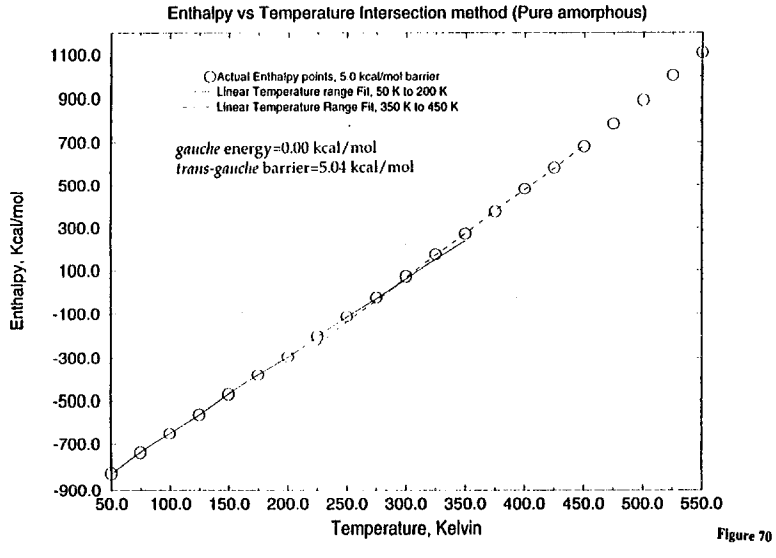

Figure 70

PE model Study: Density vs. Temperature

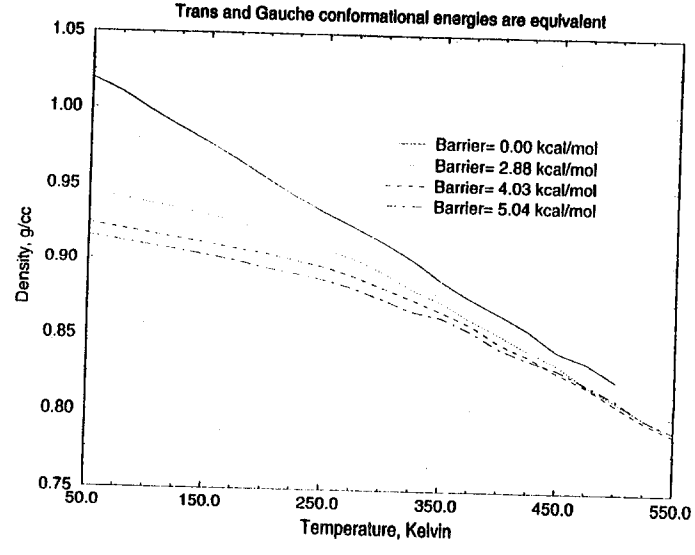

Figure 71

Torsional Barrier Effect on Compressiblity: PE model Study

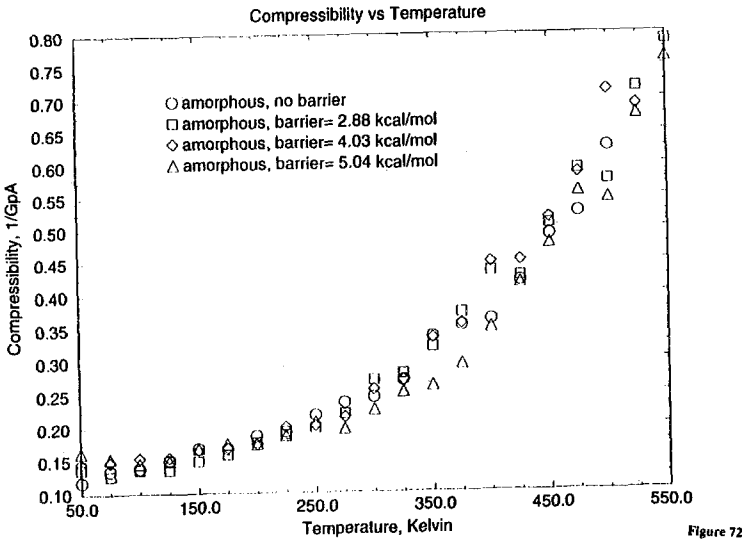

Figure 72

Amorphous PE model Study: Expansivity vs. Temperature

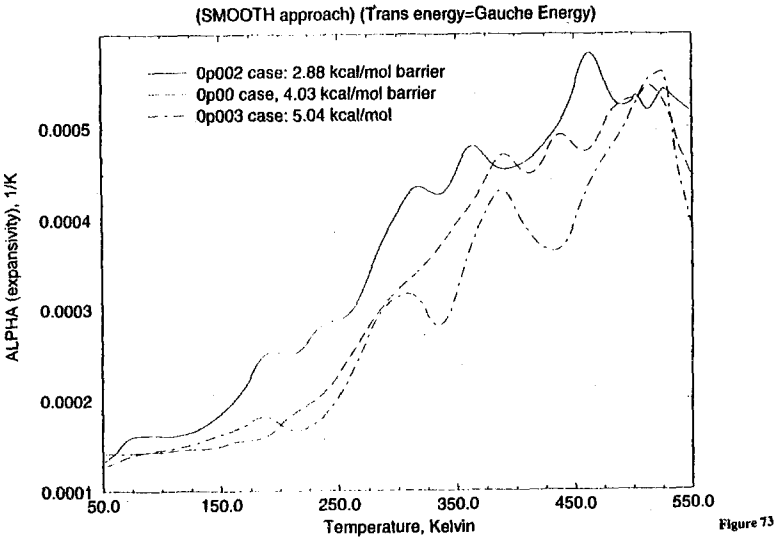

Figure 73

Amorphous PE model Study: Heat Capacity vs. Temperature

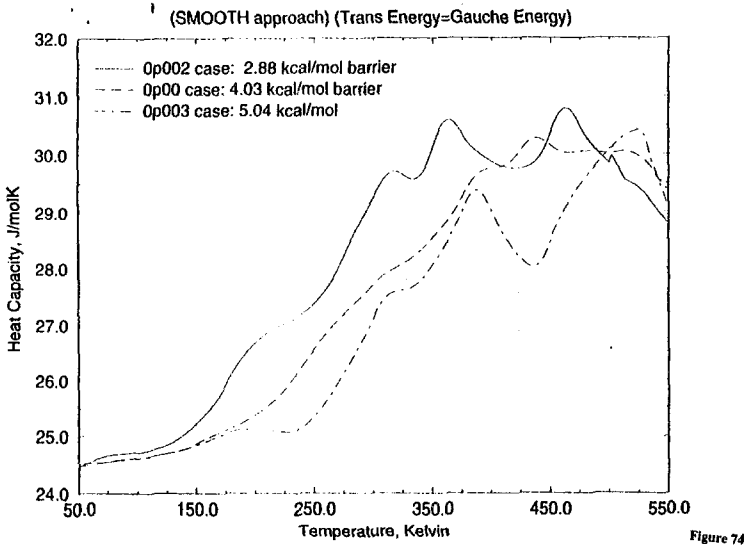

Figure 74

Average Intra Chain axis order Parameter

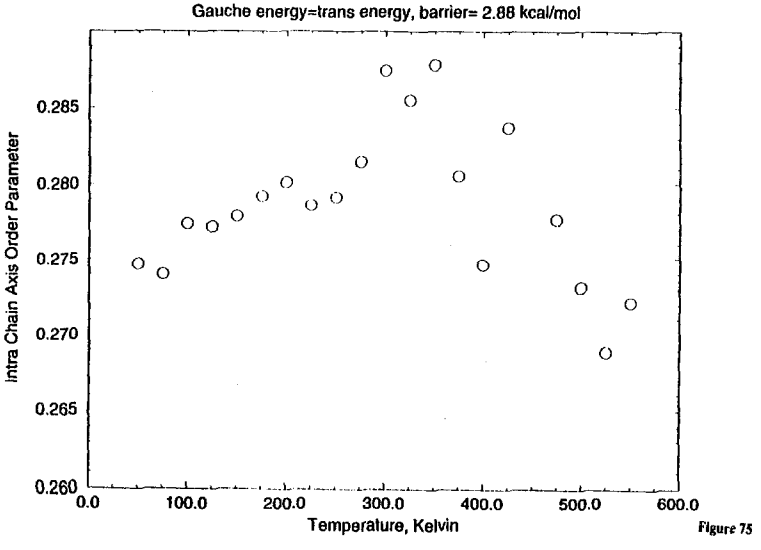

Figure 75

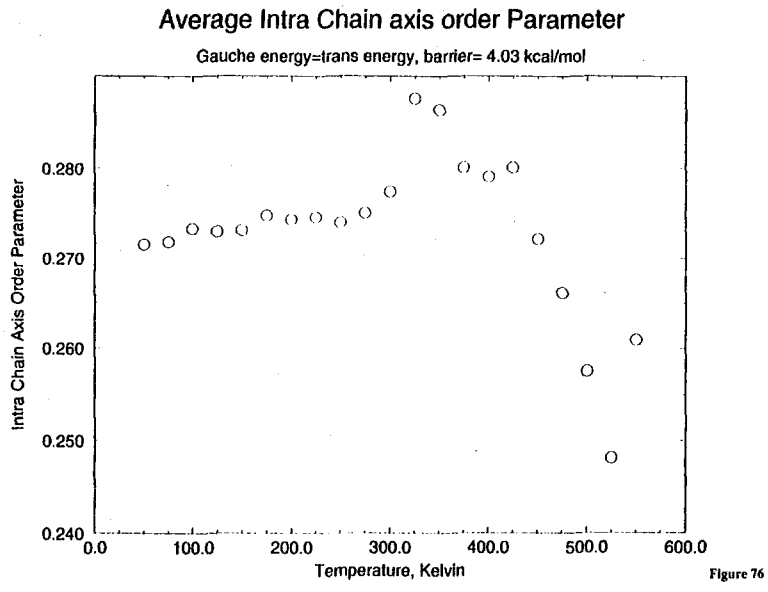

Figure 76

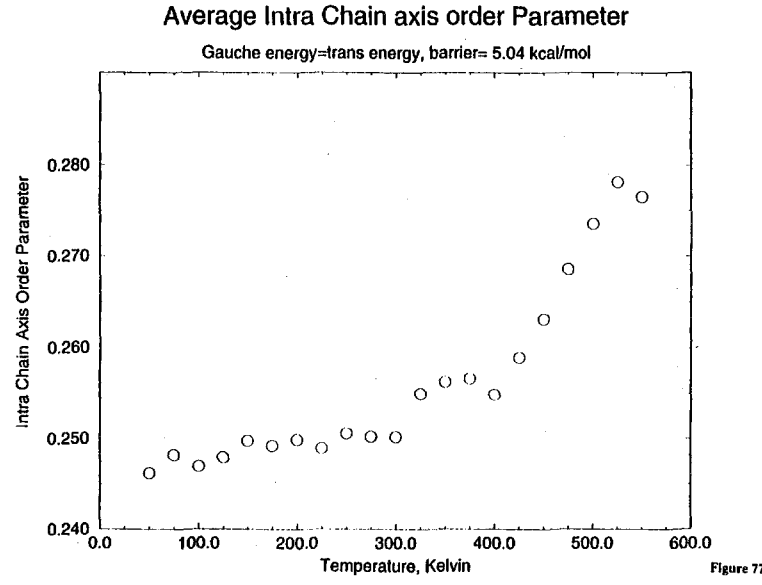

Figure 77

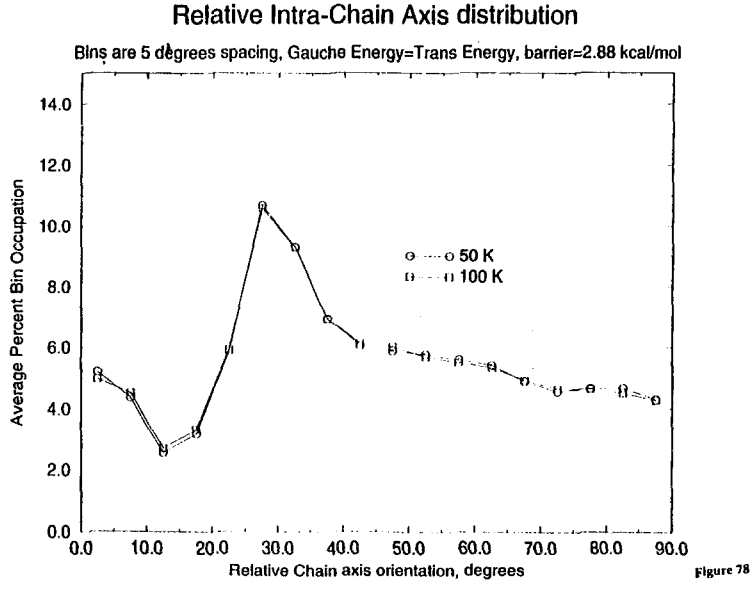

Figure 78

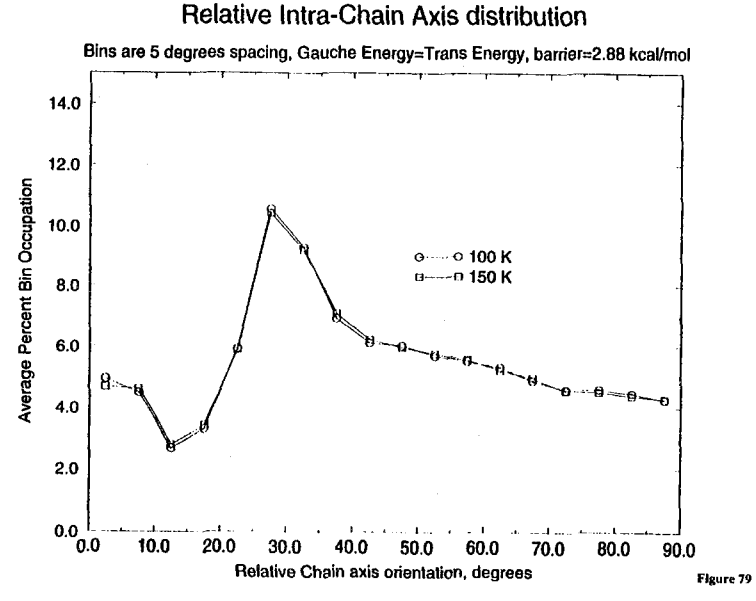

Figure 79

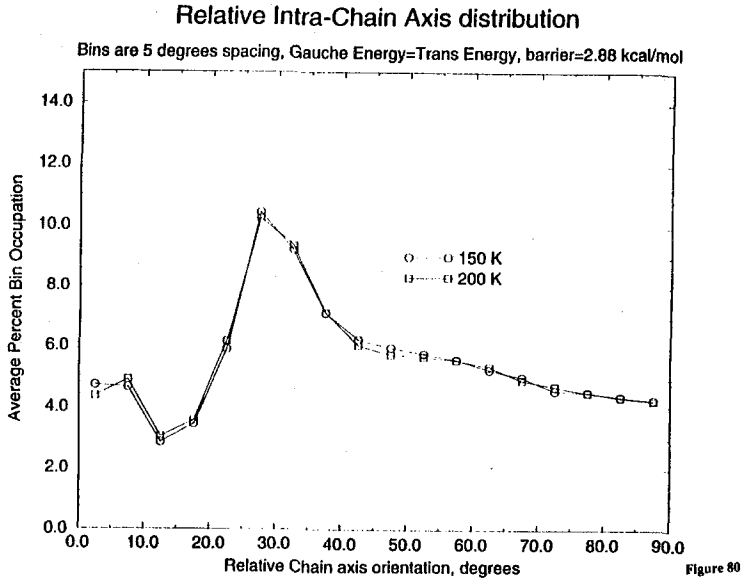

Figure 80

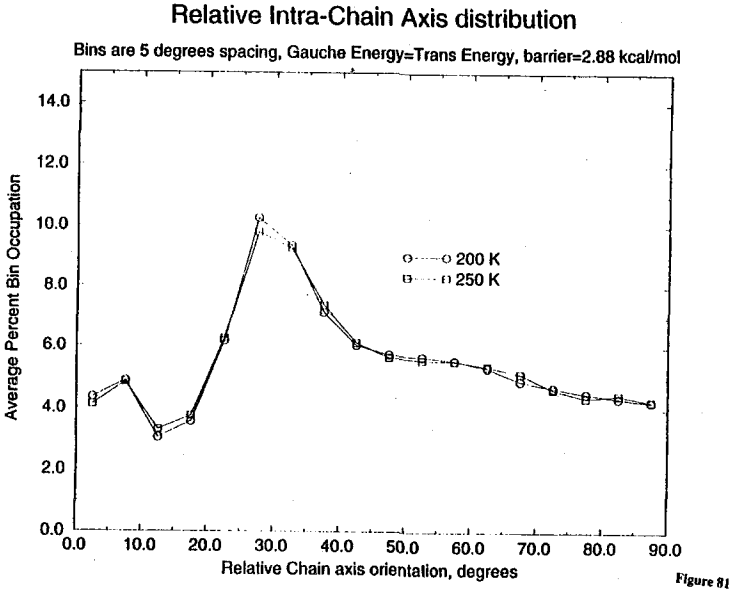

Figure 81

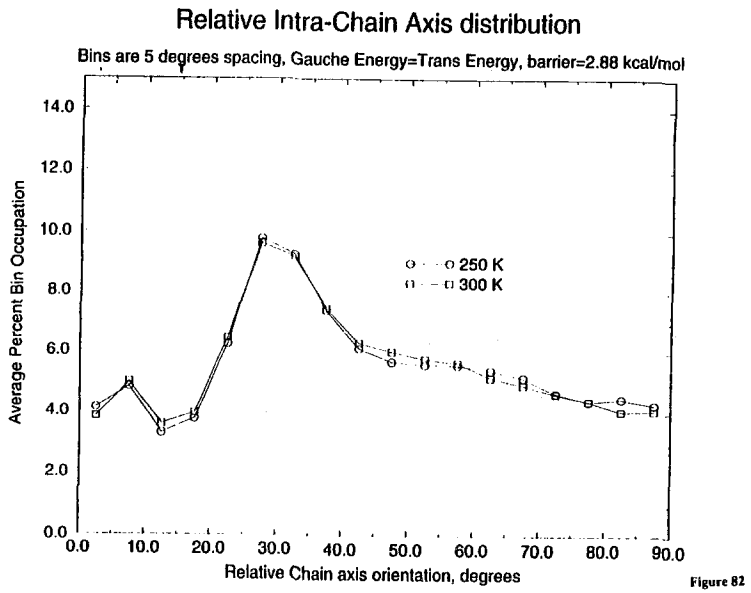

Figure 82

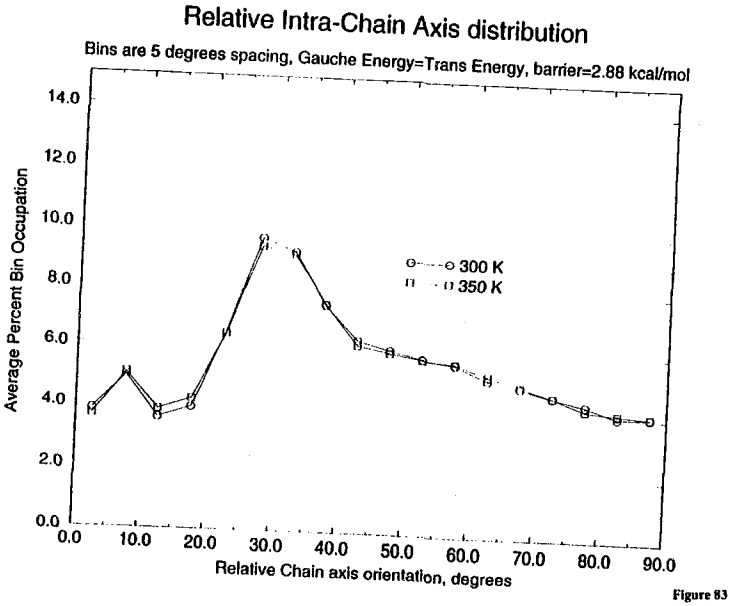

Figure 83

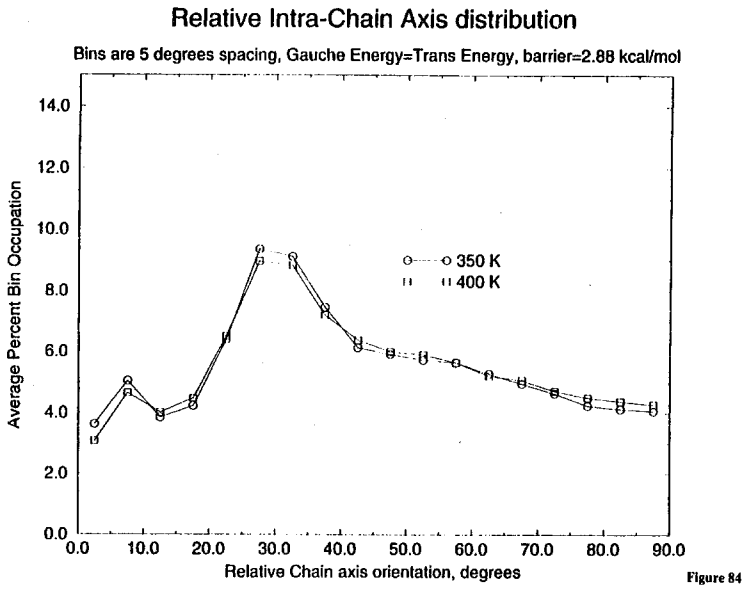

Figure 84

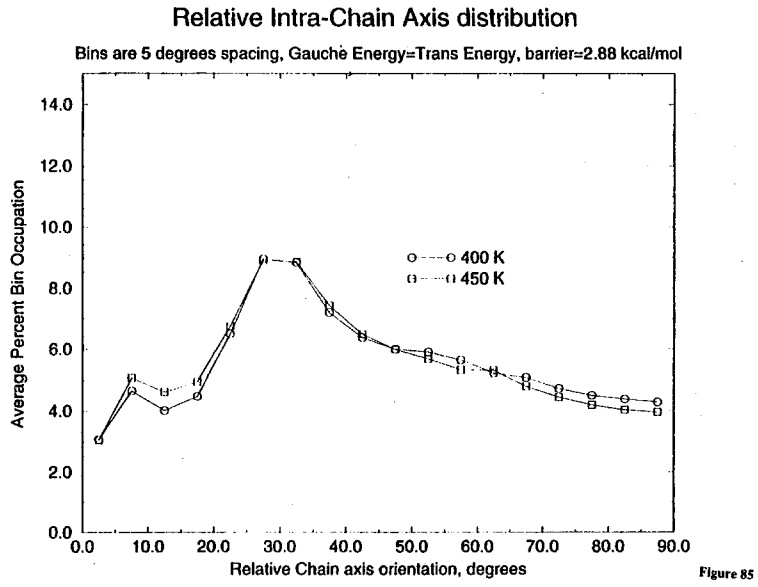

Figure 85

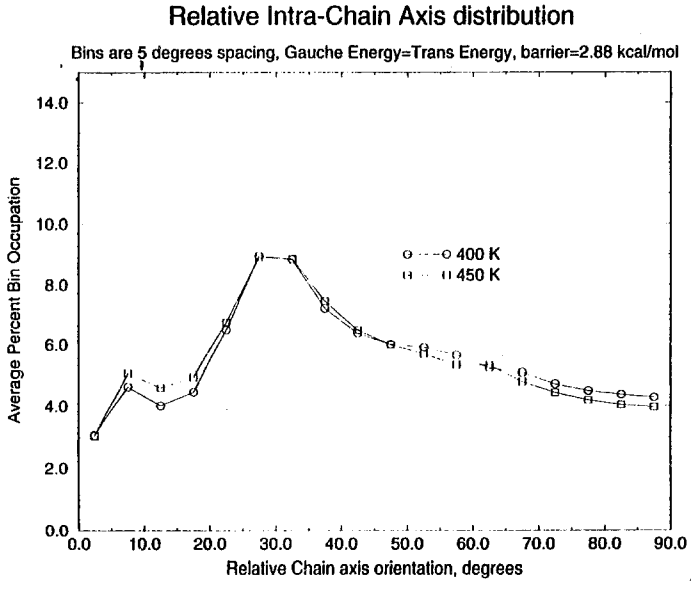

Figure 86

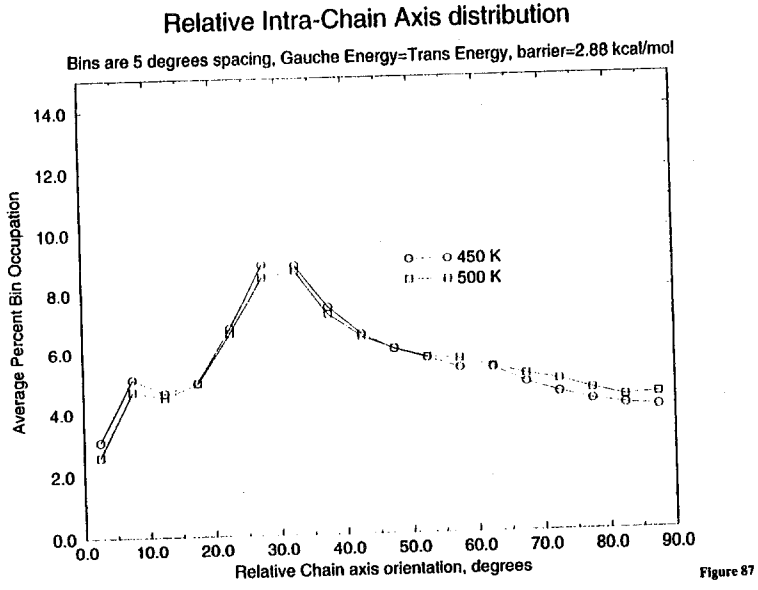

Figure 87

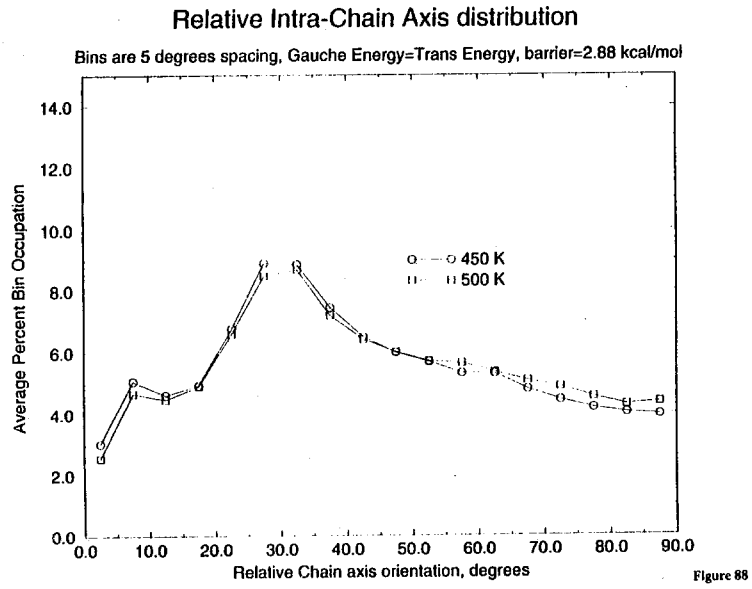

Figure 88

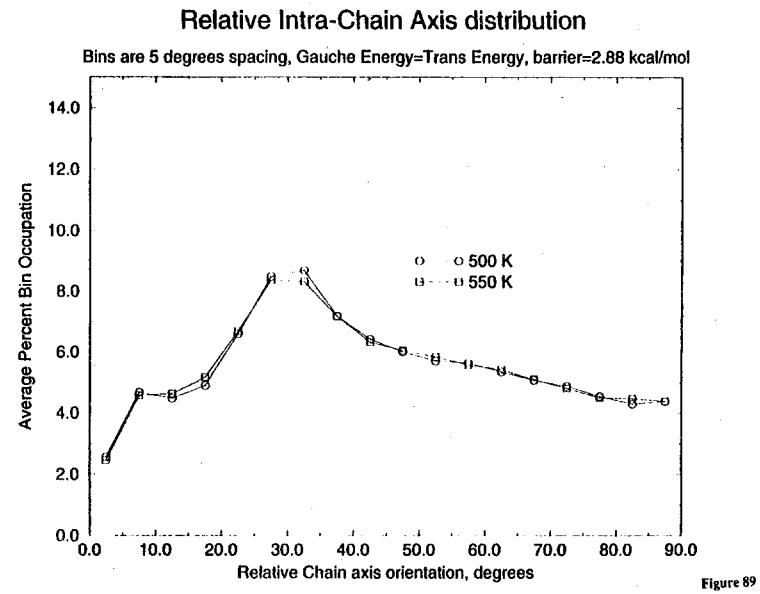

Figure 89

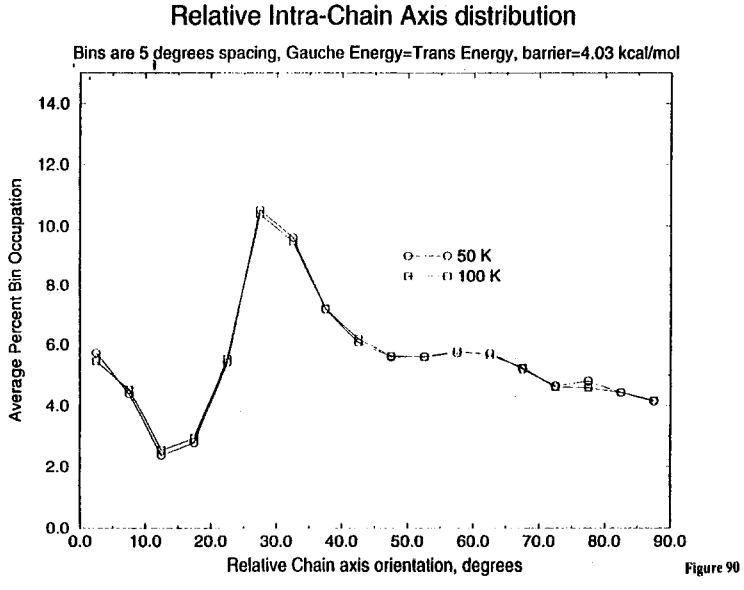

Figure 90

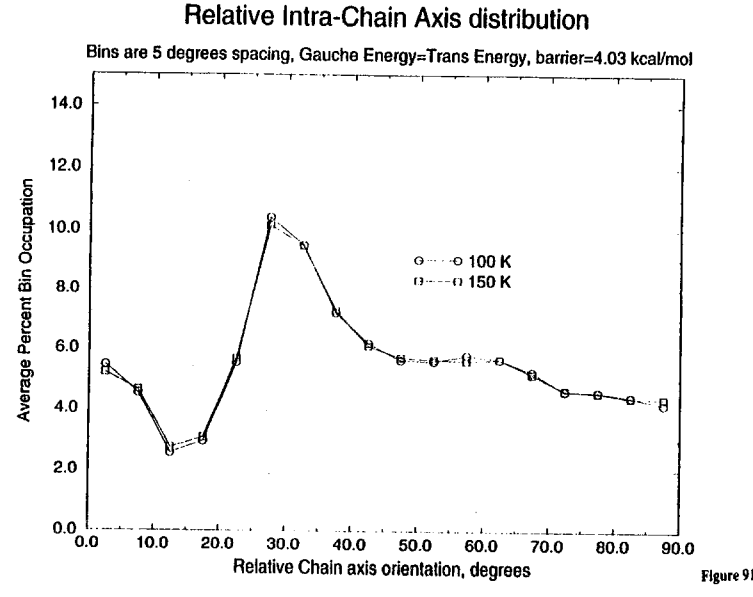

Figure 91

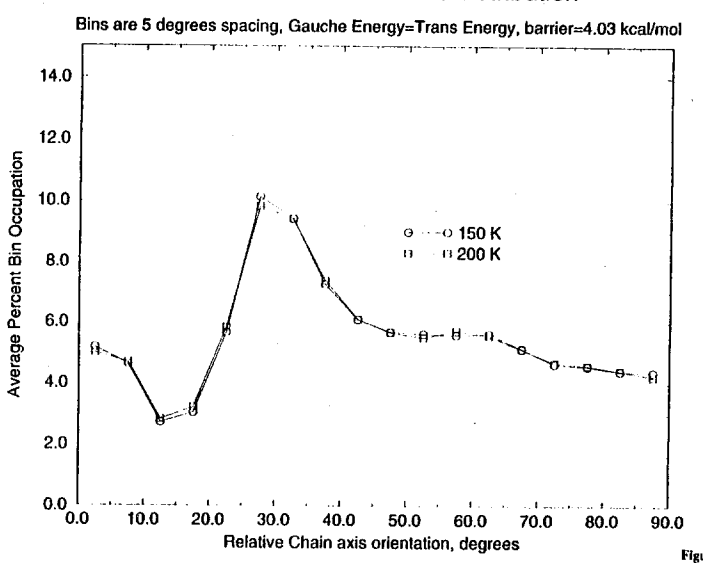

Figure 92

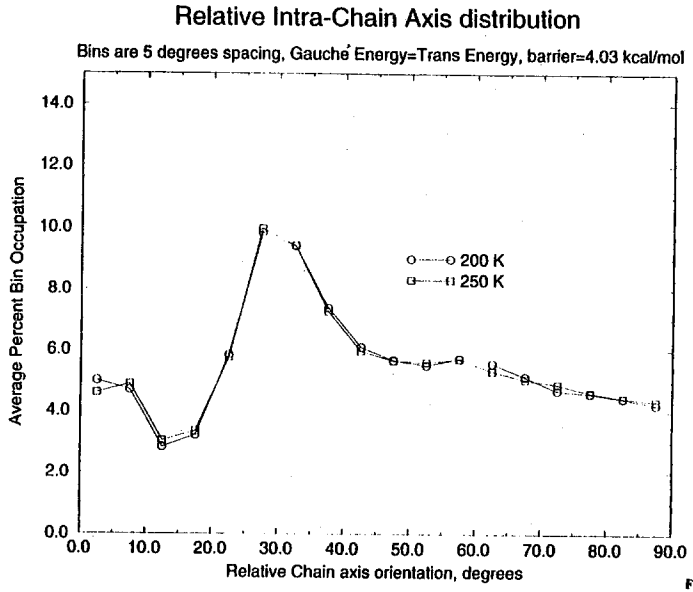

Figure 93

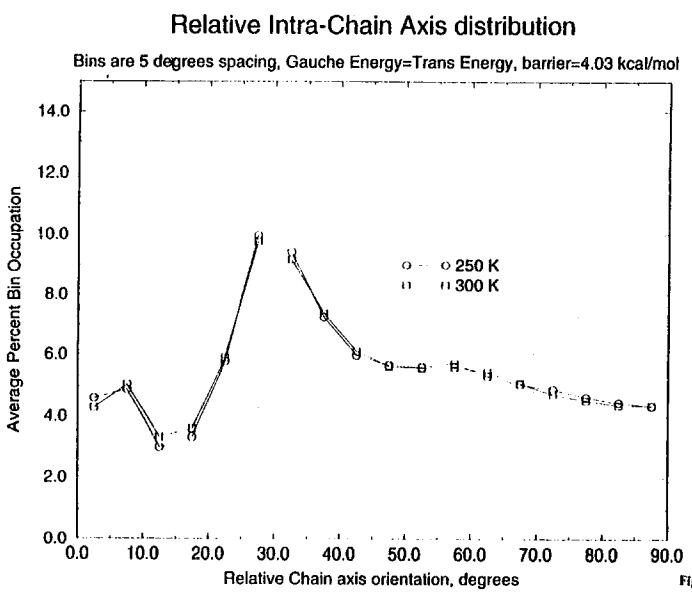

Figure 94

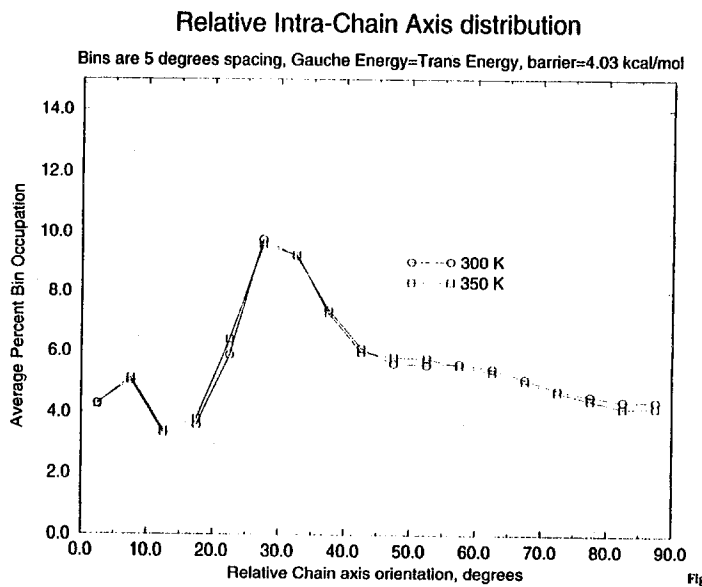

Figure 95

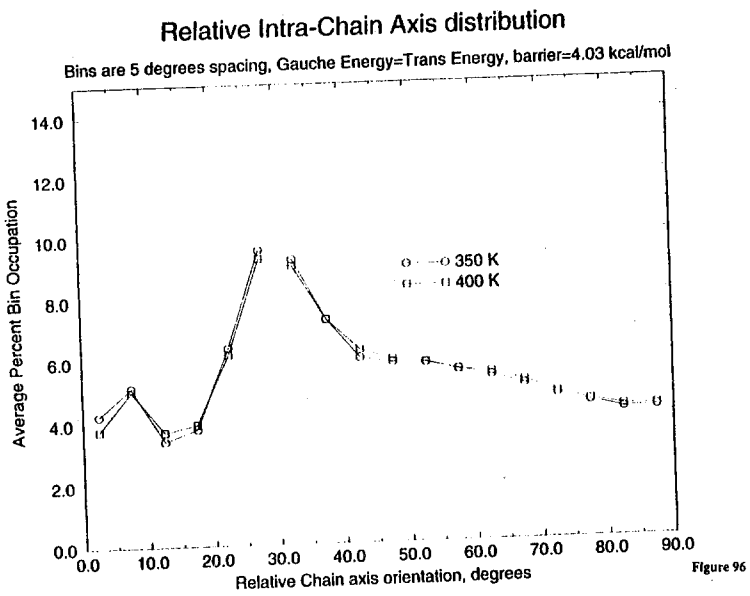

Figure 96

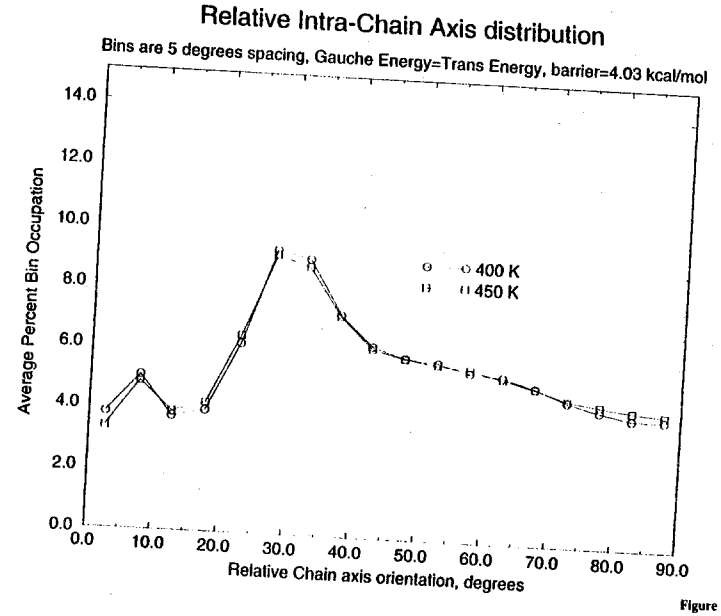

Figure 97

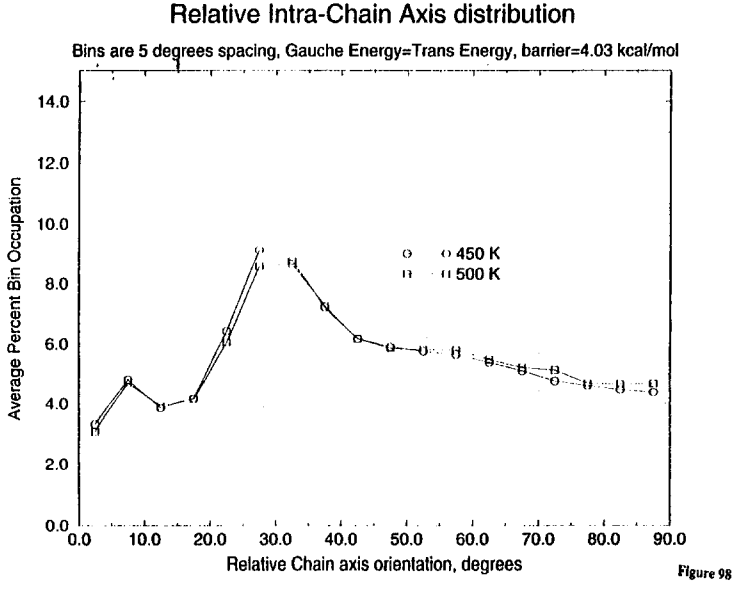

Figure 98

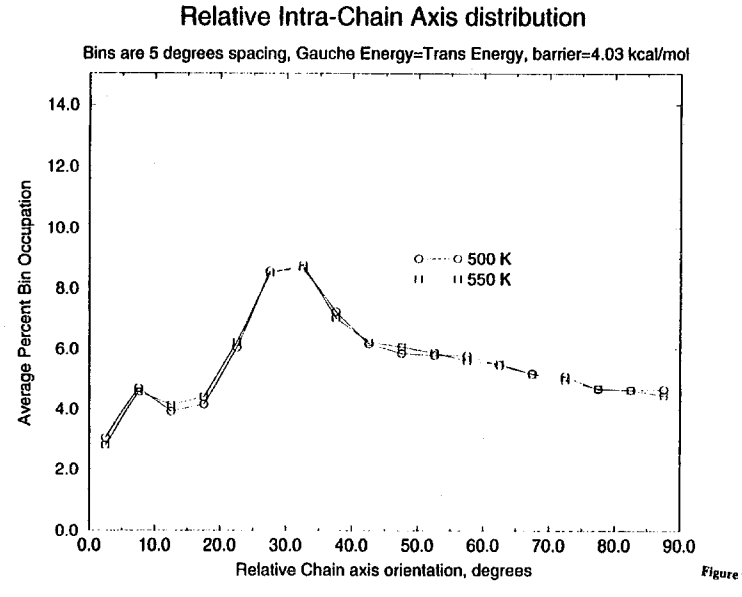

Figure 99

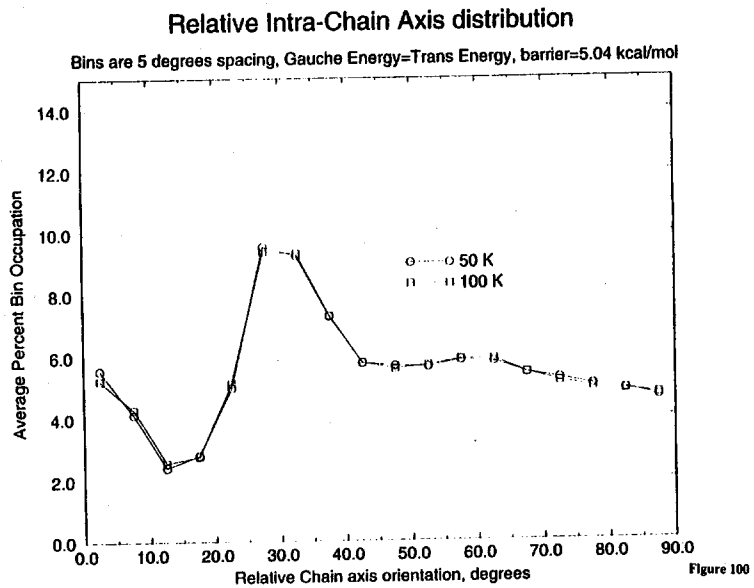

Figure 100

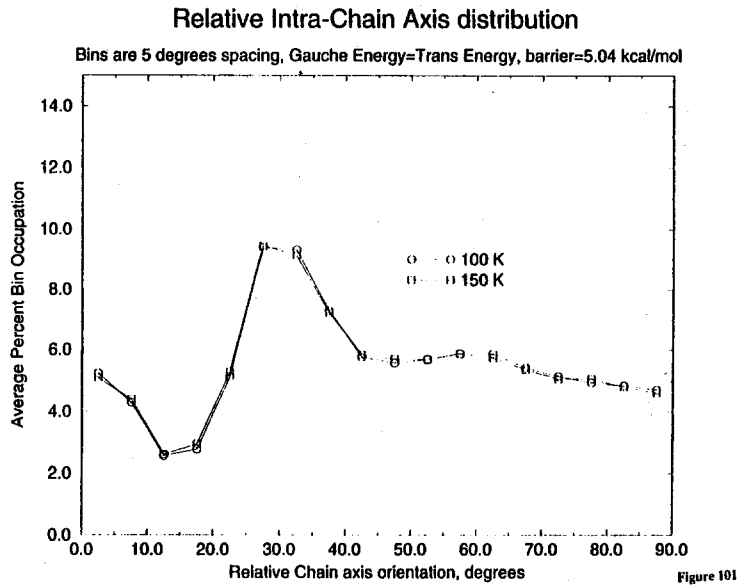

Figure 101

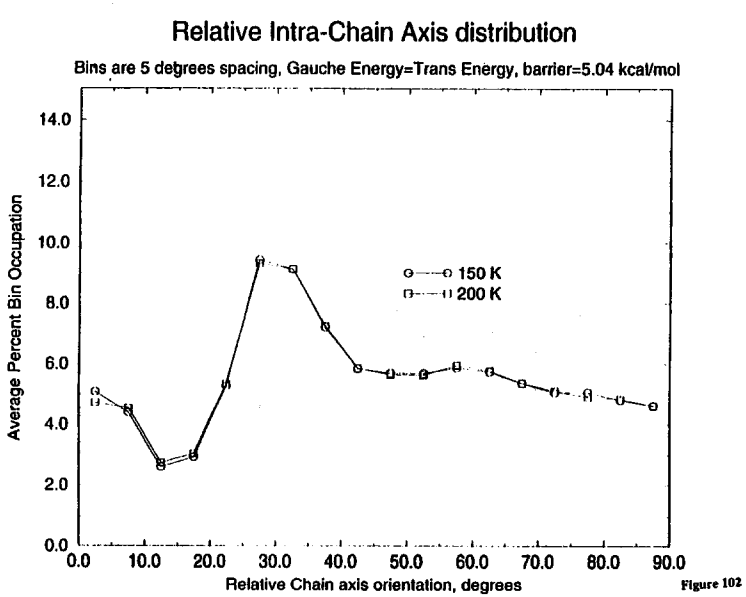

Figure 102

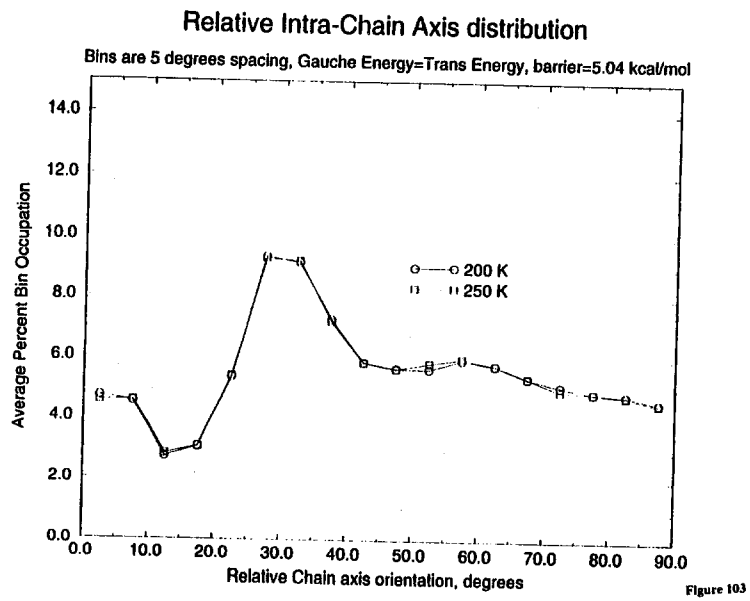

Figure 103

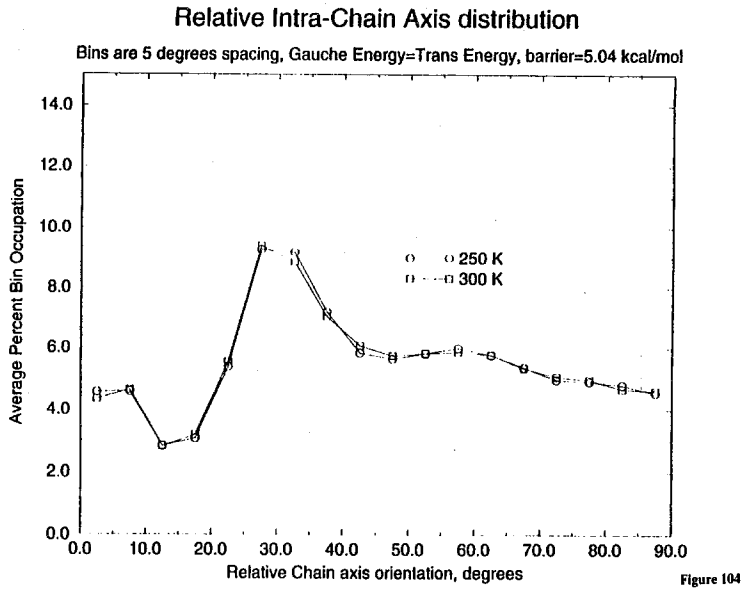

Figure 104

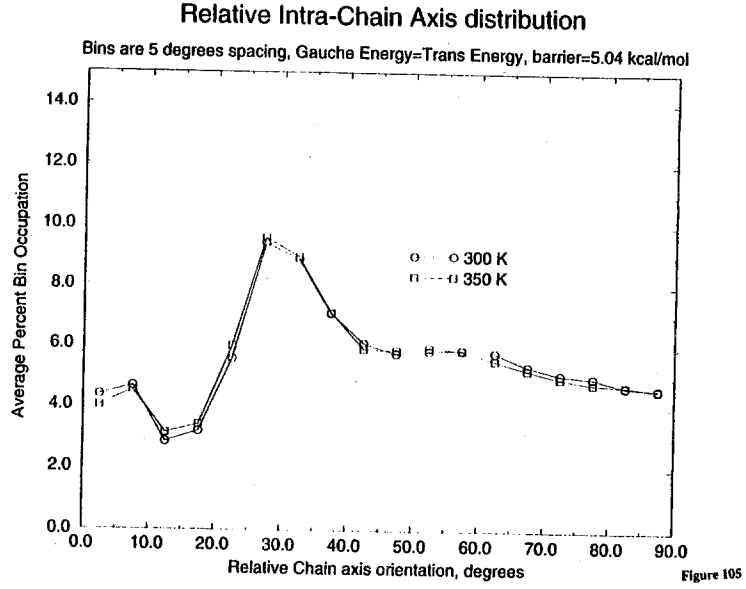

Figure 105

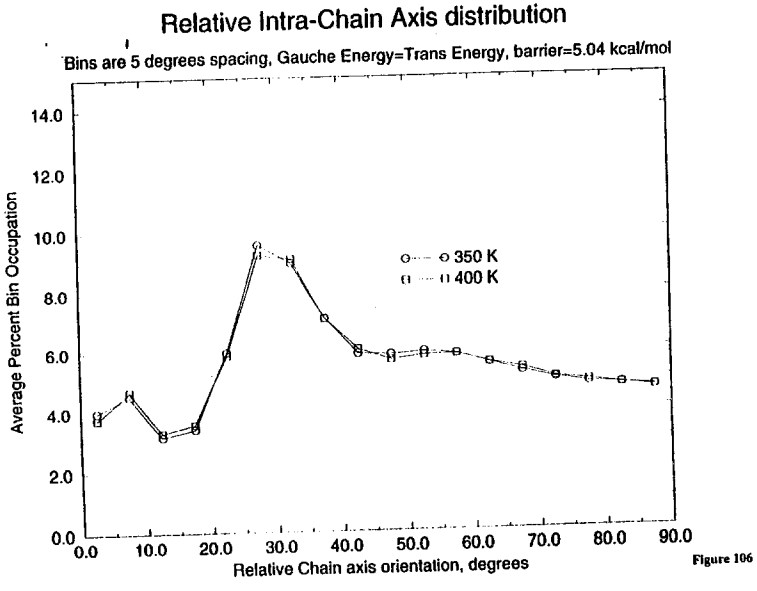

Figure 106

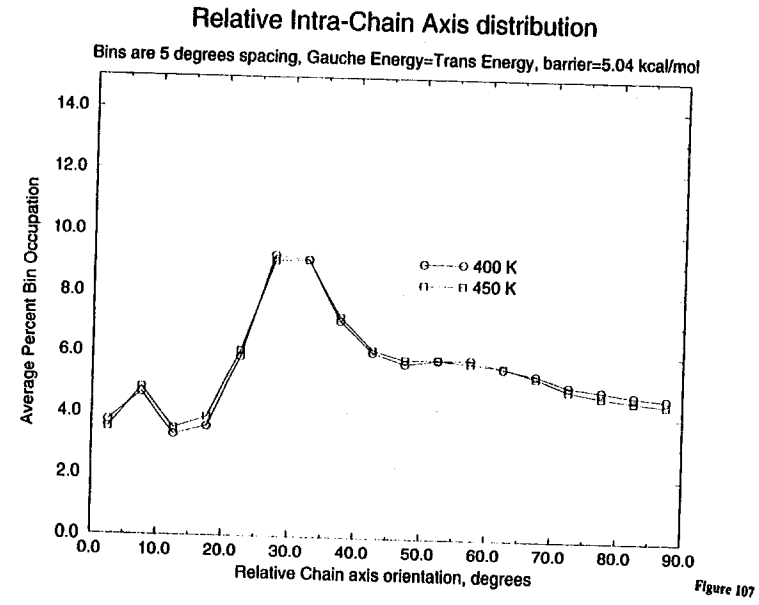

Figure 107

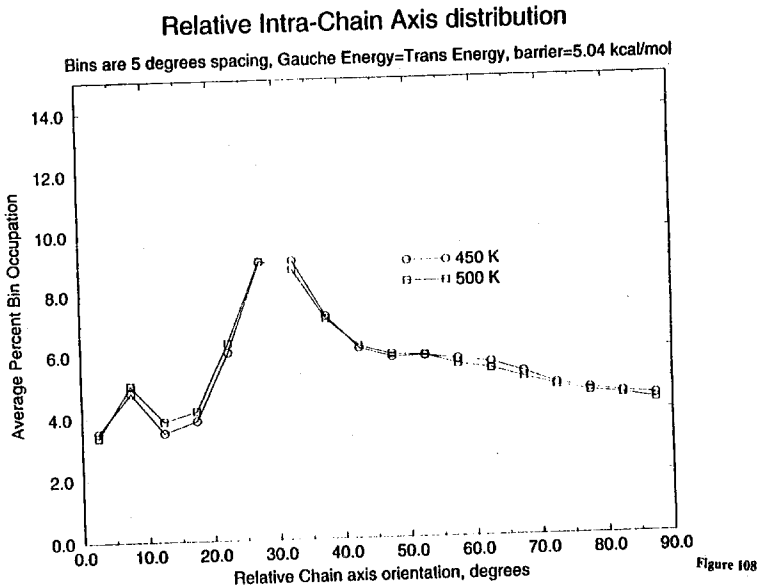

Figure 108

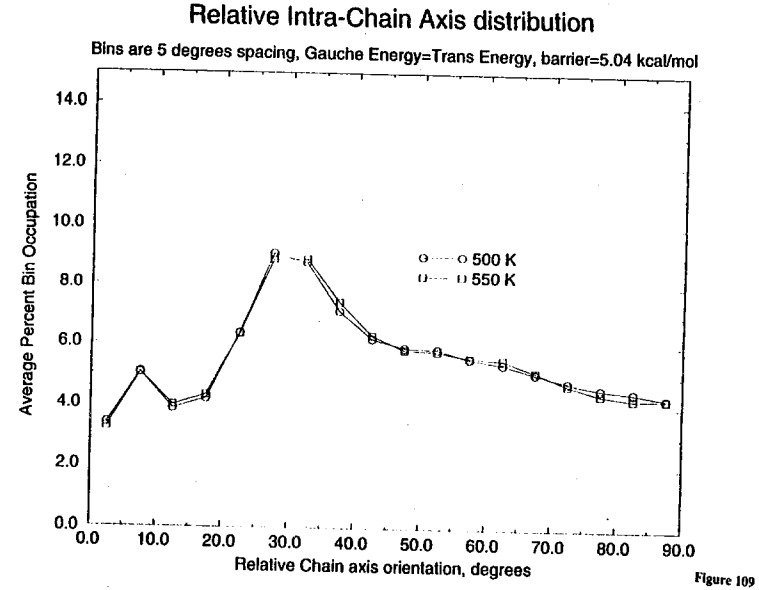

Figure 109

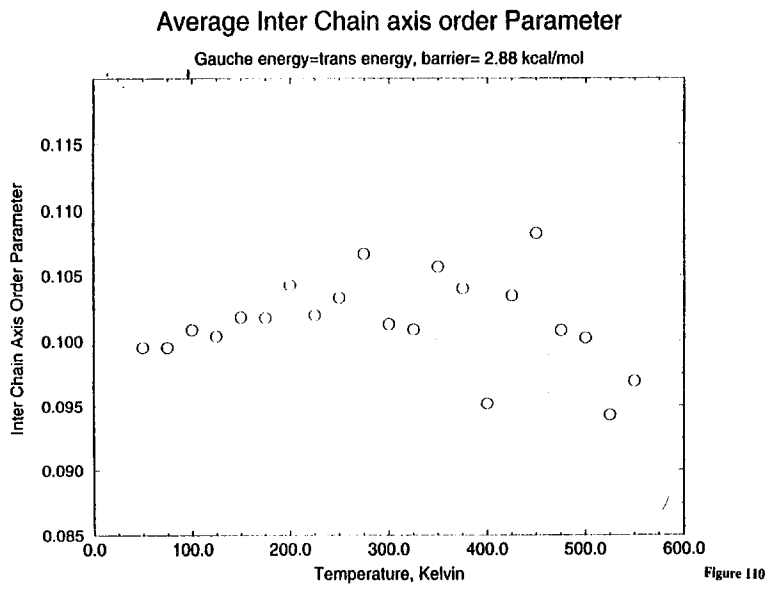

Figure 110

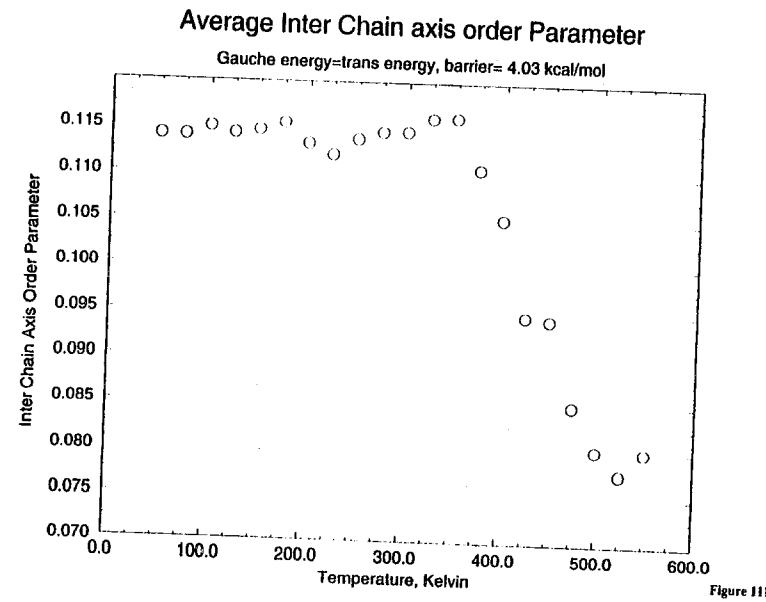

Figure 111

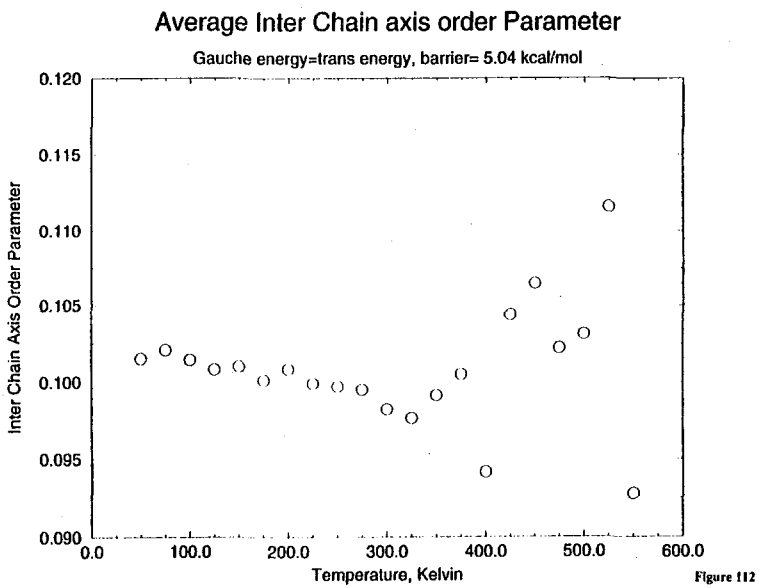

Figure 112

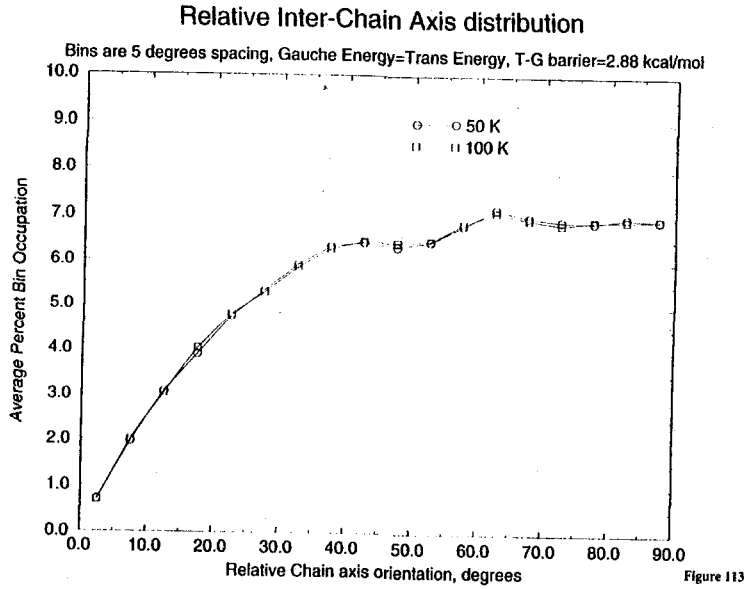

Figure 113

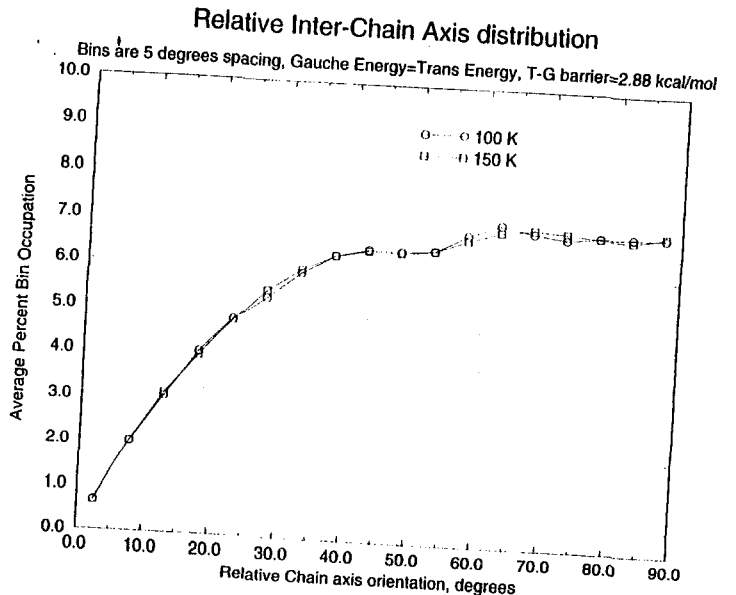

Figure 114

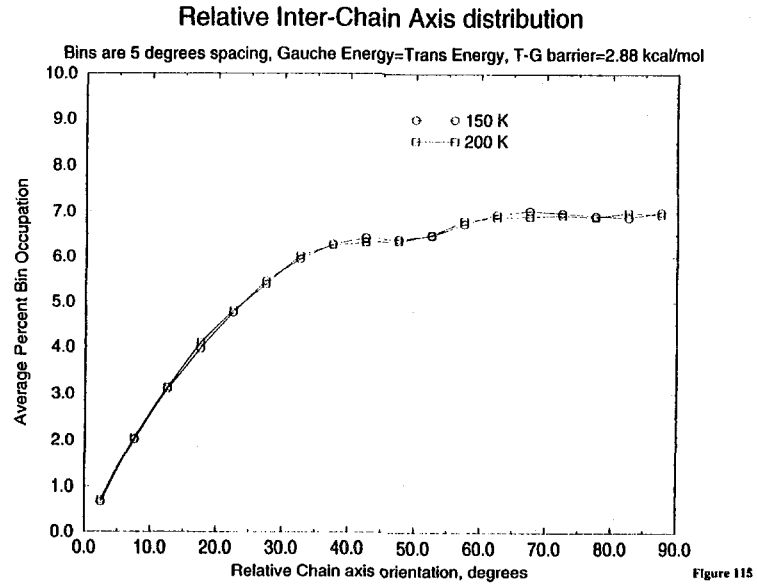

Figure 115

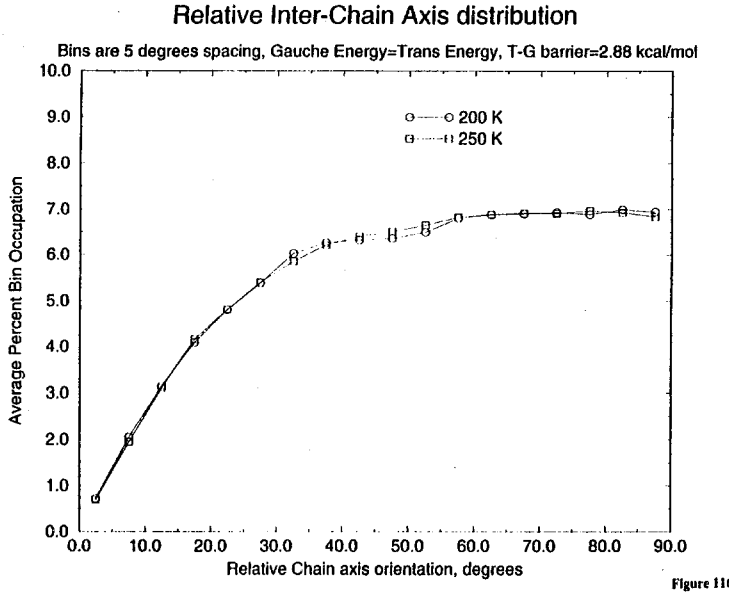

Figure 116

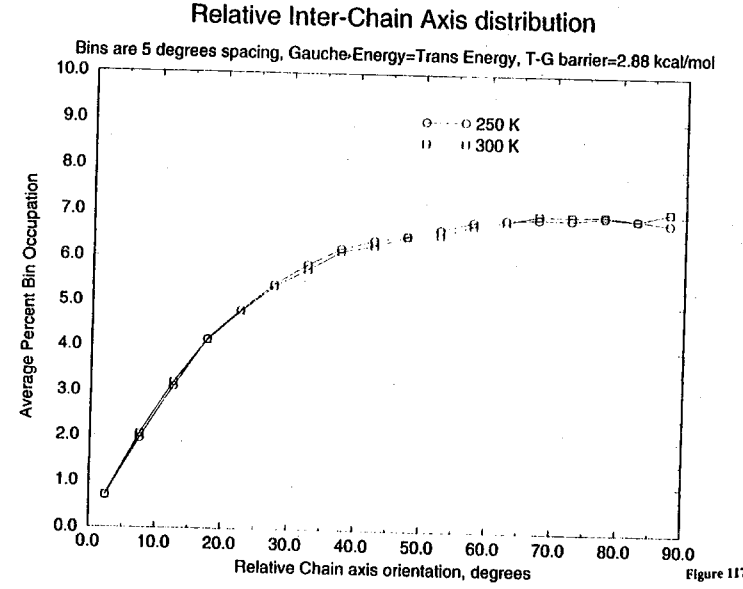

Figure 117

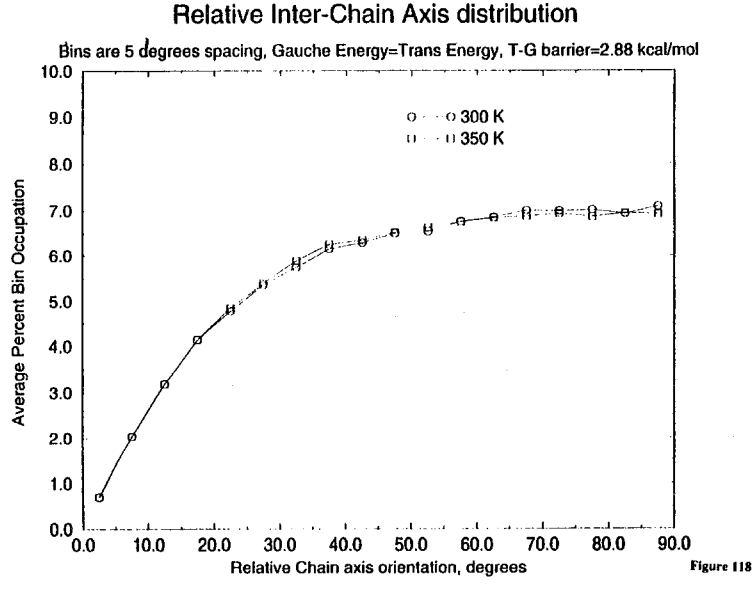

Figure 118

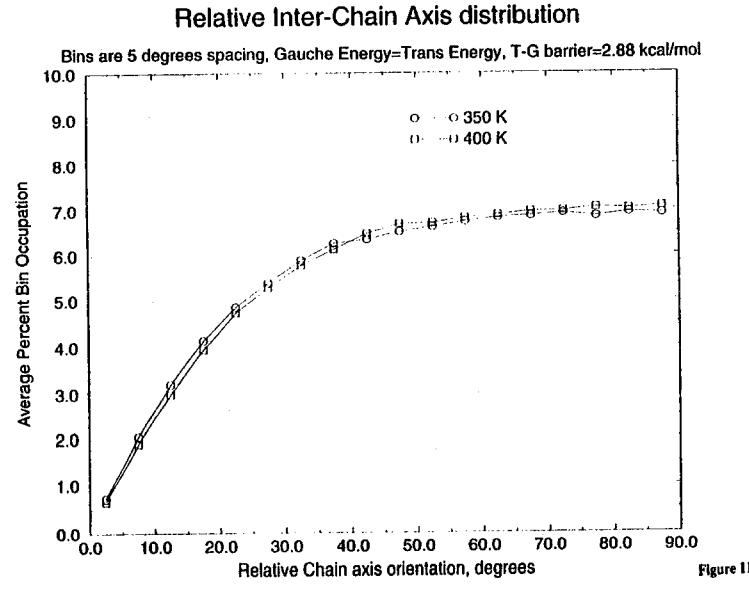

Figure 119

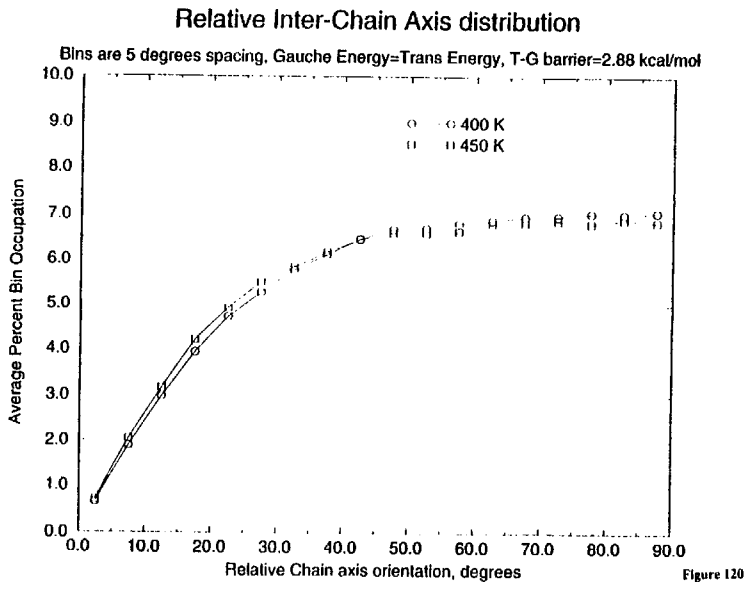

Figure 120

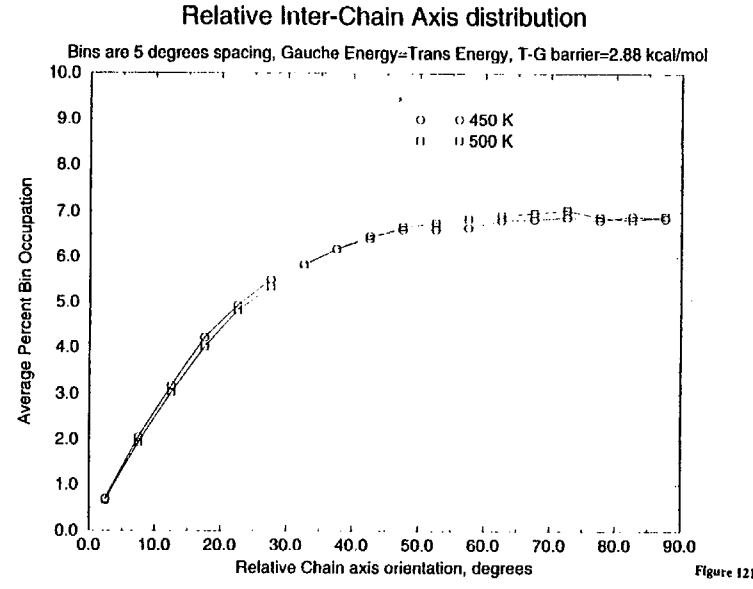

Figure 121

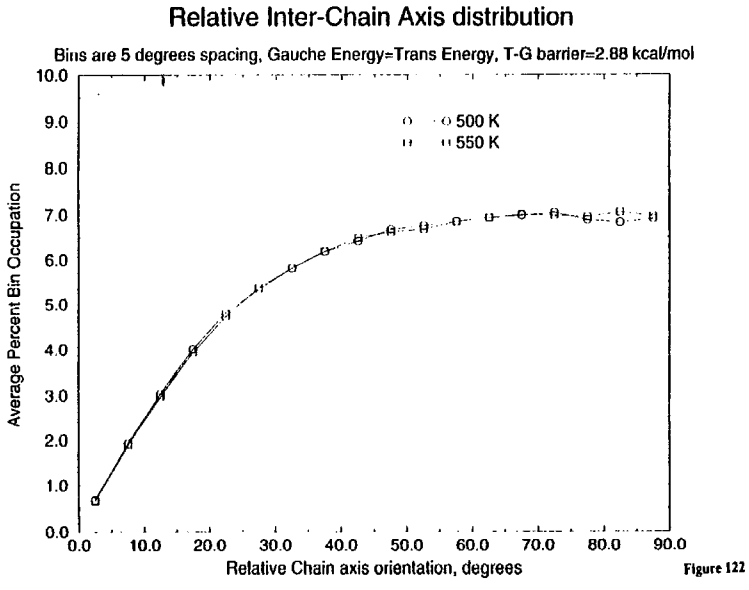

Figure 122

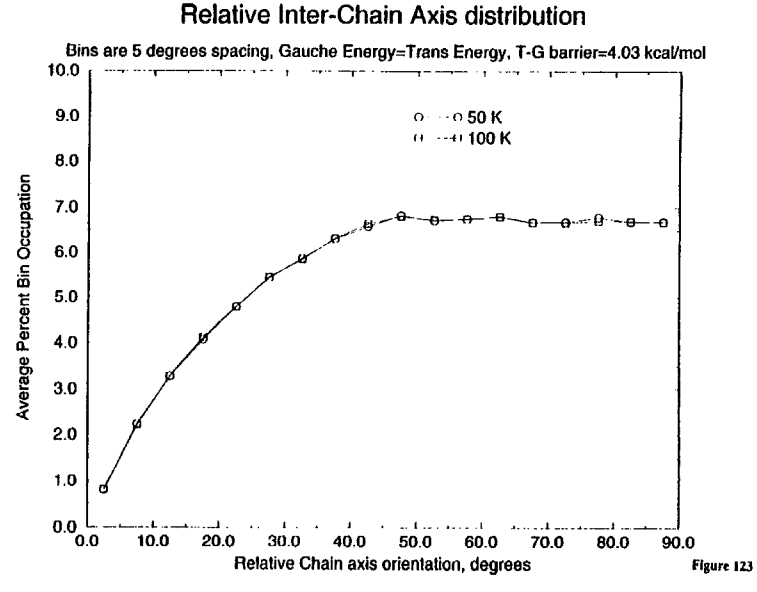

Figure 123

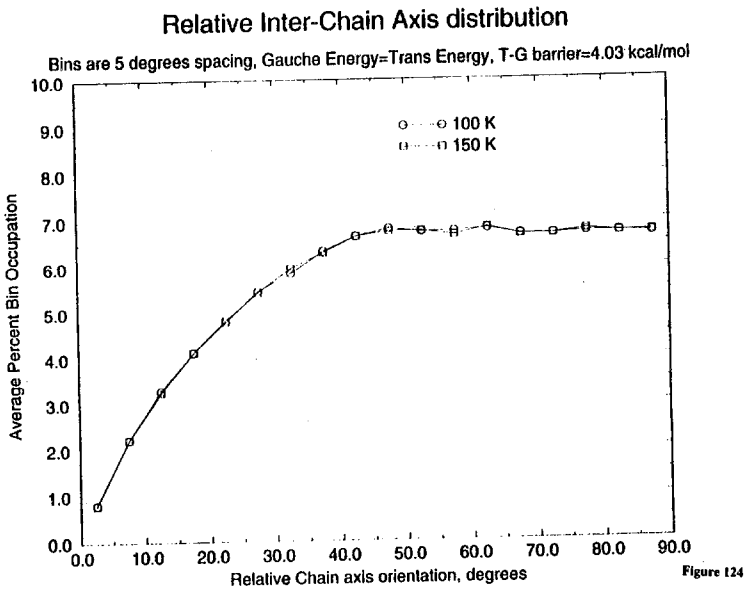

Figure 124

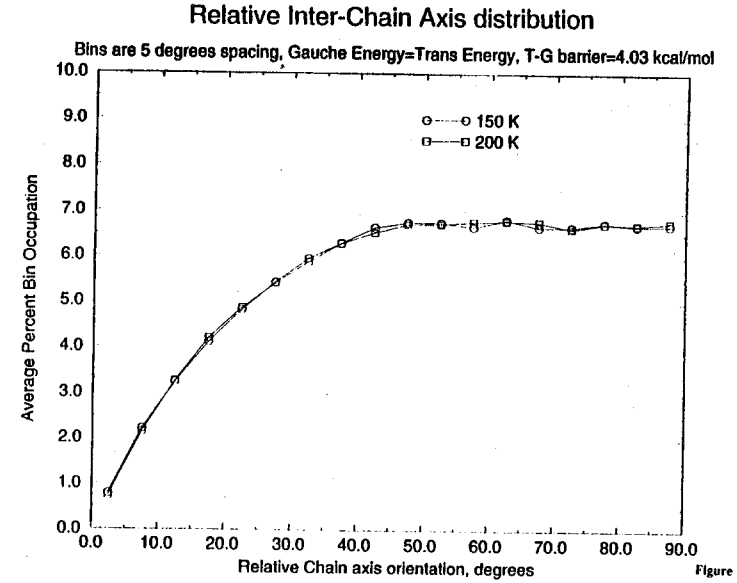

Figure 125

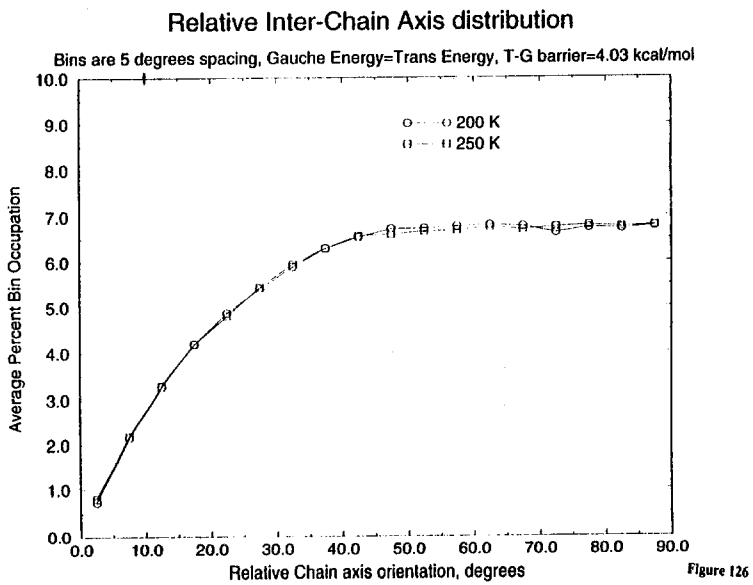

Figure 126

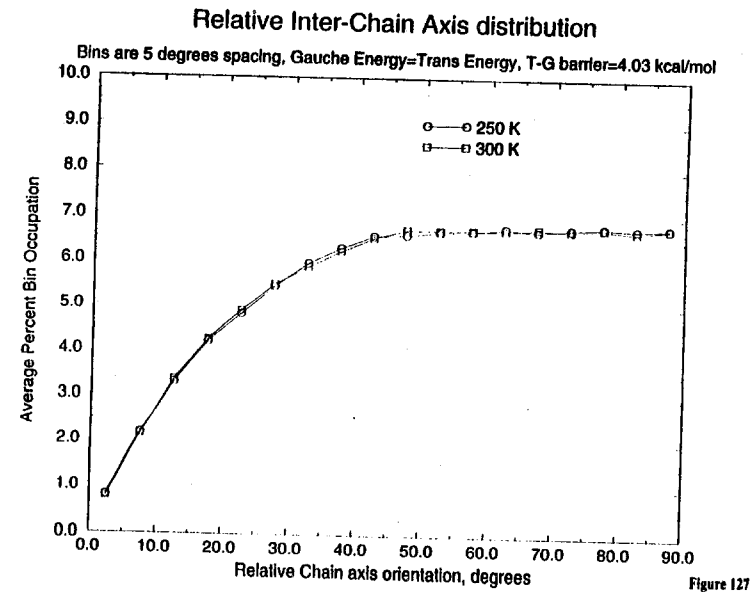

Figure 127

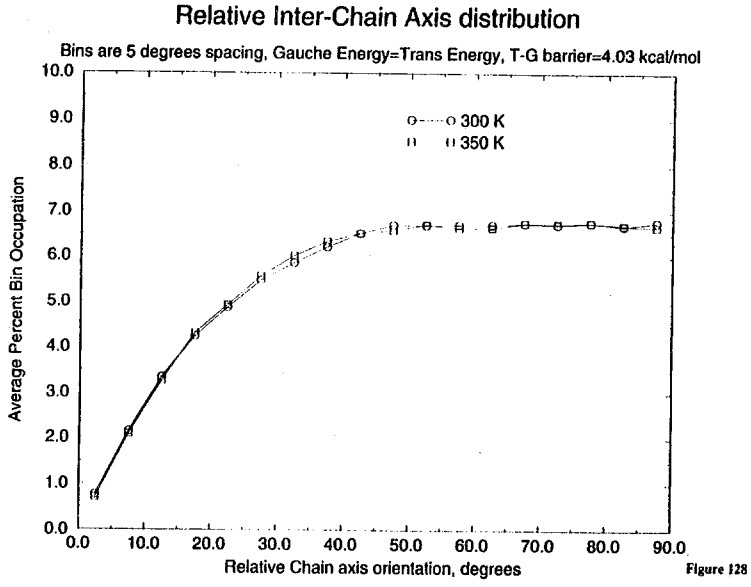

Figure 128

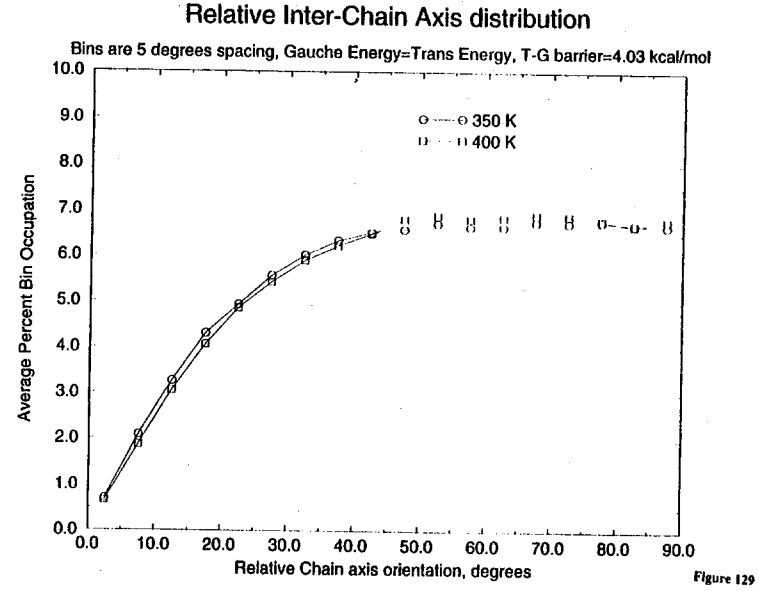

Figure 129

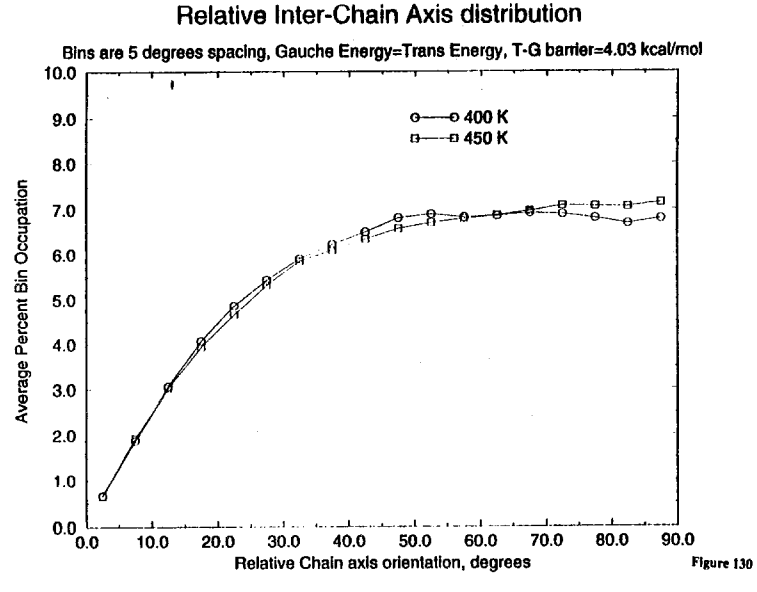

Figure 130

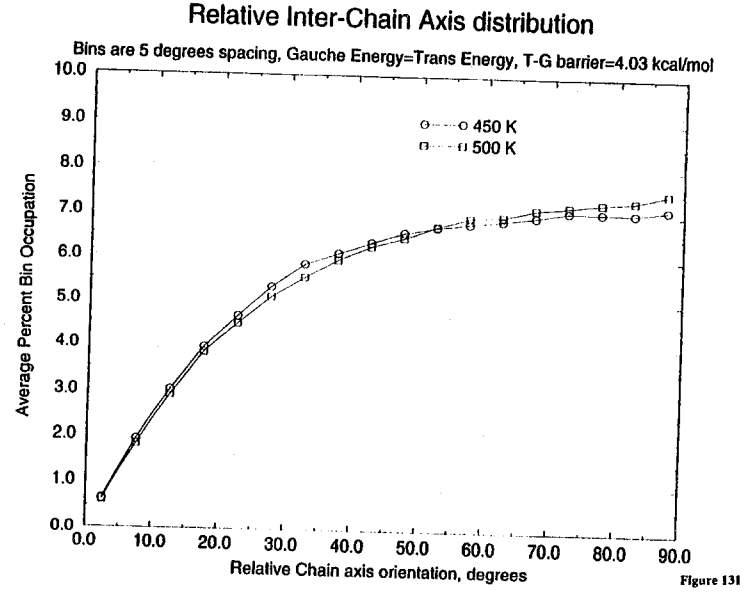

Figure 131

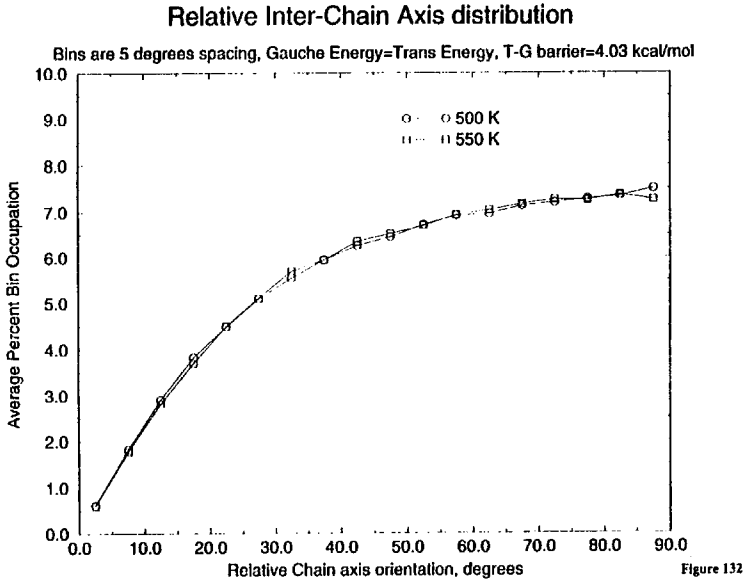

Figure 132

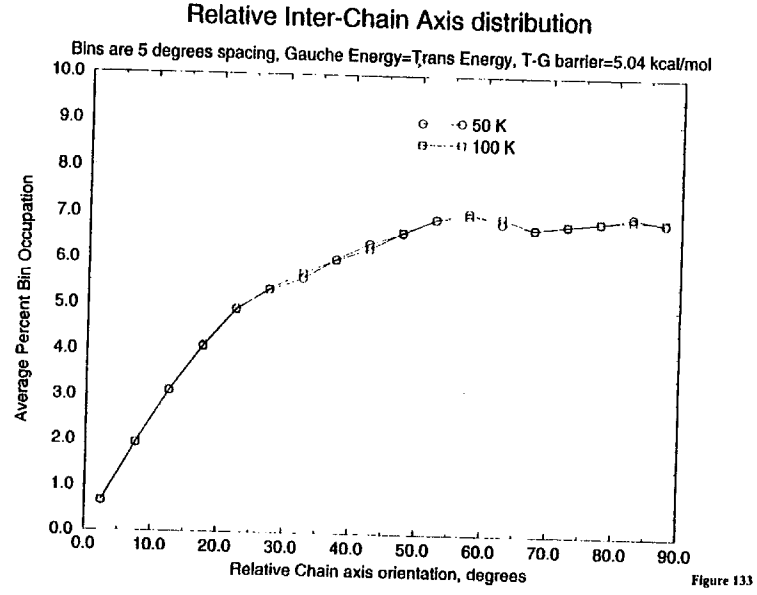

Figure 133

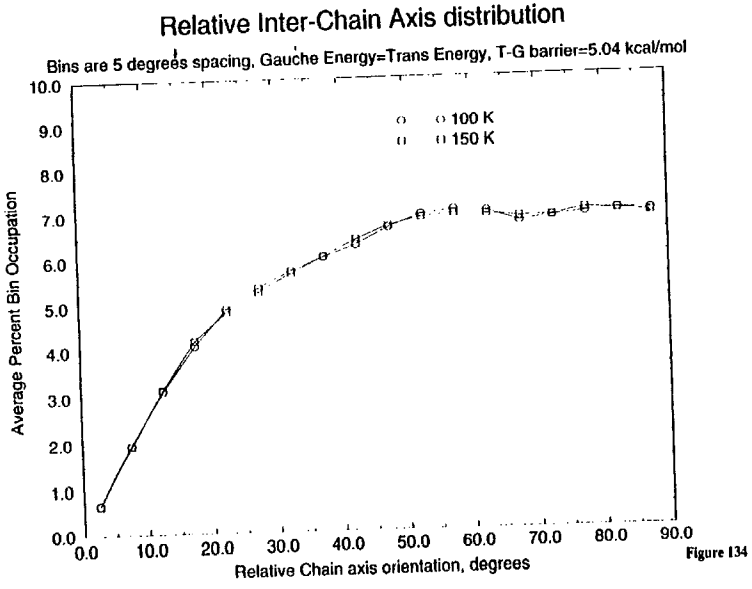

Figure 134

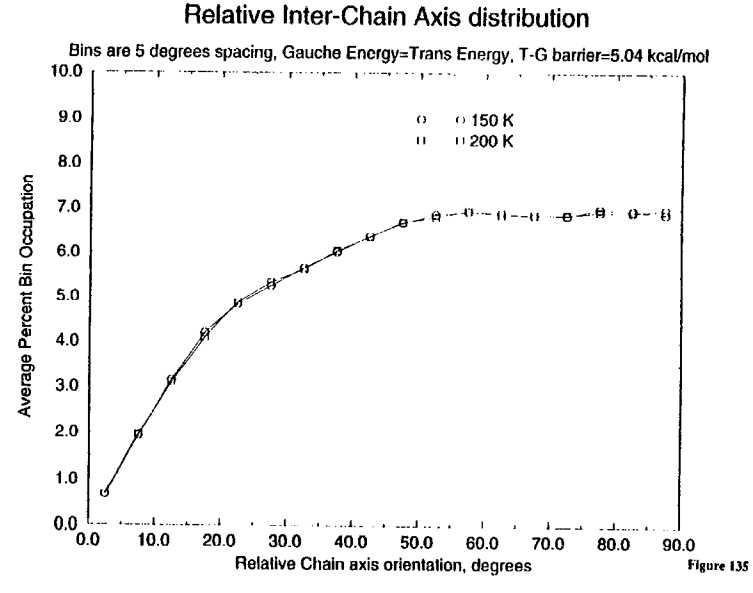

Figure 135

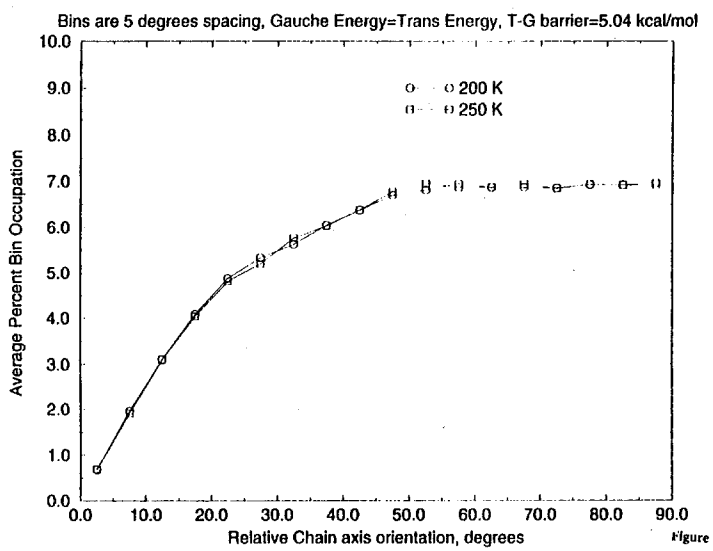

Figure 136

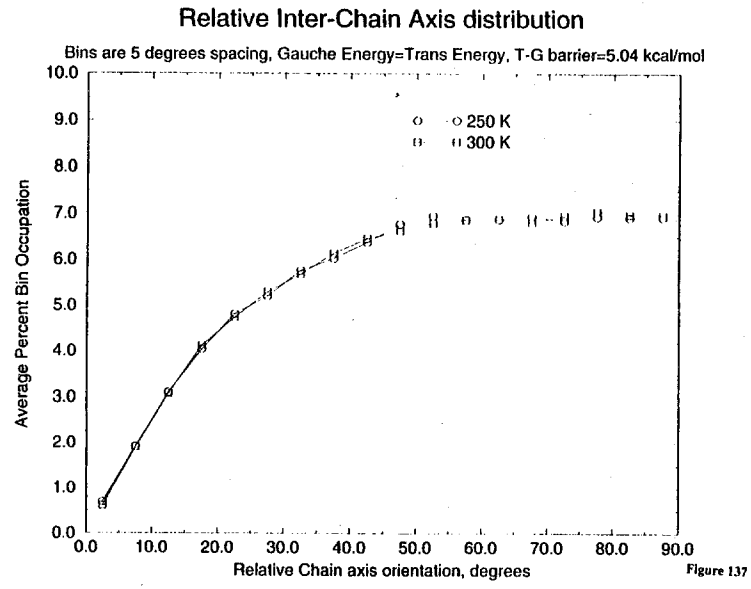

Figure 137

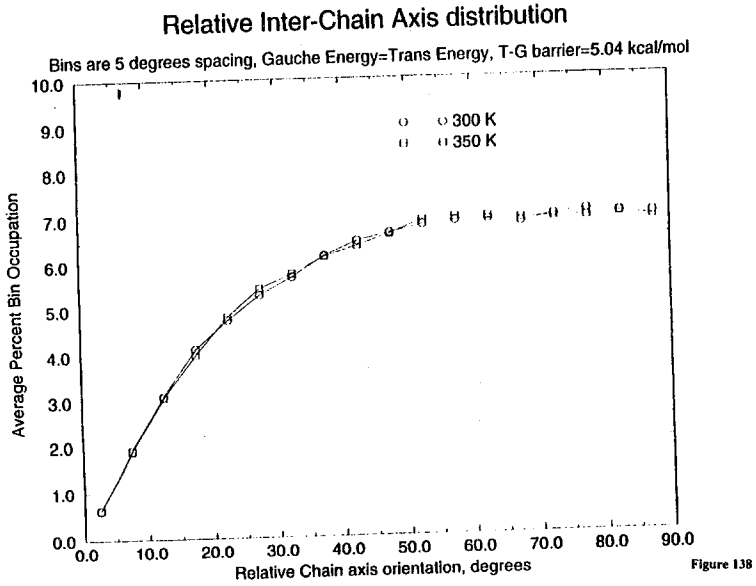

Figure 138

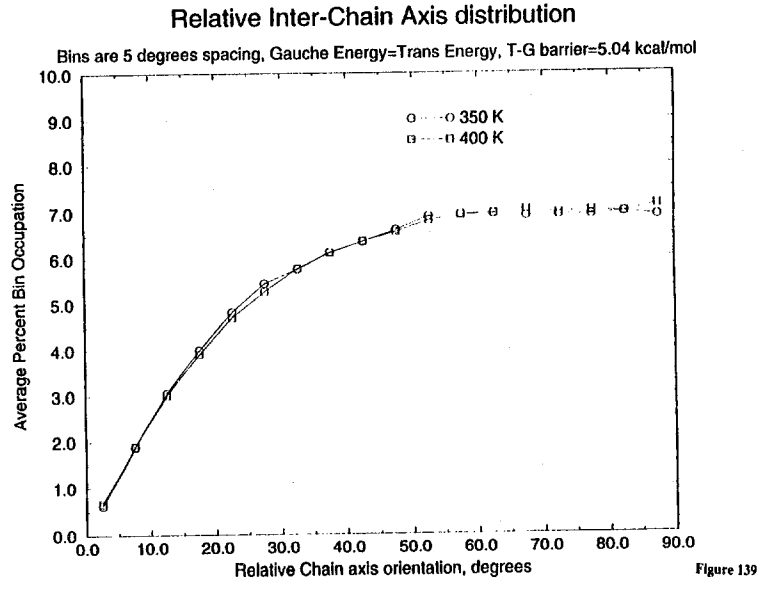

Figure 139

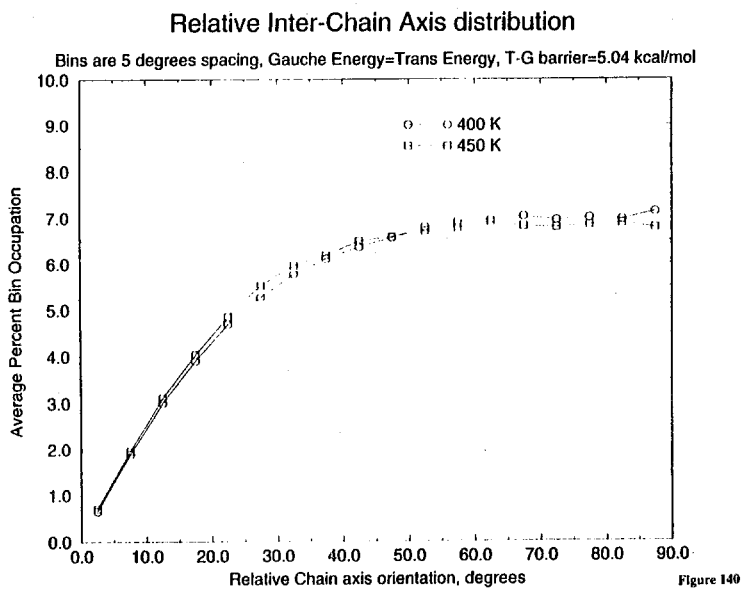

Figure 140

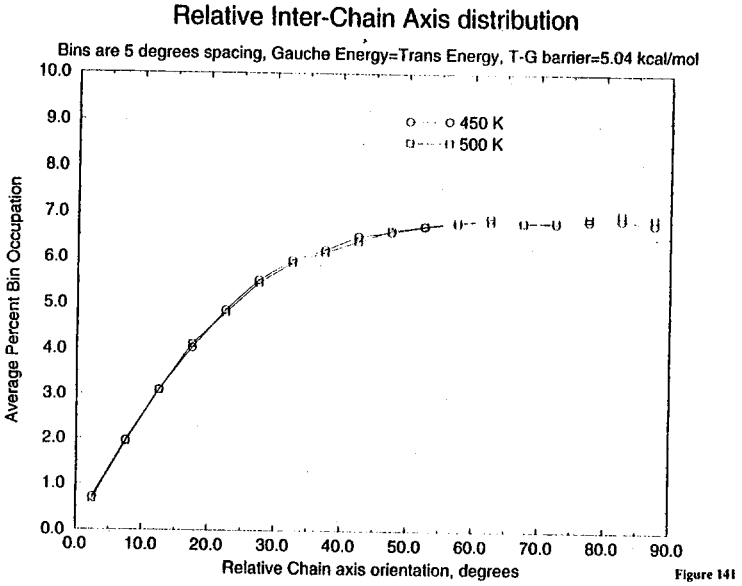

Figure 141

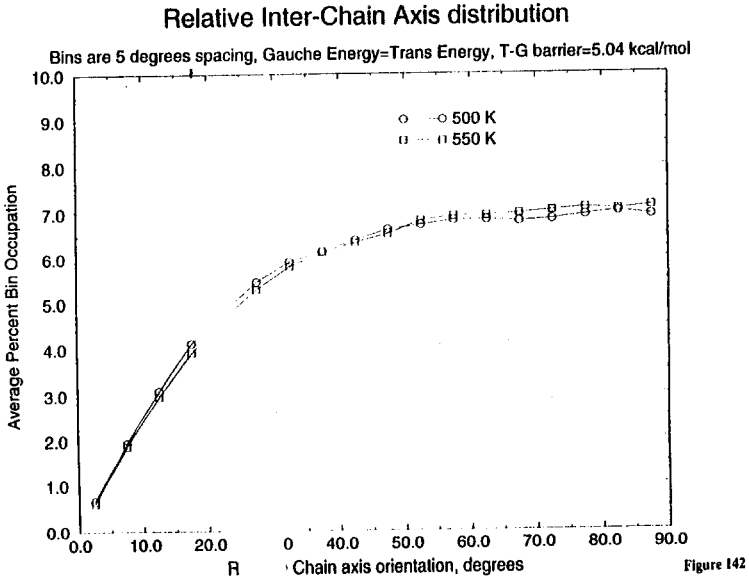

Figure 142

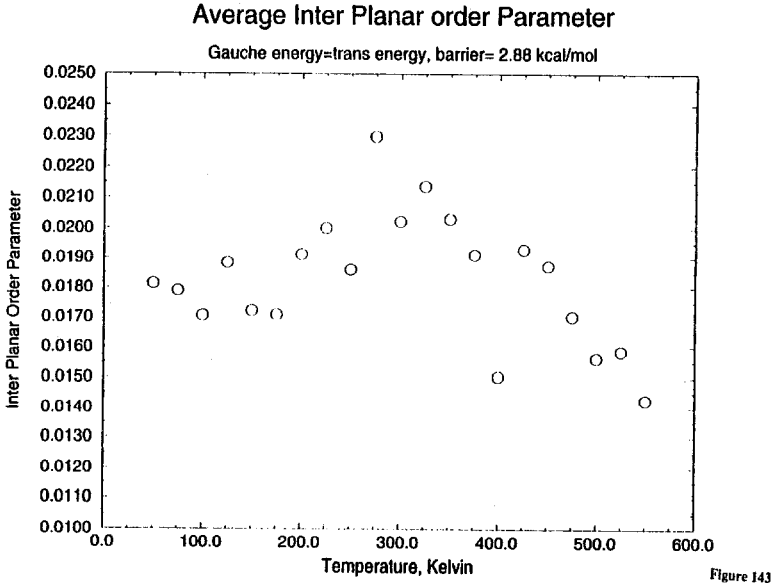

Figure 143

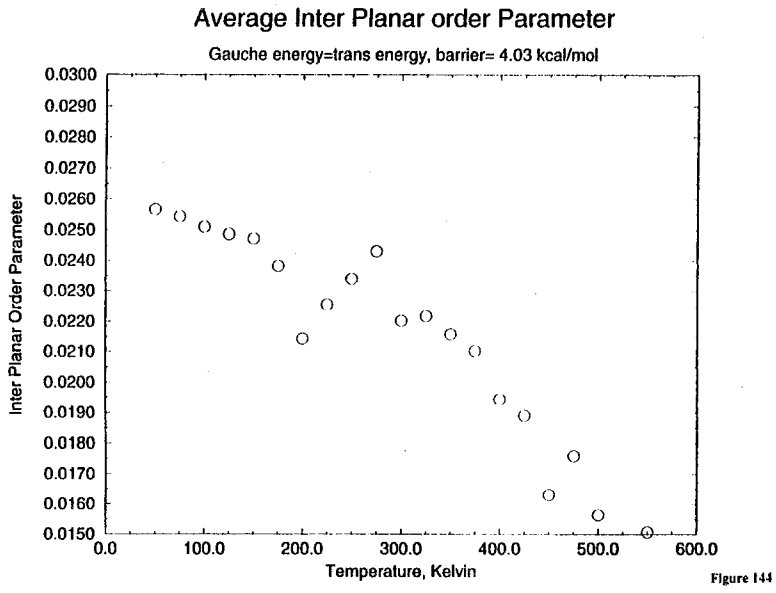

Figure 144

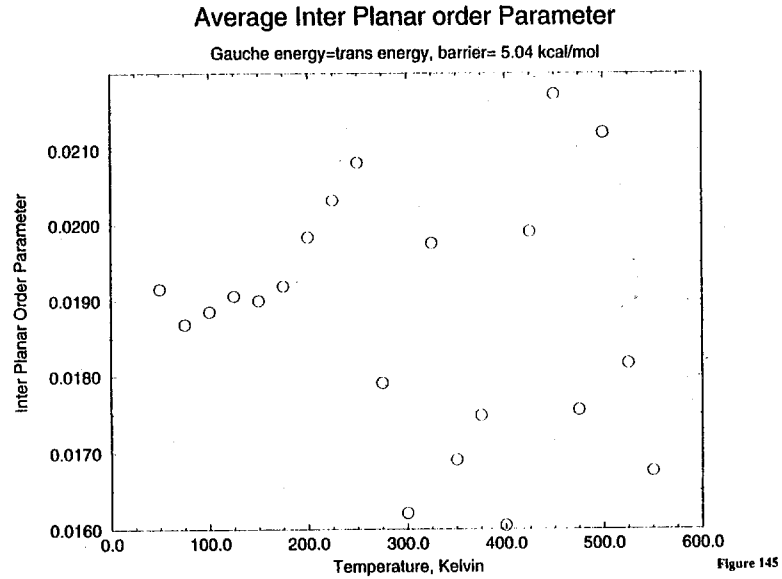

Figure 145

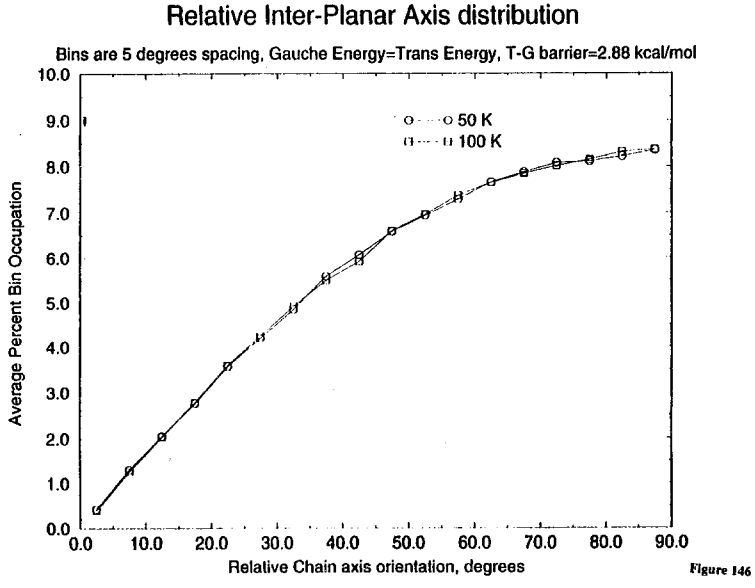

Figure 146

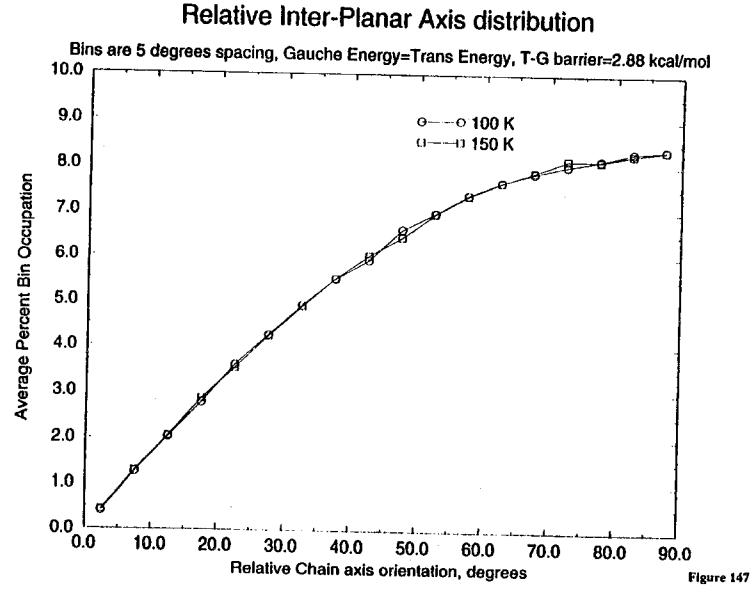

Figure 147

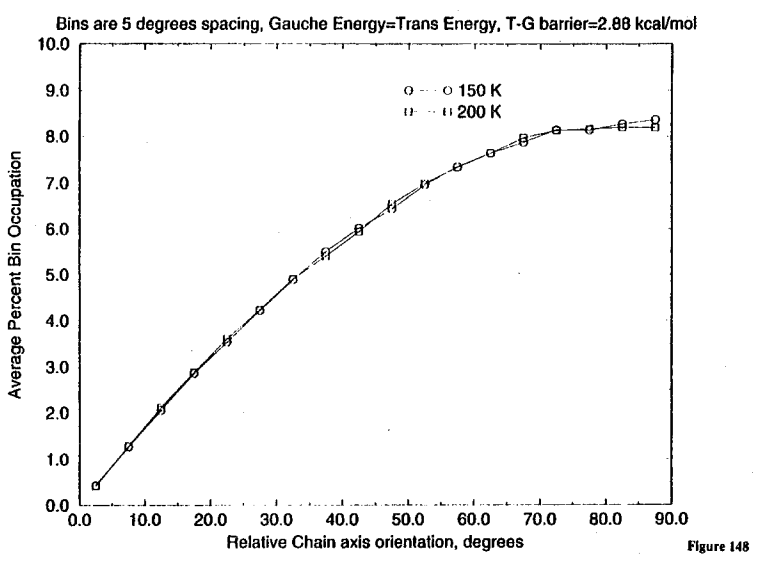

Figure 148

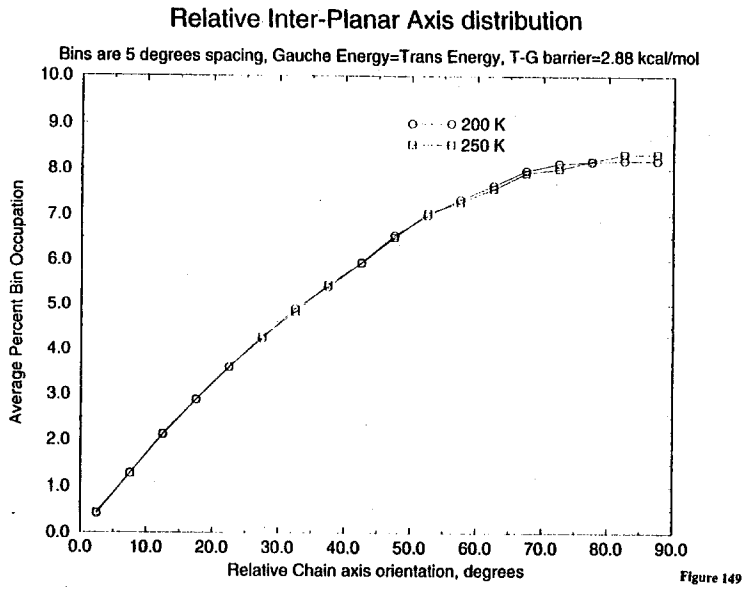

Figure 149

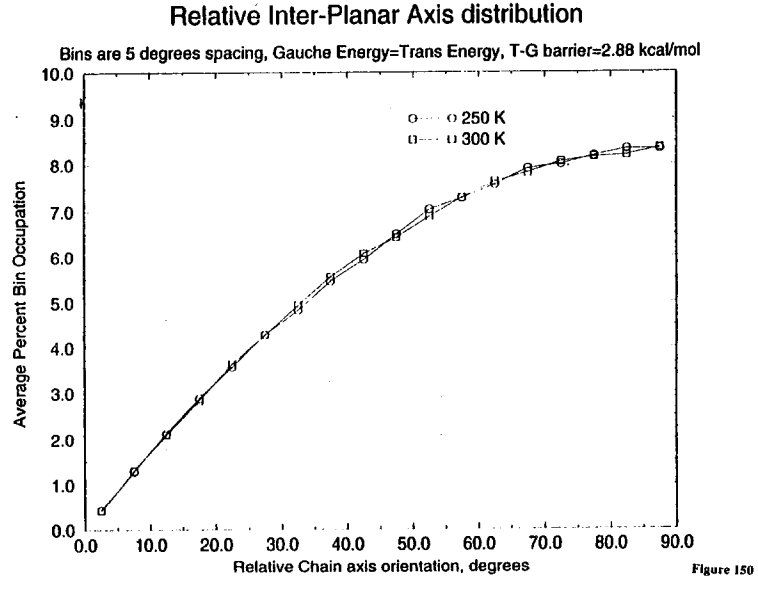

Figure 150

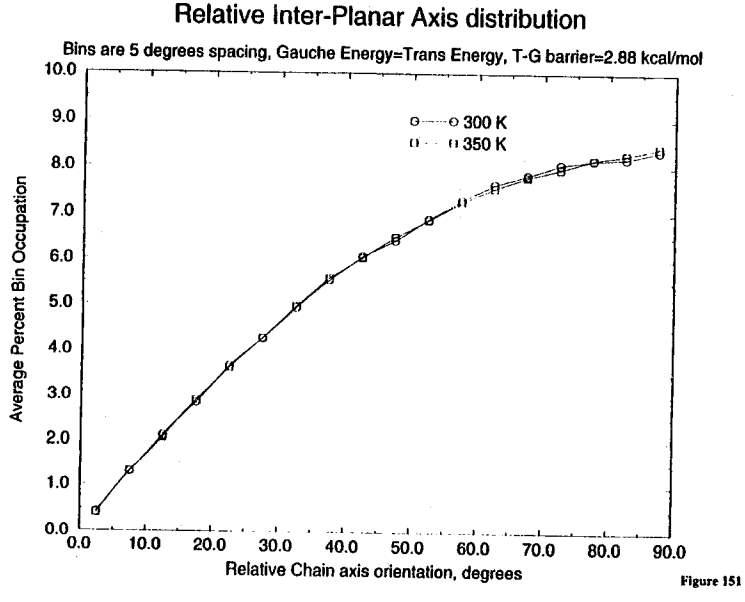

Figure 151

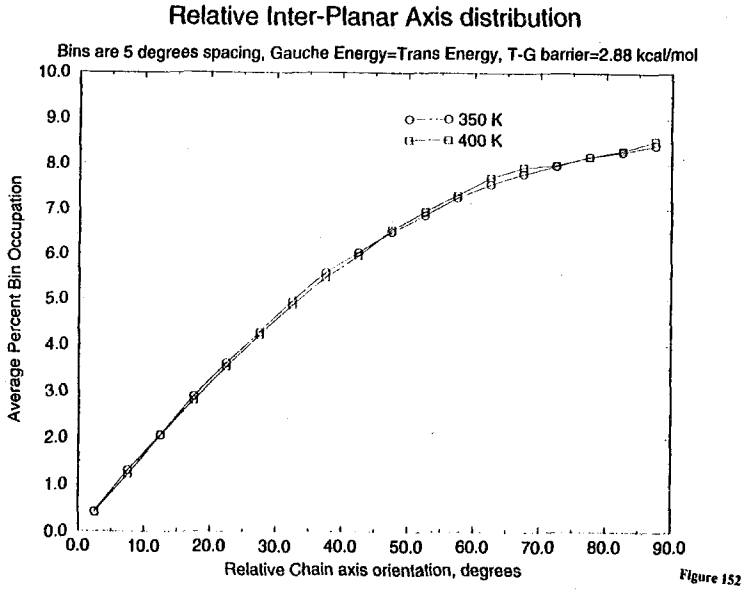

Figure 152

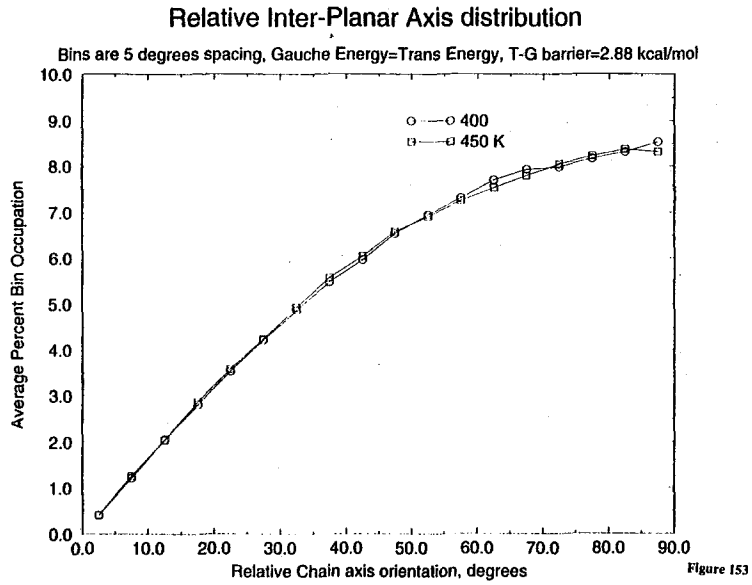

Figure 153

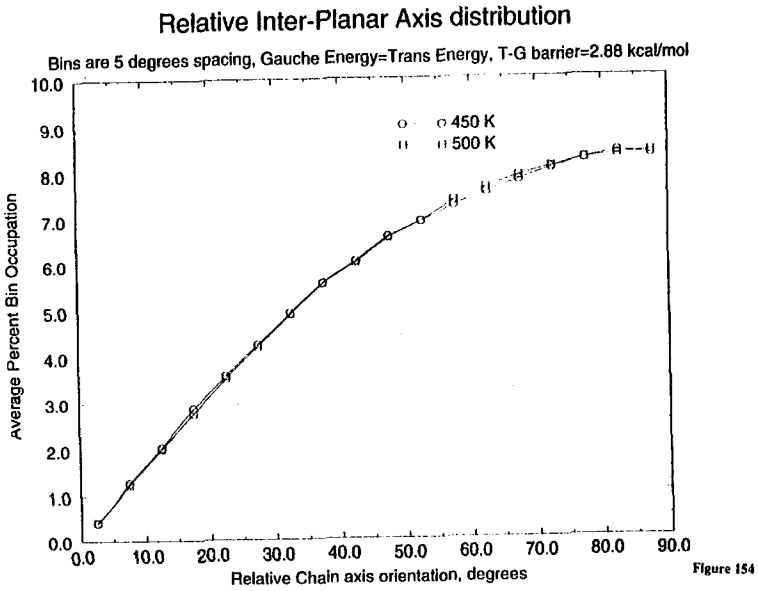

Figure 154

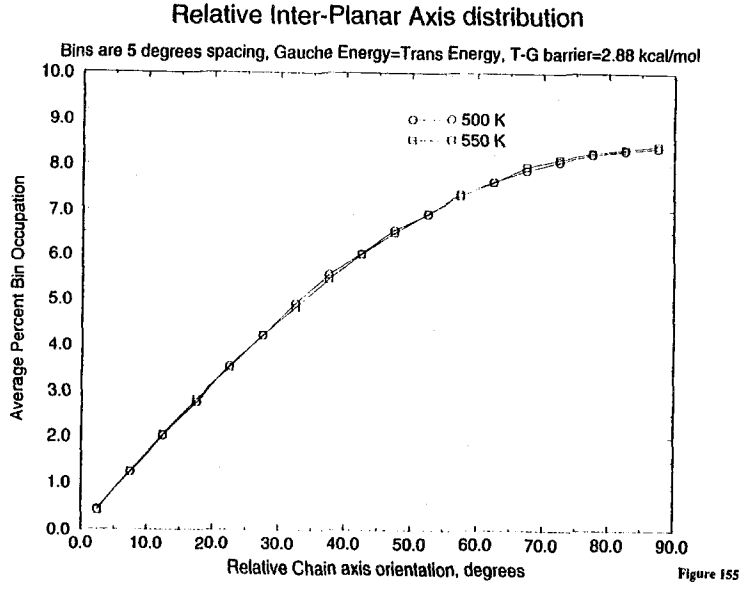

Figure 155

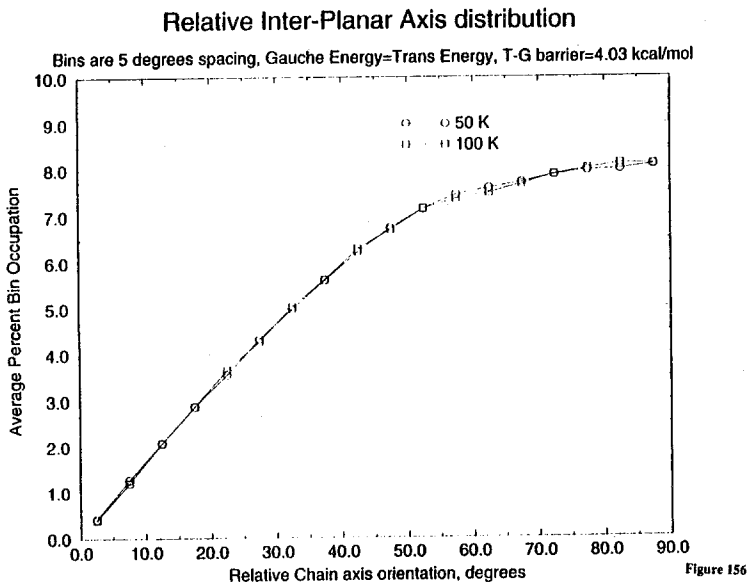

Figure 156

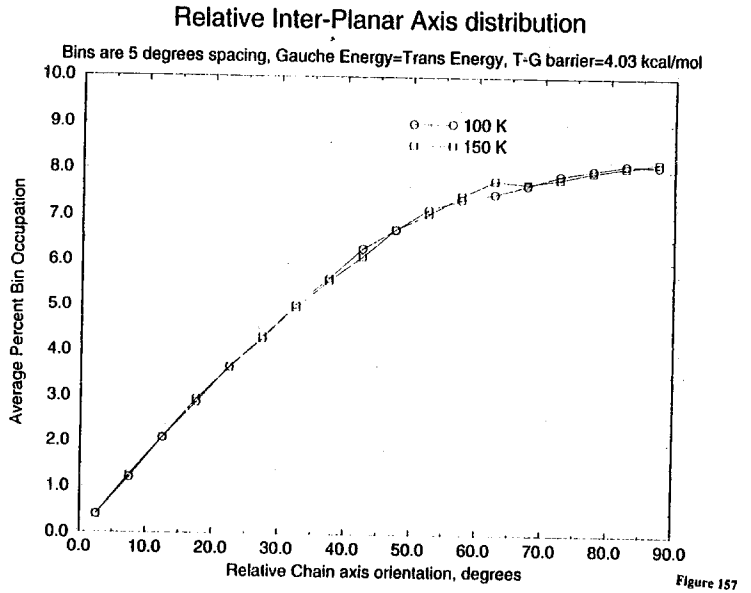

Figure 157

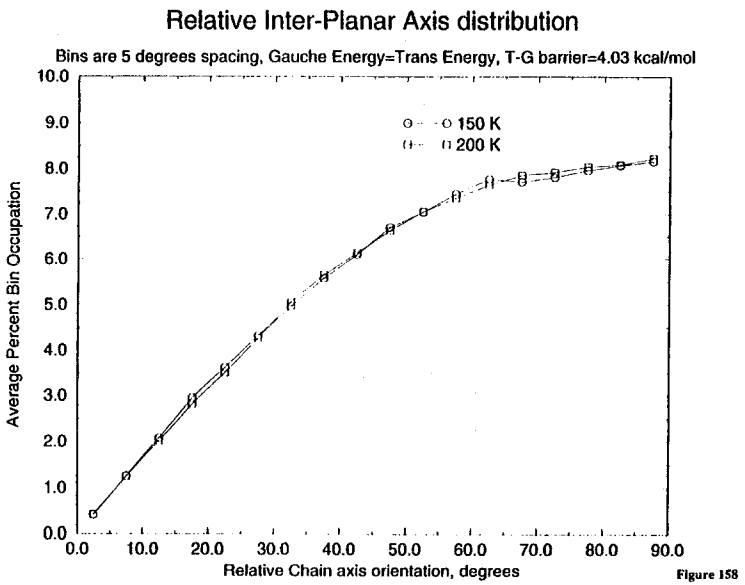

Figure 158

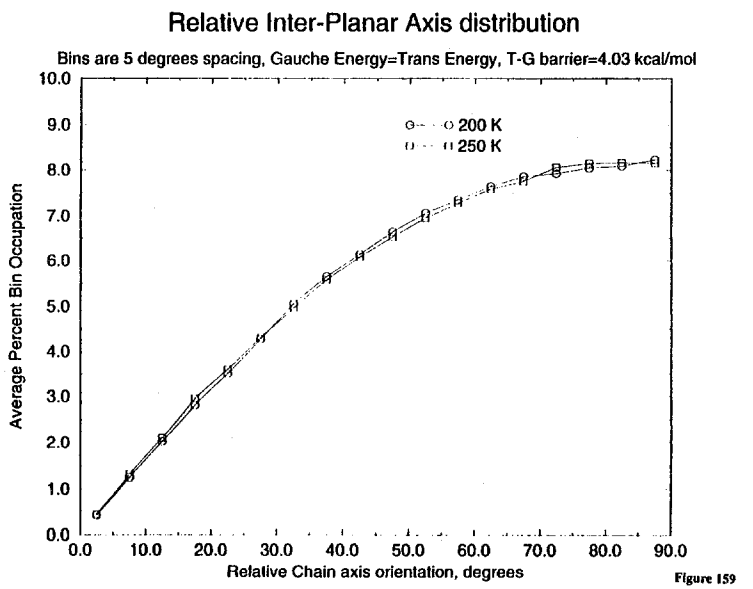

Figure 159

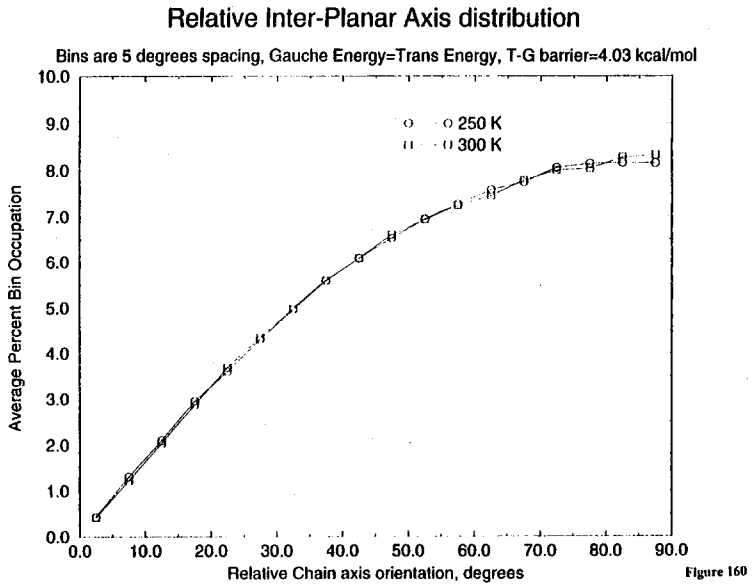

Figure 160

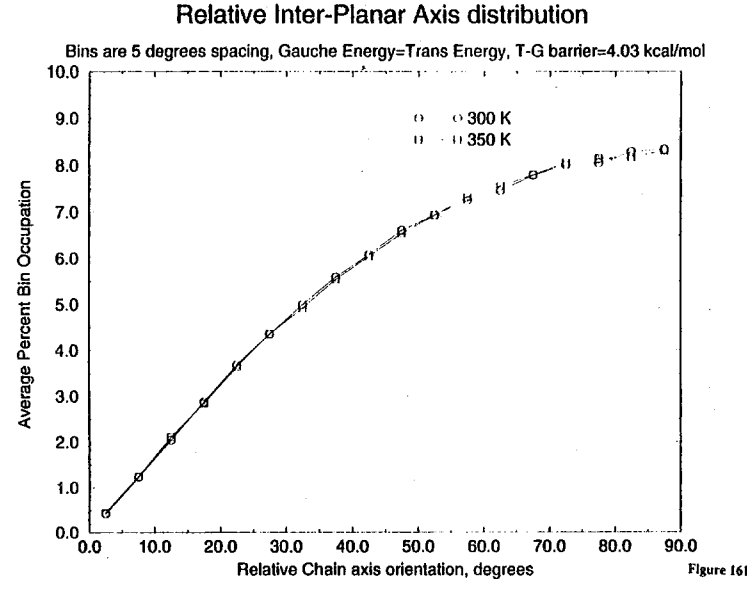

Figure 161

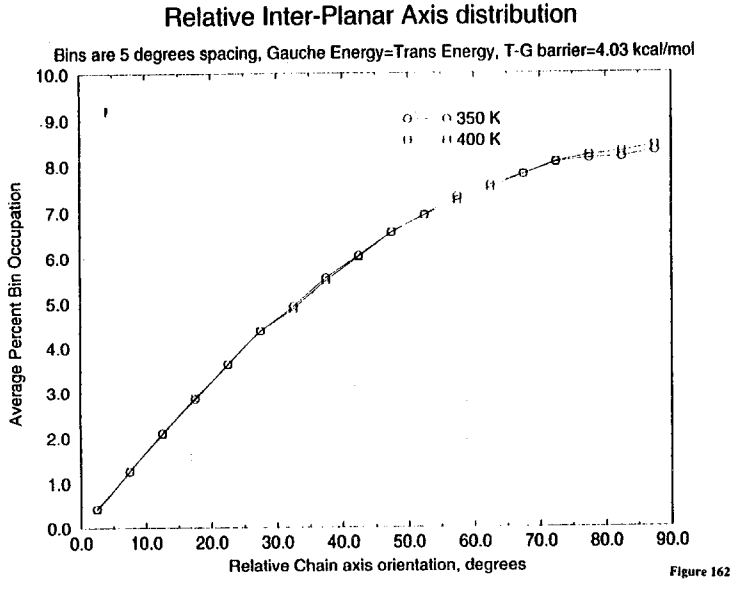

Figure 162

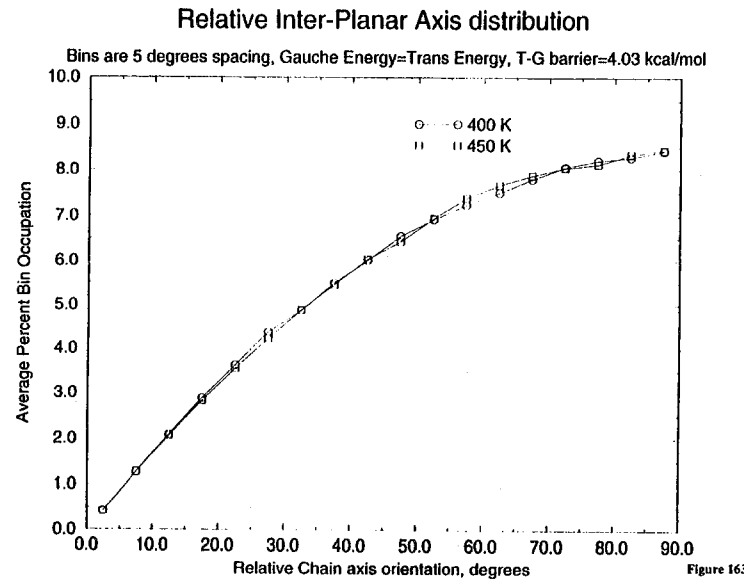

Figure 163

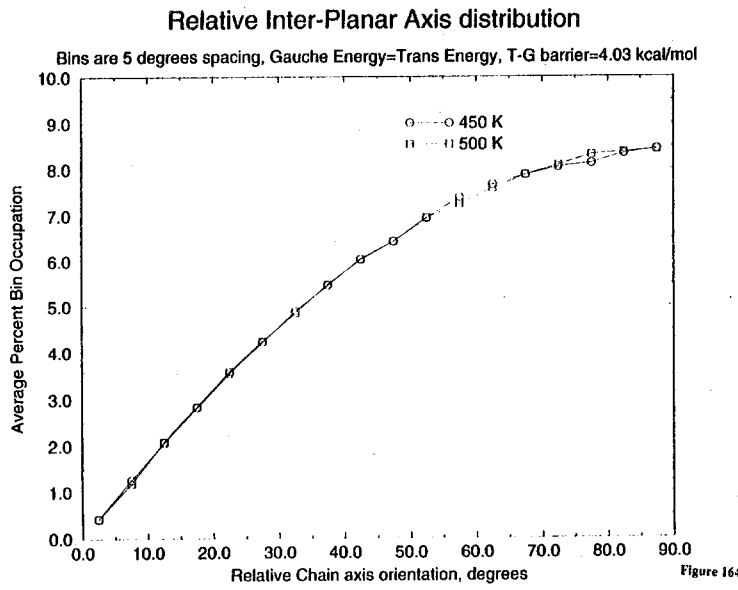

Figure 164

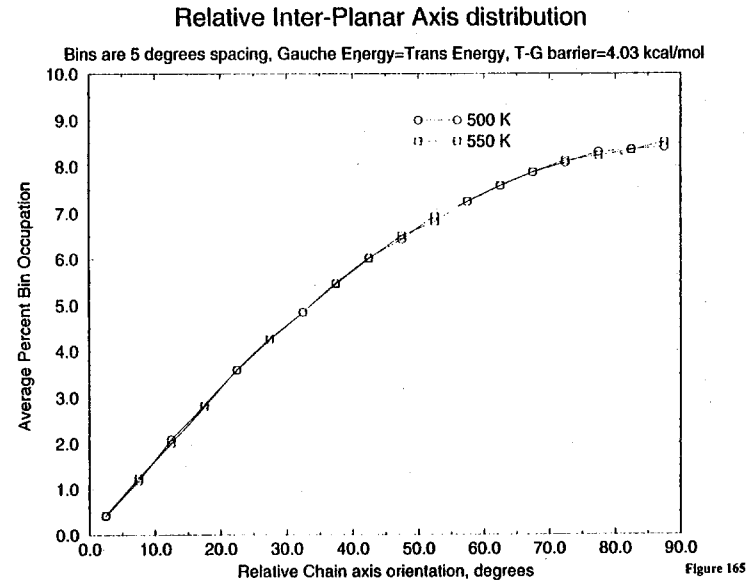

Figure 165

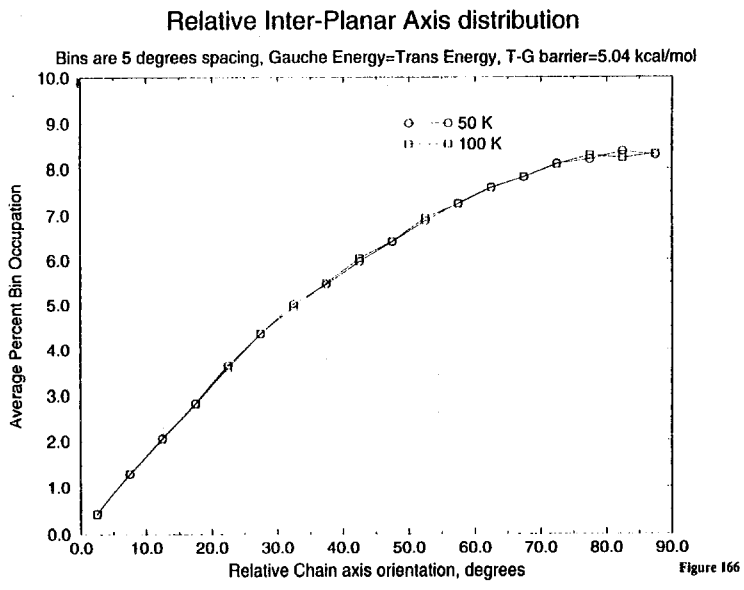

Figure 166

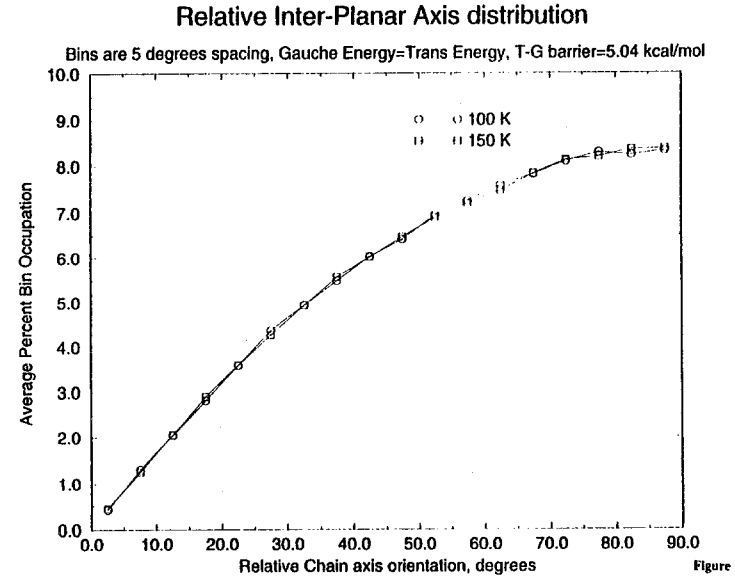

Figure 167

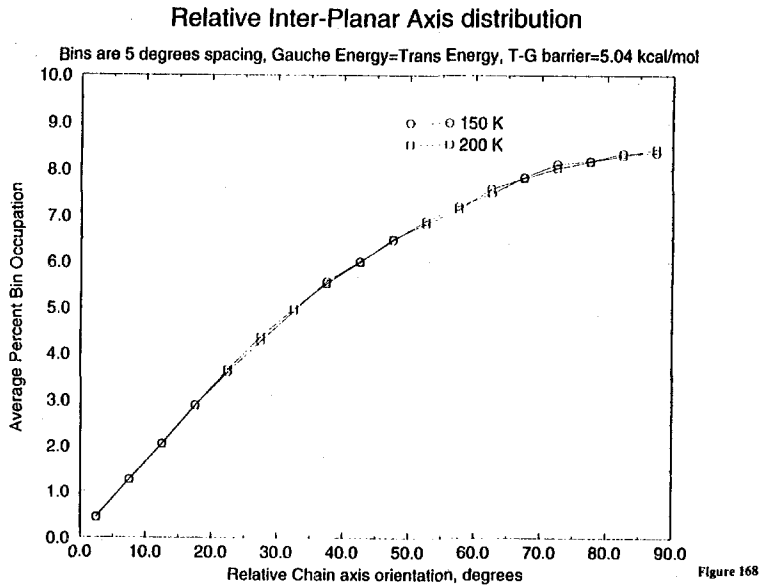

Figure 168

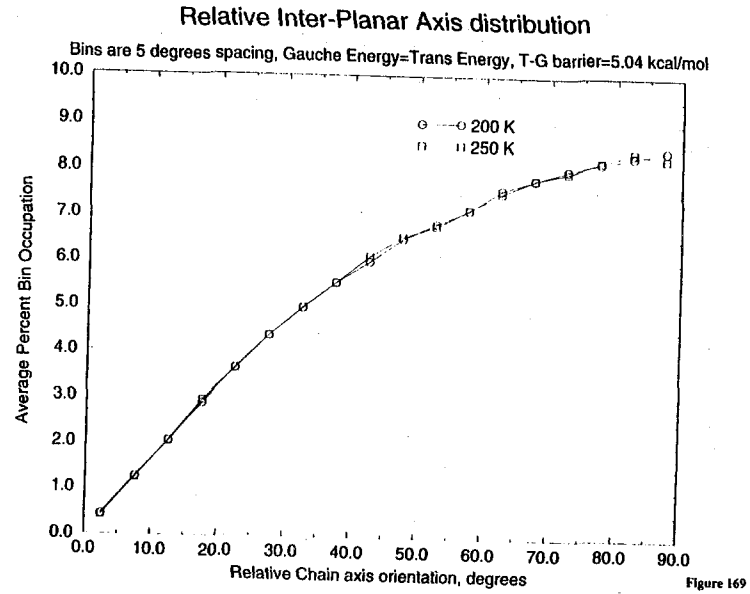

Figure 169

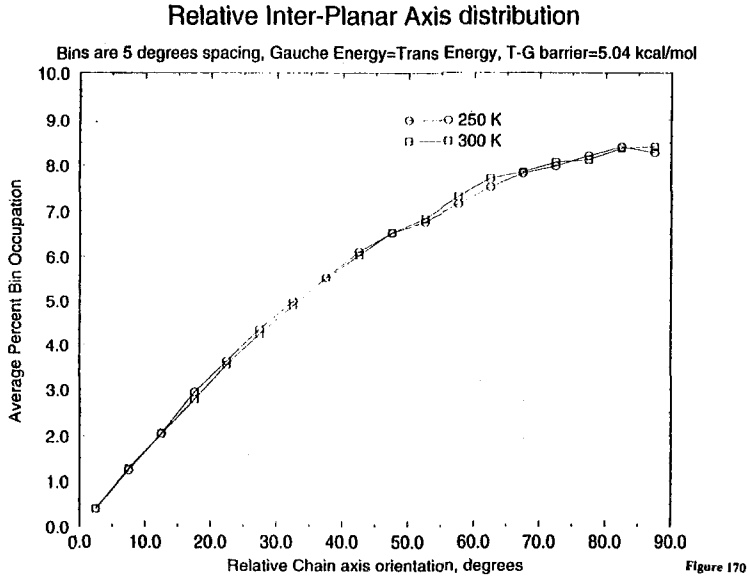

Figure 170

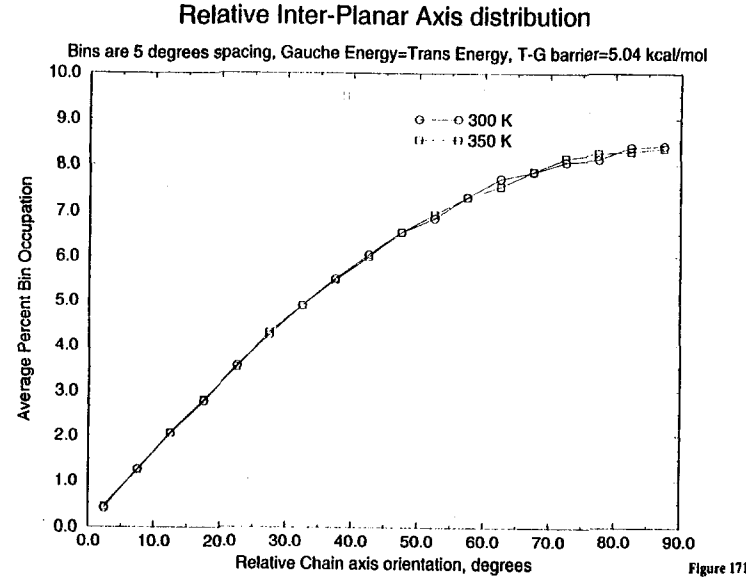

Figure 171

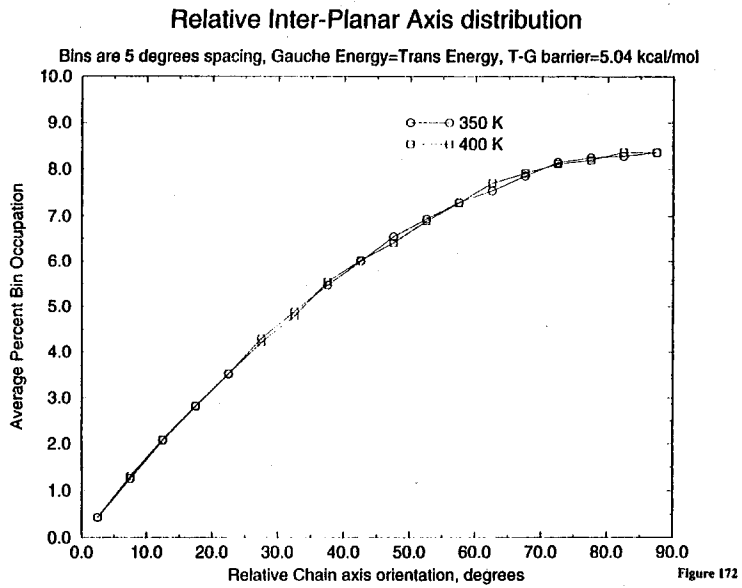

Figure 172

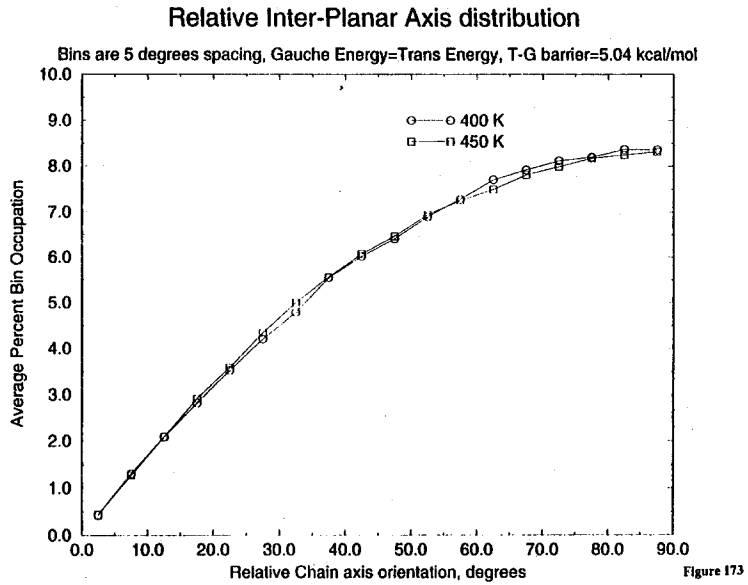

Figure 173

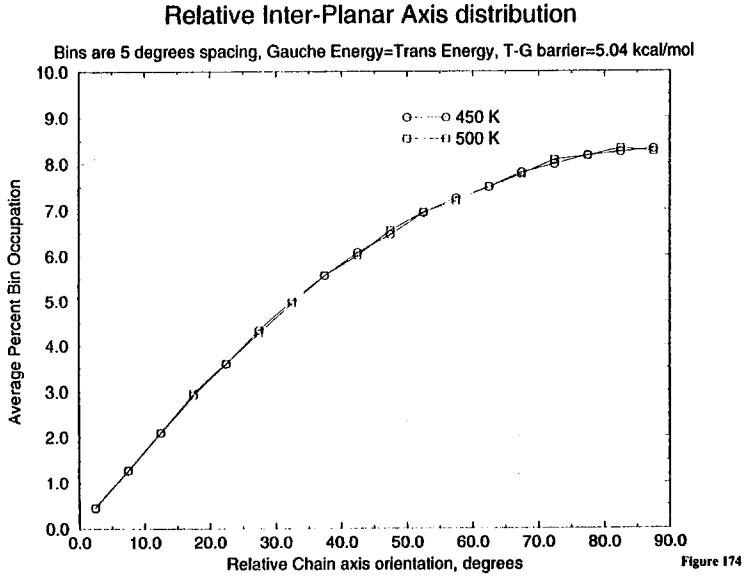

Figure 174

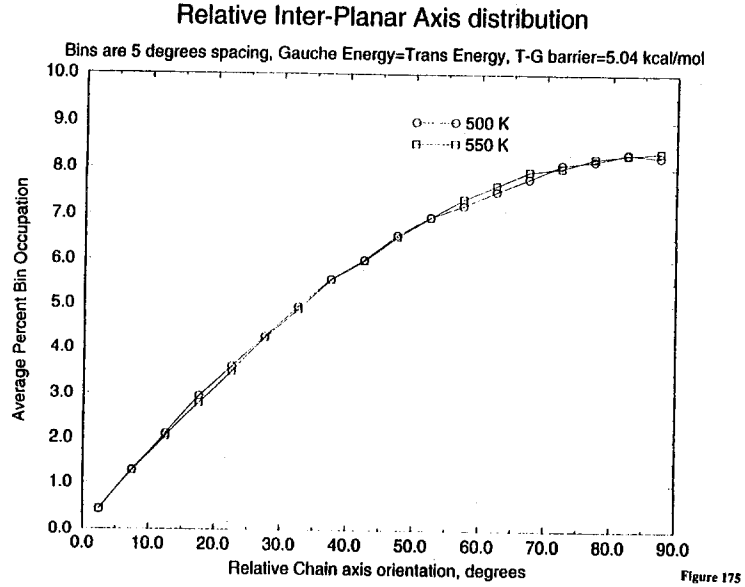

Figure 175

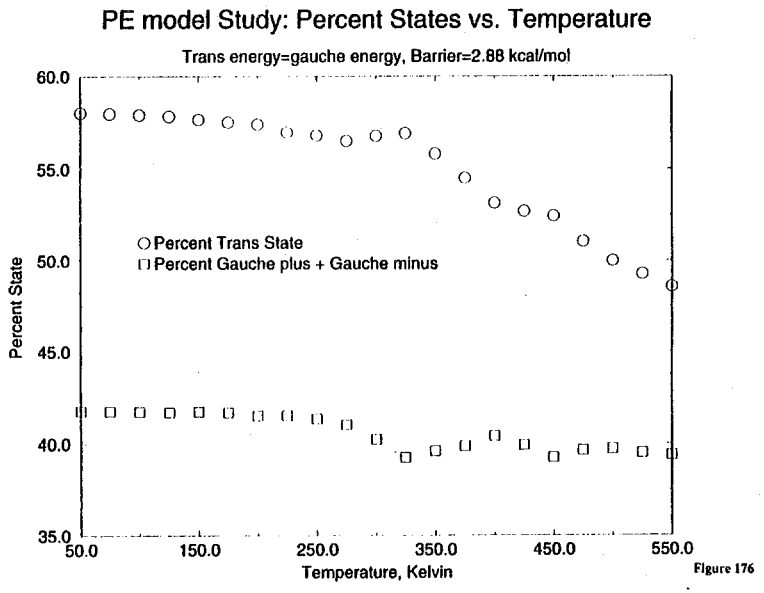

Figure 176

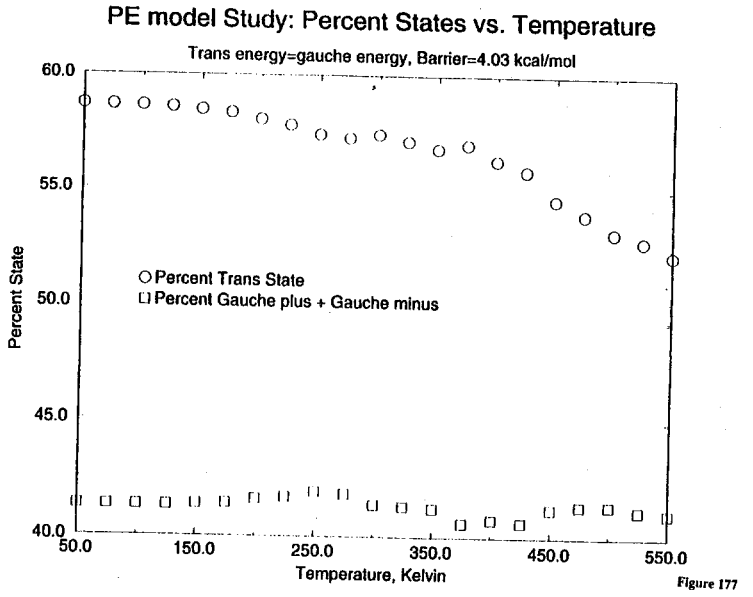

Figure 177

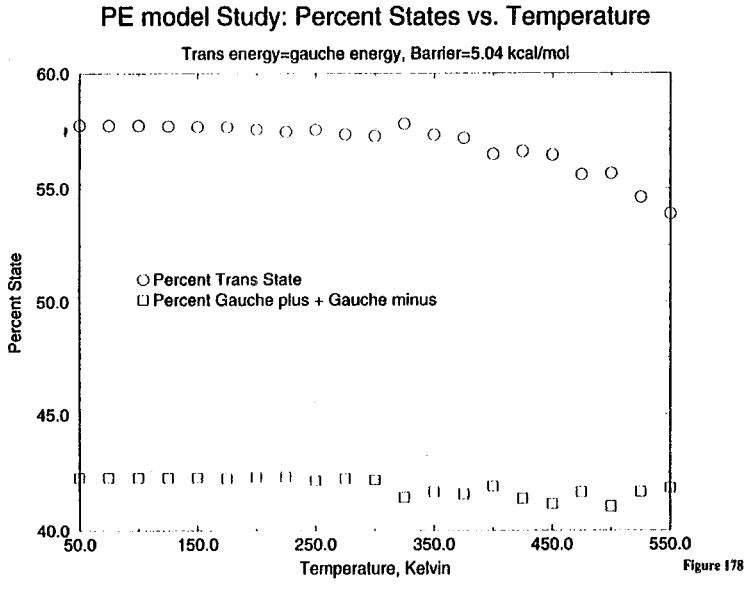

Figure 178

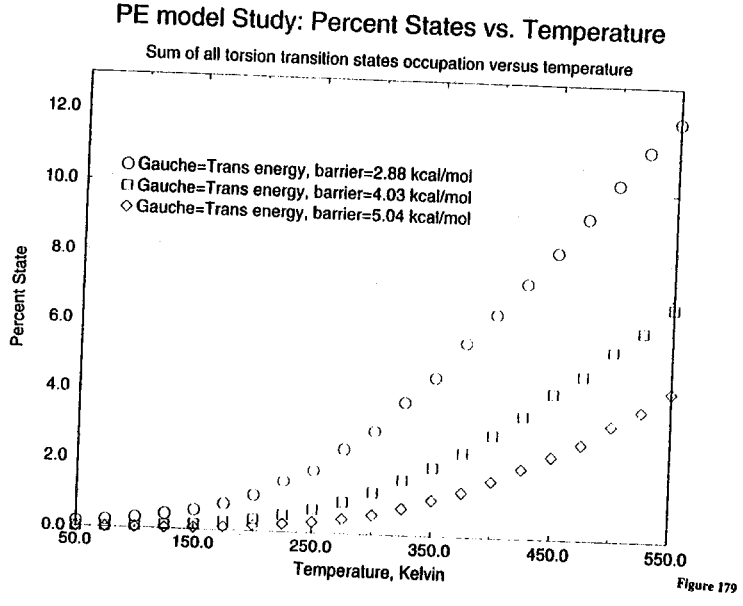

Figure 179

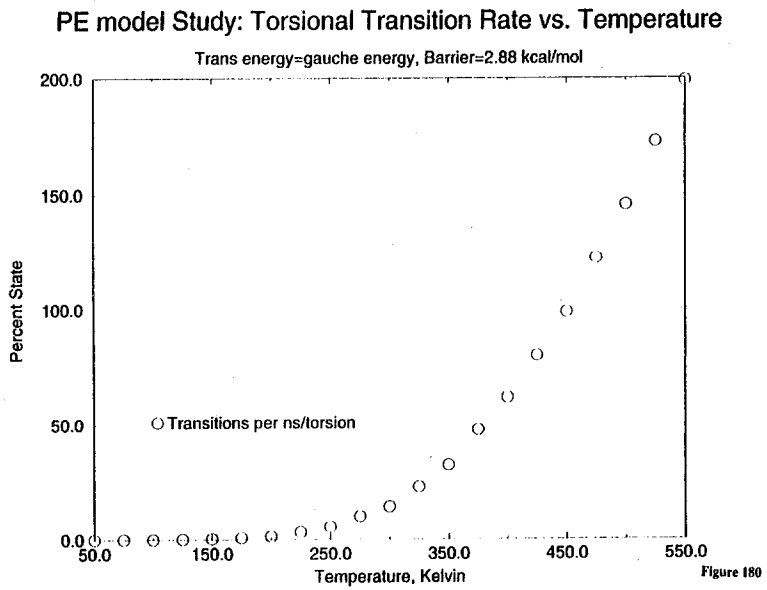

Figure 180

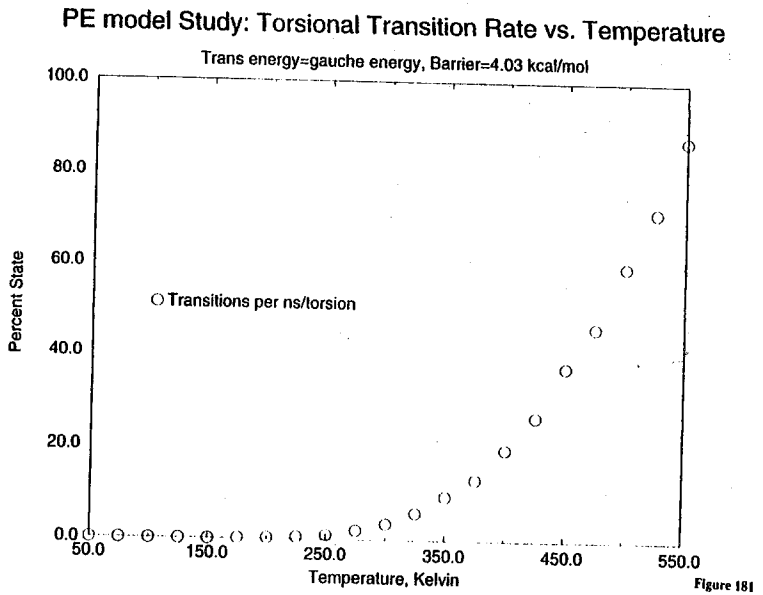

Figure 181

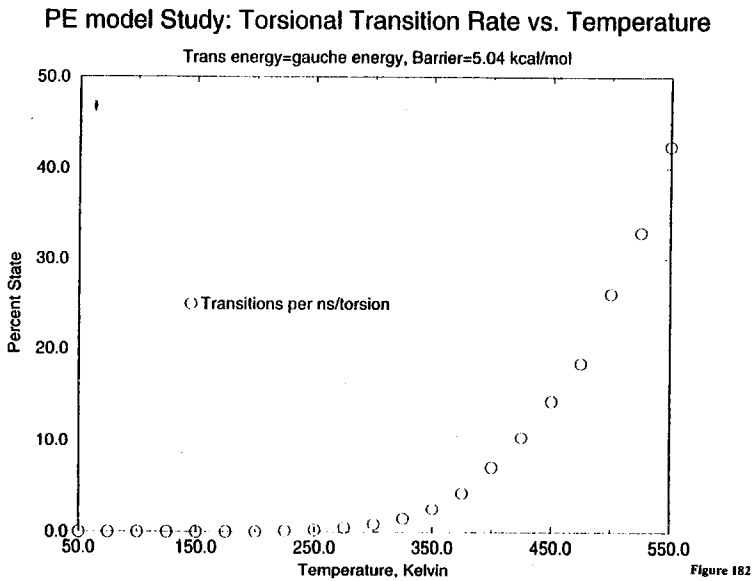

Figure 182

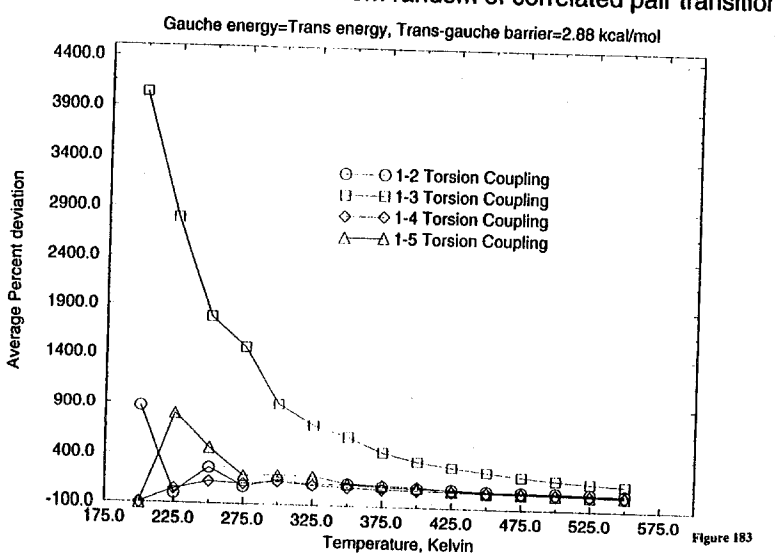

Figure 183

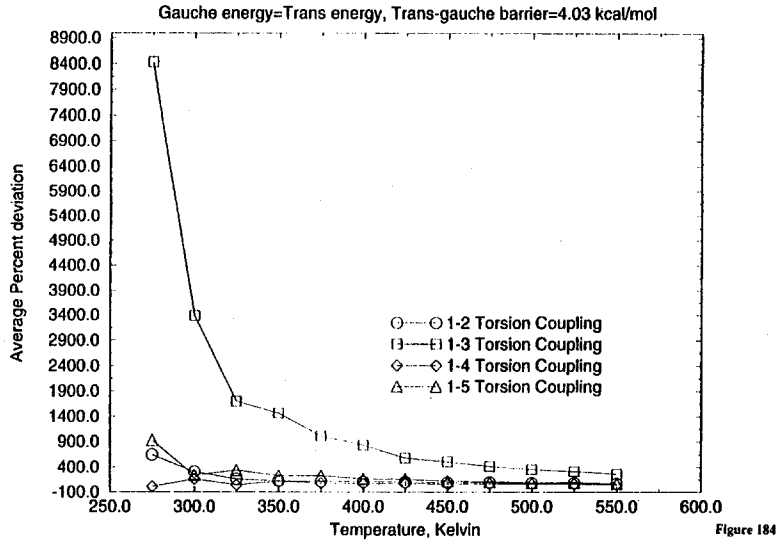

Figure 184

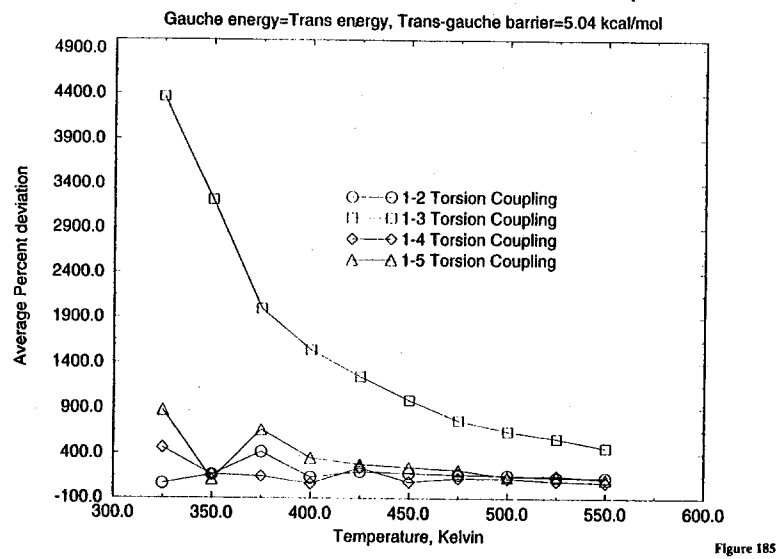

Figure 185

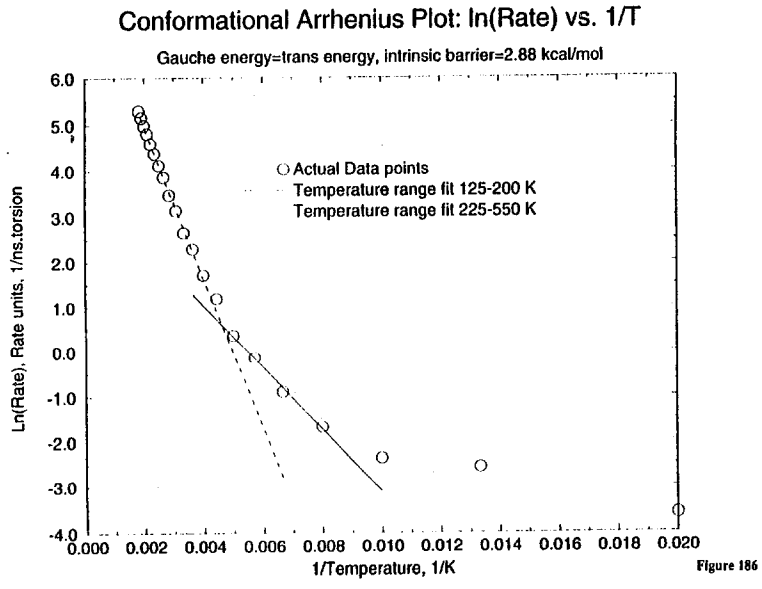

Figure 186

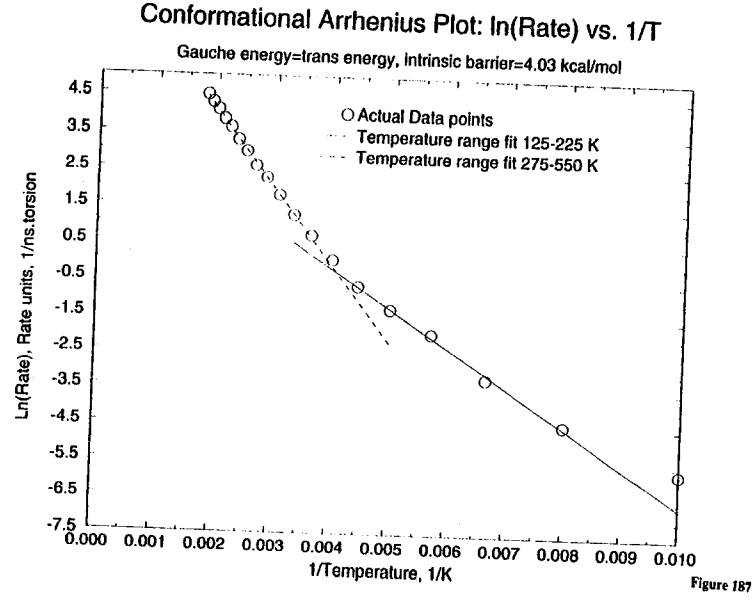

Figure 187

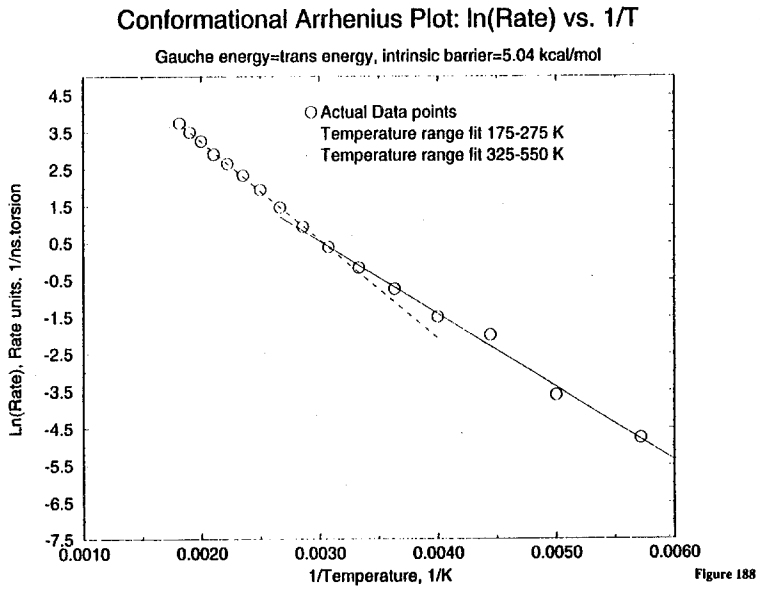

Figure 188

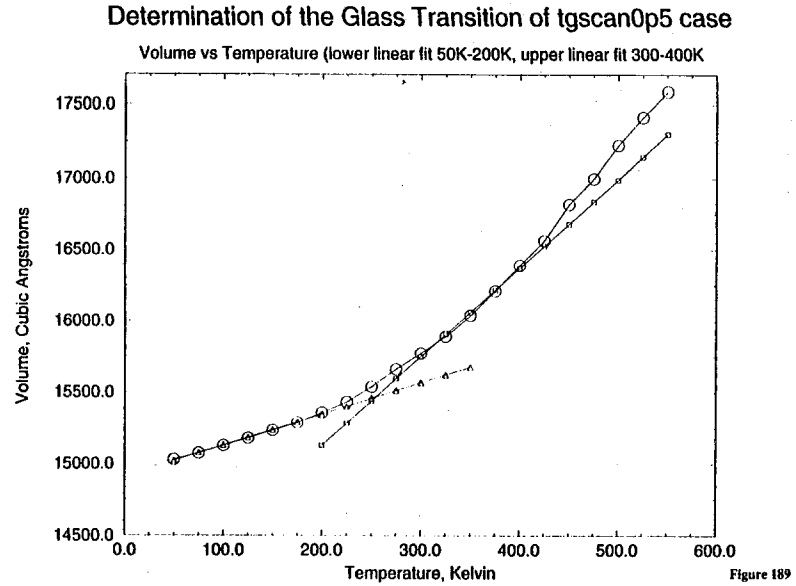

Figure 189

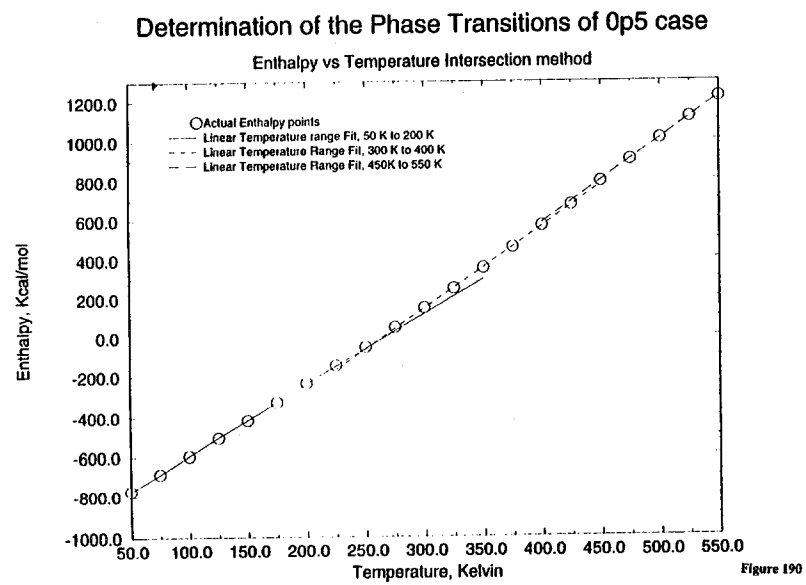

Figure 190

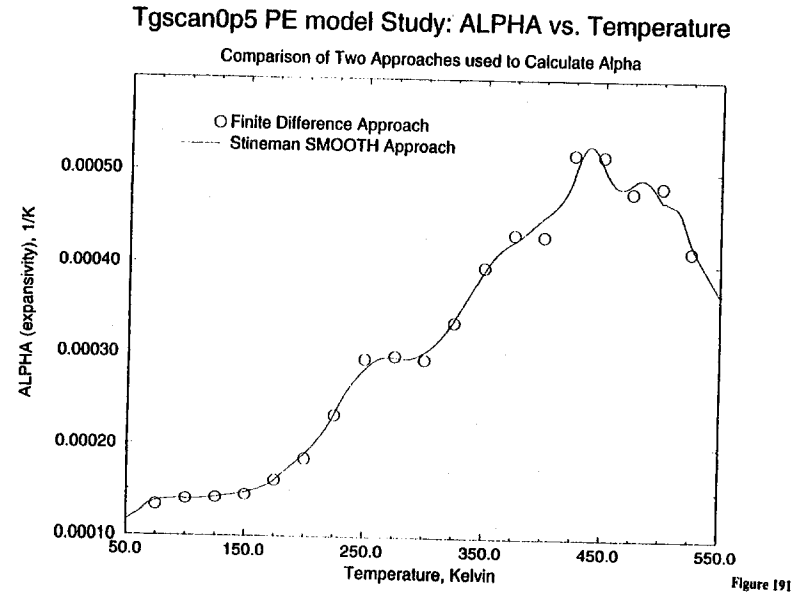

Figure 191

Tgscan0p5 PE model Study: Heat Capacity vs. Temperature

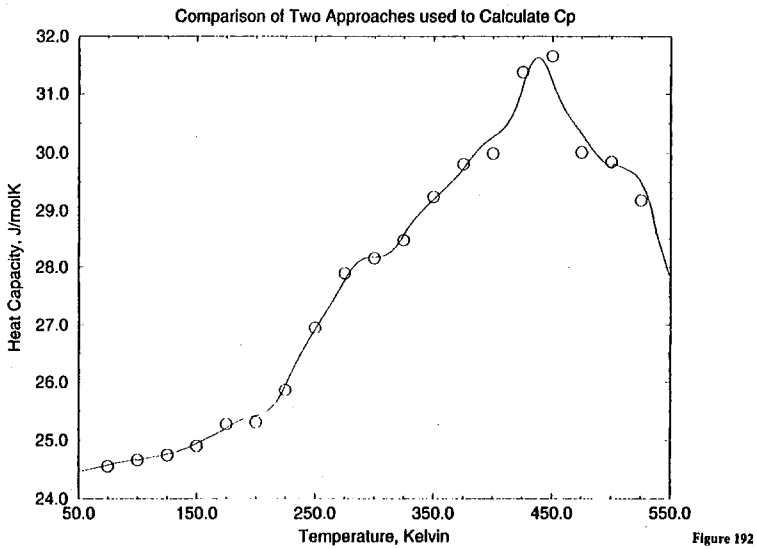

Figure 192

Determination of the Glass Transition of tgscan1p5 case

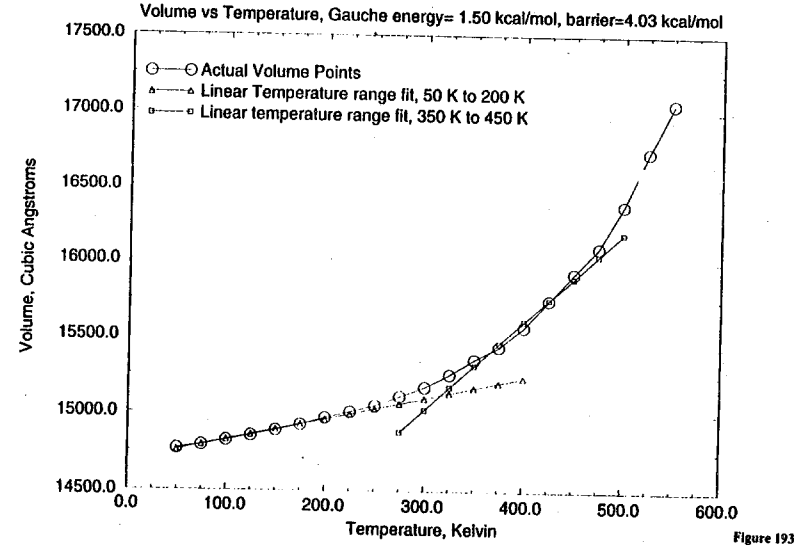

Figure 193

Determination of the Phase Transitions of tgscan1p5 case

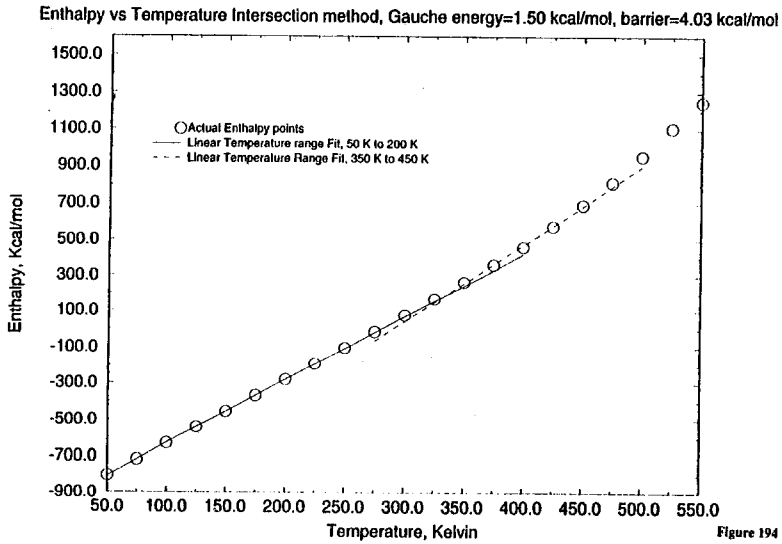

Figure 194

Determination of the Glass Transition of tgscan1p52 case

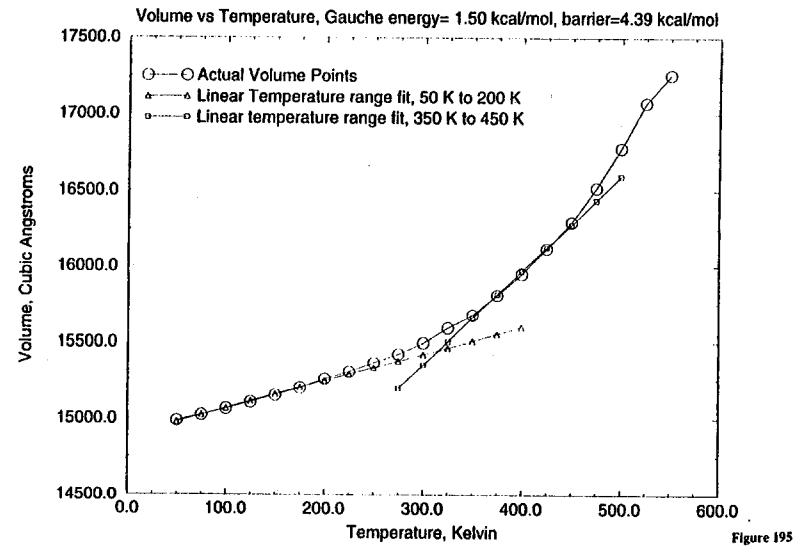

Figure 195

Determination of the Phase Transitions of tgscan1p52 case

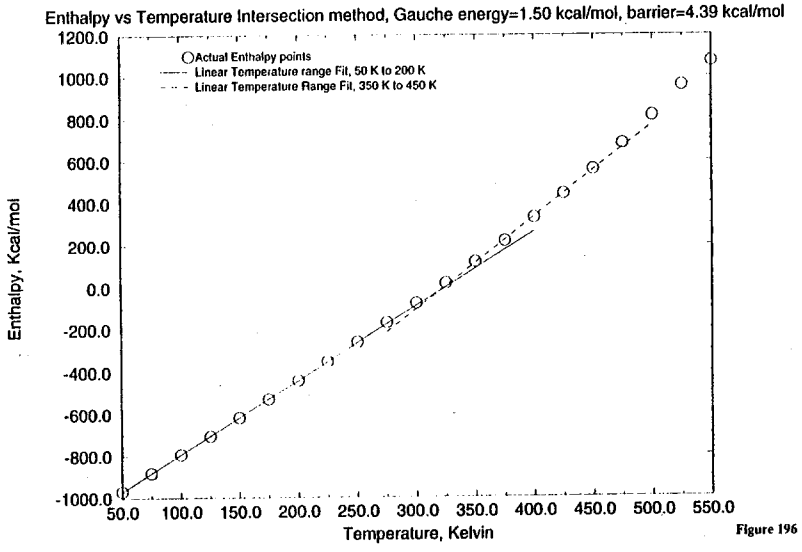

Figure 196

Torsional Barrier Effect on Compressiblity: PE model Study

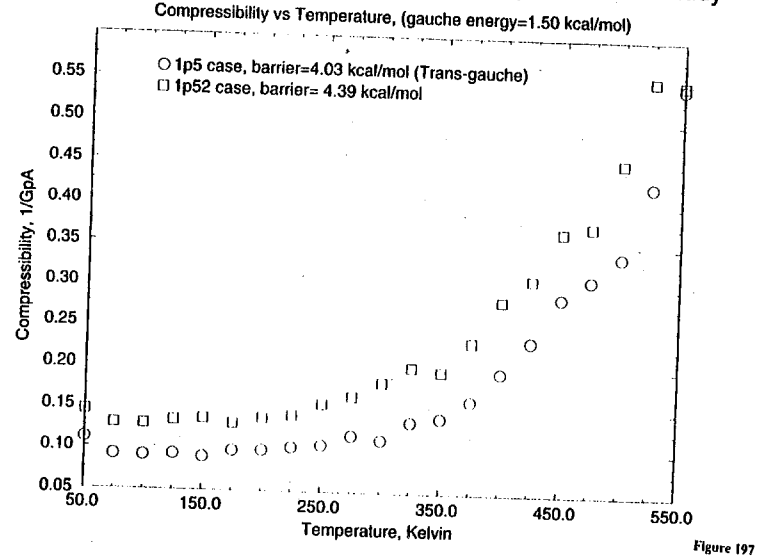

Figure 197

Highly Crystalline PE model Study: Density vs. Temperature

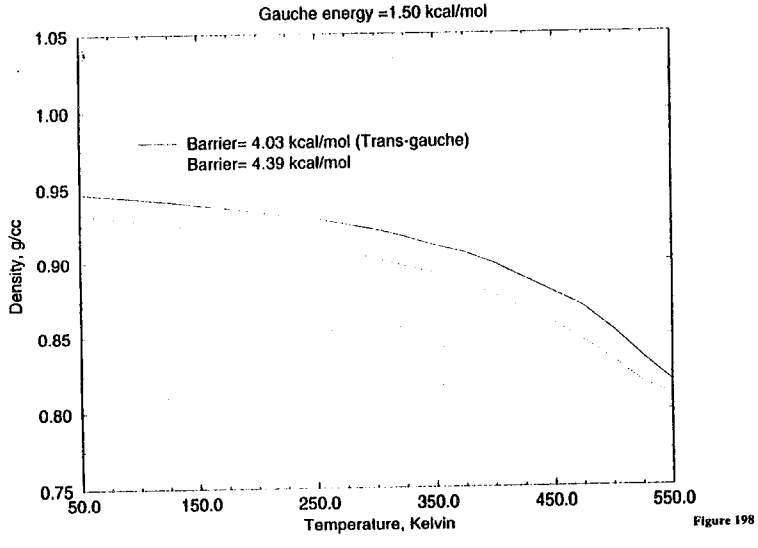

Figure 198

Highly Crystalline PE model Study: Expansivity vs. Temperature

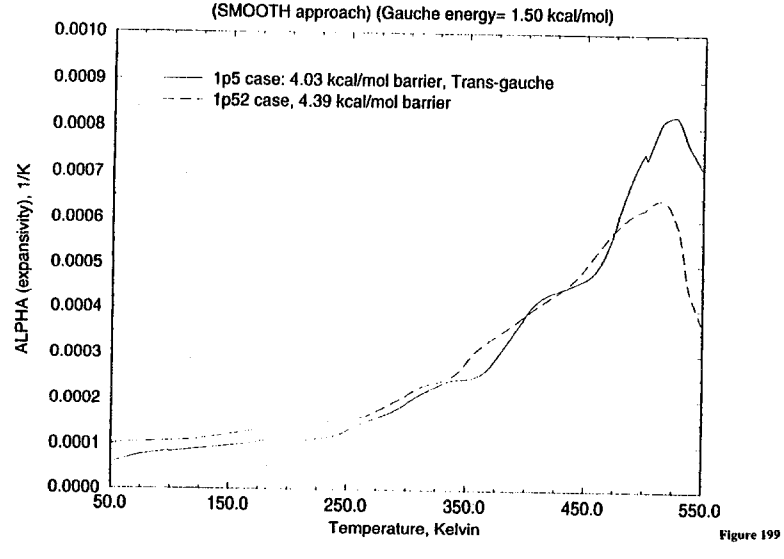

Figure 199

Highly Crystallline PE model Study: Heat Capacity vs. Temperature

(SMOOTH approach) (Gauche Energy=1.50 kcal/mol)

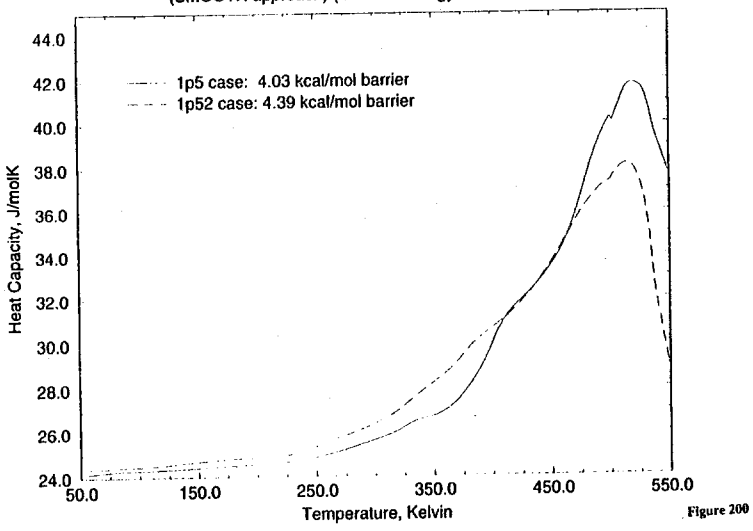

Figure 200

INV PE model Study: ALPHA vs. Temperature

Comparison of Two Approaches used to Calculate Alpha (Gauche energy=-1.16 Kcal/mol)

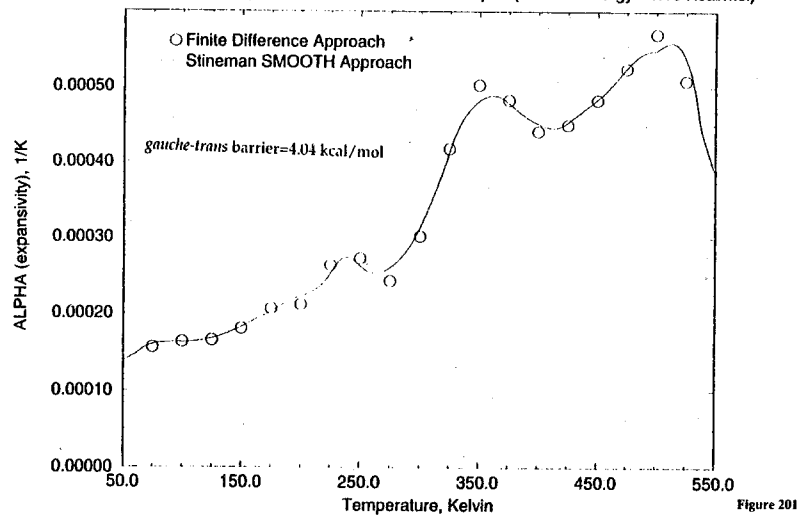

Figure 201

Determination of the Glass Transition of the INV case

Enthalpy vs Temperature (Gauche energy=-1.16 kcal/mol, Gauche-Trans barrier=4.04 kcal/mol)

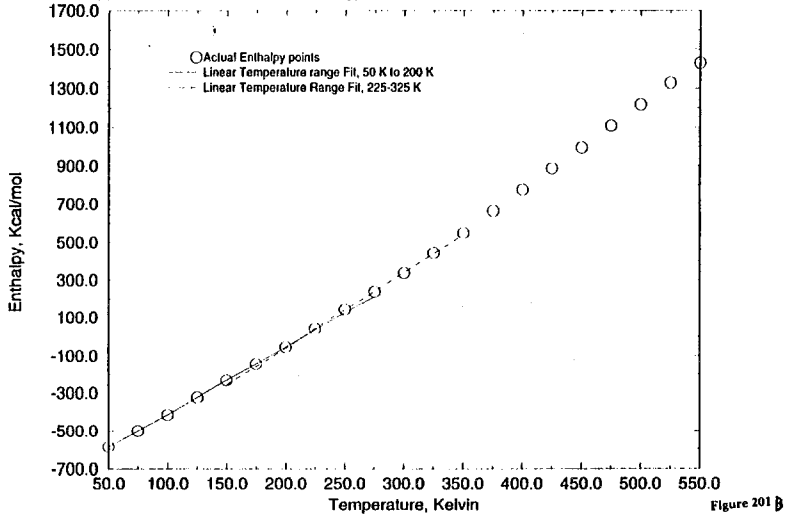

Figure 201 β

INV PE model Study: Heat Capacity vs. Temperature

Comparison of Two Approaches used to Calculate Cp (Gauche energy=-1.16 kcal/mol)

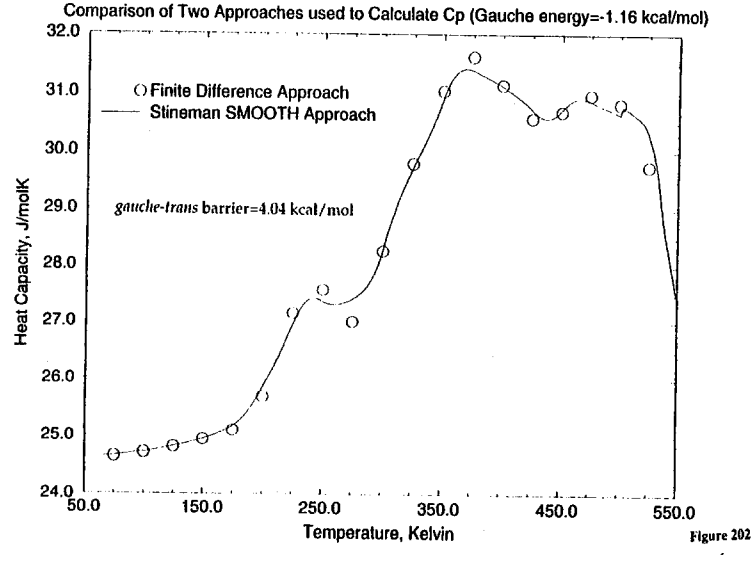

Figure 202

Determination of the Glass Transition of the INV case

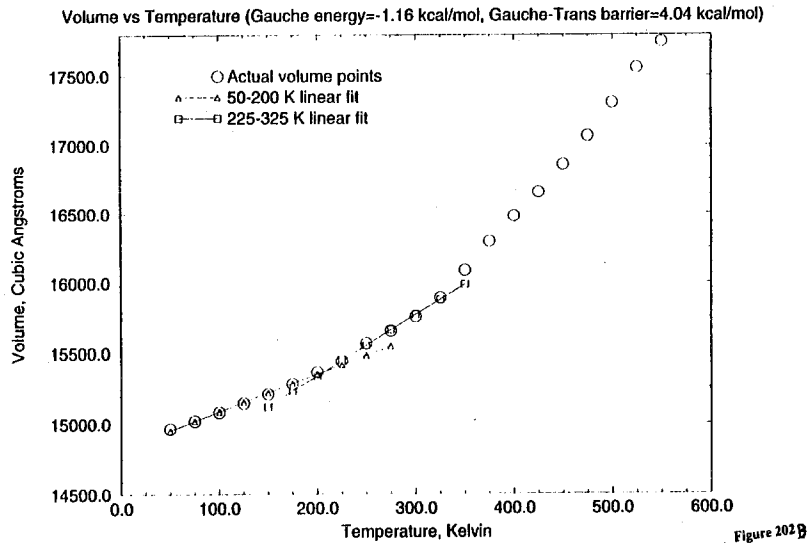

Figure 202

Determination of the Glass Transition of tgscan1p5 case

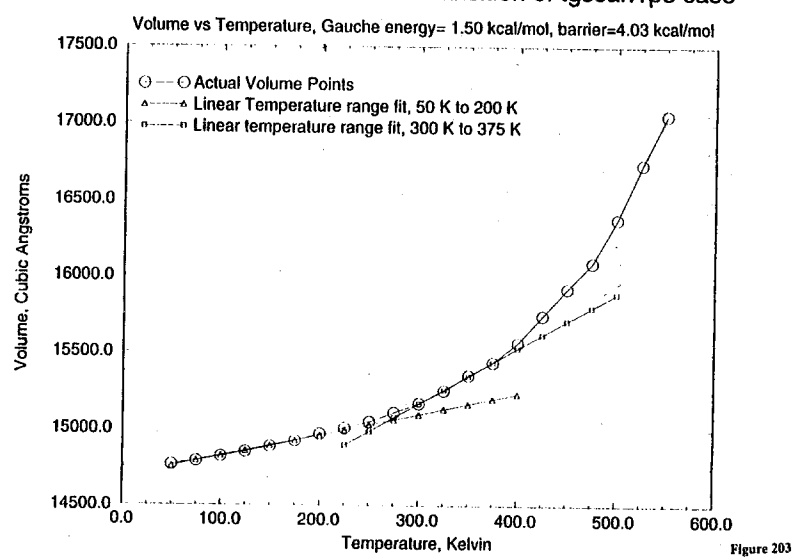

Figure 203

Determination of the Glass Transition of tgscan1p5 case

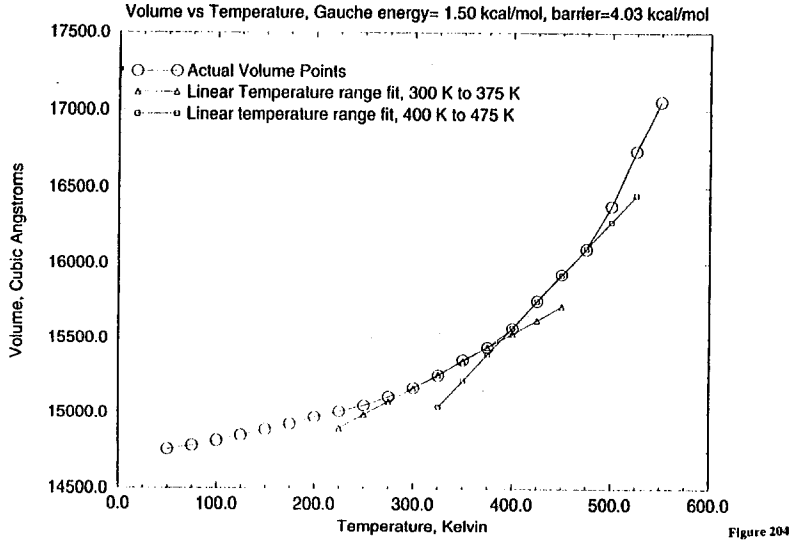

Figure 204

Determination of the Phase Transitions of tgscan1p5 case

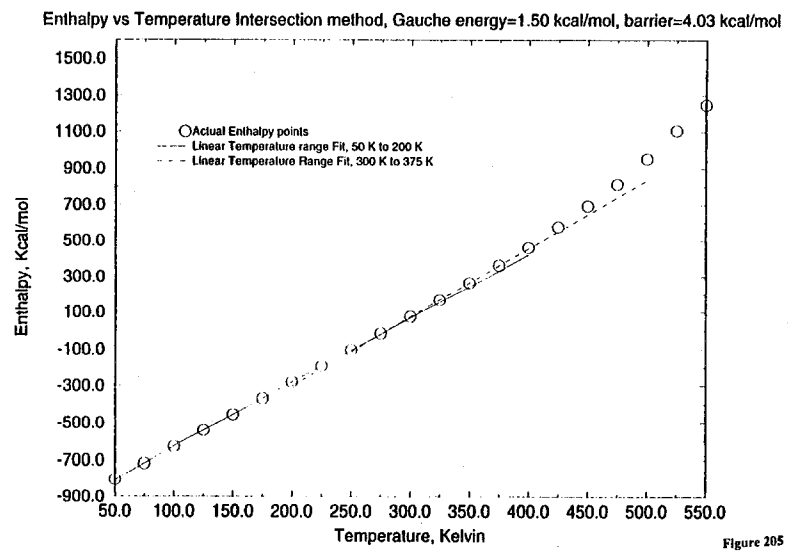

Figure 205

Determination of the Phase Transitions of tgscan1p5 case

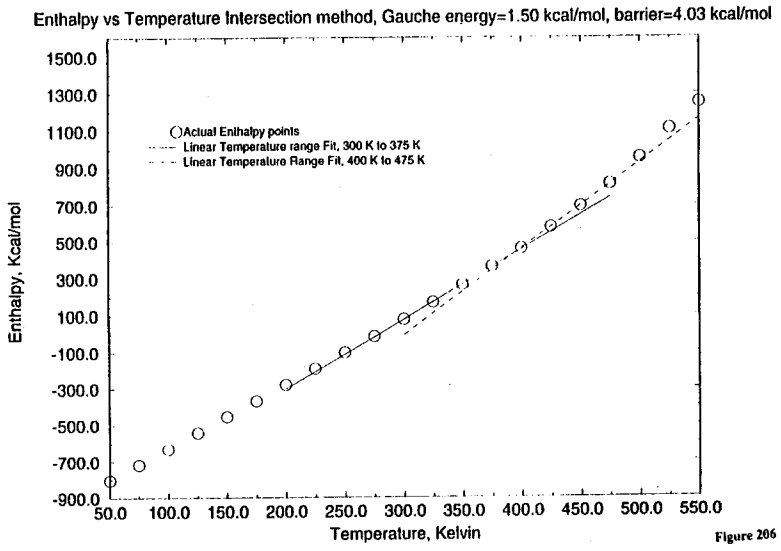

Figure 206

Average Intra Chain axis order Parameter vs. Temperature

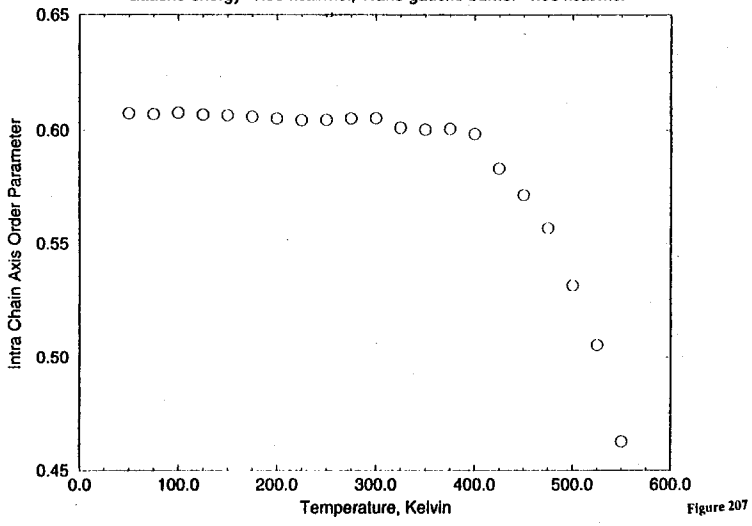

Figure 207

Relative Intra-Chain Axis distribution

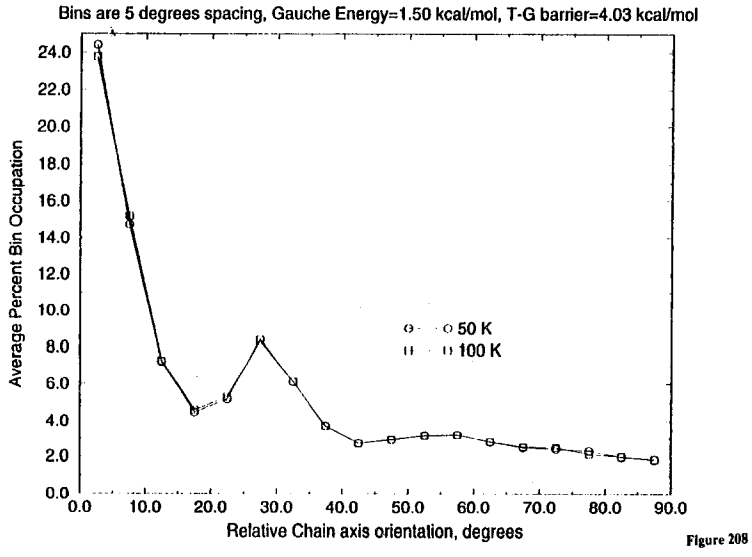

Figure 208

Relative Intra-Chain Axis distribution

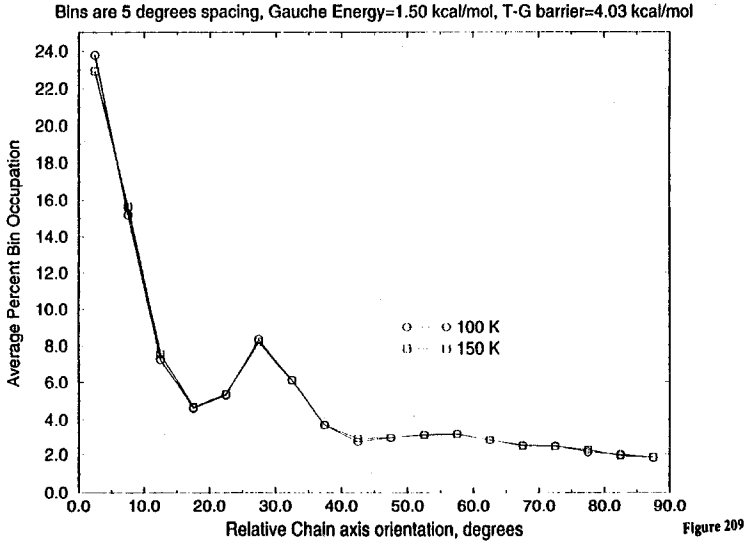

Figure 209

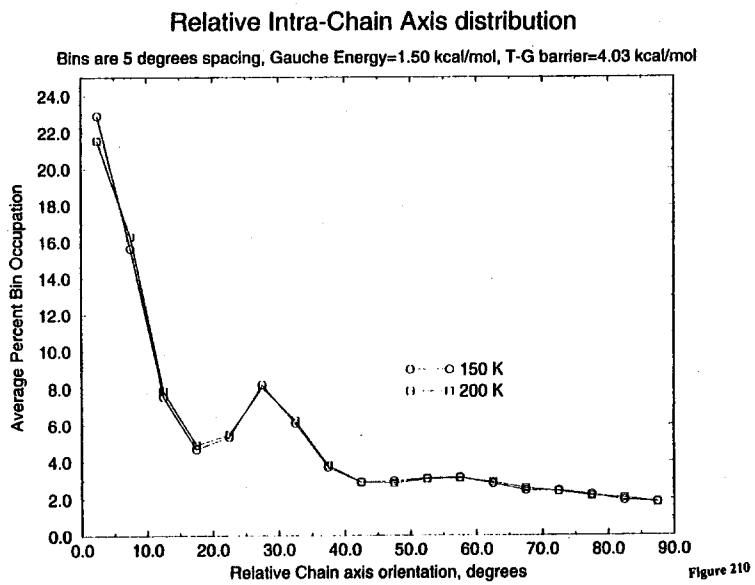

Figure 210

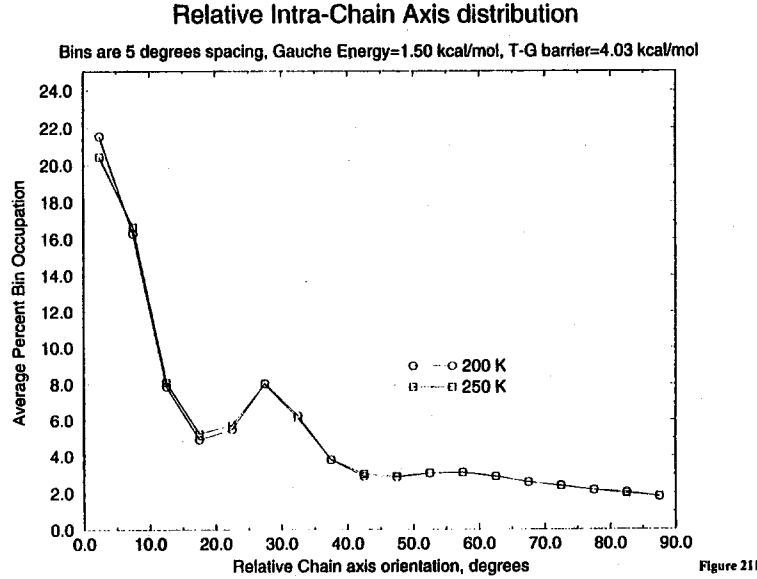

Figure 211

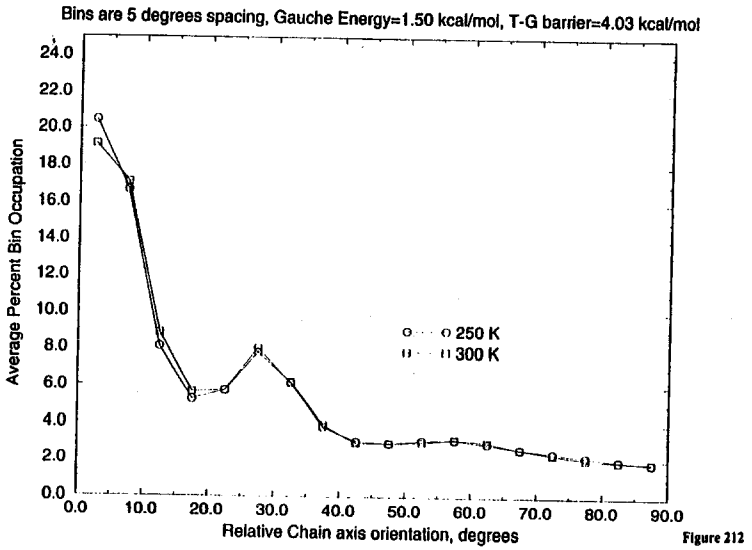

Figure 212

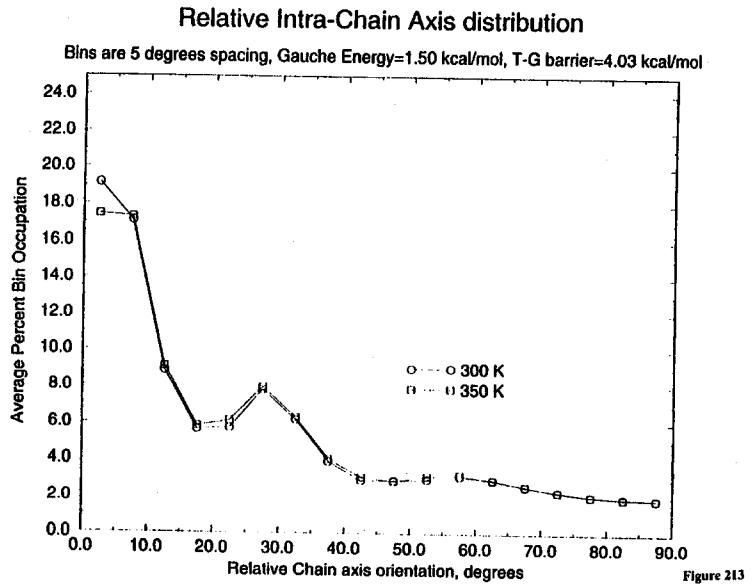

Figure 213

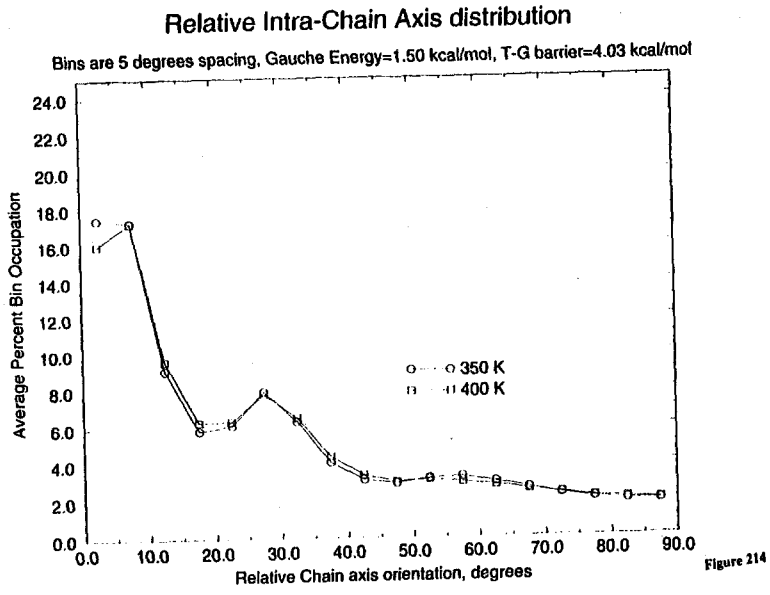

Figure 214

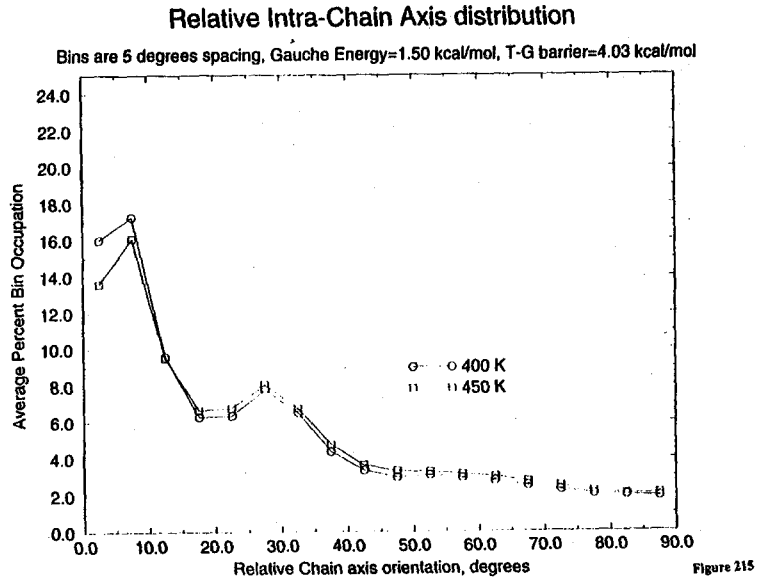

Figure 215

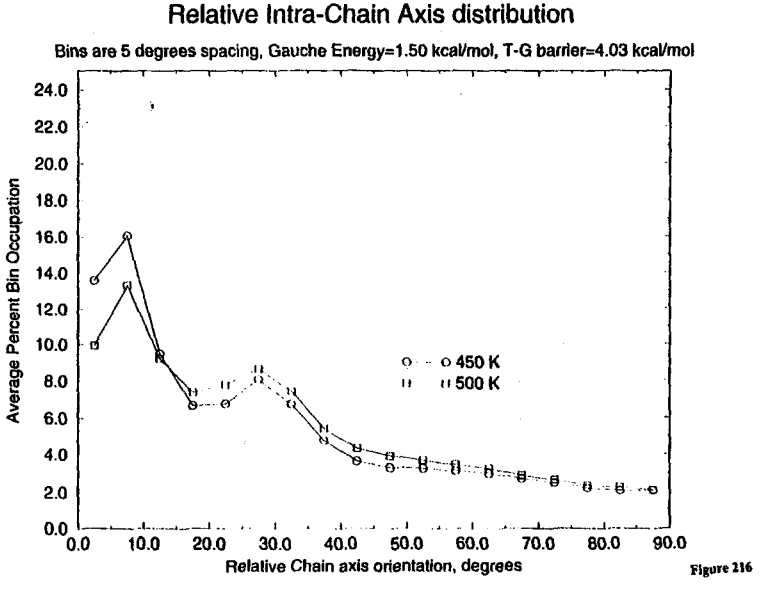

Figure 216

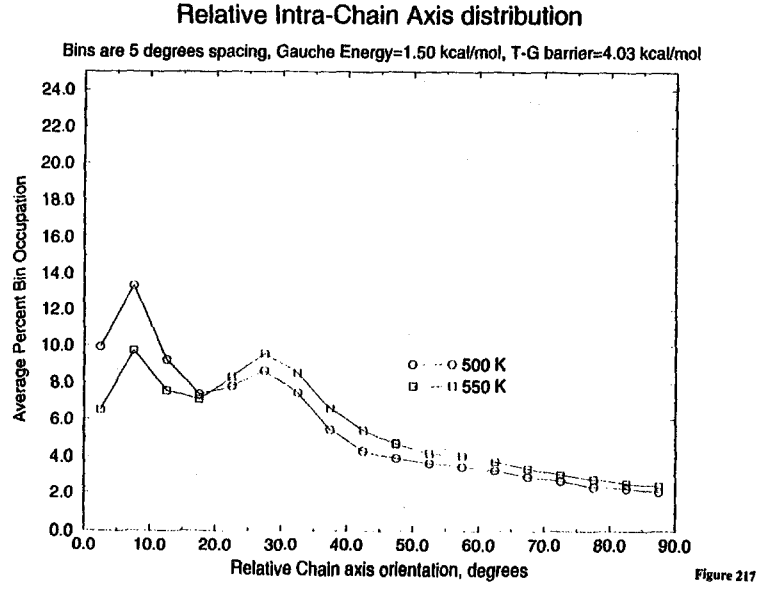

Figure 217

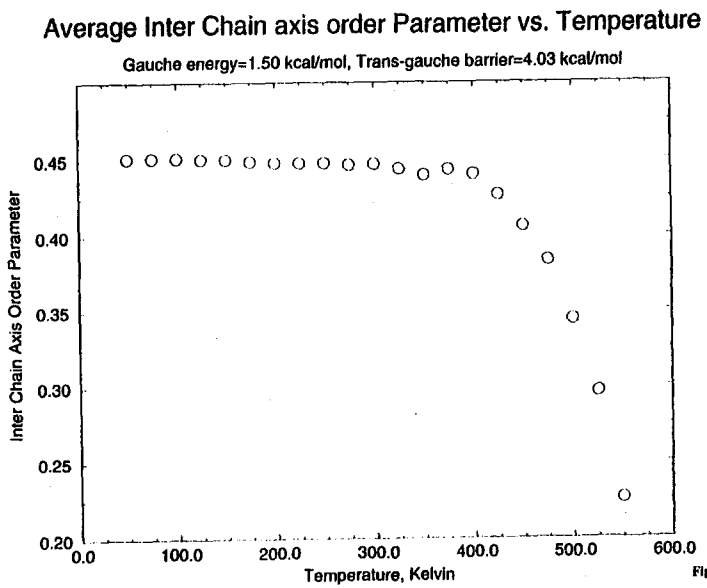

Figure 218

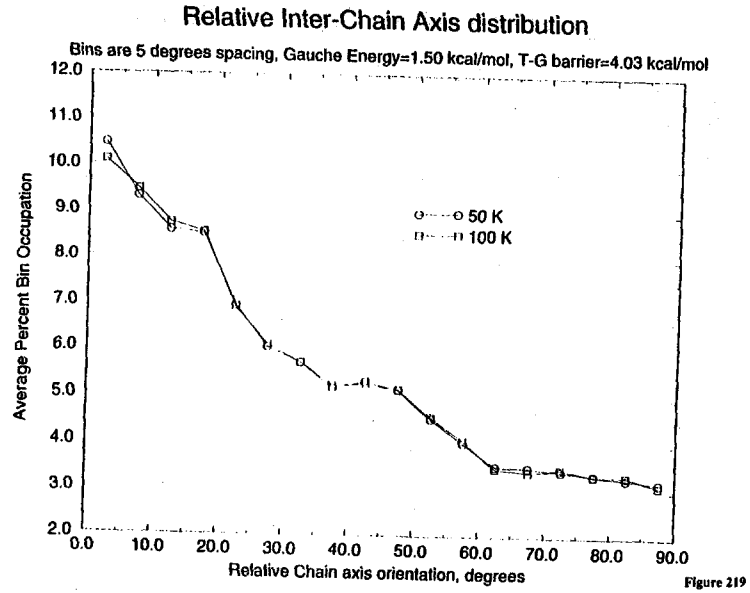

Figure 219

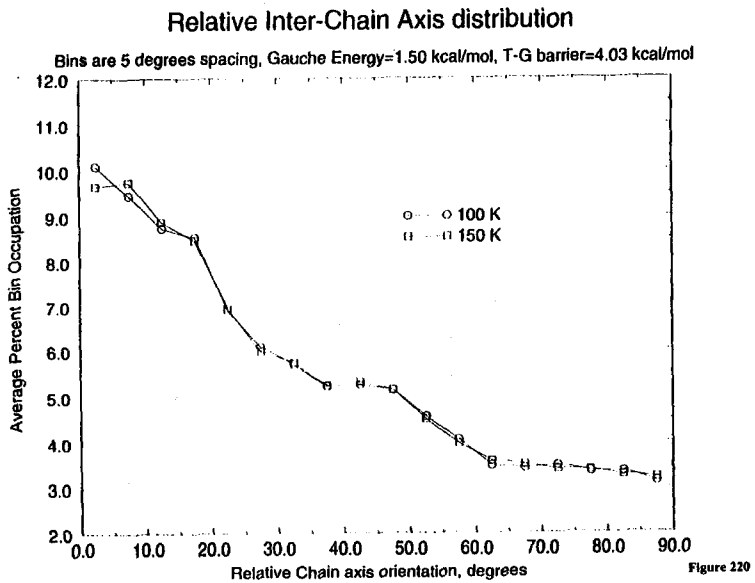

Figure 220

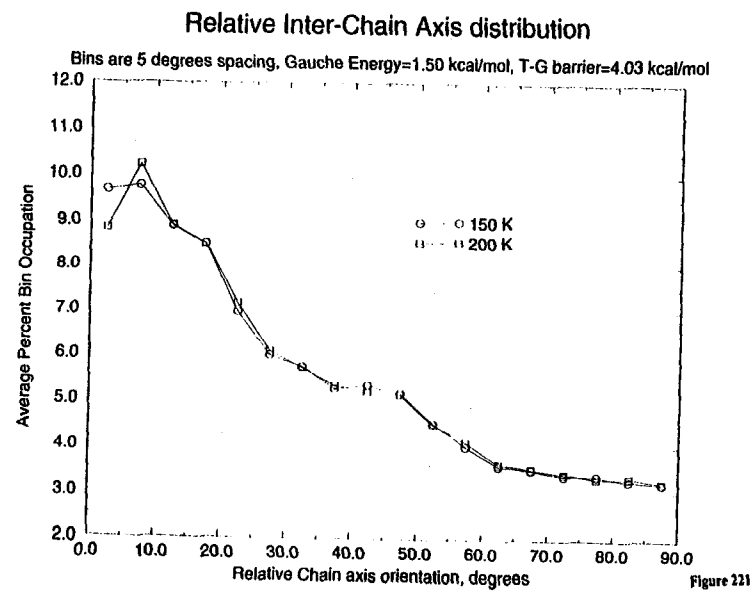

Figure 221

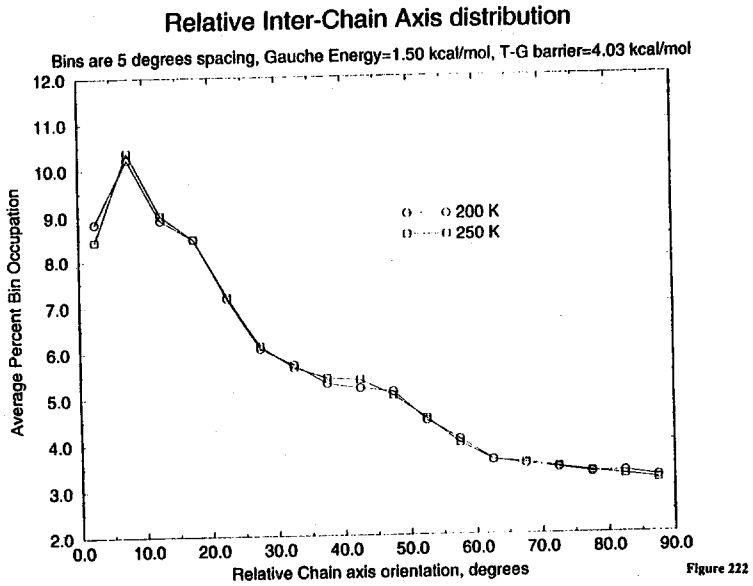

Figure 222

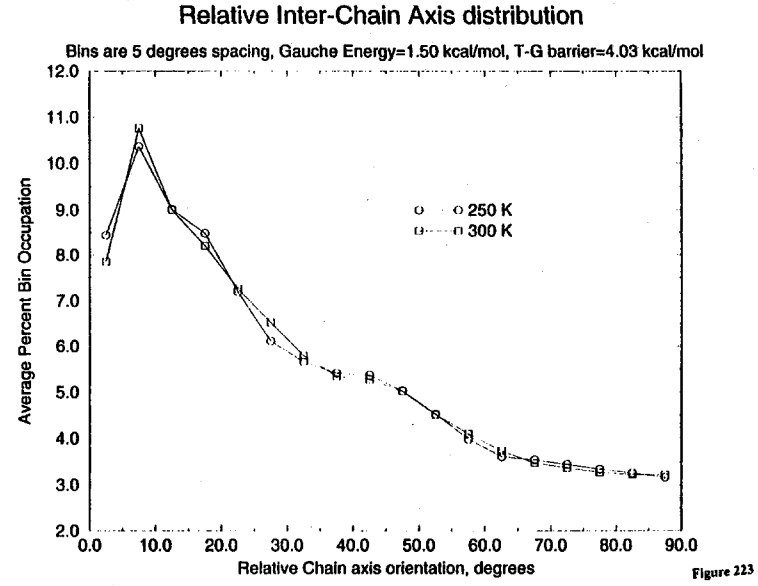

Figure 223

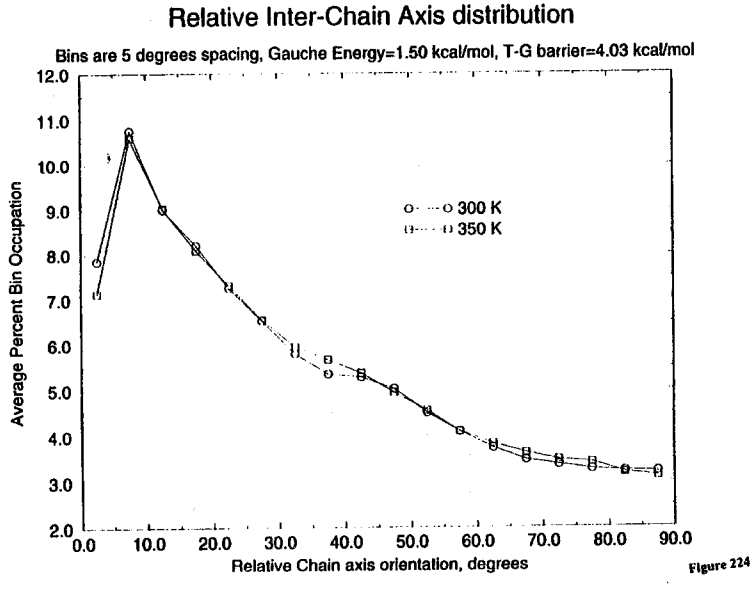

Figure 224

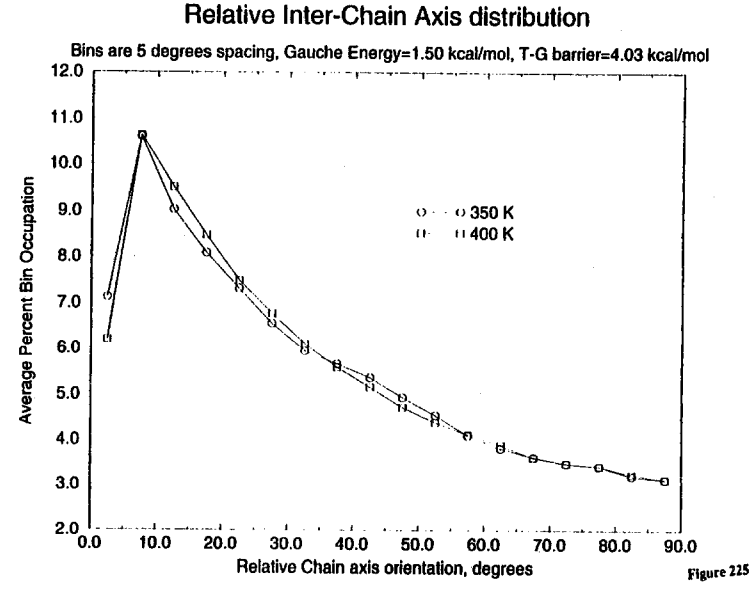

Figure 225

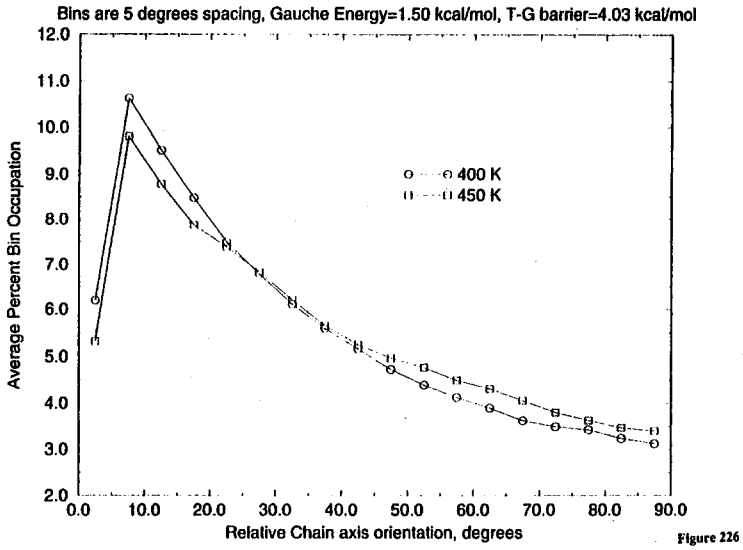

Figure 226

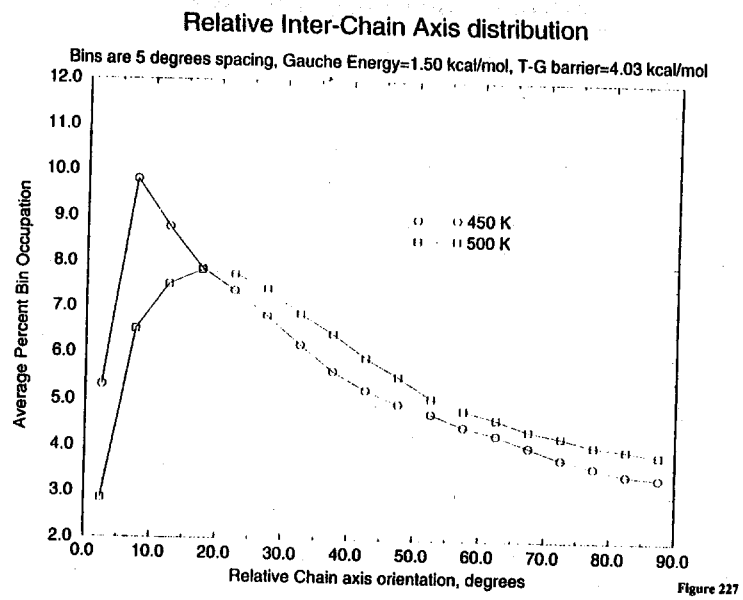

Figure 227

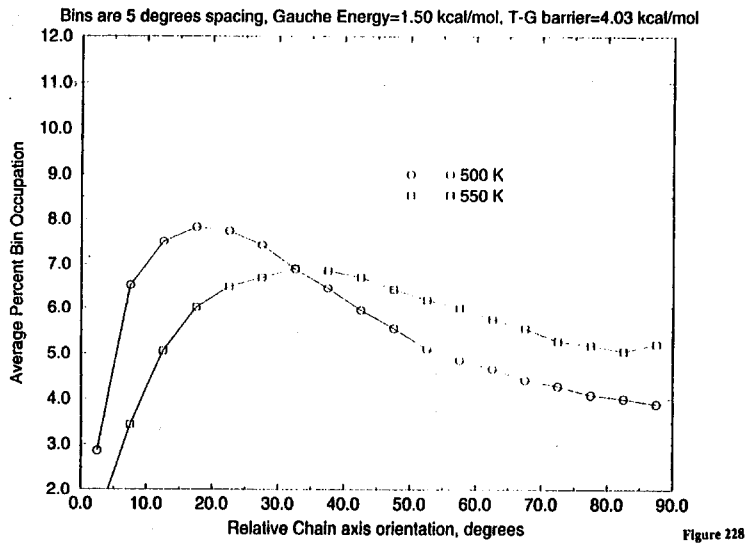

Figure 228

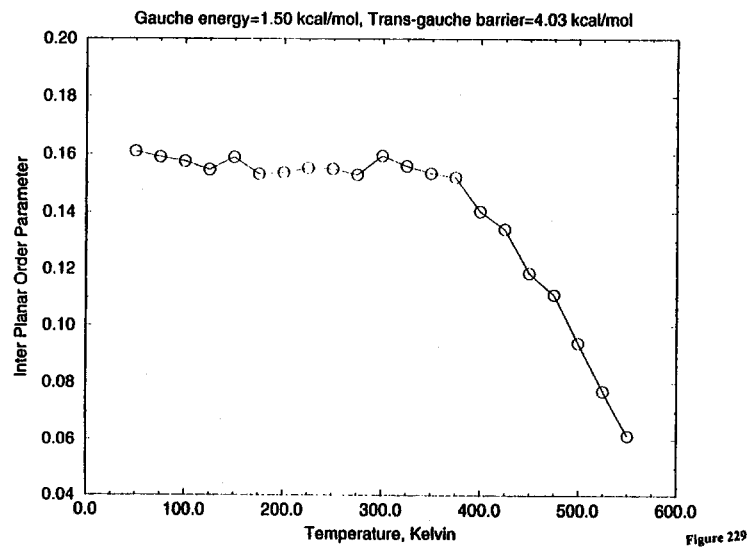

Figure 229

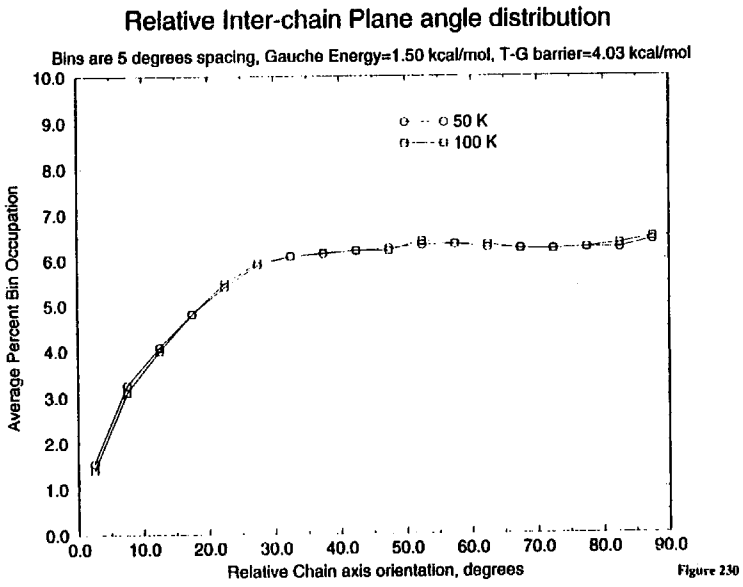

Figure 230

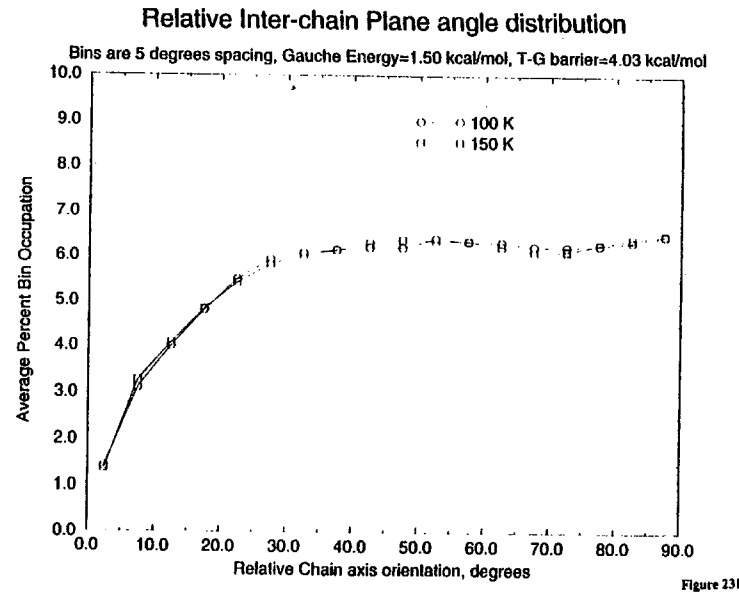

Figure 231

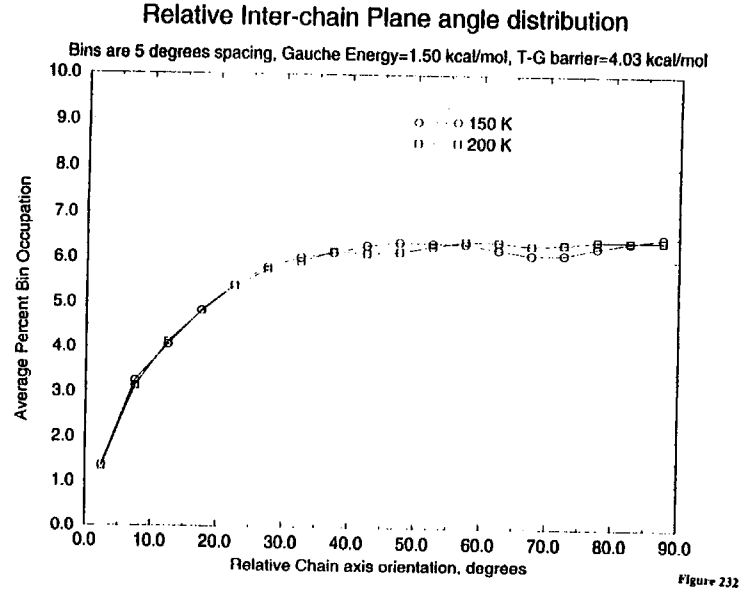

Figure 232

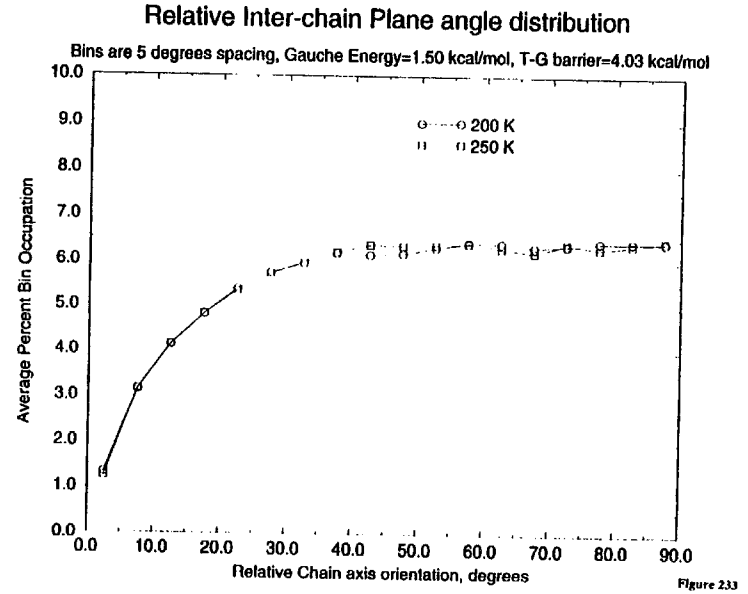

Figure 233

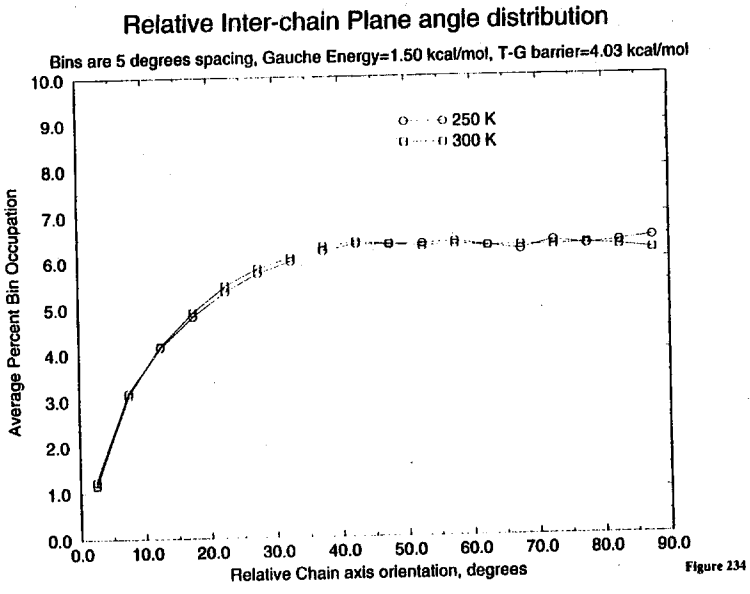

Figure 234

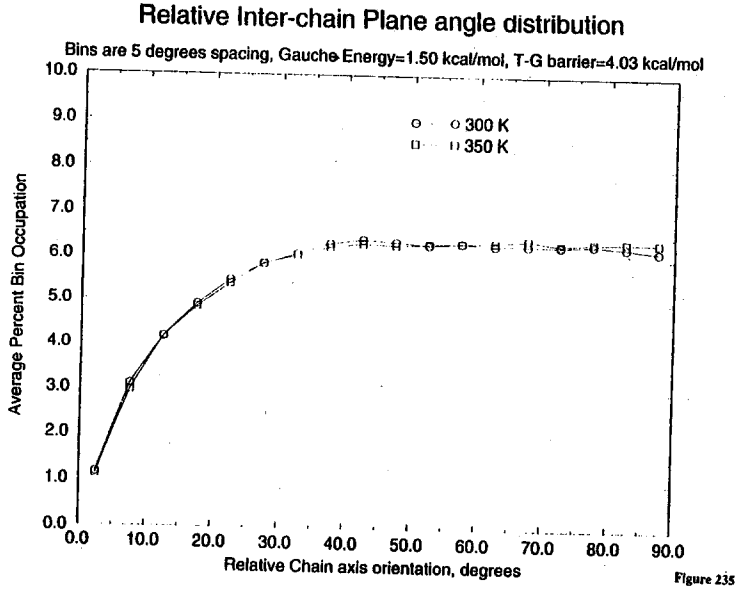

Figure 235

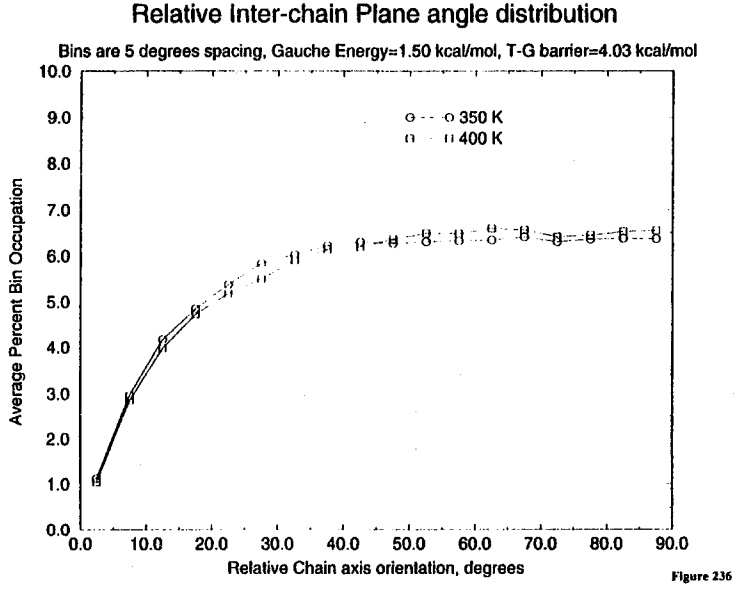

Figure 236

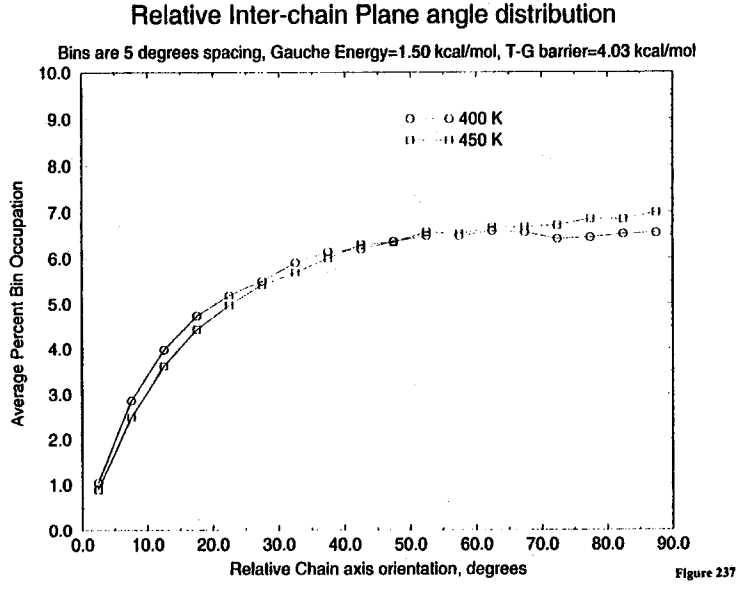

Figure 237

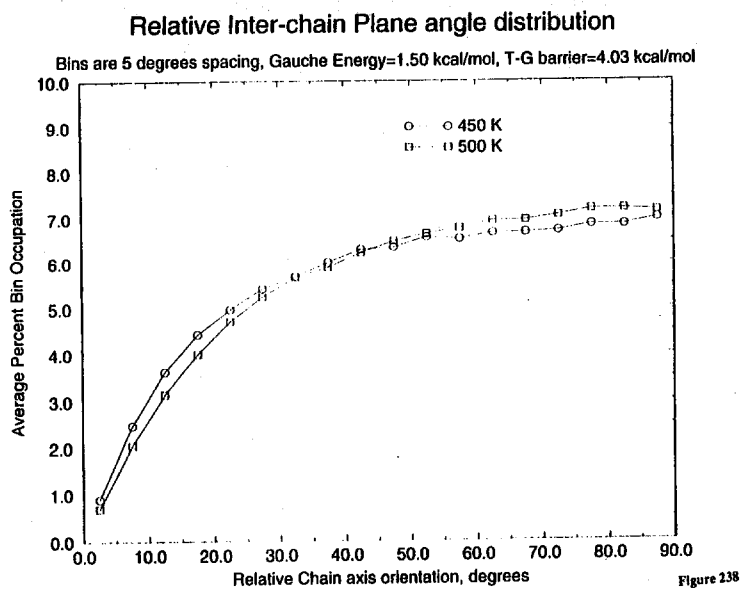

Figure 238

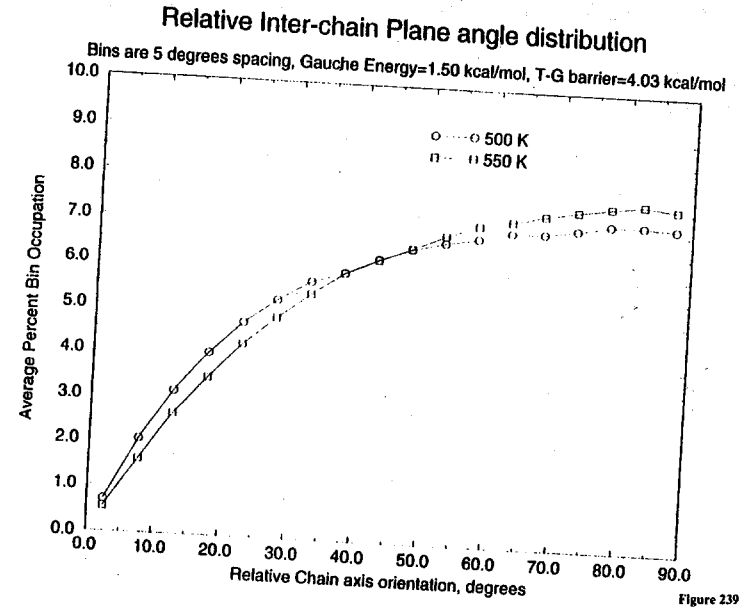

Figure 239

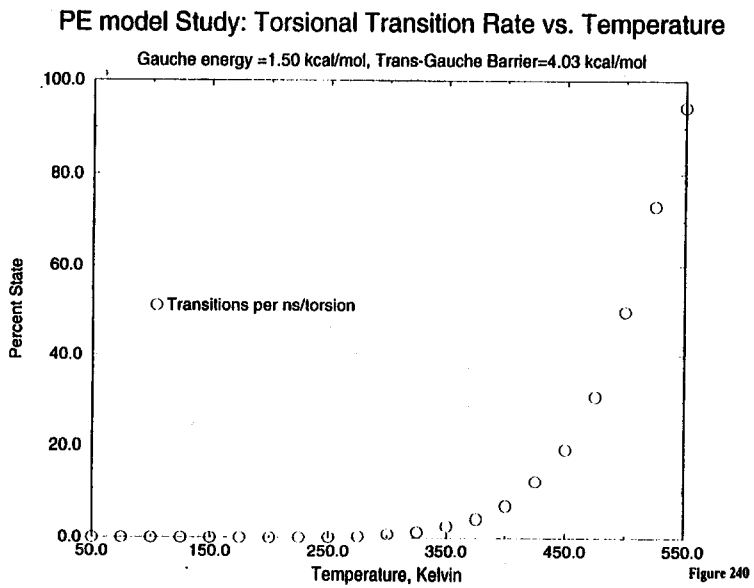

Figure 240

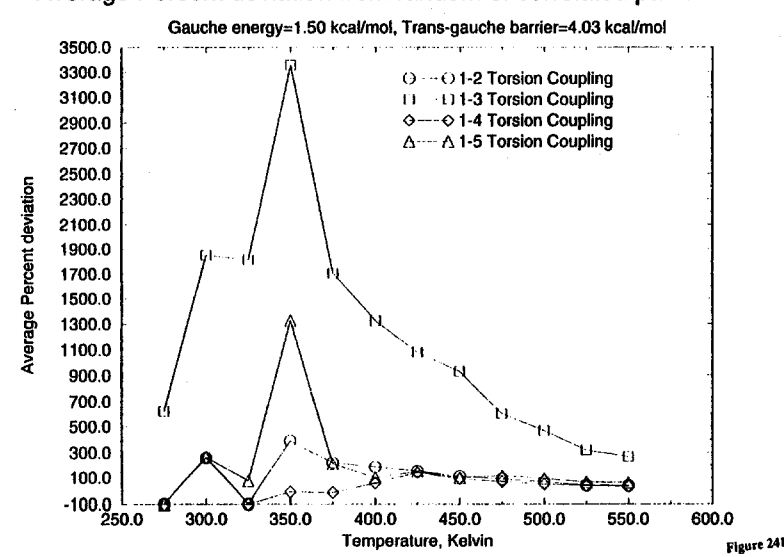

Figure 241

Conformational Arrhenius Plot: ln(Rate) vs. 1/T

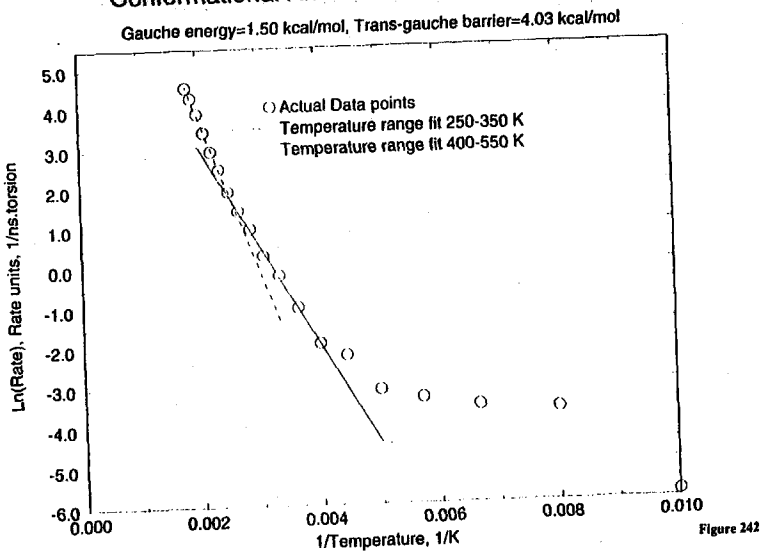

Figure 242

Determination of the Glass Transition of D0=0.112 kcal/mol case

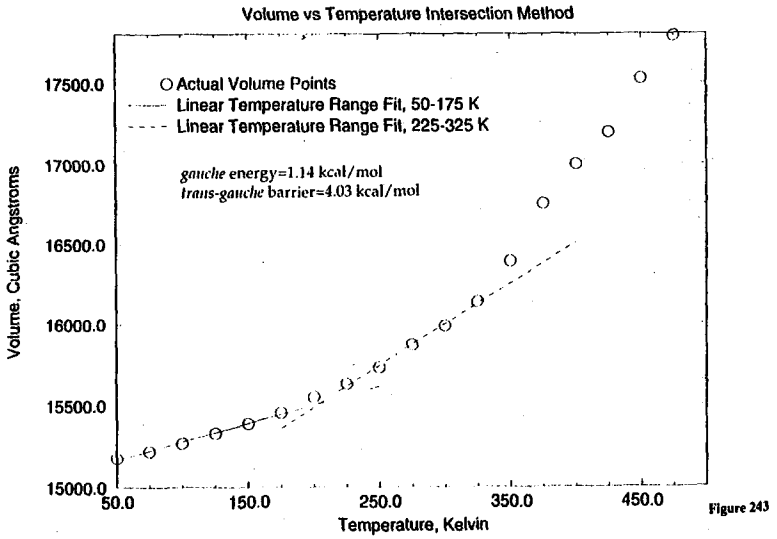

Figure 243

Determination of the Phase Transitions of D0=0.112 kcal/mol case

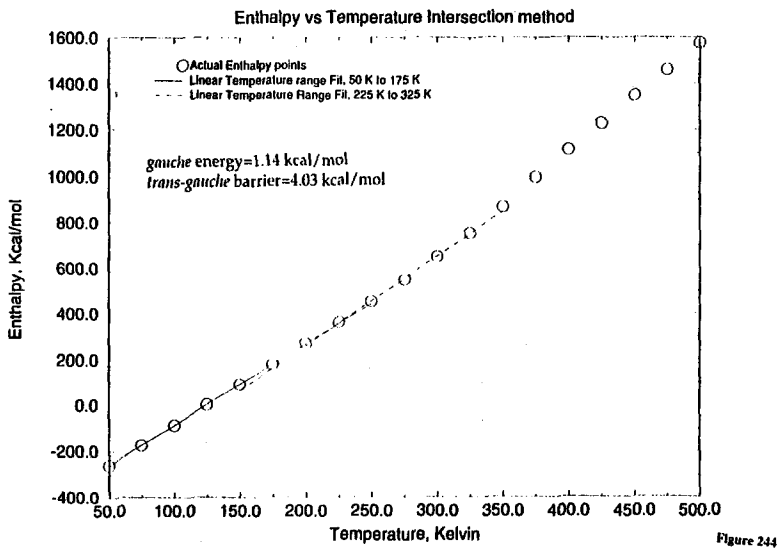

Figure 244

Determination of the Glass Transition of tgscandehi case

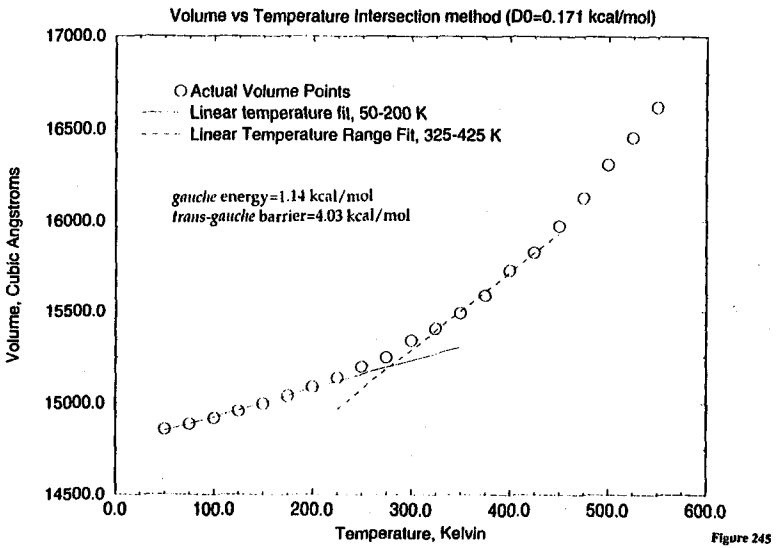

Figure 245

Determination of the Phase Transitions of high D0 case

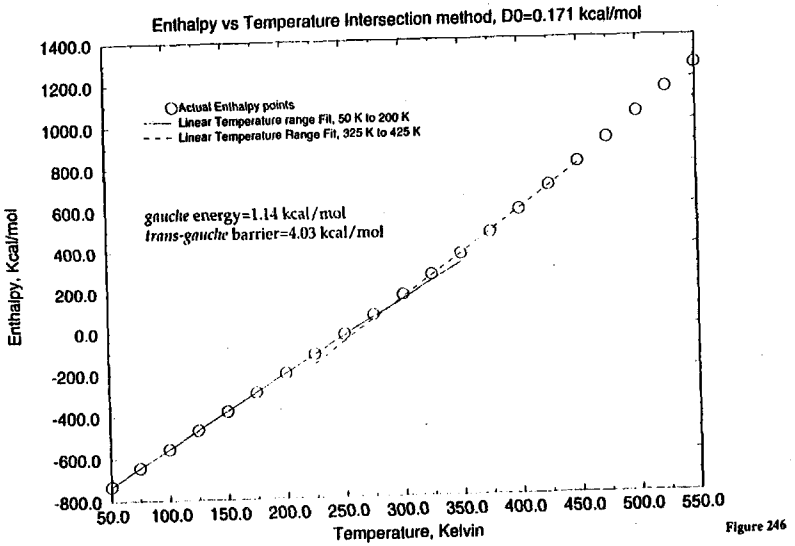

Figure 246

Determination of the Glass Transition of tgscandehi2 case

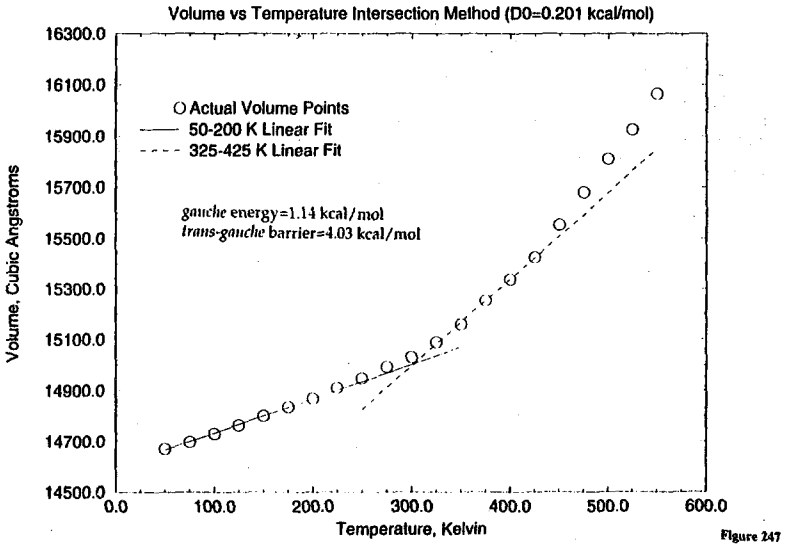

Figure 247

Determination of the Phase Transitions of high D0 case

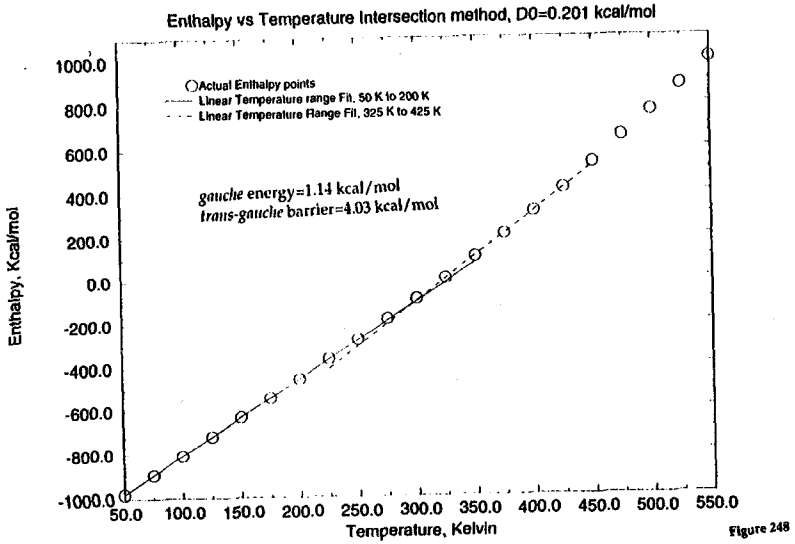

Figure 248

Tgscandelo PE model Study: Heat Capacity vs. Temperature

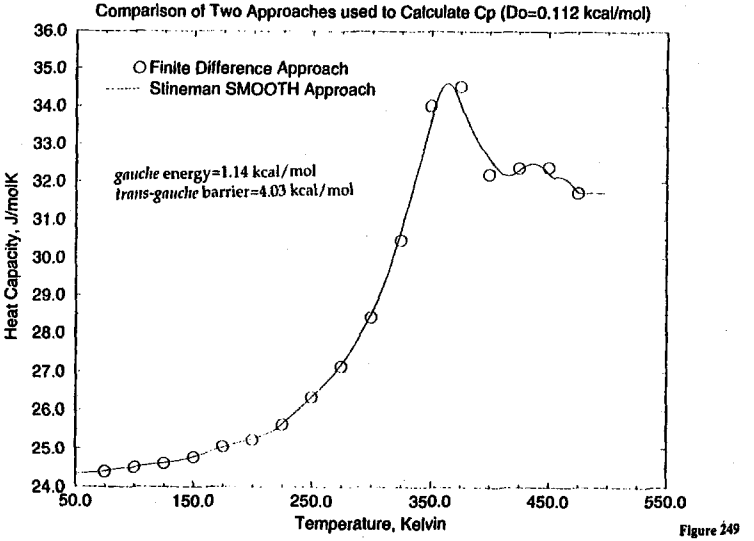

Figure 249

Tgscandelo PE model Study: ALPHA vs. Temperature

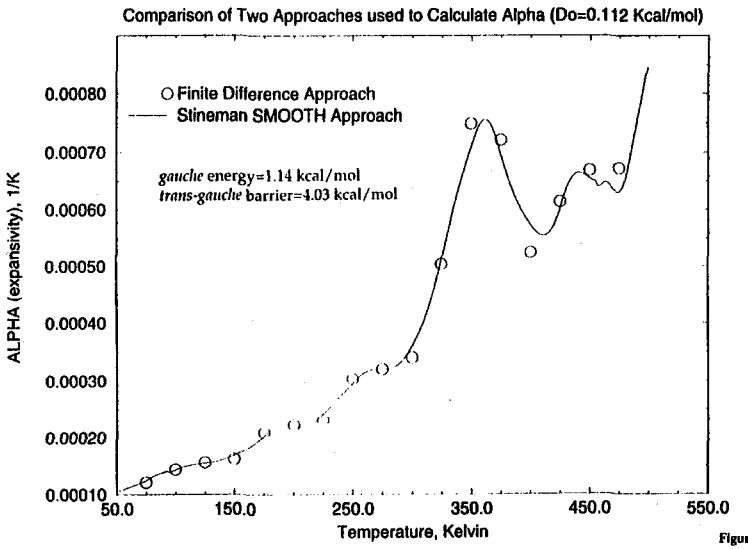

Figure 250

Tgscandehi PE model Study: ALPHA vs. Temperature

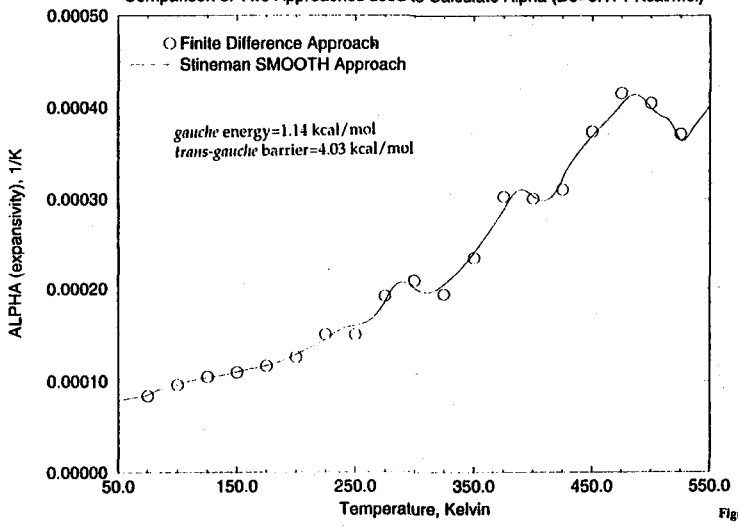

Figure 251

Tgscandehi PE model Study: Heat Capacity vs. Temperature

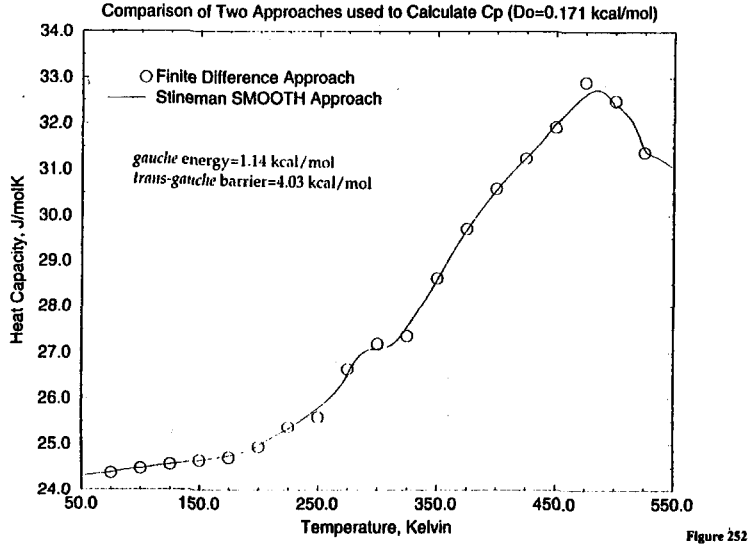

Figure 252

Tgscandehi2 PE model Study: ALPHA vs. Temperature

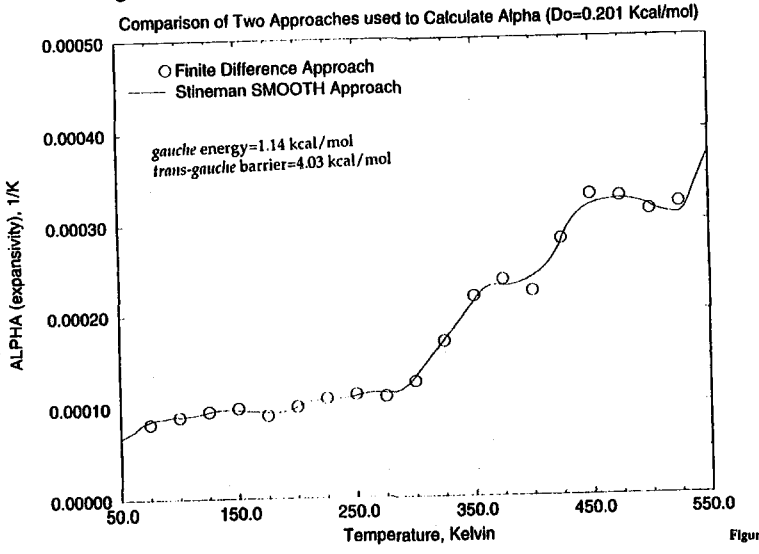

Figure 253

Tgscandehi2 PE model Study: Heat Capacity vs. Temperature

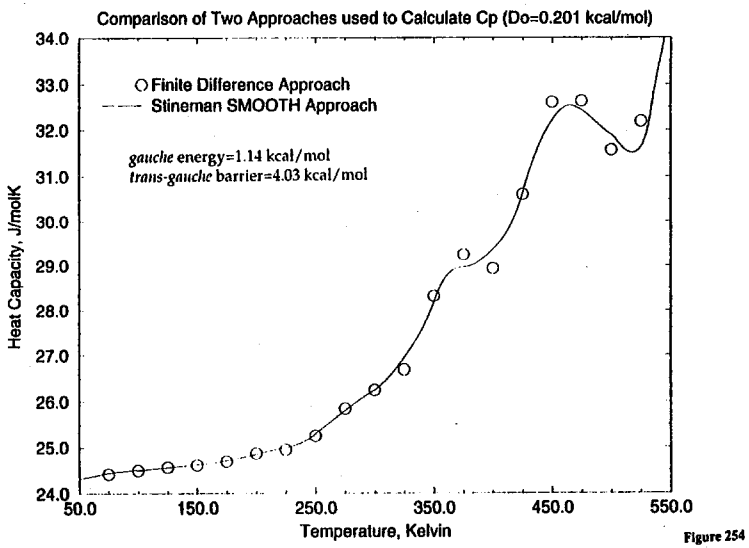

Figure 254

Lennard Jones Do Effect on Compressiblity: PE model Study

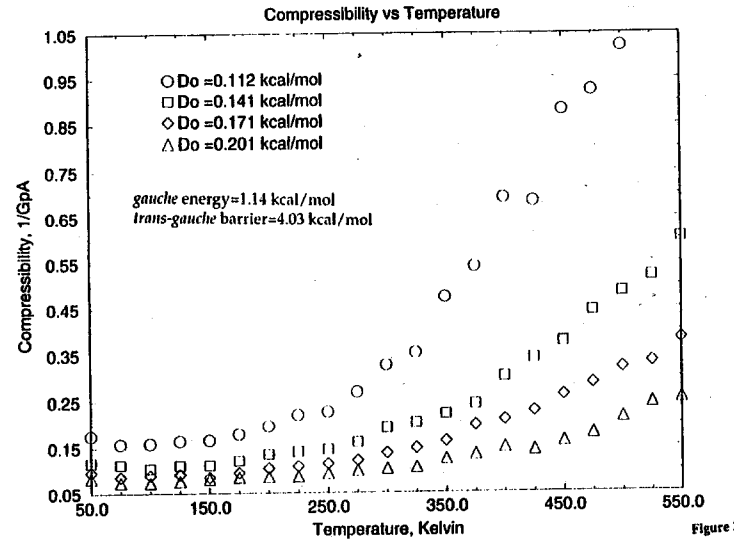

Figure 255

Figure 256

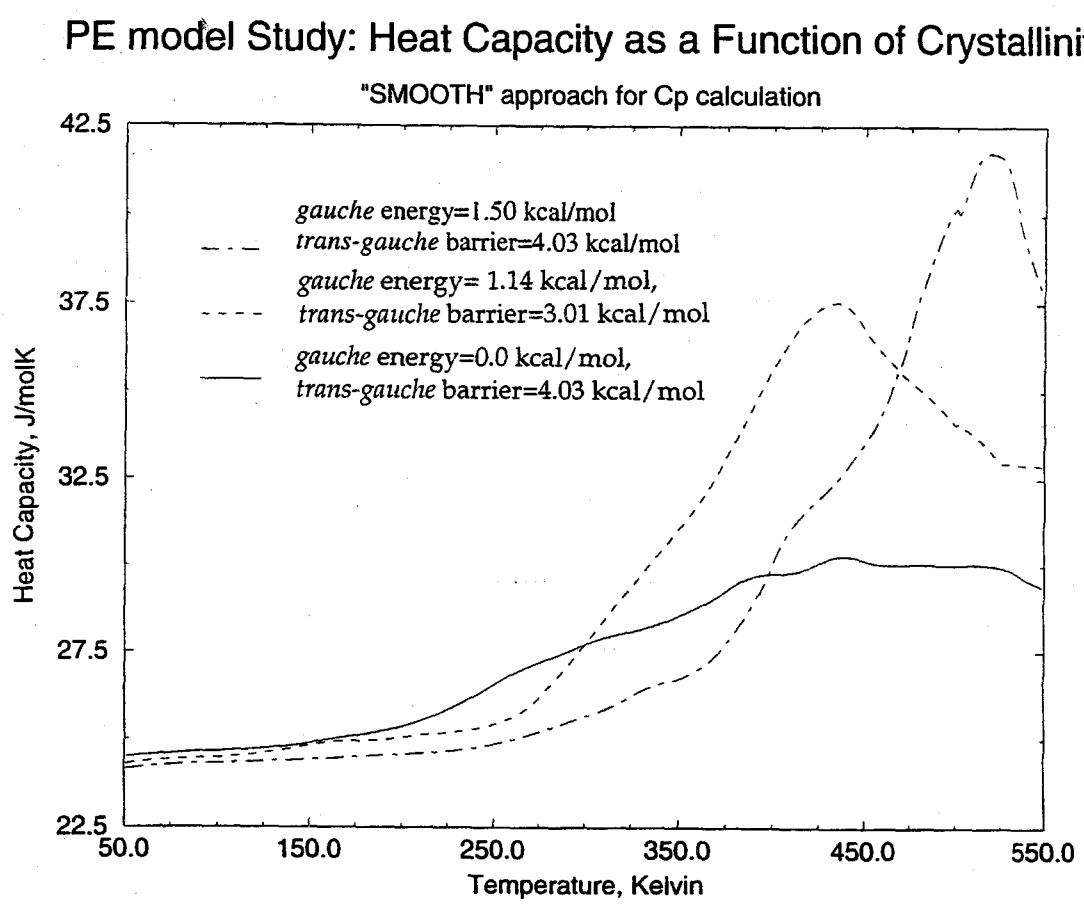

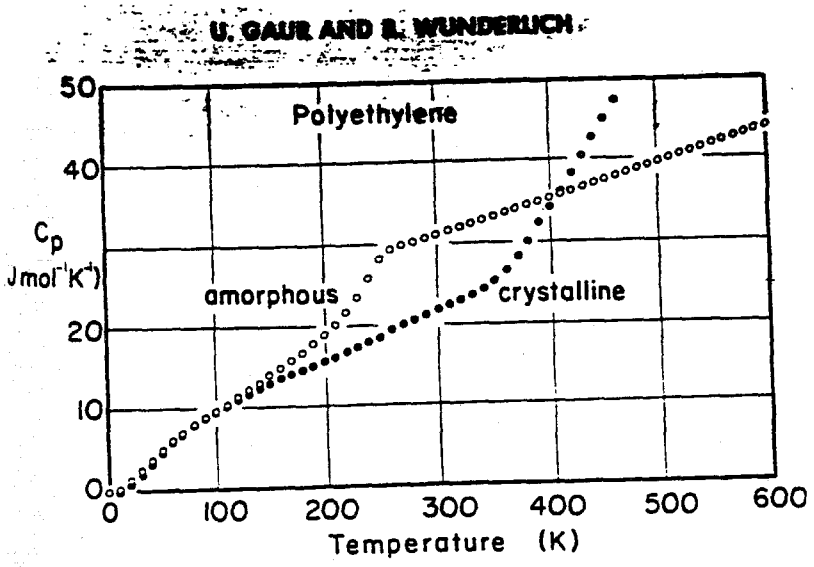

FIGURE 7. Recommended heat capacity data on amorphous and crystalline polyethylene as function of temperature.

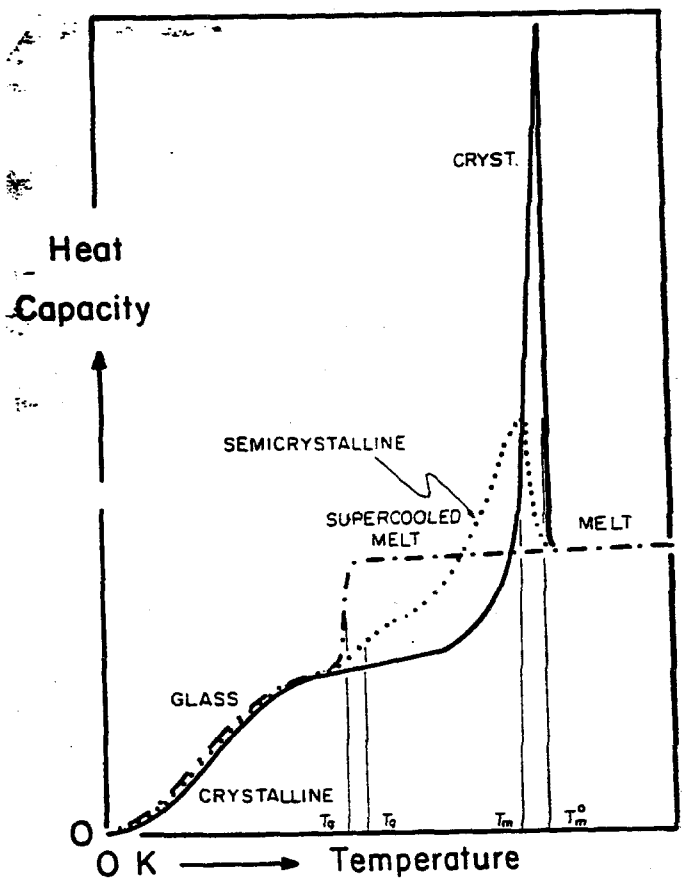

FIGURE 1. Typical schematic plot of the heat capacity vs temperature for linear macromolecules.

References

[1]Krevelen, D. W. Van; *Properties of Polymers: Their Correlation with Chemical Structure; their Numerical Estimation and Prediction from Group Contributions*, Chapter **6**, pg. 129-151 Elsevier Science Publishers, NY (1990)

[2]Kolinski, A.; Skolnick, J.; Yaris, R.; *Journal of Chemical Physics*, **84**(3), 1922-1931 (1986)

[3]Allegra, G.; Bignotti, F.; Gargani, L.; Cociani, M.; *Macromolecules*, **23**(26), 5326-5334 (1990)

[4]Boyd, R. H.; *Trends in Polymer Science*, **4**(1), 12-17 (1996)

[5]Fan, C. F.; Cagin, T.; Shi, W.; Smith, K. A.; *Macromolecular Theory Simulation*, **6**, 83-102 (1997)

[6]Bicerano, J.; *Computational Modeling of Polymers*, Chapter **11**, pg. 521, Marcel Dekker, Inc., NY (1992)

[7]Kuebler, S. C.; Schaefer, D. J.; Boeffel, C.; Pawelzik, U.; Spiess, H. W.; *Macromolecules*, **30**(21), 6597-6609 (1997)

[8]Flores, R.; Perez, J.; *Macromolecules*, **28**(21), 7171-7179 (1995)

[9]Pablo, J. J.; Laso, M.; Suter, U. W.; *Journal of Chemical Physics*, **96**(3), 2395-2403 (1992)

[10]Yamamoto, T.; *Journal of Chemical Physics*, **107**(7), 2653-2663 (1997)

[11]Manika, V.; Wunderlich, B.; *J. Phys. Chem. Ref. Data*, **20**(2), 349-404 (1991)

[12]Wunderlich, B.; Czornyj, G.; *Macromolecules*, **10**(5), 906-913, (1977)

[13]Boyd, R. H.; *Polymer*, **26**, 323-347 (1985)

[13b]page 323

[13c]page 345

[13d]page 343

[14]Boyd, R. H.; *Macromolecules*, **17**(4), 903-911 (1984)

[15]Crissman, J. M., Passaglia, E. J.; *Journal of Applied Physics*, 1971, **42**, 4636 (1971)

[16]Laredo, E.; Suarez, N.; Bello, A.; Marquez, L.; *Journal of Polymer Science: Part B: Polymer Physics*, **34**, 641-648 (1996)

[17]Mark, J. E.; *Physical Properties of Polymers Handbook*, Chapter **13**, pg. 161-175, American Institute of Physics, NY (1996)

[18]Karasawa, N.; Dasgupta, S.; Goddard III, W. A.; *Journal of Physical Chemistry*, **95**(6), 2260-2272 (1991)

[19]Stineman, Russel, W.; *Creative Computing*, July 1989 issue, pages 54-57.

[20]KaleidaGraph™, Synergy Software (PCS inc.), 2457 Perkiomen Avenue, Reading PA 19606, (215) 779-0522.

[21]Spiess, H. W.; Rosenke, K.; Sillescu, H.; *Polymer*, **21**, 757 (1980)

[22]Boyd, R. H.; Gee, R. H.; Jin, H. Y.; *Polymer Preprints*, **35**, 60 (1994)

[23]Rigby, D.; Roe, R. J.; *Journal of Chemical Physics*, **87**(12), 7285-7292 (1987)

Chapter 2

Abstract

The molecular structure of water is very simple, but its bulk properties are not yet completely understood. An approach toward understanding water's anomalous behavior is the development of accurate forcefields that reproduce its bulk properties. Therefore, fixed-charge water potentials are calculated empirically and with *ab initio* methods as describe in this chapter. The conclusion of these studies was that a fixed charge potential may describe water at a given temperature and pressure but fails under different conditions.

Therefore, various polarizable forcefields based on the covalent shell model were developed. One of the modifications of the shell model was a hyperpolarizability correction on the basic quadratic dependence of the energy on the nucleus-electron distance. A further modification was a special treatment of the hydrogen centers where polarization was higher from hydrogen to oxygen along the hydrogen-oxygen vector, and poorest away from oxygen. The last modification is consistent with electronegativity principles. A final modification was an electric shielding between the internal dipoles of the molecule. Parameters of the modified shell model were adjusted based on *ab initio* calculations of classical point charge dipoles interacting with a quantum water monomer. The final forcefield predicted excess three body energies of water trimers in very good agreement with *ab initio* calculations, which strongly suggests that the "many body effects" are *encoded* within a single water monomer.

Development of New Water Potentials from *Ab Initio*

Introduction

Water is one of the most common molecules in the planet. It is one of the fundamental ingredients required for living organisms. As a result, the understanding of water as it relates to the functioning of living matter is of great importance. As a chemical, water determines the structure of biological molecules such as DNA and proteins in what is known as hydrophobic/hydrophilic effects. Therefore the study of the interaction of water with itself and with biological systems is of great interest.

Water Picture: A simple view of how it works

Although water has a very simple structure, its behavior is quite complex due to its ability to form hydrogen bonds, whose nature is not completely understood yet. One way of looking at a hydrogen bond is a simple electrostatic interaction enhanced by water's ability to polarize itself. The counteracting force, which prevents two water molecules from collapsing into each other, is the Pauli repulsion due to the complete electron shell of both molecules as well as charge screening due to a finite distribution of charge. The restraining force may also be called Van der Waals repulsion. The cooperative binding nature of water may be explained as an enhanced polarization due to the favorable global electrostatic field of the other surrounding molecules. Finally, the behavior of bulk water may be explained in a simple way in terms of a conflict of two forces: One in which the water electrostatic field favors the polarization of each molecule to

obtain a larger dipole with an overall enhancement of the global cohesive energy, and a restraining force which is the internal energy cost of reorganizing the quantum wavefunctions in the process of self-polarization away from the molecule's equilibrium polarization value.

Water anomalies

The molecular structure of water is very simple, but the condensed system exhibits very unusual properties. An excellent review book of a compilation of water's experimentally observed anomalies has been recently published[1] as well as a summary article.[2] For example, at 0^0C and 1 atm. pressure, the molar volume of ice is 19.66 cm^3 which is higher than the molar volume of 18.0182 cm^3 for liquid water. Water also exhibits a density maximum at 3.984^0C. When pressure is added to water, its melting point is depressed rather than the observed increase for common liquids. A strange rheological property of water is a decrease in viscosity as pressure is applied to the liquid water below 20^0C and normal pressures. Tentative and reasonable explanations of the anomalies of water have been addressed by Robinson and co-workers.[2] For example, the explanation for the density maximum is attributed to the phenomenon of hydrogen bond bending where in the liquid the hydrogen bonds do not possess the open tetrahedral structure of ice, and the second neighbor shell tightens up in the liquid (higher population at 3.40 A^0). Also, O-H--O hydrogen bond interactions are interpreted as occurring at a narrow angular range. The unusually large heat capacity of liquid water is attributed to the low intermolecular frequencies

(shallow potential energy surfaces) which decrease with increasing temperature in the liquid. In contrast, the more "open" bonding of ice water is stiffer than intermolecular potential in liquid water

Water Potentials for Simulation found in the Literature

Numerous water forcefields for modeling water have appeared in the literature over the past fifteen years. A particular forcefield that was designed to explain water's anomalies has been recently published by Robinson .et. al.[2] where a "double" well potential for the water was based on special Morse off-diagonal oxygen-oxygen, hydrogen-hydrogen and oxygen-hydrogen interactions. Although the "double" well potential is successful at predicting a density maximum at 4°C, little insight is provided regarding the true origin of water's anomalies, which are most likely electrostatic in nature.

Another forcefield reported in the literature is a simple three-site point charge forcefield by Ferguson[3], with a van der Waals center on oxygen and flexible bonds. Special care was taken to make sure that the room temperature properties of water such as density and cohesive energy were reproduced. In order to verify this, a constant pressure canonical simulation on bulk liquid water (267 waters, periodic boundary conditions) was done with the Ferguson forcefield for 50 ps at 300 K and the results were encouraging. The average calculated density was 0.992 g/cc, comparable to the experimental density of water at 25°C. The calculated cohesive energy was 10.93 kcal/mol, in reasonable agreement with experimental heat of vaporization of water at 25 °C (10.48

kcal/mol). The calculated oxygen-oxygen radial distribution function resembles the experimental g(r)[4] as shown in **Figure 1**. The first peak of the calculated oxygen-oxygen g(r) occurs at 2.75 Å with a height of 3.19 while the position for the experimental first peak occurs at 2.875 Å with a height of 3.092. Nevertheless, the overall calculated water structure is in good agreement with experiment. However, one of the major problems of fixed charge models is that they are useful for only a fixed temperature and pressure. Another potential problem is that special polarization effects discussed next, are not taken into account, and therefore interactions of the water molecule with other special polarizable systems like proteins are not accurate. Another potential problem is the lack of treatment of the lone pair charge distribution in three-site models. The simple quantum chemistry explanation for lone pairs in water is the sp^3 electronic structure of oxygen, where the two lone pairs are oriented in a tetrahedral fashion with respect to the hydrogens. Lone pairs may play a major role in hydrogen bond *bending*.

Polarizable Forcefields

The next step in modeling sophistication is an electrostatic polarizable forcefield, which is a better representation of the true nature of water. Numerous reports of polarizable forcefields appear in the literature. For example, Levy *et. al.* developed a water model with dipole based atomic polarizabilities for each atom and a specially adjusted van der Waals term for oxygen.[5] The atom polarizabilities were adjusted to agree with the experimental molecular

polarizability of the water monomer. Several properties of water were reproduced such as the radial distribution functions (oxygen-oxygen and oxygen-hydrogen) and reasonable diffusion coefficients were calculated as well. However, the simulation was conducted at a fixed density of 1.00 g/cc and the equilibrium water dimer oxygen-oxygen distance and binding energy were 2.80 Å and 4.98 kcal/mol respectively compared to the corresponding experimental values of 2.98 Å and -5.40 kcal/mol.[6,7] Therefore, current efforts presented are at best processes of parametrizing semi-empirically forcefields to give the correct water structure at a given density and temperature. A forcefield that truly represents water should reproduce its experimental structure at the dimer level as well as the bulk, at all temperatures and pressures and at the present, such high standards have not been met.

Ab Initio Approach for the Determination of an Effective Constant Charge Potential through an Implicit Solvation Model

Ab initio calculations allow a detailed quantum chemical interpretation of the bonding and physical properties of molecules. In the studies that will be described in this section, the cc-PVTZ (-f) basis set at the all electron level was used. The simplest benchmark test of this *ab initio* method is the gas phase water dimer binding energy curve calculation shown in **Figure 2**. The experimental bond lengths and angle for the water monomer as well as a tetrahedral orientation for the dimer were used in the calculation. The potential energy minimum with basis set superposition error correction (BSSE) was located at an

oxygen-oxygen distance of 2.96 Å with a binding energy of -4.54 kcal/mol. The corresponding experimental values already presented were 2.97 Å and -5.40 kcal/mol respectively, in reasonable agreement with the *ab initio* calculation.

Water Dimer Solvation Studies

In a fixed charge forcefield, it is best to use an effective pair potential that has distance dependence in agreement with *ab initio* values in the bulk system. Practically speaking, it is not yet possible to do a full quantum simulation. In order to circumvent this problem, an effective *ab initio* constant-charge water dimer potential was calculated with a continuum solvent approach. The basic theory behind the solvation approach is the Born equation given by[8]

$$\Delta G_s^0 = -(q^2/2r)(1-1/D) \quad (1)$$

where "r" is the ionic radius, D is the dielectric constant of the solvent, "q" is the partial charge of the ion and ΔG_s^0 is the free energy of transferring an ion from vacuum to a medium of dielectric constant D. The linearized Poisson-Boltzmann equation may be solved for the electrostatic potentials using a finite difference scheme for a molecule, and the resulting solvation energy may be calculated. Friesner et. al. has coupled this solvation procedure to calculate solvation energies of quantum mechanical molecules by a self-consistent method where the wavefunctions are perturbed in order to get an optimum solvation energy[9]. In the mean field "water" solvation process, the atom charges increase due to polarization and this is accompanied by an energetic cost that will be referred to as the quantum reorganization energy. Therefore, the Poisson-Boltzmann

solvation method was used to construct an *ab initio* effective constant charge water dimer potential by quantum mechanically polarizing a water dimer to various extents by varying the solvation radius of the hydrogen atoms while maintaining the oxygen solvation radius fixed at 1.702 A^0 as shown in Scheme 1.

Scheme 1. Water dimer solvation geometry in the Poisson-Boltzmann solvation approach

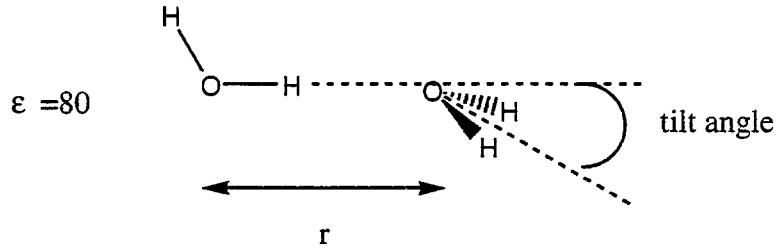

R_O=1.70 Angstroms, R_H=1.0 Angstroms, Q_O=-0.93
R_O=1.70 Angstroms, R_H=1.4 Angstroms, Q_O=-0.90

The oxygen-oxygen distance is r, the OH bond length was 0.9575 Å, the HOH angle was 104.51° and the tilt angle was set to 54.74°. As an example, when the solvation hydrogen radius was set to 1.0 A^0, the average dimer oxygen charge was -0.93 at a 2.80 Å oxygen-oxygen distance. Each average oxygen charge for the monomer and the dimer has a corresponding quantum reorganization energy. The calculations were carried out at the LMP2 level with the cc-PVTZ (-f) basis set to allow for polarization which is important in hydrogen bonded systems. The resulting water monomer curve of quantum reorganized energy vs. oxygen charge is shown in **Figure 3.** (A further application of obtaining the quantum-reorganized energy of a molecule, as a function of charge is the

determination of molecular electronegativities, a topic not discussed further in this section.) The same solvation procedure was done for the water dimer at various oxygen-oxygen distances and the resulting monomer and dimer energies were fit to a cubic polynomial as shown in **Figures 4 & 4b**. Then a dimer binding energy curve based on fixed charges was done, and the effective oxygen-oxygen interaction was calculated by

$$E_{OOVDW}(Q,r)=E_{bind}(Q,r)-E_{coul}(Q,r) \quad (2)$$

where $E_{OOVDW}(Q,r)$ is the effective oxygen-oxygen potential at a fixed charge Q and at an oxygen-oxygen distance r, $E_{bind}(Q,r)$ is the effective distance dependent binding energy derived from the curves in **Figures 4 & 4b**, and $E_{coul}(Q,r)$ is the classical electrostatic interaction of the water dimer with charge Q and oxygen-oxygen distance r. The resulting effective oxygen-oxygen forcefields were fitted to a Morse functional form and are shown in **Figure 5**. The value "m1" refers to the well depth in kcal/mol, the value "m2" refers to the scaling parameter of the Morse function, and the value "m3" refers to the inter-atomic distance in Å. These forcefields were then used to optimize the experimental Ice II crystal structure.

Forcefield Prediction of the Properties of Ice II

Water exists in many different ice forms. However, only a few of them are proton ordered such as the Ice II structure, which forms at a pressure of 2 kbar and a temperature of -60°C. Therefore, the oxygen-oxygen forcefields in **Figure 5** were used to predict various Ice II properties. Starting from the experimental Ice

II structure[10] shown in **Figure 6**, the lattice was minimized fully until the atoms and cell rms force were reduced to 0.001 (kcal/mol)/Å. The Ice II properties predicted by the various forcefields is compared to the experimental properties in Table 1.

Discussion of Results

The predicted densities by the families of oxygen-oxygen forcefields are slightly higher than the experimental value of 1.18 g/cc, but are in reasonable agreement. The lowest binding energy of -16.49 kcal/mol was calculated by the forcefield with an oxygen charge of -0.86 before zero point energy corrections. Note that the calculated binding energy was also corrected for the quantum reorganization energy of charging the monomer from the vacuum charge to a value Q for oxygen. The experimental value for the binding energy is a lattice energy with zero-point energy corrections and it cannot be compared directly with the calculated value. Even so, the calculated binding energy seems reasonable. The calculated bulk modulus for the family of forcefields are all consistently higher than the experimental adiabatic bulk modulus, and monotonically increase as a function of oxygen charge.

Conclusions

A series of *ab initio* fixed charge water dimer oxygen-oxygen forcefields were generated with the aid of the Poisson Boltzmann solvation technique. These forcefields were tested on the proton-ordered Ice II crystal. Reasonable agreement was found with the experimental properties. However, when tested

for bulk water at room temperature (using the effective Morse Potential Corresponding to an oxygen charge of -0.84, **Figure 5**), the results were disappointing. The water structure collapsed into close-packed spheres. The origin of the problem may be that the well depth value for the Morse potential of the order of 1.0 kcal/mol would tend to emphasize a closest-packing sphere arrangement rather than the more subtle electrostatic effects that are very important in water. However, the method developed here may still be useful for developing effective constant charge potentials for organic molecules.

Development of an Empirical Potential for Ice II

Since the *ab initio* derived effective constant charge potential worked for Ice II but not for bulk water, an empirical effective fixed charge forcefield was tuned to reproduce various experimental properties of Ice II with the expectation that it would reproduce liquid water's bulk properties. This time, an exponential-6 non-bond potential (also known as the Buckingham Potential) was used and the well depth (D_0) was fixed to 0.150 kcal/mol, which is the value used in the simple Lennard Jones 3-site model of Ferguson. For the functional forms of the potentials described here, please refer to Mayo .et. al.[11] The exponential-6 parameters were adjusted to give the correct density and bulk modulus of Ice II at 237.65 K and 0.283 GPa as summarized in Table 2. A simple harmonic potential was used for the bond stretch parameter and a cosine harmonic was used for the angle bend term. The parameters were also optimized such that the average bond lengths and angles for a simulation at 237.65 K and 0.283 GPa

resulted in the same values for the Ice II crystal structure. The nonbond exp-6 scaling parameter was adjusted such that the bulk modulus for the model Ice II system at 0 K at a density of 1.19 g/cc equaled the experimental value of 13.89 GPa. The final result was a predicted bulk modulus of 14.0 GPa at a density of 1.19 g/cc for the model system. Molecular dynamics were done on the Ice II system with the empirical forcefield at a temperature and pressure of 237.65 K and 0.283 GPa and the predicted values for various properties agreed favorably with experiment. The experimental lattice parameters under the same conditions are 7.76Å for *a*, *b* and *c* and the cell angle parameters α,β and γ, are 113.1°. The corresponding predicted values for the cell parameters for the last snapshot of the molecular dynamics trajectory for *a*, *b* and *c* were 7.96, 7.48 and 7.51 Å respectively and the predicted values for α, β, and γ were 112.4°, 113.7° and 111.9° respectively, in very good agreement with experiment. The average density for the trajectory at 237.65 K and 0.283 GPa was 1.195 g/cc, in excellent agreement with the experimental value of 1.189 g/cc. The experimental OH stretching frequency is 3194 cm^{-1} (Raman) and 3280 cm^{-1} (IR) and the predicted OH stretching frequency ranged from 3200.5 cm^{-1} to 3336.3 cm^{-1} from a 0 K vibrational analysis.[12] The experimental HOH bending (angle) is 1690 cm^{-1} (IR) and the calculated value ranges from 1692 cm^{-1} to 1826.3 cm^{-1}. The overall Ice II crystal oxygen-oxygen radial distribution function compares with the O-O g(r) for the experimental Ice II structure as shown in **Figure 7**. Therefore, relative agreement

was obtained between the physical properties predicted by the empirical forcefield for Ice II and the experimentally measured values.

Liquid Water Properties Predicted by the Ice II Empirical Forcefield

The empirical Ice II forcefield was used in a constant pressure molecular dynamics simulation of bulk water at 300 K. A total of 267 water molecules in the unit cell were used and the duration of the simulation was 50 ps. The results were discouraging. The oxygen-oxygen g(r) predicted by the empirical forcefield is compared with the experimental g(r) as well as the g(r) predicted by the Ferguson water model as shown in **Figure 8**. The position for the first peak predicted by the empirical model is in agreement with the experiment but the second neighbor shell structure is virtually non-existent for the empirical forcefield. A comparison of the water dimer translational behavior in solution between the well-behaved Ferguson model and the empirical model is shown in **Figure 9**. The water dimer proximity in solution is much smaller for a given time with the Ferguson model compared to the empirical model. Additionally, the separation of the water dimer in the Ferguson model occurs roughly in a step-wise fashion, which suggests that there are well-defined water shell structures. In contrast, the water dimer distance separation with the empirical model occurs in a linear fashion with respect to time. A tentative explanation for this discrepancy is that the scaling parameter of 17.0 used in the exp-6 fit has a much stiffer inner wall than the Lennard Jones function with an effective scaling parameter of 12.0. Therefore, in a collision, two molecules with a harder inner

wall will bounce inelastically more so than two molecules with a relatively softer inner wall.

Therefore, if one uses a fixed charge forcefield and adjusts the other valence and van der Waals parameters to fit a given phase of water such as Ice II at 237.65 K and 0.283 GPa, then the properties of another phase of water at a different temperature and pressure such as liquid water at 1 atmosphere and 300 K will not be reproduced accurately.

Comparison of Ab Initio Studies on the Chair Water Hexamer found on Ice II with a Fixed Charge Model

Several *ab initio* studies on the chair form of the water hexamer found in the Ice II structure was done for comparison with a fixed charge model. The molecular structure of the Ice II chair of the S6 symmetry is shown in **Figure 10**. A calculation of the binding energy of the Ice II chair was done at the all electron LMP2 level with the cc-PVTZ (-f) basis set as a function of the collective oxygen-oxygen distance. The *ab initio* and the empirical Ice II forcefield results are shown in **Figure 11**. The shape of the repulsive inner wall potential for both the *ab initio* and the empirical forcefield calculation agree. This should not come as a surprise since the exp-6 parameter for the empirical forcefield was tuned to match the experimental bulk modulus at relatively high-pressures (0.283 GPa). However, the empirical forcefield has a sharper curvature near the minimum. It is also interesting to note that the *ab initio* minimum energy for the chair structure occurs near 2.80 Å, which agrees with the experimental value of 2.78 Å

for the crystal structure. In contrast, the oxygen-oxygen distance for a water dimer is 2.98 Å. This clearly shows how the cooperative nature of water changes its behavior.

The torsional dependence of the hydrogen bond chair energy was also explored with the previously described *ab initio* method. In this study, the oxygen-oxygen distance was fixed at 2.80 Å, the internal hydrogen bonding within the "six membered" ring was conserved, and the collective torsional angle rendered with spheres in **Figure 10** was used as the variable. The potential energy surfaces calculated with *ab initio* and with a fixed charge on oxygen of -0.89 are shown in **Figure 12.** The *ab initio* potential energy curve had two minima at 140.5° and -111.0° and a saddle point at 200°. In contrast, the fixed charge model results in a featureless potential energy surface with shallow minimum at around -140°. The conclusion is that a fixed charge model does not reproduce the complex potential energy surface created by water's polarizable nature.

Design of a Polarizable Water Model

The evidence previously presented clearly suggests the need to include polarization in water. Therefore, a polarizable water forcefield based on the covalent shell model[13] was designed. The covalent shell model is based on atom-based dipoles where a nucleus with charge of +1 is linked to an electron with charge -1 with a simple harmonic spring. The energy expression is given by

$$\delta E = 0.50 * K_s (\delta R)^2 \quad (3)$$

$$\alpha_s = 332.07 * Z^2 / K_s \quad (4)$$

where K_s is the spring force constant, δR is the displacement of the electron away from the nucleus, Z is the charge of the electron, and α_s is the atomic polarizability. It is useful to define the reorganization energy of this model as the internal energy it costs the molecule to respond to an external field. In the original shell model, there are two components to the reorganization energy. The first component is the internal dipole-dipole electrostatic interactions and the second part is the harmonic spring energy. The general advantage of the covalent shell model is its higher degrees of freedom of charge distribution that allows it to better represent a polarizable system. A second advantage of the shell model is its ability to have local dipolar charge directionality and ability to adjust locally to the electric fields of other molecules. A third advantage of the shell model is that it allows an interpretation of the quantum results within a simple classical picture. However, the shell model has some disadvantages. First, the shell model assumes that the energy dependence of the shell-electron separation has a simple harmonic dependence which is reasonable as long as the electric field is small enough. The shell model is not valid for high local electric fields, a situation that may occur when two molecules are in close proximity. Therefore, a revised covalent shell model was developed. In the revised shell model, the energy dependence of the spring extension has the form

$$E=0.50K_sR^2(1+\exp(\alpha(R-R_0)/R_0)) \qquad (5)$$

Where R is the shell-electron distance, α is a scaling constant not to be confused with the polarizability, and R_0 is a constant of the order of 0.10 Å. When R is

much smaller than R_0, the function behaves harmonically, but as $R>R_0$ the spring stiffens exponentially. This function prevents the spring from overextending in the presence of large electric fields and may describe correctly hyperpolarizability effects.

Forcefield Tuning Method for the Isotropic Revised Covalent Shell Model: The "DIELINT2 HP Forcefield"

A water model was constructed based on Equation 5. The basic monomer geometry was OH bond lengths of 0.9572 Å and an HOH bond angle of 104.52^0, which is the gas phase geometry of a water monomer. Two lone pairs in the form of permanent charges of -0.049 displaced 1.00 Å from oxygen were used in the water model while conserving electroneutrality and a permanent monomer dipole moment of 1.93 Debye, which was calculated at the LMP2 level with the cc-PVTZ (-f) basis set. The plane created by the "lone pairs" and oxygen was orthogonal to the plane containing the two hydrogens and oxygen. The optimization of the revised shell parameters as well as the lone pair geometry was based on four types of of *ab initio* calculations involving dipole point charges interacting with a quantum water monomer as shown in **Figure 13**. The first test was a dipole sweep along the lone pair plane of the quantum monomer. The distance between the positive center of the dipole and the oxygen center was 1.9428 Å. The quantum result for the lone pair dipole sweep is compared to the "DIELINT2" forcefield result in **Figure 14**. The forcefield agreement with the quantum result is excellent with the exceptions of the very wide angles above 95^0.

The second test was a dipole sweep of the hydrogens along the HOH plane of the quantum water monomer. The distance between the negative center of the dipole and the oxygen center was 2.90 Å. The quantum result for the hydrogen sweep is compared to the "DIELINT2" prediction in **Figure 15**. Again, the forcefield agreement with the quantum result is excellent over most angles. The third test was a dipole approach towards oxygen along the HOH bisector as shown in **Figure 13**. The quantum result is compared to the "DIELINT2" prediction in **Figure 16**. The forcefield agreement with the quantum result is good over most distances except at close distances. This is probably due to the fact that in the quantum system there is charge shielding due to the finite electron cloud distribution in oxygen while in the "DIELINT2" classical model the charges are localized. The fourth and final test was a dipole approach to hydrogen along the HO vector. This time, agreement with the quantum calculations is excellent over most distances between the dipole and the hydrogen as shown in **Figure 17**. This means that the hydrogens in water may be described accurately in terms of classical polarizable forcefields.

Excess Three Body Energy Test of the DIELINT2 Forcefield

The "DIELINT2" forcefield generally reproduced the electrostatic responses of a quantum water monomer to point dipole tests. However, in order to test for water cooperativity effects of the DIELINT2 forcefield, excess three body energies of various water trimers were compared to quantum results.

The excess three-body energy for a water trimer is defined as

$E_{xs} = E_{trimer} - E_{12} - E_{13} - E_{23}$ (6)

where E_{trimer} is the Hartree Fock binding energy of a trimer, E_{12} is the binding energy of the dimer with monomers 1 and 2, E_{13} is the binding energy of the dimer with monomers 1 and 3, and E_{23} is the binding energy of the dimer with monomers 2 and 3. A total of fifty-seven different water monomer configurations were used in the test. The configurations of the trimers were generated by molecular dynamics with the forcefield TIP4P. Dr. Dan Mainz, a member of the Goddard group, provided the Hartree Fock level quantum energy calculations.

The excess three body energies predicted by the DIELINT2 forcefield were graphed against the quantum results in **Figure 18.** The agreement between the predictions of the DIELINT2 forcefield with quantum are qualitatively acceptable with the exception of four geometries where the forcefield predicts much more positive excess three body energies than quantum. These geometries have in common a trimer geometry where each hydrogen of the central water monomer points to the oxygen of a unique water monomer. Therefore, a test was devised where the energy of the interaction of two point dipoles interacting with each hydrogen of a water monomer was compared to the energy of interaction of a point charge dipole with one hydrogen of a water monomer as shown in **Figure 19.**

A new "excess" binding energy may be defined as

$E_{xsdip} = E_{bind\text{-}2dipoles} - 2E_{bind\text{-}1dipole}$ (7)

where $E_{bind\text{-}2dipoles}$ is the binding energy between a water monomer and two dipoles as shown in the left of **Figure 19**, and $E_{bind\text{-}1dipole}$ is the binding energy between a water monomer and one dipole as shown in the right of **Figure 19.** The quantum value for E_{xsdip} was +0.25 kcal/mol while the DIELINT2 forcefield prediction resulted in a value of +1.50 kcal/mol. The results for the dipole test are consistent with the actual trimer molecule calculations. The tentative explanation of why the DIELINT2 model over-predicts the excess three body energy may lie in the way the shells are oriented when a single dipole interacts with a water monomer as shown in the right hand side in Scheme 2. The hydrogen electron that is not interacting with the dipole is polarized into the vacuum, which is not very physical because electron density should flow from the hydrogen towards the oxygen according to electronegativity principles. Based on this observation, a new forcefield was devised where the polarization of the electron in hydrogen is dependent on its orientation, and reaches a maximum when it is displaced toward oxygen along the HO bond vector. Additionally, the polarization of oxygen was "split" into three components to allow for anisotropic polarization. This new forcefield is described in the next section.

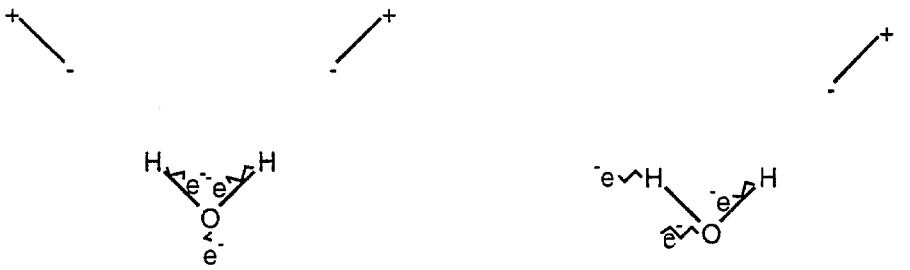

electron-shell configuration
in the presence of two dipoles

electron-shell configuration
in the presence of one dipole

Scheme 2. Depiction of the electrons-shell configuration in the presence of two dipoles and the presence of one dipole.

Introduction of Hydrogen Polarizability Anisotropy to the Revised Covalent Shell Model as Well as a Three-component Oxygen Polarizability

The shortcoming of the revised covalent shell model was an unphysical polarizability when one dipole (or one molecule) interacts favorably with one hydrogen along the HO vector as shown in Scheme 2. A more physical behavior would require the electron density on hydrogen to polarize much more favorable towards oxygen than any other direction. A proposed anisotropic covalent shell model for hydrogen is

$$E_{Hanis} = (K_1 + K_2\cos(\theta))R^2(1 + \exp(\alpha(R-R_0)/R_0)) \quad (8)$$

where E_{Hanis} is the energy dependence of the spring attaching the electron to the nucleus of hydrogen, and θ is the angle between the nucleus-electron vector and the hydrogen-oxygen vector. K_1 is a positive number and K_2 is usually a negative number whose magnitude is smaller than K_1. This means that the largest polarizability or conversely, the smallest force constant occurs when the nucleus-electron vector on the hydrogen atom is at 0^0 with respect to the HO bond vector.

The lowest polarizability of the hydrogen electron occurs when the nucleus-electron vector is pointing at 180^0 away from the HO vector. Therefore, the behavior of the shell-electron described in Equation 8 is at least qualitatively correct in terms of electronegativity principles, where charge transfer from hydrogen to oxygen occurs much better than charge transfer in any other direction in space.

Similarly, the polarizability of oxygen was allowed to be different along each of three axes. The first axis, which runs along the HOH bisector, is defined as the x-axis. The hydrogen-hydrogen vector defines the y-axis and the z-axis is defined by the cross product of the x-axis and y-axis vector. Therefore, the energy dependence of the electron "spring" of oxygen is given by

$$E_x=0.50K_xX^2(1+\exp(\alpha(X-R_0)/R_0)) \qquad (9)$$

$$E_y=0.50K_yY^2(1+\exp(\alpha(Y-R_0)/R_0)) \qquad (10)$$

$$E_z=0.50K_zZ^2(1+\exp(\alpha(Z-R_0)/R_0)) \qquad (11)$$

where X, Y and Z refer to the components of the nucleus-electron vector components and K_x, K_y, and K_z refer to the force constants along each orthogonal direction. Therefore, the polarizability of oxygen is isotropic only if K_x, K_y and K_z are identical.

Determination of the Forcefield Parameters for the Revised Shell Model with Anisotropic Hydrogen Polarizability

A series of five test cases shown in **Figure 19** were developed to fit the polarizability parameters of hydrogen (Equation 8) and oxygen (Equations 9-11). The test dipole on oxygen is a "stick" with charges of +0.395 and -0.395 separated by 1.1718 Å and the distance from oxygen to the positive center on the dipole is 1.9428 Å. Similarly, the test dipole on hydrogen is a "stick" with charges of -0.790 and +0.790 separated by 0.5859 Å, and the distance from hydrogen to the negative center on the dipole is 1.9428 Å. The orientation of the test dipoles in the oxygen side is tetrahedral. The classical dipoles only interact with the water monomer and not with themselves. In this water model, "lone pairs" with the same charge and configuration as the DIELINT2 forcefield were used. Finally, the potential energy of the nucleus-electron vector was minimized by an orientation along the external electric field lines, and therefore, angular forces on the dipole vectors were not taken into account in the minimization.

The best fit parameters for the revised shell model with anisotropic polarizability for hydrogen were 1450 kcal/mol/Å^2 for K_1, -300 kcal/mol/Å^2 for K_2, 0.0800 Å for R_0, and 5.00 for α. The best fit parameters for oxygen polarizability along the "x-axis" (Equations 9-11) were 800 kcal/mol/Å^2 for K_x, 0.17 Å for R_0, and 5.00 for α. The best fit parameters for oxygen polarizability along the "y-axis" and "z-axes" were 720 kcal/mol/Å^2 for both K_y and K_z. The

forcefield prediction values for the five-dipole test cases as well as the quantum results are shown in Table 3.

The forcefield dipole test agreement with quantum was marginal with a RMS (root mean square) deviation from quantum for the test cases 1-4 of 0.545 kcal/mol. Case number five was not included in the RMS calculation since its result was not very sensitive to the choice of forcefield parameters. Test case number one is especially problematic, with a forcefield predicted energy difference of 1.242 kcal/mol versus a quantum energy difference of 0.246 kcal/mol (see **Figure 19**).

The predicted trimer excess three body energies (Equation 6) by the forcefield are compared to the quantum results in **Figure 20**. The overall RMS difference between the fifty seven excess three body energies calculated by quantum versus the values calculated by the forcefield was 0.238 kcal/mol. Although the overall agreement between the quantum and forcefield result was good, there is still room for improvement for the trimer configuration where a central water molecule is a hydrogen bond donor to two water molecules. The problem trimer geometry is analogous to test 1 in **Figure 19.**

Redesign of the Revised Shell Model with Anisotropic Hydrogen Polarizability, Isotropic Oxygen Polarizability and a High internal Dielectric

A new shell model was developed with anisotropic hydrogen shell polarizability (Equation 8), isotropic oxygen polarizability (Equation 5) and an internal dielectric of 1000.0 for interactions between atomic dipoles within the same molecule. The best-fit polarizability parameters for hydrogen were 550 kcal/mol/Å^2 for K_1, -400 kcal/mol/Å^2 for K_2, and 0.0650 Å for R_0 and 5.00 for α. The best fit isotropic polarizability parameters for oxygen were 380 kcal/mol/Å^2 for K_s, 0.12 Å for R_0 and 5.00 for α. The forcefield prediction values for the five dipole test cases as well as the quantum results are shown in Table 4.

The predicted trimer excess three body energies (Equation 6) by the forcefield are compared to the quantum results in **Figure 21**. The overall RMS difference between the fifty seven excess three body energies calculated by quantum versus the values calculated by the forcefield was 0.1477 kcal/mol. The overall agreement of the forcefield trimer result with quantum is excellent for all geometries. Therefore, it may be concluded that the dipole tests in **Figure 19** are sensitive to the behavior of the water monomer and may be useful in "extracting" many body effects from a single quantum molecule. However, the ultimate test of the newly developed potential is bulk water.

Alternative Water Forcefields of the Future: The Charge Equilibration (QEq)-Covalent Shell Model Hybrid System

A successful water forcefield must reproduce the quantum behavior of water. There may be multiple water potential forms that reproduce the key aspects of the electrostatic behavior of water. A strongly recommended new approach for treating water is to combine the charge equilibration approach[24] with a shell model on oxygen only. The charge equilibration approach is based on electronegativity and the principle that charge must flow from hydrogen to oxygen is readily enforced. However, the shell model on oxygen takes care of positive excess two body energy effects such as the one represented in test 2 in **Figure 19.**

Conclusion of the Investigation of the Nature of Water

Valuable lessons have been learned from the electrostatic studies on water described in this chapter. The first lesson is that a fixed charge forcefield will never be able to describe the physical properties of water at all temperatures and pressures. The second lesson is that the shell model with a harmonic dependence on the energy of the nucleus-electron spring fails at relatively high electric field and as a result, a new energy function was introduced that overcomes this problem. The third observation is that isotropic polarization for each atomic dipole does not adequately describe three body effects involving a central water molecule donating a hydrogen bond to two water molecules with

oxygen acceptors. This problem was corrected by introducing an anisotropic polarizability for each hydrogen, retention of isotropic polarizability on oxygen, and a special high internal dielectric for the internal dipole-dipole interactions. The modified forcefield gives five key insights on the way a quantum water monomer works. The first insight is that charge transfer between hydrogen and oxygen occurs mainly from hydrogen to oxygen along the hydrogen-oxygen bond vector. The second key insight is that the charge transfer from hydrogen to oxygen is decoupled from the polarization of oxygen. This observation was made possible by the fact that the best forcefield had internal dielectric screening of the internal dipoles in the water monomer. The third key insight is that polarization in the oxygen atom is isotropic. The fourth key insight is that "lone pairs" may be represented by small, non-polarizable point charges displaced from oxygen in a tetrahedral orientation. The final insight is that the properties leading to the cooperative behavior of water may be "encoded" within a single water monomer.

Software and Methods

The Pseudo Spectral General Valence Bond (PSGBV) version 2.35 software was used for all quantum chemical calculations.

Table 1. Properties of Ice II predicted by the Self-Consistent Fixed Charge *Ab Initio* Forcefields

Oxygen charge Forcefield(Q)	Crystal density, g/cc	Binding energy* kcal/mol	Bulk Modulus GPa
-0.800	1.18	-15.44	16.3
-0.820	1.19	-15.91	17.2
-0.840	1.20	-16.30	18.3
-0.860	1.20	-16.49	19.7
-0.880	1.21	-16.41	21.1
-0.900	1.22	-16.00	22.7
Exp.	1.18**	-16.20***	13.89****

*Zero point energy was not taken into account in the calculated binding energy.
**Kamb, B.; Hamilton, W. C.; LaPlaca, S. J.; Prakash, A.; *J. Chem Phys.*, 55(4), p. 1934. 1971
***Townsend, M.; Rice, S. A.; *J. Chem. Phys.* 79(5), p. 2496, 1983; value is lattice energy.
****Clouter, M. J.; Kiefte, H.; Gagnon; R. E.; *J. Chem. Phys.* 92(3), 1909,1990; Adiabatic modulus was measured at 0.283 GPa.

Table 2. Empirical best-fit forcefield parameters for the Ice II structure at 237.65 K and 0.283 GPa.

Forcefield Type	**Parameter 1**	**Parameter 2**	**Parameter 3**
	Ro	Do	Scaling parameter
	Angstroms	kcal/mol	
Oxygen *exp-6*	*3.46*	*0.150*	*17.00*
	Ro	Force constant	
OH	Angstroms	Kcal/mol/Angst.	
bond *harmonic*	*0.934*	*880.00*	
HOH angle term	Equilibrium angle	Force constant	
Cosine	Degrees	Kcal/mol/radian	
Harmonic	*109.7*	*90.00*	

Table 3. Comparison of forcefield dipole tests on classical water monomer with results of quantum water monomer (LMP2, cc-PTZ (-f)) dipole tests.

Test Case number	Quantum Energy Kcal/mol	Forcefield Energy kcal/mol
1	0.246	1.242
2	0.053	-0.281
3	-0.627	-0.348
4	-0.319	-0.226
5	*-27.79*	*-27.11*
	RMS cases 1-4:	0.54534 kcal/mol

Table 4. Comparison of forcefield dipole tests on classical water monomer with results of quantum water monomer (LMP2, cc-PTZ (-f)) dipole tests. The forcefield included a molecular internal dielectric of 1000.0.

Test Case number	Quantum Energy Kcal/mol	Forcefield Energy kcal/mol
1	0.246	0.565
2	0.053	0.126
3	-0.627	-0.579
4	-0.319	-0.376
5	-27.79	-27.86
	RMS cases 1-4:	0.1678 kcal/mol

Figure 1

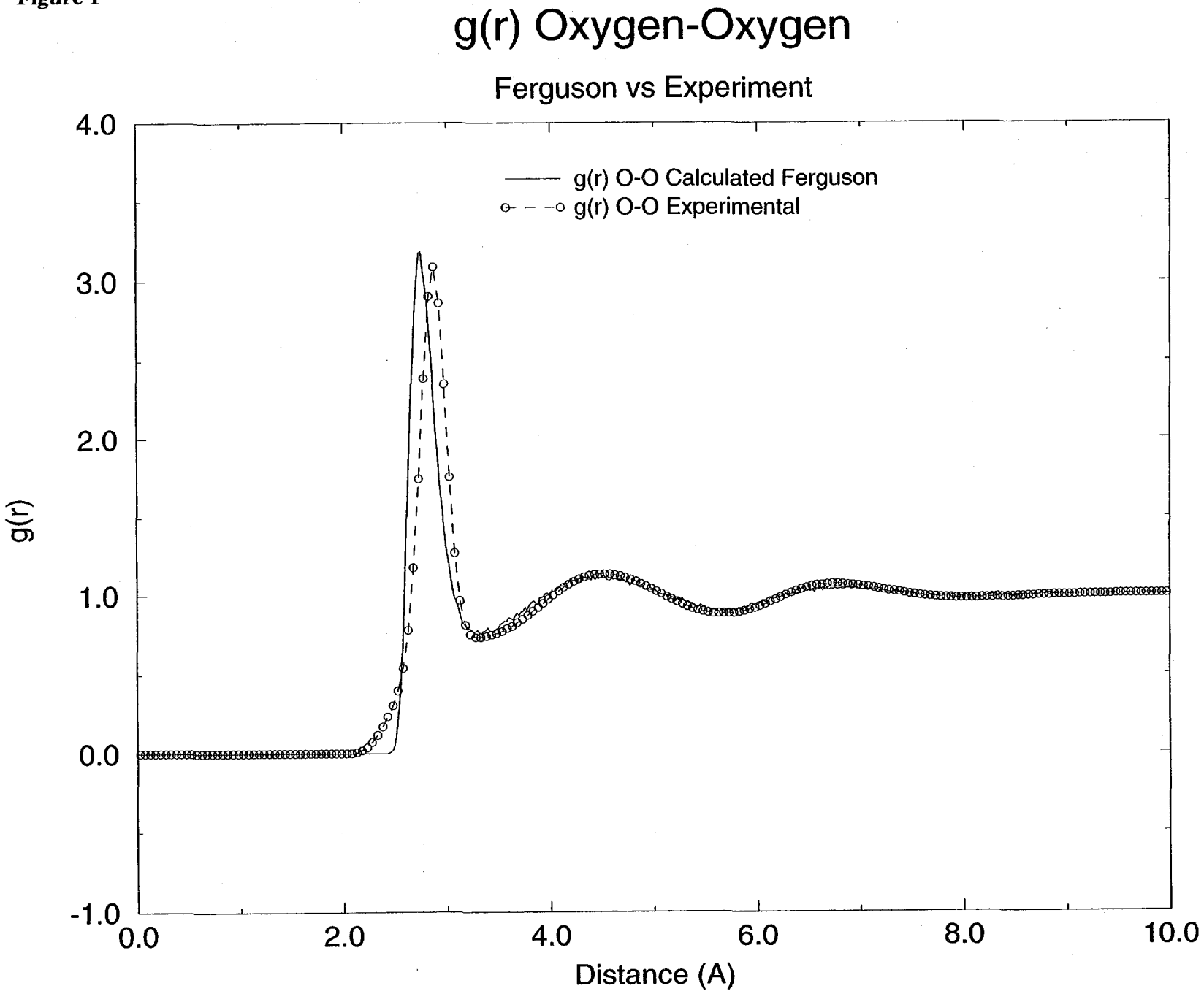
g(r) Oxygen-Oxygen
Ferguson vs Experiment
g(r) O-O Calculated Ferguson
g(r) O-O Experimental
g(r)
Distance (A)
4.0
3.0
2.0
1.0
0.0
-1.0
0.0
2.0
4.0
6.0
8.0
10.0

Figure 2

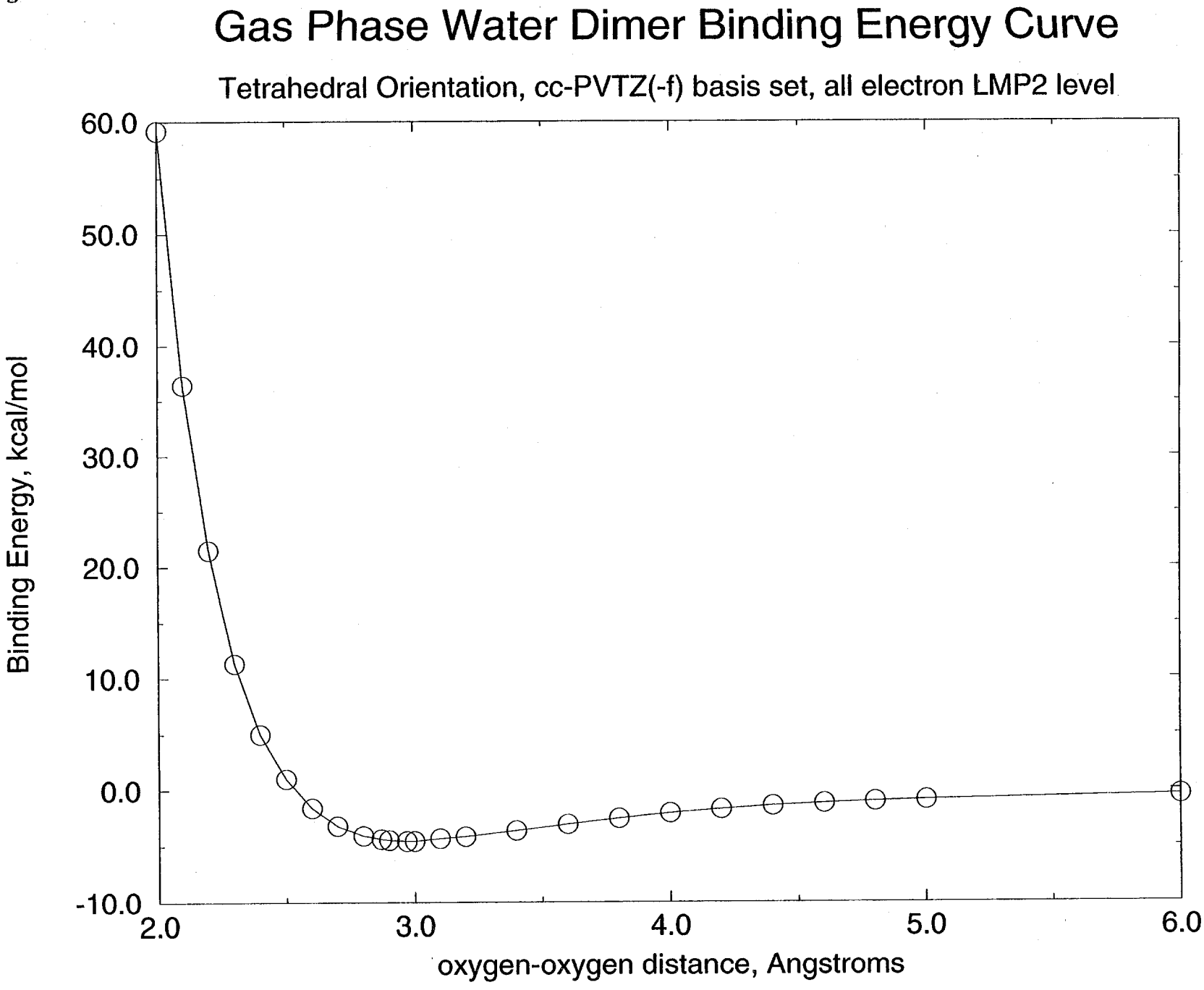
Gas Phase Water Dimer Binding Energy Curve
Tetrahedral Orientation, cc-PVTZ(-f) basis set, all electron LMP2 level
Binding Energy, kcal/mol
60.0
50.0
40.0
30.0
20.0
10.0
0.0
-10.0
2.0
3.0
4.0
5.0
6.0
oxygen-oxygen distance, Angstroms

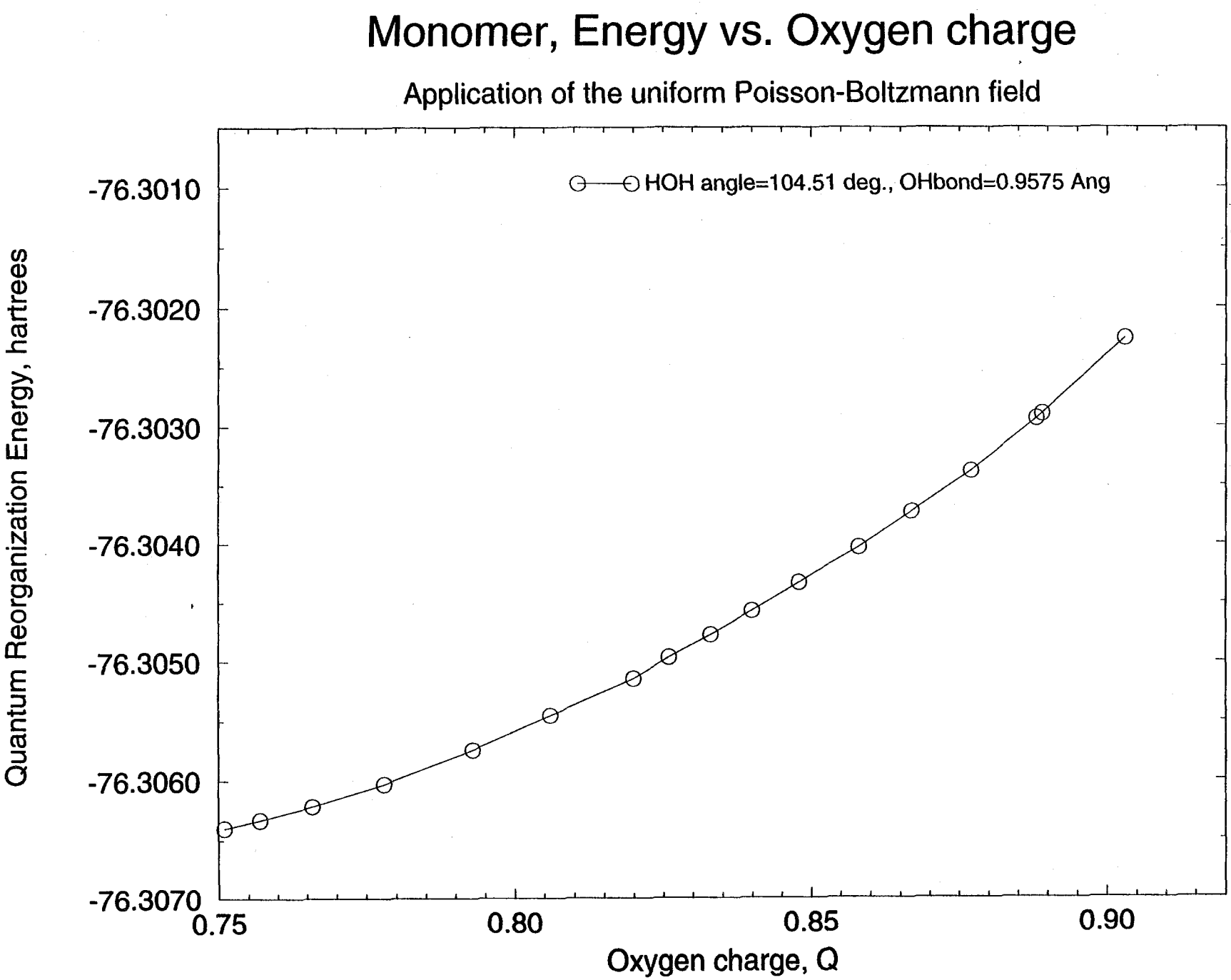
Monomer, Energy vs. Oxygen charge
Application of the uniform Poisson-Boltzmann field
HOH angle=104.51 deg., OHbond=0.9575 Ang
Quantum Reorganization Energy, hartrees
-76.3010
-76.3020
-76.3030
-76.3040
-76.3050
-76.3060
-76.3070
0.75
0.80
0.85
0.90
Oxygen charge, Q

Figure 4

Figure 4

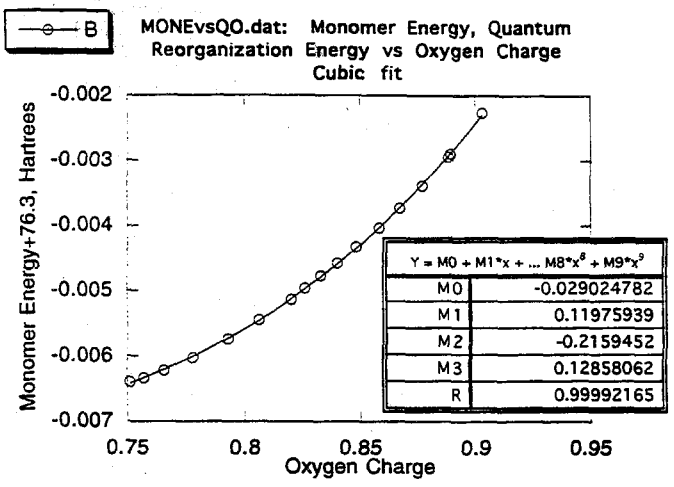
B
MONEvsQO.dat: Monomer Energy, Quantum Reorganization Energy vs Oxygen Charge Cubic fit
Monomer Energy+76.3, Hartrees
Oxygen Charge
Y = M0 + M1*x + ... M8*x^8 + M9*x^9
M0 -0.029024782
M1 0.11975939
M2 -0.2159452
M3 0.12858062
R 0.99992165

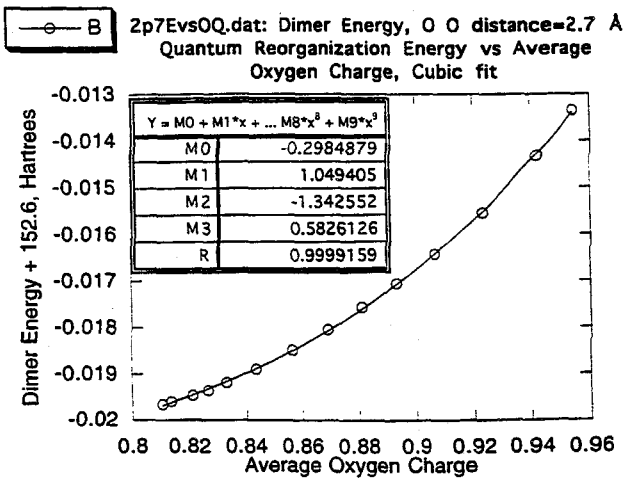
B
2p7EvsOQ.dat: Dimer Energy, O O distance=2.7 Å Quantum Reorganization Energy vs Average Oxygen Charge, Cubic fit
Dimer Energy + 152.6, Hartrees
Average Oxygen Charge
Y = M0 + M1*x + ... M8*x^8 + M9*x^9
M0 -0.2984879
M1 1.049405
M2 -1.342552
M3 0.5826126
R 0.9999159

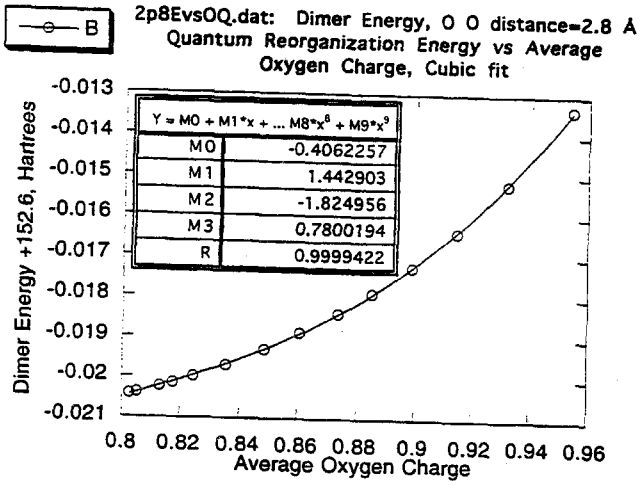
B
2p8EvsOQ.dat: Dimer Energy, O O distance=2.8 Å Quantum Reorganization Energy vs Average Oxygen Charge, Cubic fit
Dimer Energy +152.6, Hartrees
Average Oxygen Charge
Y = M0 + M1*x + ... M8*x^8 + M9*x^9
M0 -0.4062257
M1 1.442903
M2 -1.824956
M3 0.7800194
R 0.9999422

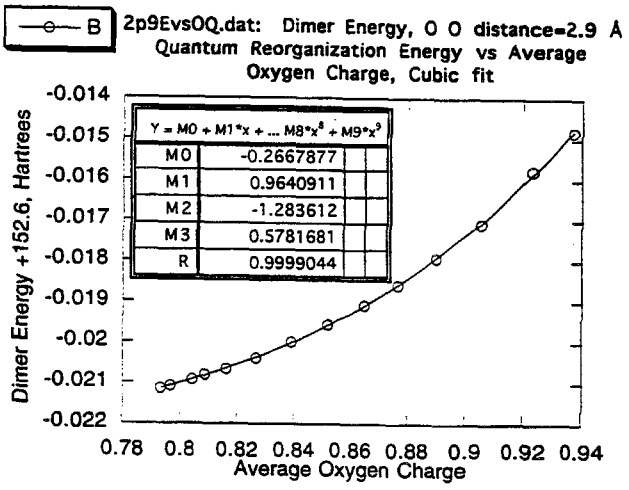
B
2p9EvsOQ.dat: Dimer Energy, O O distance=2.9 Å Quantum Reorganization Energy vs Average Oxygen Charge, Cubic fit
Dimer Energy +152.6, Hartrees
Average Oxygen Charge
Y = M0 + M1*x + ... M8*x^8 + M9*x^9
M0 -0.2667877
M1 0.9640911
M2 -1.283612
M3 0.5781681
R 0.9999044

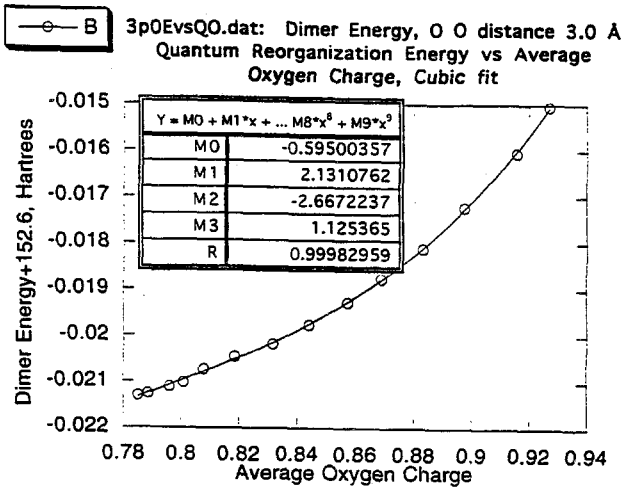
B
3p0EvsQO.dat: Dimer Energy, O O distance 3.0 Å Quantum Reorganization Energy vs Average Oxygen Charge, Cubic fit
Dimer Energy+152.6, Hartrees
Average Oxygen Charge
Y = M0 + M1*x + ... M8*x^8 + M9*x^9
M0 -0.59500357
M1 2.1310762
M2 -2.6672237
M3 1.125365
R 0.99982959

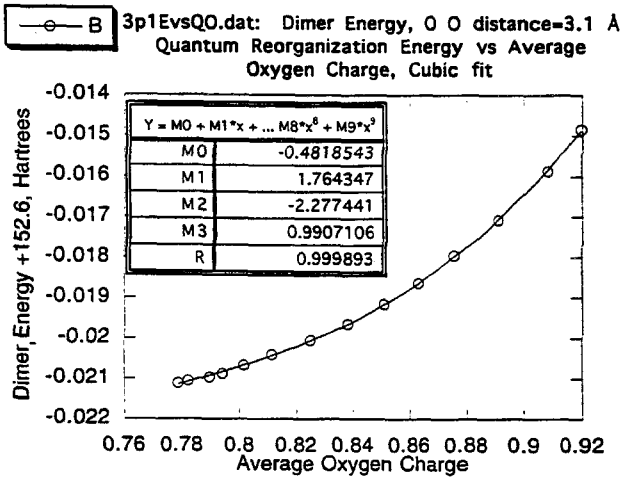
B
3p1EvsQO.dat: Dimer Energy, O O distance=3.1 Å Quantum Reorganization Energy vs Average Oxygen Charge, Cubic fit
Dimer Energy +152.6, Hartrees
Average Oxygen Charge
Y = M0 + M1*x + ... M8*x^8 + M9*x^9
M0 -0.4818543
M1 1.764347
M2 -2.277441
M3 0.9907106
R 0.999893

Figure 4b

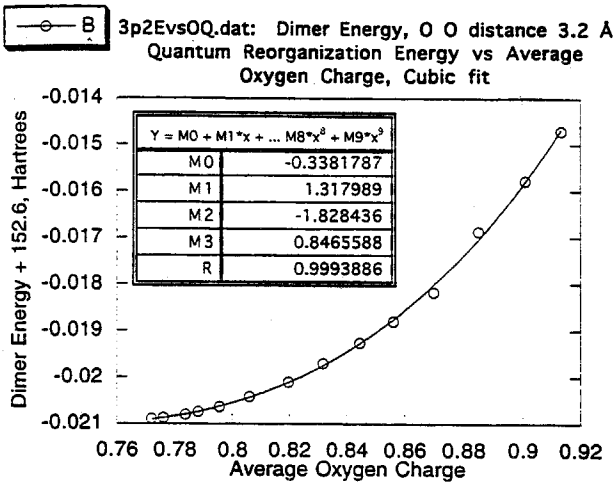
B
3p2EvsOQ.dat: Dimer Energy, O O distance 3.2 Å
Quantum Reorganization Energy vs Average
Oxygen Charge, Cubic fit
Y = M0 + M1*x + ... M8*x^8 + M9*x^9
M0 -0.3381787
M1 1.317989
M2 -1.828436
M3 0.8465588
R 0.9993886
Dimer Energy + 152.6, Hartrees
-0.014
-0.015
-0.016
-0.017
-0.018
-0.019
-0.02
-0.021
0.76 0.78 0.8 0.82 0.84 0.86 0.88 0.9 0.92
Average Oxygen Charge

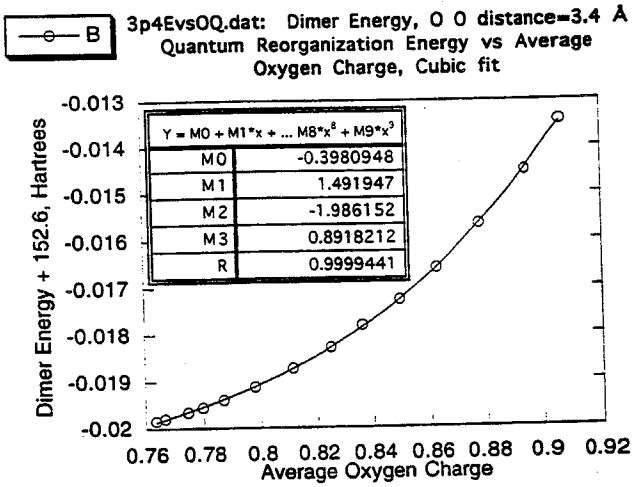
B
3p4EvsOQ.dat: Dimer Energy, O O distance=3.4 Å
Quantum Reorganization Energy vs Average
Oxygen Charge, Cubic fit
Y = M0 + M1*x + ... M8*x^8 + M9*x^9
M0 -0.3980948
M1 1.491947
M2 -1.986152
M3 0.8918212
R 0.9999441
Dimer Energy + 152.6, Hartrees
-0.013
-0.014
-0.015
-0.016
-0.017
-0.018
-0.019
-0.02
0.76 0.78 0.8 0.82 0.84 0.86 0.88 0.9 0.92
Average Oxygen Charge

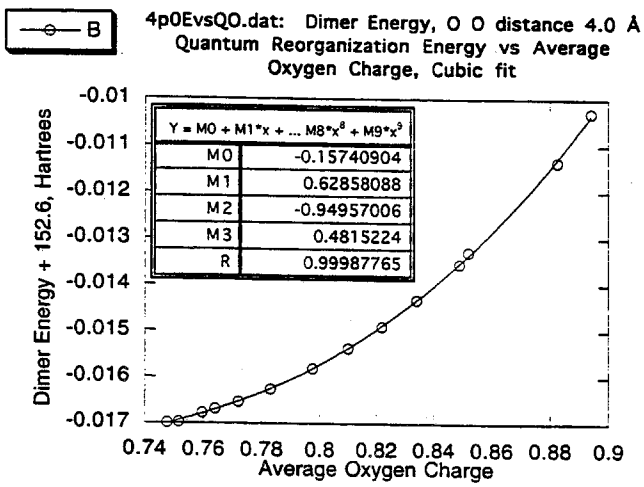
B
4p0EvsQO.dat: Dimer Energy, O O distance 4.0 Å
Quantum Reorganization Energy vs Average
Oxygen Charge, Cubic fit
Y = M0 + M1*x + ... M8*x^8 + M9*x^9
M0 -0.15740904
M1 0.62858088
M2 -0.94957006
M3 0.4815224
R 0.99987765
Dimer Energy + 152.6, Hartrees
-0.01
-0.011
-0.012
-0.013
-0.014
-0.015
-0.016
-0.017
0.74 0.76 0.78 0.8 0.82 0.84 0.86 0.88 0.9
Average Oxygen Charge

Figure 5

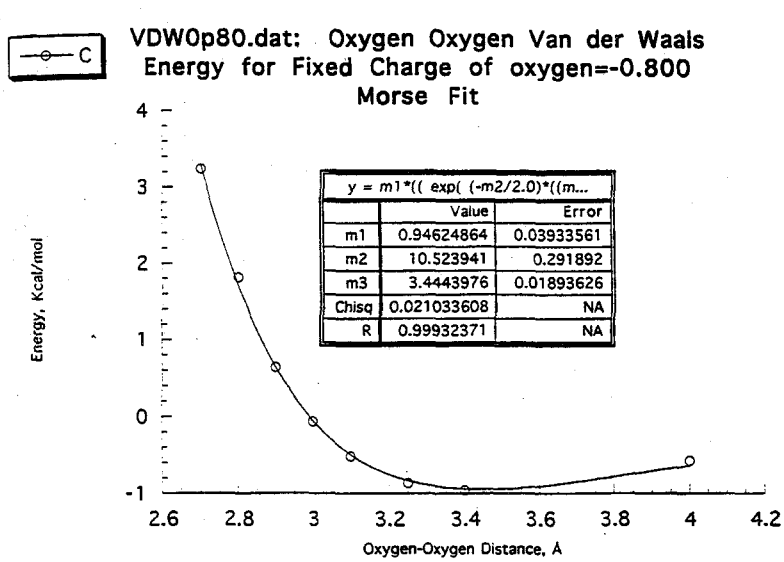
C
VDW0p80.dat: Oxygen Oxygen Van der Waals Energy for Fixed Charge of oxygen=-0.800 Morse Fit
y = m1*((exp((-m2/2.0)*((m...
Value Error
m1 0.94624864 0.03933561
m2 10.523941 0.291892
m3 3.4443976 0.01893626
Chisq 0.021033608 NA
R 0.99932371 NA
Energy, Kcal/mol
Oxygen-Oxygen Distance, A

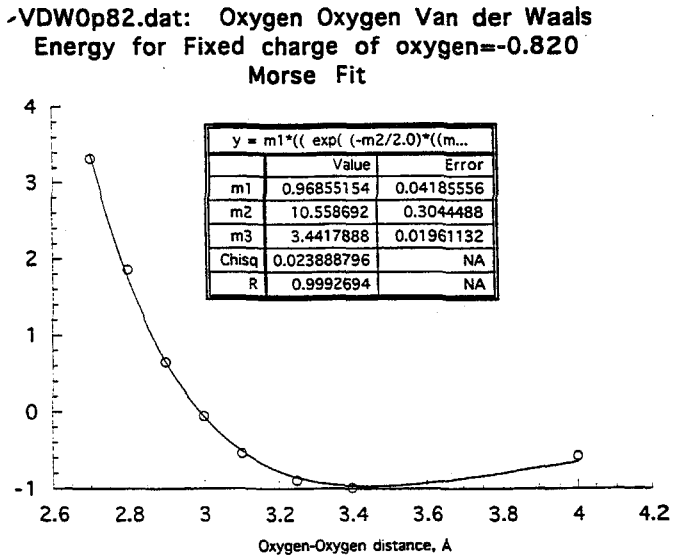
VDW0p82.dat: Oxygen Oxygen Van der Waals Energy for Fixed charge of oxygen=-0.820 Morse Fit
y = m1*((exp((-m2/2.0)*((m...
Value Error
m1 0.96855154 0.04185556
m2 10.558692 0.3044488
m3 3.4417888 0.01961132
Chisq 0.023888796 NA
R 0.9992694 NA
Oxygen-Oxygen distance, A

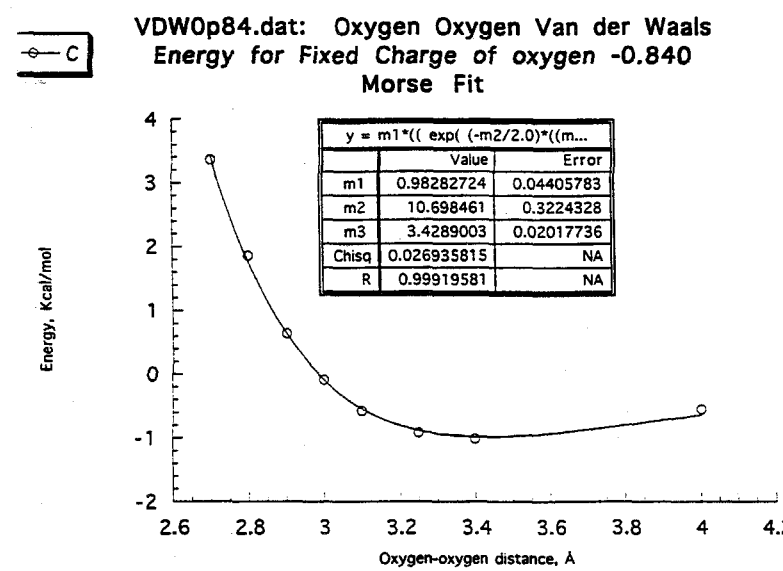
C
VDW0p84.dat: Oxygen Oxygen Van der Waals Energy for Fixed Charge of oxygen -0.840 Morse Fit
y = m1*((exp((-m2/2.0)*((m...
Value Error
m1 0.98282724 0.04405783
m2 10.698461 0.3224328
m3 3.4289003 0.02017736
Chisq 0.026935815 NA
R 0.99919581 NA
Energy, Kcal/mol
Oxygen-oxygen distance, A

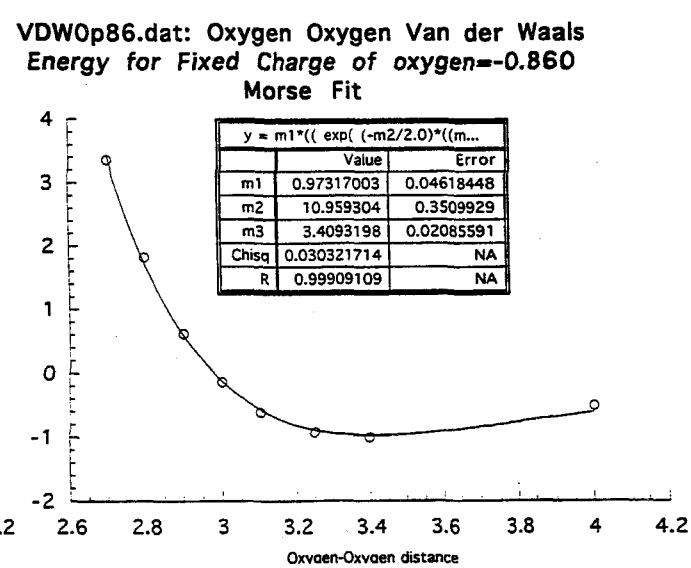
VDW0p86.dat: Oxygen Oxygen Van der Waals Energy for Fixed Charge of oxygen=-0.860 Morse Fit
y = m1*((exp((-m2/2.0)*((m...
Value Error
m1 0.97317003 0.04618448
m2 10.959304 0.3509929
m3 3.4093198 0.02085591
Chisq 0.030321714 NA
R 0.99909109 NA
Oxygen-Oxygen distance

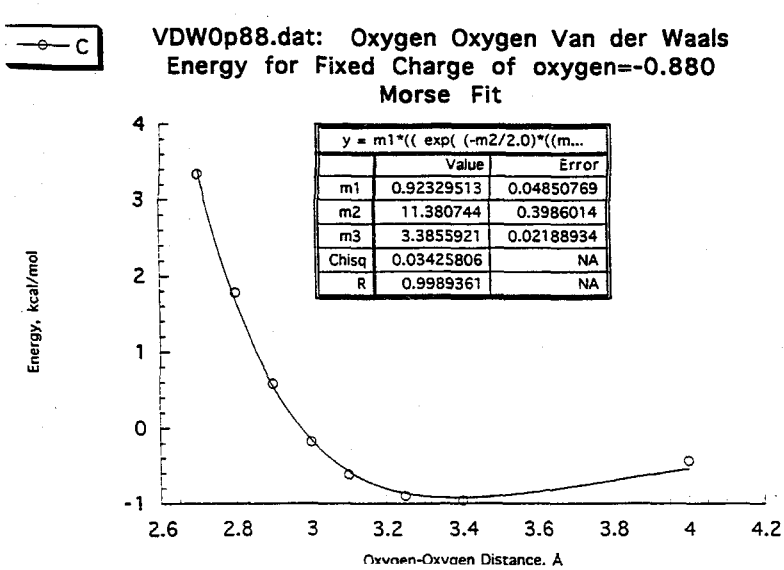
C
VDW0p88.dat: Oxygen Oxygen Van der Waals Energy for Fixed Charge of oxygen=-0.880 Morse Fit
y = m1*((exp((-m2/2.0)*((m...
Value Error
m1 0.92329513 0.04850769
m2 11.380744 0.3986014
m3 3.3855921 0.02188934
Chisq 0.03425806 NA
R 0.9989361 NA
Energy, kcal/mol
Oxygen-Oxygen Distance, A

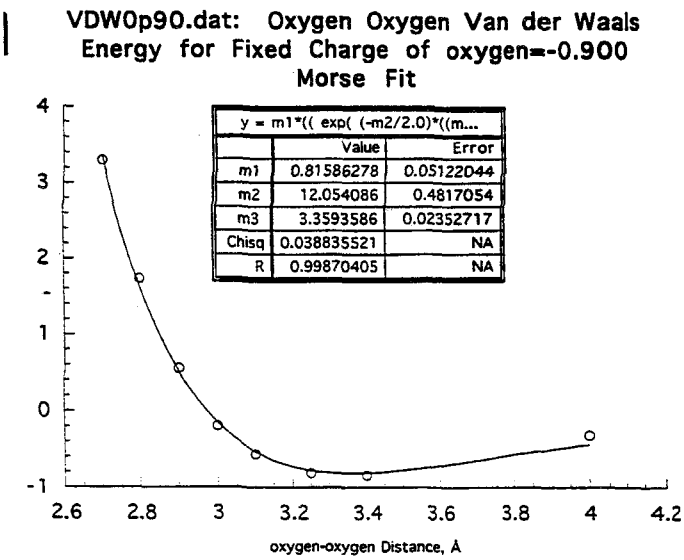
VDW0p90.dat: Oxygen Oxygen Van der Waals Energy for Fixed Charge of oxygen=-0.900 Morse Fit
y = m1*((exp((-m2/2.0)*((m...
Value Error
m1 0.81586278 0.05122044
m2 12.054086 0.4817054
m3 3.3593586 0.02352717
Chisq 0.038835521 NA
R 0.99870405 NA
oxygen-oxygen Distance, A

Figure 6. Crystal structure of Ice II.

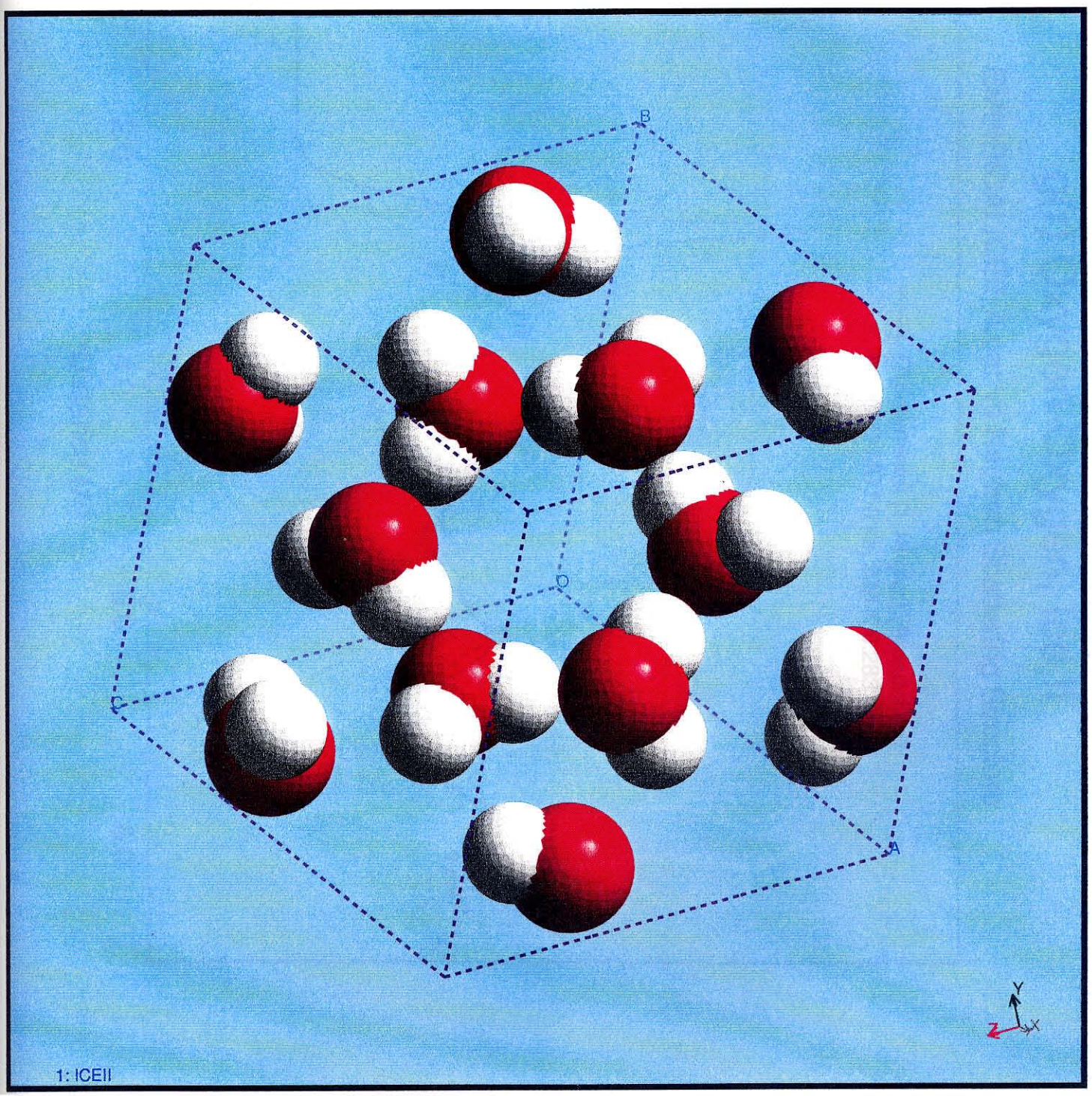

Figure 7

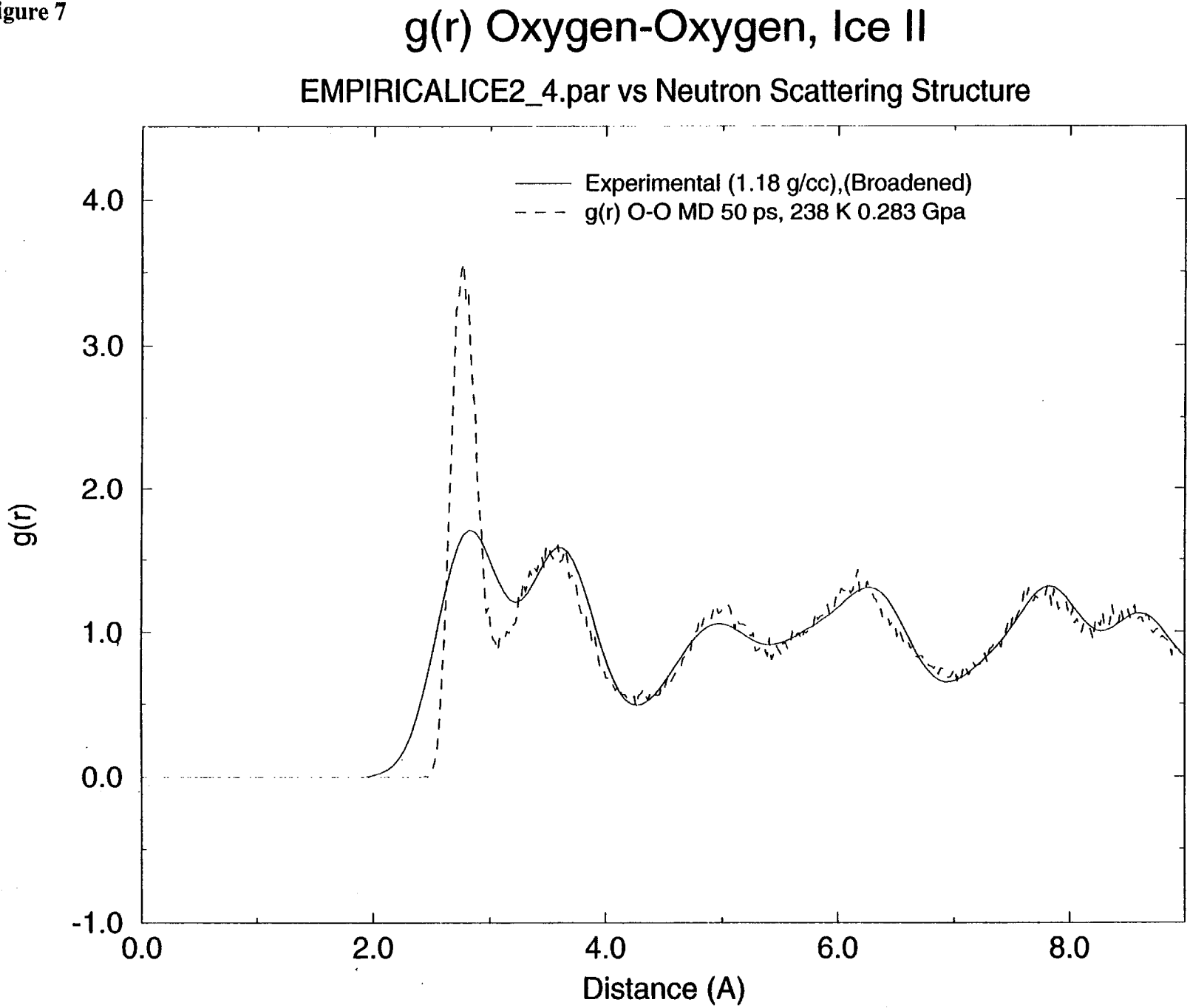
g(r) Oxygen-Oxygen, Ice II
EMPIRICALICE2_4.par vs Neutron Scattering Structure
Experimental (1.18 g/cc),(Broadened)
g(r) O-O MD 50 ps, 238 K 0.283 Gpa
g(r)
4.0
3.0
2.0
1.0
0.0
-1.0
0.0
2.0
4.0
6.0
8.0
Distance (A)

Figure 8

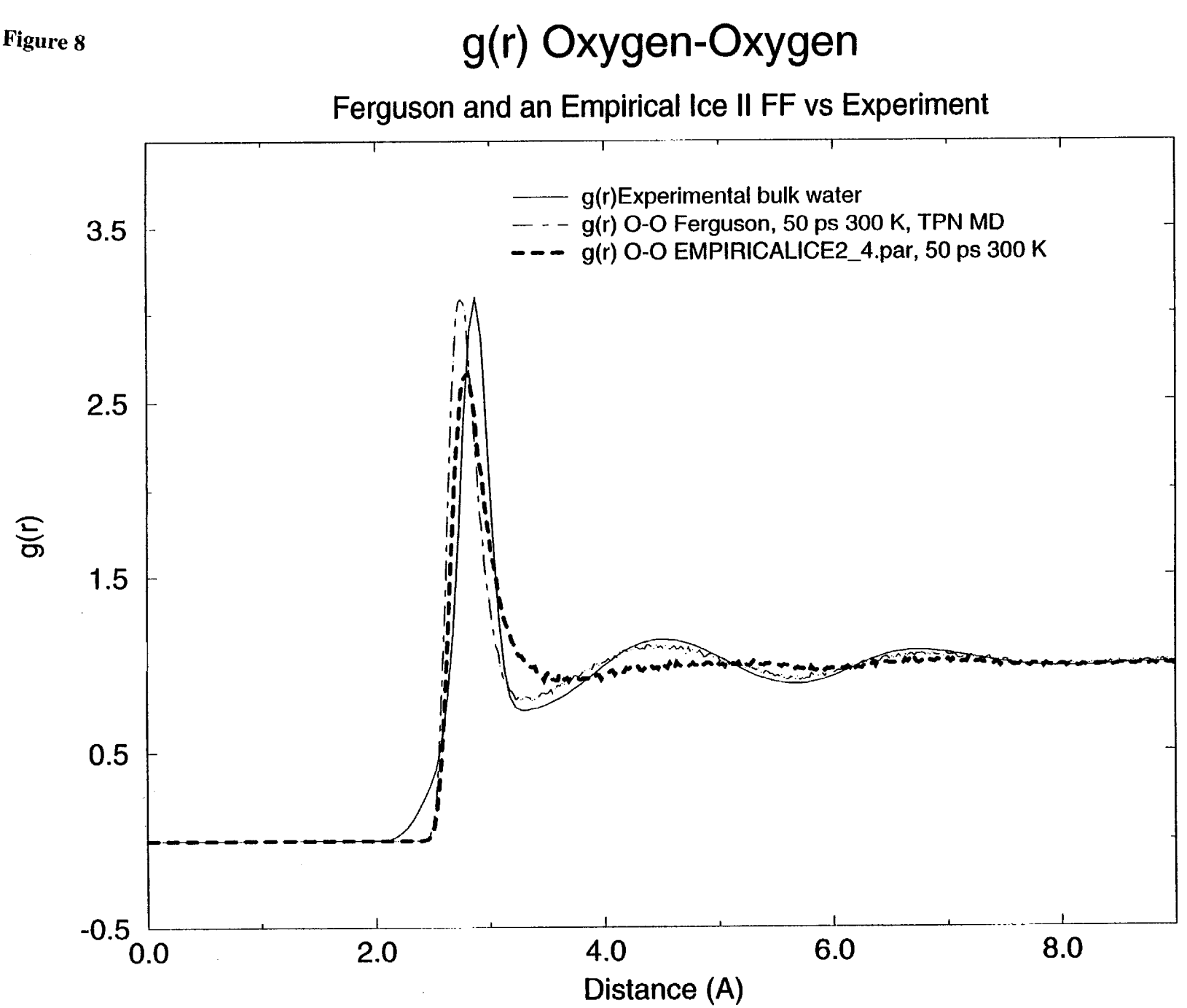
g(r) Oxygen-Oxygen
Ferguson and an Empirical Ice II FF vs Experiment
g(r)Experimental bulk water
g(r) O-O Ferguson, 50 ps 300 K, TPN MD
g(r) O-O EMPIRICALICE2_4.par, 50 ps 300 K
g(r)
3.5
2.5
1.5
0.5
-0.5
0.0
2.0
4.0
6.0
8.0
Distance (A)

Figure 9

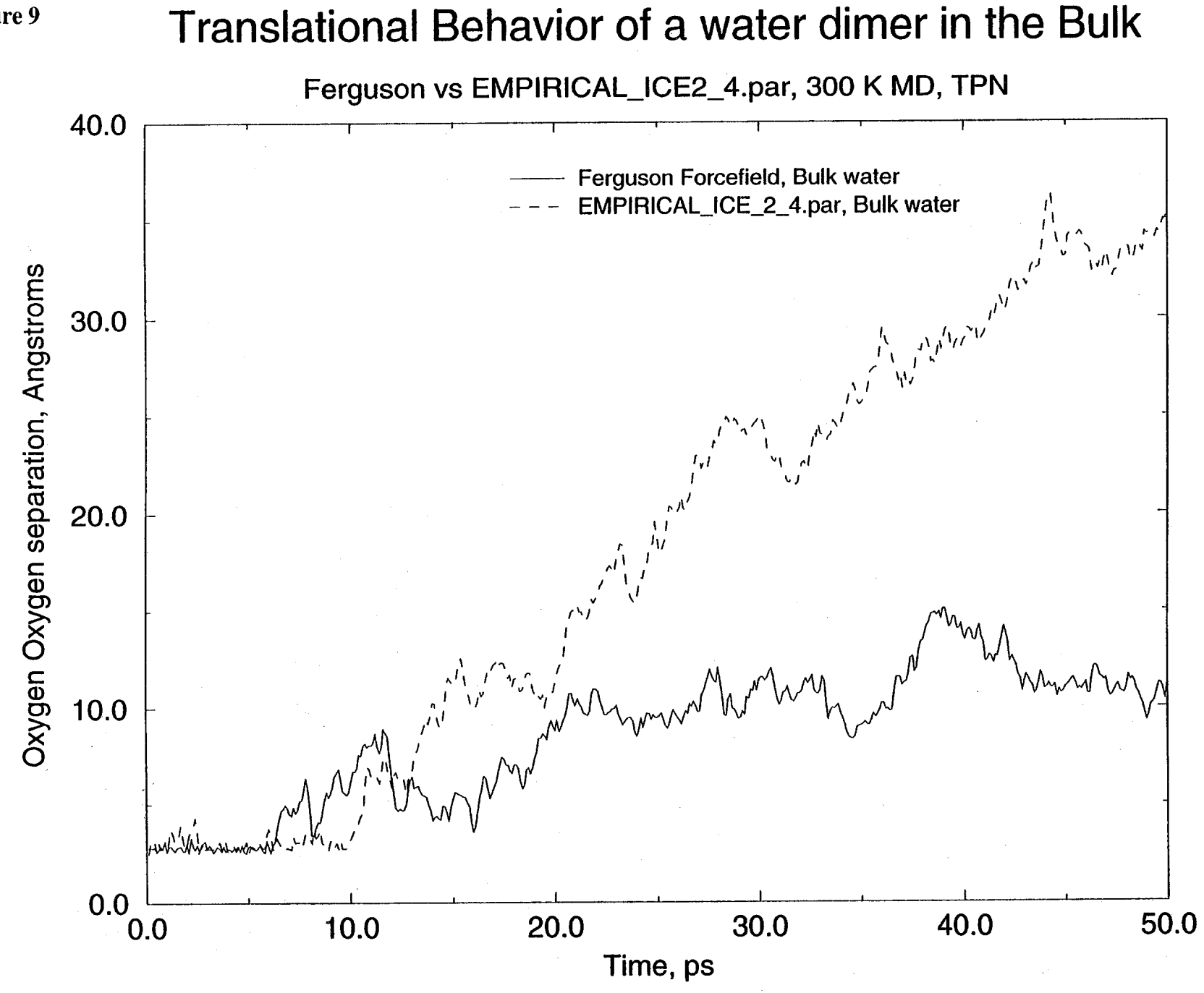
Translational Behavior of a water dimer in the Bulk
Ferguson vs EMPIRICAL_ICE2_4.par, 300 K MD, TPN
Ferguson Forcefield, Bulk water
EMPIRICAL_ICE_2_4.par, Bulk water
Oxygen Oxygen separation, Angstroms
Time, ps
0.0
10.0
20.0
30.0
40.0
50.0

Figure 10. Structure of water hexamer used in *ab initio* studies.

Figure 11

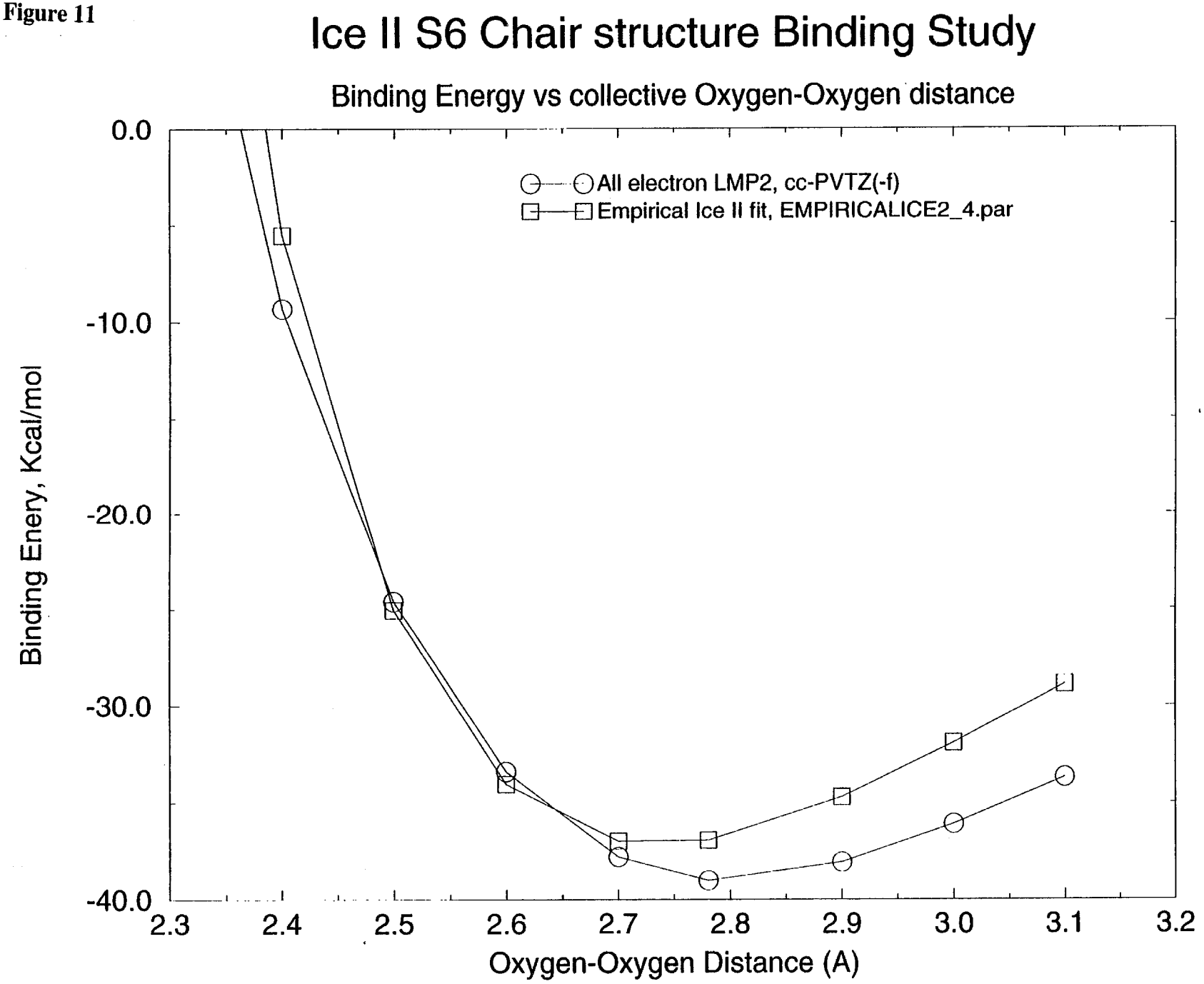
Ice II S6 Chair structure Binding Study
Binding Energy vs collective Oxygen-Oxygen distance
All electron LMP2, cc-PVTZ(-f)
Empirical Ice II fit, EMPIRICALICE2_4.par
Binding Enery, Kcal/mol
0.0
-10.0
-20.0
-30.0
-40.0
2.3
2.4
2.5
2.6
2.7
2.8
2.9
3.0
3.1
3.2
Oxygen-Oxygen Distance (A)

Figure 12

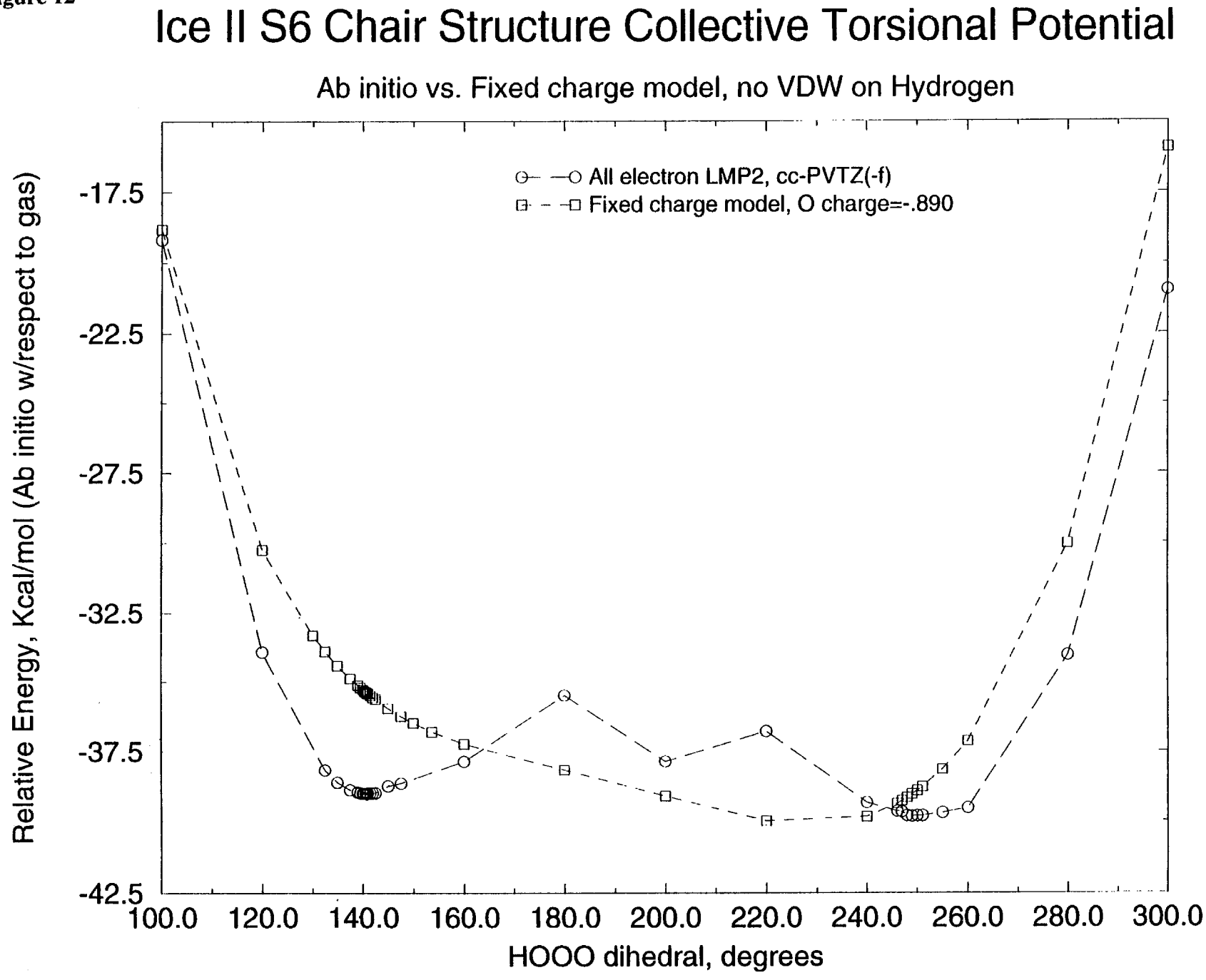
Ice II S6 Chair Structure Collective Torsional Potential
Ab initio vs. Fixed charge model, no VDW on Hydrogen
All electron LMP2, cc-PVTZ(-f)
Fixed charge model, O charge=-.890
Relative Energy, Kcal/mol (Ab initio w/respect to gas)
-17.5
-22.5
-27.5
-32.5
-37.5
-42.5
100.0
120.0
140.0
160.0
180.0
200.0
220.0
240.0
260.0
280.0
300.0
HOOO dihedral, degrees

Figure 13

FORCE FIELD CALIBRATION METHODS:

DIPOLE "SWEEP" OF LONE PAIRS

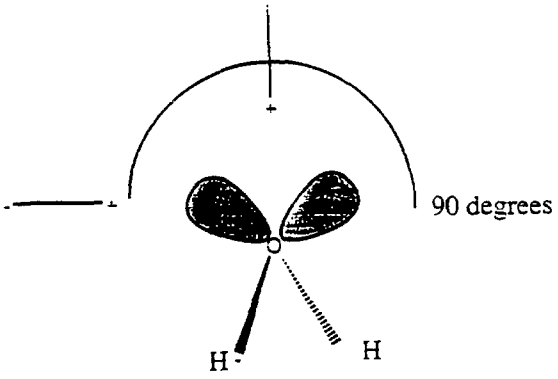

0 degrees example of lone pair dipole sweep

DIPOLE "SWEEP" OF HYDROGENS

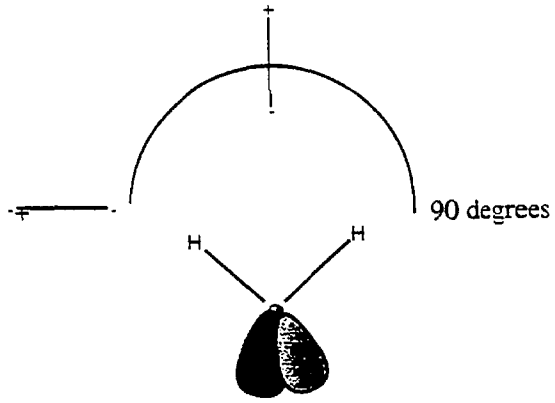

0 degrees example of hydrogen dipole sweep

OXYGEN DIPOLE APPROACH (at 0 degrees)

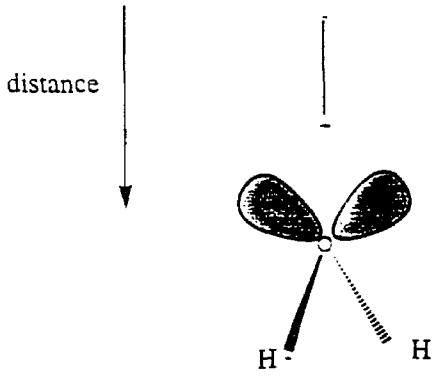

HYDROGEN DIPOLE APPROACH (along OH vector)

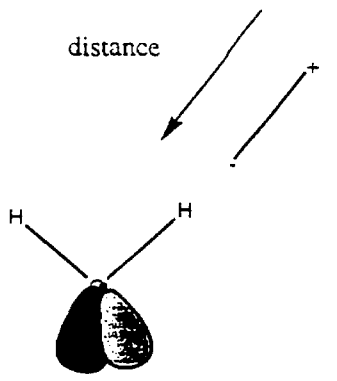

Figure 14

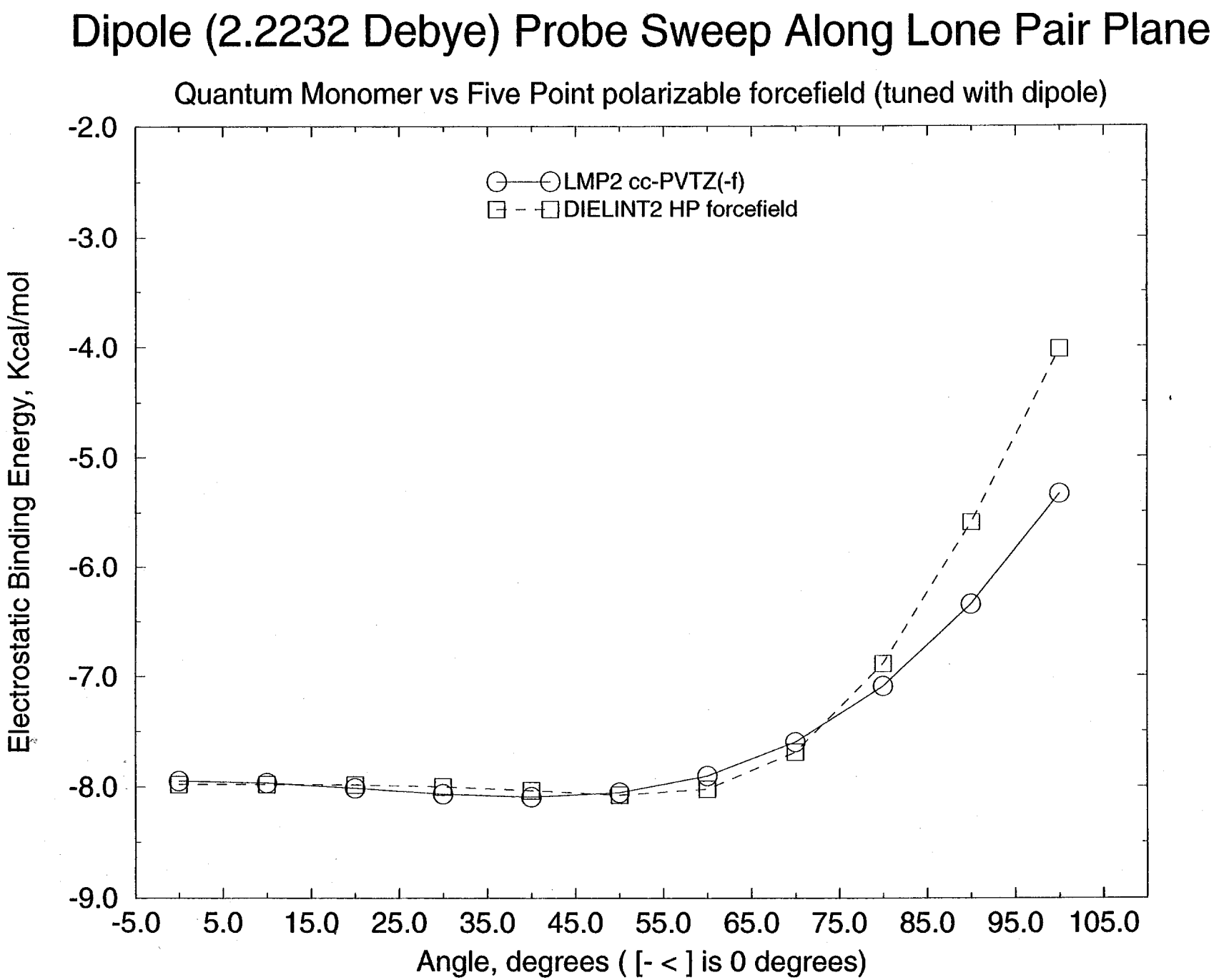
Dipole (2.2232 Debye) Probe Sweep Along Lone Pair Plane
Quantum Monomer vs Five Point polarizable forcefield (tuned with dipole)
LMP2 cc-PVTZ(-f)
DIELINT2 HP forcefield
Electrostatic Binding Energy, Kcal/mol
-2.0
-3.0
-4.0
-5.0
-6.0
-7.0
-8.0
-9.0
-5.0
5.0
15.0
25.0
35.0
45.0
55.0
65.0
75.0
85.0
95.0
105.0
Angle, degrees ([- <] is 0 degrees)

Figure 15

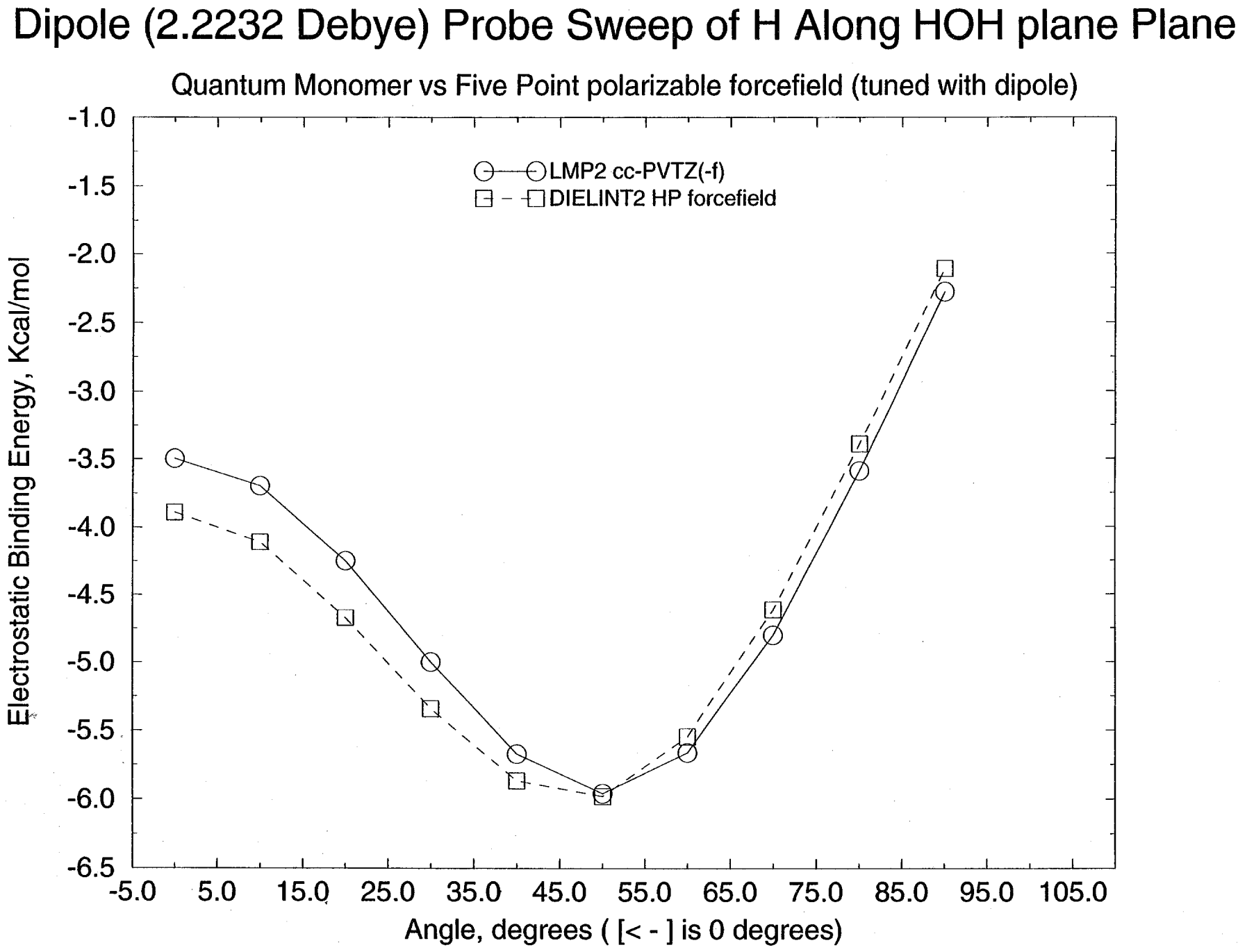
Dipole (2.2232 Debye) Probe Sweep of H Along HOH plane Plane
Quantum Monomer vs Five Point polarizable forcefield (tuned with dipole)
LMP2 cc-PVTZ(-f)
DIELINT2 HP forcefield
Electrostatic Binding Energy, Kcal/mol
-1.0
-1.5
-2.0
-2.5
-3.0
-3.5
-4.0
-4.5
-5.0
-5.5
-6.0
-6.5
-5.0
5.0
15.0
25.0
35.0
45.0
55.0
65.0
75.0
85.0
95.0
105.0
Angle, degrees ([< -] is 0 degrees)

Figure 16

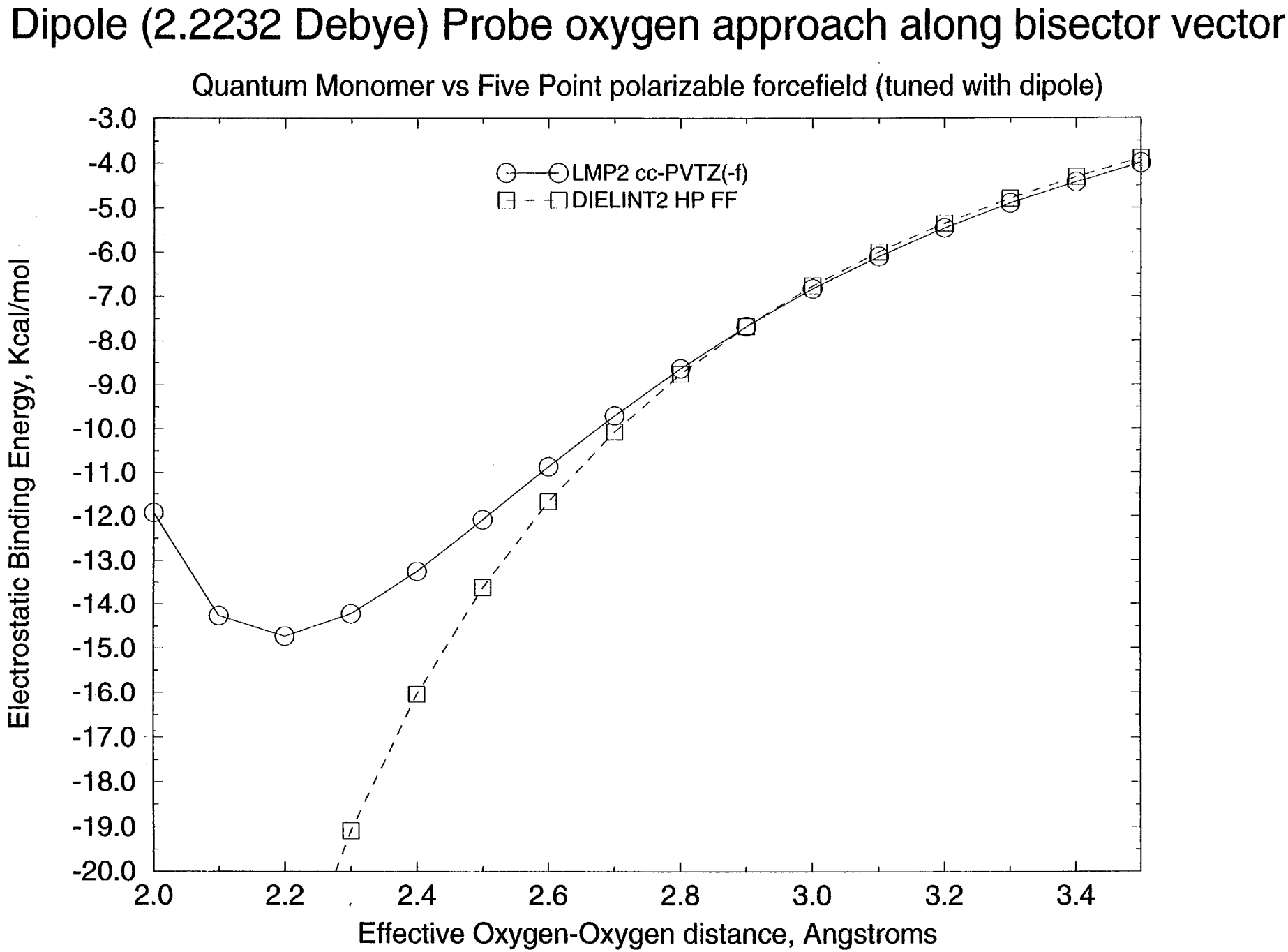
Dipole (2.2232 Debye) Probe oxygen approach along bisector vector
Quantum Monomer vs Five Point polarizable forcefield (tuned with dipole)
LMP2 cc-PVTZ(-f)
DIELINT2 HP FF
Electrostatic Binding Energy, Kcal/mol
-3.0
-4.0
-5.0
-6.0
-7.0
-8.0
-9.0
-10.0
-11.0
-12.0
-13.0
-14.0
-15.0
-16.0
-17.0
-18.0
-19.0
-20.0
2.0
2.2
2.4
2.6
2.8
3.0
3.2
3.4
Effective Oxygen-Oxygen distance, Angstroms

Figure 17

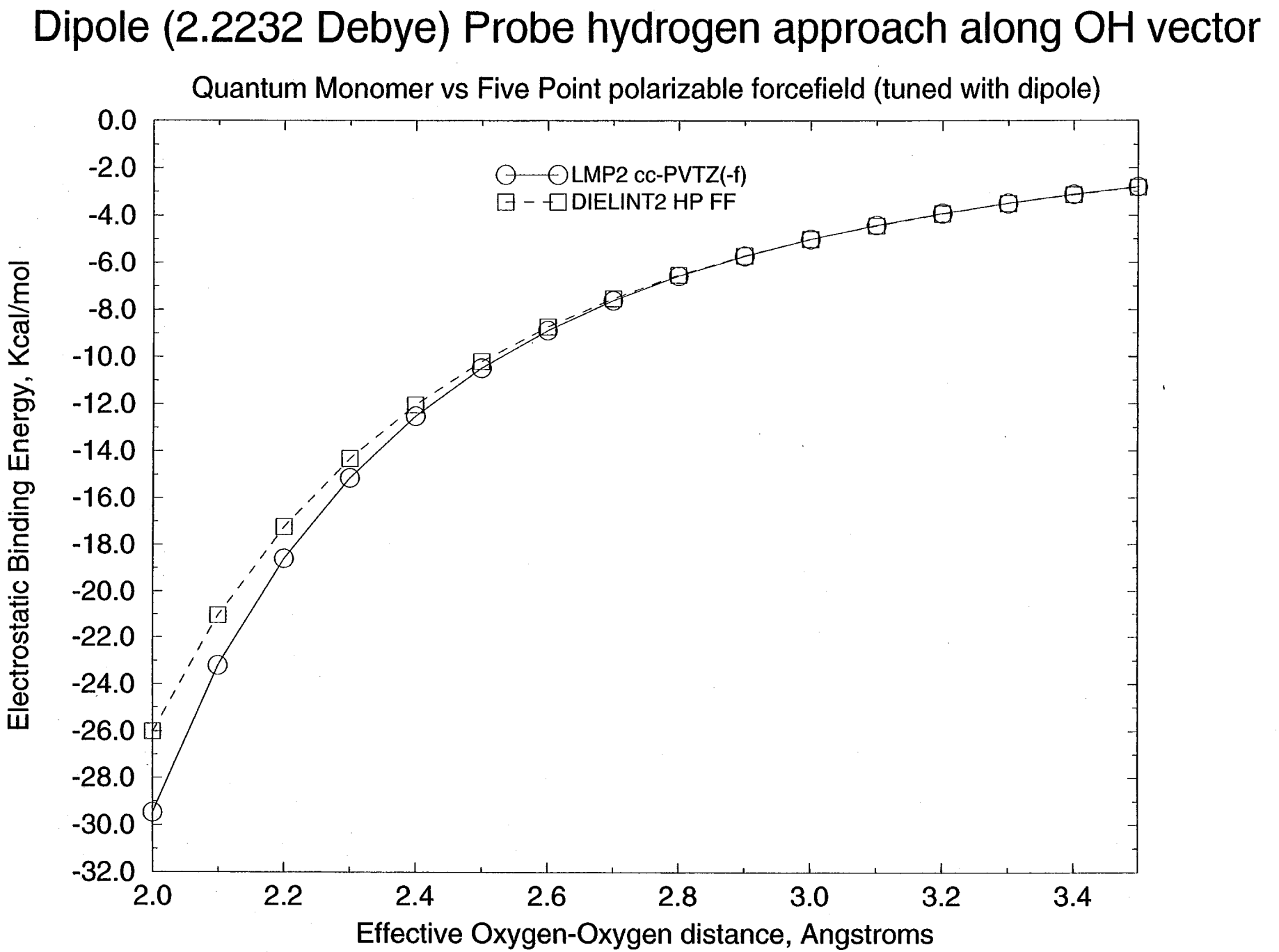
Dipole (2.2232 Debye) Probe hydrogen approach along OH vector
Quantum Monomer vs Five Point polarizable forcefield (tuned with dipole)
LMP2 cc-PVTZ(-f)
DIELINT2 HP FF
Electrostatic Binding Energy, Kcal/mol
0.0
-2.0
-4.0
-6.0
-8.0
-10.0
-12.0
-14.0
-16.0
-18.0
-20.0
-22.0
-24.0
-26.0
-28.0
-30.0
-32.0
2.0
2.2
2.4
2.6
2.8
3.0
3.2
3.4
Effective Oxygen-Oxygen distance, Angstroms

Figure 18

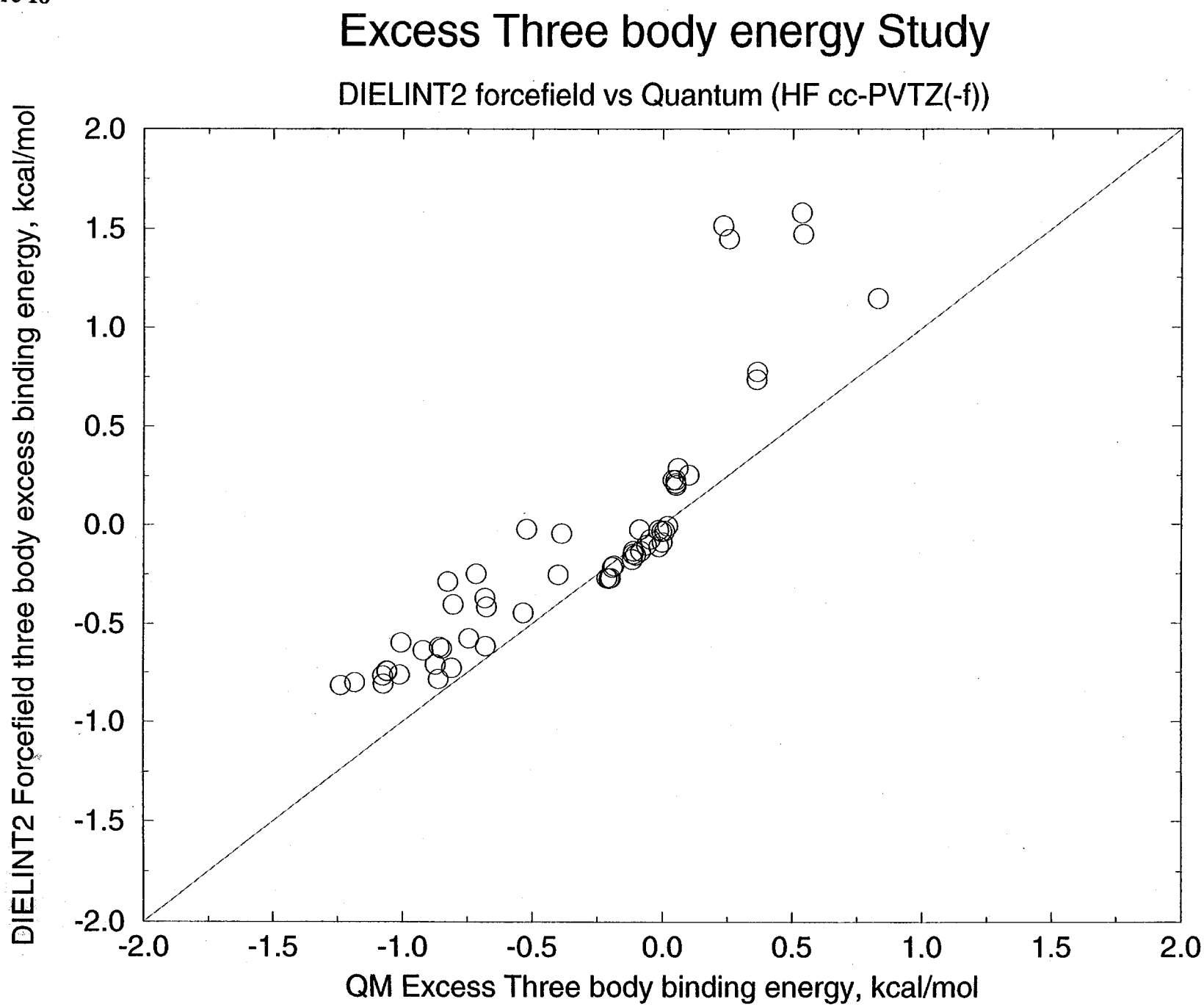
Excess Three body energy Study
DIELINT2 forcefield vs Quantum (HF cc-PVTZ(-f))
DIELINT2 Forcefield three body excess binding energy, kcal/mol
QM Excess Three body binding energy, kcal/mol
2.0
1.5
1.0
0.5
0.0
-0.5
-1.0
-1.5
-2.0
-2.0
-1.5
-1.0
-0.5
0.0
0.5
1.0
1.5
2.0

Figure 19. Classic dipole tests on quantum water monomer for polarizable forcefield calibration.

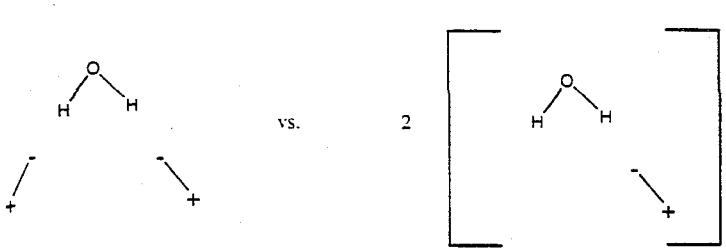

TEST 1: Quantum Energy Difference: +0.246 kcal/mol

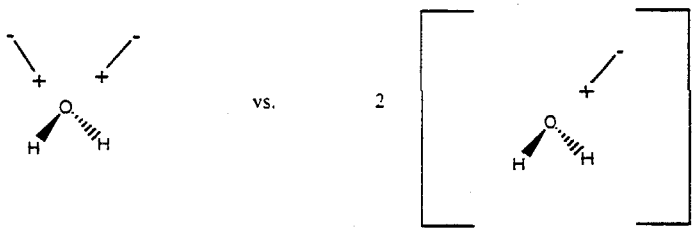

TEST 2: Quantum Energy Difference: +0.053 kcal/mol

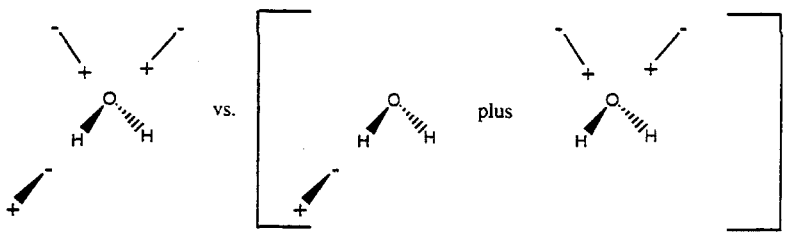

TEST 3: Quantum Energy Difference: -0.627 kcal/mol

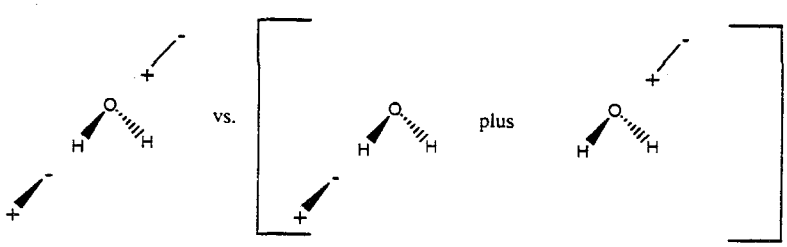

TEST 4: Quantum Energy Difference: -0.319 kcal/mol

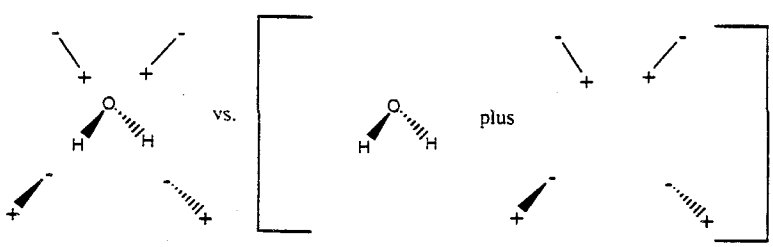

TEST 5: Quantum Energy Difference: -27.79 kcal/mol

Figure 20

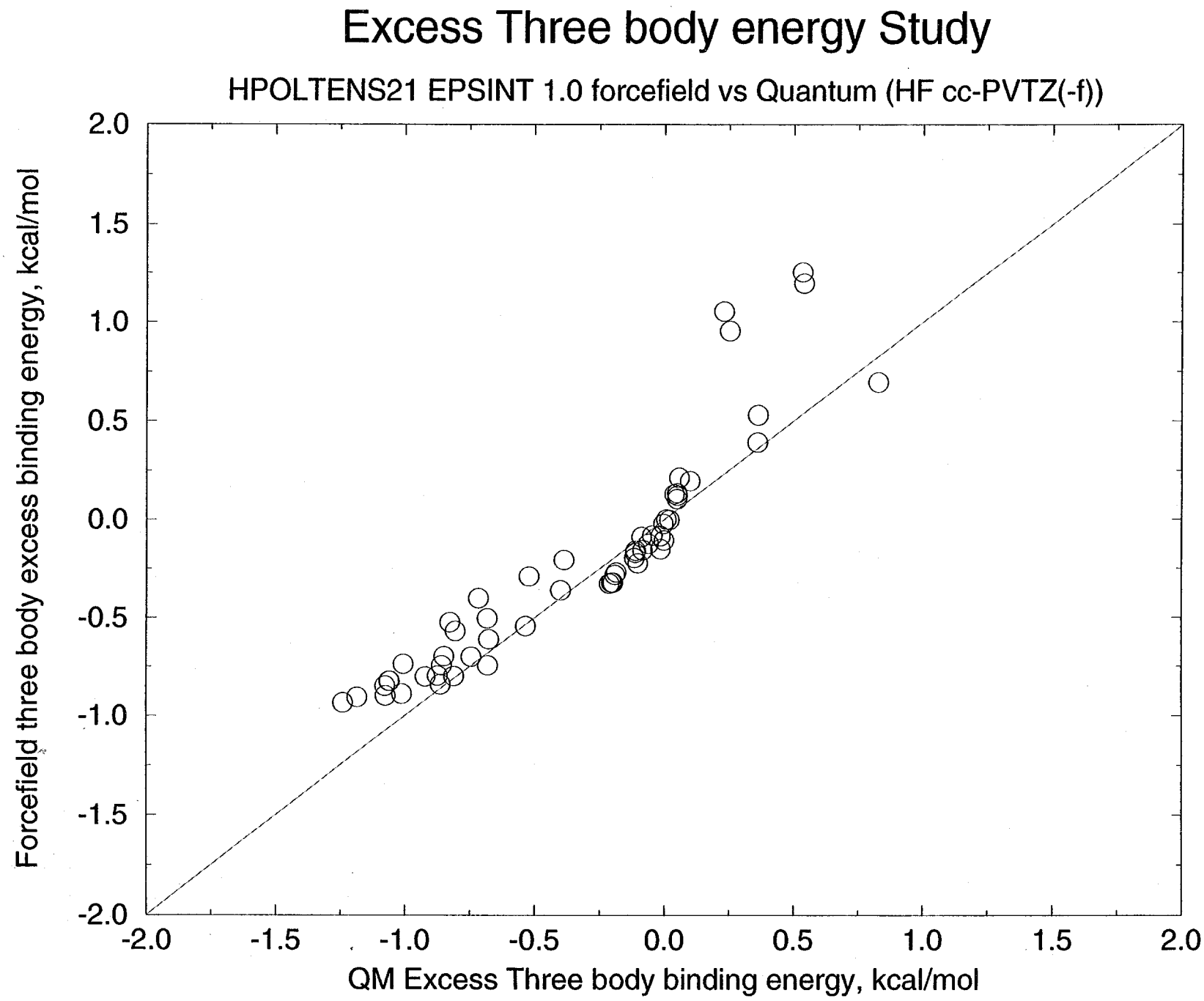
Excess Three body energy Study
HPOLTENS21 EPSINT 1.0 forcefield vs Quantum (HF cc-PVTZ(-f))
Forcefield three body excess binding energy, kcal/mol
QM Excess Three body binding energy, kcal/mol
2.0
1.5
1.0
0.5
0.0
-0.5
-1.0
-1.5
-2.0
-2.0
-1.5
-1.0
-0.5
0.0
0.5
1.0
1.5
2.0

Figure 21

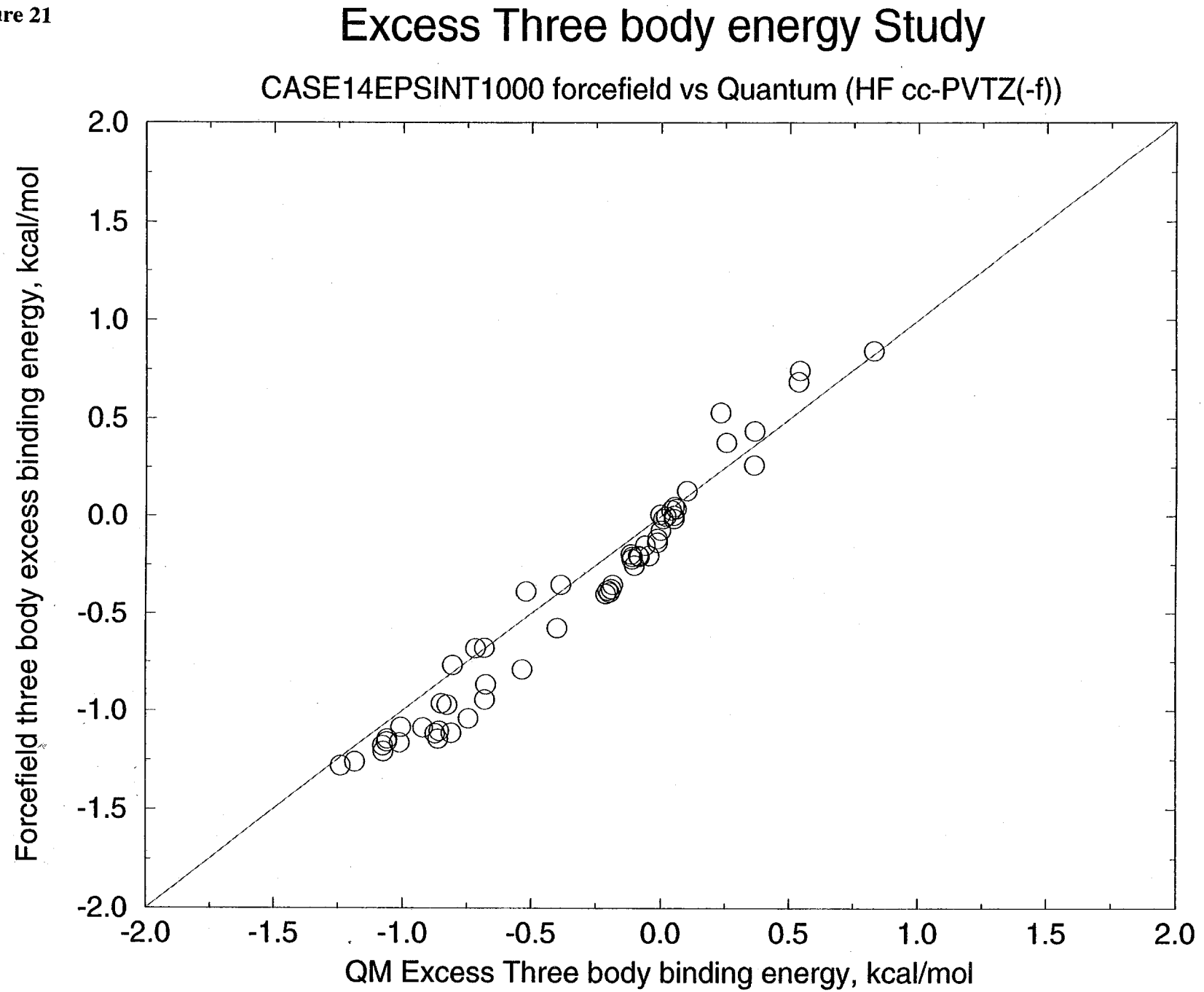
Excess Three body energy Study
CASE14EPSINT1000 forcefield vs Quantum (HF cc-PVTZ(-f))
Forcefield three body excess binding energy, kcal/mol
QM Excess Three body binding energy, kcal/mol
2.0
1.5
1.0
0.5
0.0
-0.5
-1.0
-1.5
-2.0
-2.0
-1.5
-1.0
-0.5
0.0
0.5
1.0
1.5
2.0

References

1. Robinson, G. W.; Zhu, S. B.; Singh, S.; Evans, M. W.; *Water in Biology, Chemistry and Physics: Experimental Overviews and Computational Methodologies*, **9**, World Scientific Publishing Co. Pte. Ltd., 1997.
2. Cho, C. H.; Surjit, S.; Robinson, G. W.; *J. Chem. Phys.*, **107**(19), 7979-7988 (1997)
3. Ferguson, D. M.; *J. Comp. Chem.*, **16**, 501-511 (1995)
4. Soper, A. K.; Phillips, M. G.; *Chemical Physics*, **107**, 47-60 (1986)
5. Bernardo, D. N.; Ding, Y.; Krogh-Jespersen, K.; Levy, R. M.; *J. Phys. Chem.*, **98**, 4180-4187 (1994)
6. Odutola, J. A.; Dyke, T. R.; *J. Chem. Phys.*, **72**, 5062 (1980)
7. Curtiss, L. A.; Frurip, D. J.; Blander, M. J.; *J. Chem. Phys.*, **71**, 2703 (1979)
8. Rashin, A. A.; Honig, B.; J. *Phys Chem.*, **89**, 5588-5593 (1985)
9. Edinger, S. R.; Cortis, C.; Shenkin, P. S.; Friesner, R. A.; *J. Phys. Chem.*, B, **101**(7), 1190-1197 (1997)
10. Kamb, B.; Hamilton, W. C.; LaPlaca, S. J.; Prakash, A.; *J. Chem. Phys.* **55**(4), 1934 (1971)
11. Mayo, S. L.; Olafson, B. D.; Goddard, W. A.; *J. Phys. Chem.*, **94**(26), 8897-8909 (1990)
12. *Ibid* 1, p. 105, Ch. 4
13. Karasawa, N.; Goddard III, W. A.; *Macromolecules*, **25**(26), 7268-7281 (1992)
14. Rappe, A. K.; Goddard III, William A.; *J. Phys. Chem.*, **95**(8), 3358-3363 (1991)

Chapter 3

Abstract

The electronic nose designed by the Lewis group is based on an array of polymer sensors filled with carbon black. The relative change in resistivity of a given polymer sensor upon exposure to a given solvent vapor is believed to be the result of polymer swelling. Therefore, the experimentally determined relative change in resistivity of a polymer sensor was related to the atomistically calculated intrinsic bulk properties of a series of twenty two solvents (esters and alcohols) through a permeability equation. The modeled bulk properties were the electrostatic, Van der Waals and hydrogen bond cohesive energy densities (cal/cc) as well as the molar volume.

Based on the relationship/correlation between the relative change in resistivity and the permeability for all of the twenty two solvents in each of seven detectors, the identity of a total of 11/22 solvents were "back" predicted correctly, 5/22 solvents were predicted correctly within the second best choice, and 4/22 solvents were predicted correctly within the best third choice according to a root mean square calculation. Therefore, a total of 19/22 solvents were predicted correctly within the best three candidates for each trial solvent. The results in this study clearly show that modeling is a valuable analytical tool that may be used in the electronic nose project.

Direct Correlation between Theory and Experiment: The Artificial Nose Project

Introduction

The olfactory system in living organisms is a sophisticated sensing device that is the least well understood in the mammalian nervous system. Yet olfaction has played an important role in an organism's ability to recognize airborne molecules that indicate physical danger and feeding. In mammals, subtle differences in molecular structure and functional groups can be readily detected due to a set of olfactory receptor neurons, which are linked to the central nervous system (*CNS*). Several types of receptor neurons are stimulated to different degrees by odorant molecules and the result is an interpretation of the group signals sent by the olfactory cells to the *CNS*. Specifically, there are seven different proteins on the surface of receptor neurons, and these molecule-recognizing proteins occur at different proportions in olfactory neuron cells, and the result is a large variety of possible cell receptors. Biological studies of olfactory receptor neurons in mice has shown that aliphatic odorants stimulate the release of calcium into the cytosol to different degrees depending on the identity of the molecule.[1] Besides having biological implications, a synthetic "nose" may be of great utility in the area of molecular gas identification, specifically in the perfume industry, in the military where the identification of noxious gases would be of primary importance, as well as remote sensing devices. A particular design of a synthetic nose has been experimentally constructed by the Lewis group, in which sensors are made up of different polymers loaded with carbon black. The basic principle behind this detector is that the relative resistivity of the polymer will increase as a function of how much the molecular gas swells the polymer. The swelling or permeation process of the polymer will depend

upon the nature of the polymer as well as the nature of the penetrant molecule. Therefore, one can envision an array of different polymers with carbon black that will give rise to a specific change in resistivity upon exposure to a vapor of a particular molecule. The pattern of relative change in resistivities along an array of polymer sensors for a given molecule would ideally be unique in order to unambiguously identify the molecule. Finally, it would be of great value to be able to correlate from first principles the change of resistivity of a given polymer sensor with the nature of the solute such as its size, hydrogen bonding, electrostatic and dispersive character. With such understanding, one might have more information for building a series of sensors for specific compounds such as nerve gases or air bound compounds emanating from explosives. Therefore, in this report a successful correlation of the intrinsic bulk properties of a series of solvent molecules with the experimental relative change in resistivity of the sensors upon exposure to the corresponding vapor is presented. The correlation method is based upon precise molecular modeling of the polymer and pure solvent bulk state energetics and the relationship between permeability, solubility and diffusivity.

P=S*D

The permeability of a given solute on a polymer is given by[2]

$$P = A\exp\left(\frac{\Delta H_S}{kBT} - \frac{E_D}{kBT}\right) \qquad (1)$$

where A is the exponential prefactor related to entropy, ΔH_S is the heat of sorption of the solute and E_D is the activation energy for diffusion of the molecule in the polymer. The main model developed during the course of this study for the heat of sorption is

$$\frac{\Delta Hs}{kBT} = \sum_{i=1}^{3} Ci\left[CEDi(solvent) - CEDi(polymer)\right] * \frac{MVsolvent}{RT} \quad (2)$$

where k_BT is the Boltzmann constant times the temperature, i=1 refers to the electrostatic component, i=2 refers to the dispersive component, i=3 refers to the hydrogen bond component, C_i refers to the best fit coefficient for the difference between the ith component of a given solvent with cohesive energy density (cal/cc) component $CED_{i(solvent)}$ and the ith component of a given polymer cohesive energy density (cal/cc) $CED_{i(polymer)}$, and $MV_{solvent}$ is the calculated bulk molar volume of the solvent (cc/mol). Similarly, the activation energy for diffusion is given by

$$\frac{E_D}{k_BT} = C_4 * \frac{MVsolvent}{RT} \quad (3)$$

where E_D is the activation energy of diffusion and C_4 is the best-fit coefficient to the molar volume. This relation is obtained based on the experimental observation that the diffusion coefficient of various molecules is linearly related to the molar volume of the penetrant in the case where the actual temperature is greater than the glass transition (T_g) of the polymer[2b]. However, the approximation in Equation 3 is used for all polymer sensors regardless of T_g. Additionally, the diffusion coefficient of organic vapors on polymers is also dependent on the concentration (c) of the penetrant:[2c]

$D=D_{c=0}f(c)$ (4)
$f(c)= \exp(\alpha c)$ (5)

However, in this study the concentration effect of the organic vapor in the polymer on its diffusion coefficient is neglected. A further approximation is that the entropy term implicit in the pre-exponential factor is the same for all solvents.

The cohesive energy components correspond to the pure bulk states of the solvent and the polymer. Strictly speaking, it would be desirable to compute the actual heats of sorption for the various molecules in a given polymer, and these results are reported in the next chapter. However, for the sake of expediency, a correlation was done between experiment and theory based on quantities corresponding to the pure bulk states of the polymer and the respective solvents. Nearly linear correlations between the experimentally determined change with resistivity and the permeability-related expression (Equations 1-3) were found for the different polymer sensors. The results for the calculated electrostatic, dispersive and hydrogen bond cohesive energy density components for various solvents as well as their calculated molar volume are summarized in Table I.

The experimentally determined relative resistivity of various polymer sensors upon exposure to vapor solvents was correlated with the calculated Hansen cohesive energy components and molar volumes via the permeability equation (Equations 1-3) as discussed previously and the resulting best fit parameters for the various polymer sensors are given in Table III.. The relative resistivity change was back "predicted" for the series of odorants as a function of polymer sensor using the best fit coefficients listed in Table III for Equation 2 and these results are summarized in Table IV.

Discussion of Results

The experimental and predicted relative changes in resistivities for seven detectors upon exposure to twenty-two different odorants are shown in Table IV. The experimental uncertainty as well as the differences between the calculated and the experimental signals are included as well. The correlation plots between the predicted and experimentally determined relative change in resistivities for each of the detectors is shown in Figures 1-7. The slopes and the Pearson R values for the correlation plots are listed in Table V as well as the corresponding Figure number. The correlation was particularly good for polysulfone, poly (4-hydroxy styrene) and PEVA (polyethylene-co- vinyl acetate) and especially poor for Poly (methyl methacrylate) based on both correlation slope and the Pearson R value for the linear fit. Poly (sulfone) is glassy at room temperature since is has a Tg of 463 K.

Polysulfone may be able to discriminate very well between solvents of different sizes since the free volume fraction is small and the free volume distribution may be narrow, resulting in a "molecular" sieve effect. Additionally, the experimental relative change in resistivity in polysulfone ranges from 0 to 1.0, which makes it a particularly good high-resolution sensor. An additional characteristic of Polysulfone is its sulfone polar groups, although their influence in discriminating molecules is not particularly clear.

The poly (ethylene-co-vinyl acetate) detector also correlates reasonably well with the theoretical relative change in resistivity. However the relative change in resistivity range is smaller compared to poly (sulfone) indicating that it is less discriminating towards ester and alcohol solvents. A possible explanation that accounts for this

observation is that PEVA contains polar ester functional groups due to the vinyl content (18 %), as well as nonpolar components due to the poly (ethylene) content (82 %). An additional factor is that PEVA probably has a glass transition below room temperature and as a result there will be a large free volume fraction which will decrease the sensitivity towards molecules of different sizes compared to high glass transition polymers such as poly (sulfone).

The third particularly good detector in terms of signal correlation with theoretical prediction is poly (4-hydroxy styrene). This detector is particularly sensitive to molecules functionalized with highly polar groups such as alcohol, obviously due to the hydroxyl functional group. However, the sensitivity of this sensor to moderately polar or nonpolar solvents such as esters is particularly low.

To illustrate the predicting capabilities of an array of sensors, a didactic procedure was devised in which the relative change in resistivity signals of a molecule from the seven sensors was used to identify the molecule. The odorant identity was established from the lowest root mean square differences of all potential odorants for each of the seven sensors. Ideally, the experimental signal pattern of each molecule over an array of seven detectors should closely match the predicted signal of the same molecule using the permeability equation with the best-fit constants. Actually, the predicted signals of some molecules in some sensors have deviations from the experimental values because the fits were not perfect, and therefore it may be necessary to have a threshold number of sensors to unambiguously identify the molecule .The "identity" of twenty-two odorants was "back" predicted using the information of all of the seven sensors and the results are illustrated in Table VI. The odorant molecule

being identified is shown in bold in the first column. If a match was found within the best three possibilities, it was highlighted in bold in the second through fourth columns respectively. In summary, eleven out of twenty two solvents were identified, and 9/22 were identified within as second or third choices. This means that given the experimental signal of a given solvent molecule, there is a 20/22 chance that it will be found within the three best predicted candidates (lowest three root mean square choices) for the seven sensors case. These statistics are especially good considering that the molecules used in this study are based on very limited chemistry, only two families, esters and alcohols. Nonetheless, the current model shows that the best predicted three candidate solvents are very closely related to the odorant molecule being identified, supporting the assertion that the model can be used for chemical identification purposes.. For example, when 3-pentanol is chosen as a test solvent, the number one, two and three best candidates are 2-pentanol, n-butanol and 3-pentanol respectively. All three best choices are linear low carbon number alcohols, just as 3-pentanol. Another example is the "test" solvent iso-amyl alcohol in which the three best candidate solvents were n-hexanol, n-heptanol and n-amyl alcohol. Even though the identity of iso-amyl alcohol was not predicted within the best three possibilities, the identity of all of the candidate solvents was very similar in nature to it. The other case that was completely missed was the test solvent n-amyl alcohol where the predicted first three possible candidates were n-butanol, 3-pentanol and 2-pentanol. As in the iso-amyl alcohol, the three candidate solvents were very similar in nature to the test solvent. NO alcohol was ever identified as esters and vice-versa.

In a further test, all possible combinations of six sensors were used to "back" predict the identity of the solvents based on a lowest RMS match value. The best combination of six detectors is reported in Table VII and Table VIII since the quality of the predictions was exactly the same for these two cases. The results in Table VII correspond to the case of six detectors where the poly (caprolactone) sensor was excluded. The results in Table VIII correspond to the case where the poly (ethylene-co-vinyl acetate) sensor was excluded. Using six detectors, eleven solvents were predicted correctly as the best candidate, six detectors were predicted correctly in the second best ranking, and three solvents were predicted correctly in the third place ranking. These results are slightly superior to the seven detector case where five detectors were predicted correctly with second best ranking, and three detectors were predicted correctly in the third place ranking. As in the seven detector case, most if not all of the three best predicted candidate solvents were very similar in nature to the test solvent in the six sensors study. In summary, the probability that the experimental solvent will be found within the best three predicted candidate solvents is 20/22 for the six best detectors.

Finally, all possible combinations of three sensors were used to "back" predict the identity of the solvents based on a lowest RMS value match value. The best combination of three detectors was Polysulfone, Poly (ethylene-co-vinyl acetate) and poly (4-hydroxy styrene). The results for the solvent predictions are reported in Table IX The accuracy of the predictions was almost as good as the six and seven detector cases. Eleven solvents were predicted correctly at the first rank level; four solvents were predicted in the second rank level and four solvents were predicted correctly in

the third rank level. In summary, the probability that the experimental solvent will be found within the best three predicted candidate solvents is 19/22 for the three best detectors.

Conclusion

The experimentally determined relative change in resistivities for a series of solvents in an array of seven carbon black filled polymer detectors were successfully modeled with calculated solvent bulk properties through a permeability equation. From these models, it was found that three good sensors are sufficient to "back" identify most (19/22) of the solvents correctly within the first three best predictions for each test case solvent. Very slight improvement was gained by using all seven detectors to "back" identify the solvents where (20/22) of the solvents were found within the three best predictions for each test case solvent.

The current model should be most useful in selecting materials for chemically sensitive detectors. For example, from the modeling studies reported, it becomes apparent that the sensors in which there is a clear correlation between modeling and experiment are those with high glass transitions, and/or with highly selective functional groups. Therefore, sensors such as Bisphenol A Polycarbonate, polystyrene, poly (lactams) such as poly (caprolactam), and poly (acrylonitrile) would be highly desirable since they have high glass transitions that would discriminate readily between different molecular sizes and/or special functional groups that would interact favorably with specific kinds of solvents.

Finally, this work may be extended towards the identification and first principles prediction of the sensor signal patterns of compounds of military and biological interest

that would be too costly or harmful to measure in the laboratory such as nerve gases (VX, Sarin), volatile derivatives of trinitrotoluene, MX and other explosive materials..

Modeling Procedures

A method was developed to determine precisely the cohesive energies of solvents and polymers based on periodic boundary conditions. The procedure is to build the original unit cell of twelve solvent molecules at 50% the target density with the amorphous builder in the Cerius2 software package with a Van der Waals radius-scaling factor of 0.30. This study used the experimental density of the solvent/polymer as the target density. The charges of the isolated solvent or polymer molecules were based on the charge equilibration method[3] and the rest of the parameters were taken from the Dreidiing forcefield.[4] (However, it is recommended to use quantum mechanical electrostatic potential derived charges (ESP) for electronically complex molecules such as trinitro toluene). Then the potential energy of the bulk system is minimized for 5000 steps or until the atom rms force converges to 0.10 kcal/molÅ. Then dynamics is done for 750 steps (1fs/step) at a temperature of 700 K using canonical fixed volume dynamics (TVN) to relax the system more efficiently and then the atoms are minimized locally with the previous procedure. Then the reduced cell coordinates are decreased such that the density is 64 % of the target or experimental density. Then the atoms' coordinates are minimized and dynamics is done on the system with the previously described procedure. Then the atom coordinates are minimized, holding the cell fixed. The compression and relaxation procedure is repeated a total of five times until the density reaches 120 % of the target density. Then the cell parameters are

increased such that the density is 116 % of the target density. Then the atom coordinates are minimized, followed by 750 steps of dynamics at 700 K and atom minimization is carried out once again. The expansion and relaxation procedure is repeated in five uniform steps until the target density (100 %) is reached. Then all of the degrees of freedom are allowed to relax in a minimization involving the cell and the atoms' coordinates. Cohesive energy density components are calculated by subtracting the potential energy of the bulk system from the sum of the non-relaxed potential energy of the individual molecules. Ten independent relaxed samples were created in this way, and the average Hansen cohesive energy components and molar volumes were computed as well as the standard deviations. The polymer calculations were performed in a similar way, except four polymer chains were used in a unit cell, and the number of monomers in each chain was determined such that the total volume of the four chains was approximately 5900 $Å^3$. The initial polymer amorphous structures were constructed using a one-dimensional rotational isomeric states (RIS) approach to achieve a correct distribution of conformational states. Finally, the fitting of the coefficients of the permeability equation (Equations 1-3) was done with the Office 97 *Excel* Software package.

References

[1]Sato, T.; Hirono, J.; Tonoike, M.; Takebayashi, M.; *Journal of Neurophysiology*, **72**(6), 2980 (1994)
[2]Krevelen, D. W. Van; Properties of Polymers: *Their Correlation with Chemical Structure; their Numerical Estimation and Prediction from Group Contributions*, Elsevier Science Publishers, NY (1990), pg 536
[2b]Ibid 1, page 575
[2c]Ibid 1, page 574
[3]Rappe, A. K.; Goddard, W. A. III; *Journal of Physical Chemistry*, **95**(8), 3358-3363, (1991)
[4]Mayo, S. L.; Olafson, B. D.; Goddard, W. A. III.; *Journal of Physical Chemistry*, **94**(26), 8897-8909 (1990)

Table I. Calculated cohesive energy density components and molar volumes for various solvents.

Cohesive energies are in cal/cc units and the molar volume is given in cc/mol.

Solvent	Electrostatic CED, cal/cc	Dispersive CED, cal/cc	Hydrogen bond CED cal/cc	Molar Volume cc/mol	Total CED cal/cc
2-pentanol	-53.320	-76.480	-21.620	99.045	-151.420
3-pentanol	-47.890	-76.870	-17.640	100.170	-142.400
Amylacetate	-40.190	-87.130	0.000	137.040	-127.310
Butylacetate	-41.750	-90.280	0.000	119.753	-132.030
Decylacetate	-21.020	-83.680	0.000	220.135	-104.700
Ethanol	-146.000	-51.350	-60.290	52.351	-257.640
Ethylacetate	-68.990	-90.330	0.000	87.238	-159.310
Hexylacetate	-34.830	-87.720	0.000	151.805	-122.550
Iso-amylalcohol	-59.820	-73.870	-25.770	99.045	-159.460
Isoamylacetate	-38.670	-87.240	0.000	135.613	-125.900
Isoamylbenzoate	-23.040	-96.520	0.000	186.659	-119.560
Isoamylbutyrate	-25.340	-86.170	0.000	168.343	-111.520
Isoamylcaproate	-20.830	-83.740	0.000	202.489	-104.570
Isoamylpropionate	-30.360	-82.810	0.000	155.065	-113.170
Isobutylacetate	-45.050	-85.870	0.000	121.001	-130.920
Isopropylacetate	-57.200	-86.260	0.000	104.218	-143.460
n-amylalcohol	-59.530	-75.460	-24.440	100.170	-159.420
n-heptanol	-37.630	-76.590	-16.010	133.568	-130.230
n-hexanol	-46.420	-77.970	-16.990	116.110	-141.380
n-propanol	-94.680	-60.770	-38.370	69.879	-193.820
Octanol	-33.800	-79.910	-13.880	147.990	-127.590
Octylacetate	-26.420	-85.950	0.000	187.249	-112.370
Propylacetate	-54.900	-88.060	0.000	104.218	-142.960
n-butanol	-64.310	-61.580	-26.820	88.242	-152.720

Table II . Calculated cohesive energy density components for various polymers.

Sensor	Electrostatic CED, cal/cc	Dispersive CED, cal/cc	Hbond CED, cal/cc	Density g/cc	Total CED, cal/cc
Caprolactone	-35.310	-87.340	0.000	1.090	-122.650
Polysulfone	-29.760	-108.980	0.000	1.300	-138.740
PMMA	-31.190	-59.320	0.000	1.110	-90.510
PEVA	-10.820	-74.200	0.000	0.960	-85.020
PE	-1.000	-84.460	0.000	0.880	-85.450
PEO	-68.360	-95.900	-3.840	1.130	-168.100
4-HydroxyPS	-28.660	-64.480	-13.510	1.090	-106.660

Table III. Best fit permeability equation constants for Equation 2 for each of seven detectors.

Sensor	A Prexp	C4 Diffusion	C1 Electrostatic	C2 Dispersion	C3 Hbond
Caprolactone[a]	0.1165	1.8090	0.0115	0.1637	0.2056
Polysulfone[b]	6.6045	-10.9816	0.0760	0.0350	0.2603
PMMA[c]	11.3873	-10.5002	0.1653	0.0736	0.1834
PEVA [d]	0.7058	0.0152	0.0723	0.0823	0.1490
PE[e]	0.2519	3.4577	0.0271	0.1996	0.2561
PEO[f]	0.2006	3.4888	-0.0214	0.0911	0.0911
4-HydroxyPS[g]	1404.0528	-57.0429	0.1272	-0.1853	0.2107

[a]Outliers decylacetate and hexylacetate were excluded from fit. [b]Outliers butylacetate and n-amyl alcohol were excluded from fit. [c]Outliers hexylacetate and propylacetate were excluded from fit. [d]Outliersdecylacetate and n-amylacetate were excluded from fit. [e]Outliers decylacetate and hexylacetate were excluded from fit. [f]Outliers decylacetate and hexylacetate were excluded from fit. [g]Outliers decylacetate and propylacetate were excluded from fit.

Table IV. Predicted relative resistivities of various solvents on polymer sensors using the best fit constants on Table III.

Sensor Caprolactone Solvent name	Experimental Relative change In Resistivity	Experimental Uncertainty	Calculated Relative change in Resistivity	Calculated-Exptl. Difference
2-pentanol	0.0909	0.0089	0.0975	0.0066
3-pentanol	0.1383	0.0106	0.1117	-0.0266
Amylacetate	0.1896	0.0069	0.1762	-0.0134
Butylacetate	0.1513	0.0151	0.1502	-0.0011
Decylacetate*	0.0779	0.0129	0.3033	0.2254
Ethanol	0.0648	0.0079	0.0687	0.0039
Ethylacetate	0.1192	0.0076	0.1337	0.0145
Hexylacetate*	0.2387	0.0203	0.1826	-0.0561
Iso-amylalcohol	0.1250	0.0139	0.0897	-0.0353
Isoamylacetate	0.1827	0.0736	0.1755	-0.0072
Isoamylbenzoate	0.0972	0.0104	0.1342	0.0370
Isoamylbutyrate	0.2277	0.0248	0.2126	-0.0151
Isoamylcaproate	0.2712	0.0277	0.2802	0.0090
Isoamylpropionate	0.2207	0.0201	0.2307	0.0100
Isobutylacetate	0.1562	0.0105	0.1732	0.0170
Isopropylacetate	0.1297	0.0108	0.1581	0.0284
n-amylalcohol	0.1084	0.0125	0.0896	-0.0188
n-heptanol	0.1213	0.0079	0.1233	0.0020
n-hexanol	0.1087	0.0090	0.1103	0.0016
n-propanol	0.0702	0.0046	0.0876	0.0174
Octanol	0.1276	0.0075	0.1221	-0.0055
Octylacetate	0.2466	0.0212	0.2292	-0.0174
Propylacetate	0.2002	0.0243	0.1508	-0.0494
n-butanol	0.0786	0.0054	0.1196	0.0410

*Solvent was excluded from fit.

Table IVB. Polysulfone results.

Sensor Polysulfone Solvent name	Experimental Relative change In Resistivity	Experimental Uncertainty	Calculated Relative change in Resistivity	Calculated-Exptl. Difference
2-pentanol	0.3850	0.0409	0.3677	-0.0173
3-pentanol	0.4159	0.0340	0.4536	0.0377
Amylacetate	0.5065	0.0507	0.5163	0.0098
Butylacetate*	0.9463	0.0705	0.6799	-0.2664
Decylacetate	0.1632	0.0564	0.1980	0.0348
Ethanol	0.2953	0.0263	0.3415	0.0462
Ethylacetate	0.9467	0.0797	0.9288	-0.0179
Hexylacetate	0.5329	0.0419	0.4333	-0.0996
Iso-amylalcohol	0.3139	0.0748	0.2869	-0.0270
Isoamylacetate	0.4121	0.2033	0.5440	0.1319
Isoamylbenzoate	0.2334	0.0876	0.2791	0.0457
Isoamylbutyrate	0.3998	0.0287	0.4015	0.0017
Isoamylcaproate	0.2668	0.0368	0.2633	-0.0035
Isoamylpropionate	0.4438	0.0572	0.4672	0.0234
Isobutylacetate	0.6114	0.0684	0.6510	0.0396
Isopropylacetate	0.7440	0.0400	0.7612	0.0172
n-amylalcohol*	0.4658	0.0503	0.2919	-0.1739
n-heptanol	0.2939	0.0321	0.2442	-0.0497
n-hexanol	0.4025	0.0374	0.3106	-0.0919
n-propanol	0.3320	0.0191	0.3787	0.0467
Octanol	0.1676	0.0194	0.2053	0.0377
Octylacetate	0.3639	0.0861	0.2863	-0.0776
Propylacetate	0.8482	0.0460	0.7763	-0.0719
n-butanol	0.4228	0.0396	0.3929	-0.0299

*Solvent was excluded from fit.

Table IVC. Poly (methyl methacrylate) results.

Sensor PMMA Solvent name	Experimental Relative change in Resistivity	Experimental Uncertainty	Calculated Relative change in Resistivity	Calculated-Exptl. Difference
2-pentanol	0.3911	0.0650	0.4445	0.0534
3-pentanol	0.4451	0.0461	0.5615	0.1164
Amylacetate	0.3082	0.0863	0.4421	0.1339
Butylacetate	0.7001	0.0599	0.6032	-0.0969
Decylacetate	0.1999	0.0511	0.2201	0.0202
Ethanol	0.3371	0.0939	0.3329	-0.0042
Ethylacetate	0.7694	0.0505	0.6895	-0.0799
Hexylacetate*	0.6675	0.1647	0.3866	-0.2809
Iso-amylalcohol	0.3716	0.0692	0.3377	-0.0339
Isoamylacetate	0.5224	0.2795	0.4835	-0.0389
Isoamylbenzoate	0.1553	0.0320	0.2680	0.1127
Isoamylbutyrate	0.6223	0.1329	0.4316	-0.1907
Isoamylcaproate	0.2745	0.0689	0.3048	0.0303
Isoamylpropionate	0.5367	0.1100	0.4796	-0.0571
Isobutylacetate	0.4704	0.1015	0.5592	0.0888
Isopropylacetate	0.4809	0.0712	0.5934	0.1125
n-amylalcohol	0.4946	0.0554	0.3342	-0.1604
n-heptanol	0.3281	0.0927	0.3244	-0.0037
n-hexanol	0.4022	0.1019	0.3675	-0.0347
n-propanol	0.4589	0.0821	0.4112	-0.0477
Octanol	0.2190	0.0650	0.2684	0.0494
Octylacetate	0.2897	0.0782	0.2839	-0.0058
Propylacetate*	0.8928	0.1590	0.6199	-0.2729
n-butanol	0.4491	0.0888	0.4934	0.0443

*Solvent was excluded from fit

Table IVD. Poly (ethylene-co-vinyl acetate) results.

Sensor PEVA Solvent name	Experimental Relative change in Resistivity	Experimental Uncertainty	Calculated Relative change in Resistivity	Calculated-Experimental Difference
2-pentanol	0.2284	0.0306	0.2393	0.0109
3-pentanol	0.2642	0.0305	0.2778	0.0136
Amylacetate*	0.4594	0.0244	0.3388	-0.1206
Butylacetate	0.3443	0.0325	0.3447	0.0004
Decylacetate*	0.2136	0.0568	0.4038	0.1902
Ethanol	0.1804	0.0274	0.1590	-0.0214
Ethylacetate	0.2786	0.0413	0.3131	0.0345
Hexylacetate	0.3707	0.0224	0.3414	-0.0293
Iso-amylalcohol	0.2465	0.0725	0.2068	-0.0397
Isoamylacetate	0.3910	0.1572	0.3493	-0.0417
Isoamylbenzoate	0.2749	0.0565	0.3008	0.0259
Isoamylbutyrate	0.4272	0.0306	0.3975	-0.0297
Isoamylcaproate	0.3982	0.0317	0.4235	0.0253
Isoamylpropionate	0.4215	0.0298	0.4066	-0.0149
Isobutylacetate	0.3871	0.0475	0.3509	-0.0362
Isopropylacetate	0.2888	0.0427	0.3294	0.0406
n-amylalcohol	0.2374	0.0540	0.2070	-0.0304
n-heptanol	0.2517	0.0425	0.2555	0.0038
n-hexanol	0.2441	0.0321	0.2448	0.0007
n-propanol	0.1725	0.0315	0.2007	0.0282
Octanol	0.2570	0.0483	0.2480	-0.0090
Octylacetate	0.3364	0.0433	0.3657	0.0293
Propylacetate	0.3326	0.0423	0.3305	-0.0021
n-butanol	0.2198	0.0395	0.2559	0.0361

* Solvent was excluded from fit.

Table IVE. Poly (ethylene) results.

Sensor Poly(ethylene) Solvent name	Experimental Relative change in Resistivity	Experimental Uncertainty	Calculated Relative change in Resistivity	Calculated-Experimental Difference
2-pentanol	0.1634	0.0312	0.1831	0.0197
3-pentanol	0.1814	0.0391	0.2194	0.0380
Amylacetate	0.4463	0.0771	0.3876	-0.0587
Butylacetate	0.3248	0.0793	0.3205	-0.0043
Decylacetate*	0.1937	0.0426	0.7890	0.5953
Ethanol	0.1207	0.0248	0.1106	-0.0101
Ethylacetate	0.2192	0.0406	0.2689	0.0497
Hexylacetate*	0.5949	0.0311	0.4089	-0.1860
Iso-amylalcohol	0.2523	0.0689	0.1624	-0.0899
Isoamylacetate	0.4451	0.1708	0.3876	-0.0575
Isoamylbenzoate	0.2092	0.0634	0.2906	0.0814
Isoamylbutyrate	0.5946	0.0501	0.5065	-0.0881
Isoamylcaproate	0.6414	0.0695	0.7183	0.0769
Isoamylpropionate	0.6019	0.0716	0.5514	-0.0505
Isobutylacetate	0.3092	0.0662	0.3777	0.0685
Isopropylacetate	0.2472	0.0274	0.3323	0.0851
n-amylalcohol	0.2255	0.0582	0.1624	-0.0631
n-heptanol	0.2400	0.0234	0.2482	0.0082
n-hexanol	0.2516	0.0600	0.2140	-0.0376
n-propanol	0.1166	0.0270	0.1537	0.0371
Octanol	0.2719	0.0444	0.2470	-0.0249
Octylacetate	0.5746	0.0754	0.5504	-0.0242
Propylacetate	0.3654	0.0381	0.3154	-0.0500
n-butanol	0.1363	0.0196	0.2317	0.0954

*Solvent was excluded from fit.

Table IVF. Poly (ethylene-oxide) results.

Sensor PEO Solvent name	Experimental Relative change in Resistivity	Experimental Uncertainty	Calculated Relative change in Resistivity	Calculated-Exptl. Difference
2-pentanol	0.2992	0.0146	0.3493	0.0501
3-pentanol	0.3624	0.0240	0.3643	0.0019
Amylacetate	0.5780	0.0205	0.5102	-0.0678
Butylacetate	0.4569	0.0398	0.4309	-0.0260
Decylacetate*	0.2299	0.0185	0.8670	0.6371
Ethanol	0.2380	0.0200	0.2875	0.0495
Ethylacetate	0.3659	0.0321	0.3813	0.0154
Hexylacetate*	0.7255	0.0485	0.5403	-0.1852
Iso-amylalcohol	0.3905	0.0434	0.3492	-0.0413
Isoamylacetate	0.4931	0.2107	0.5004	0.0073
Isoamylbenzoate	0.3789	0.0251	0.4865	0.1076
Isoamylbutyrate	0.6336	0.0424	0.5914	-0.0422
Isoamylcaproate	0.6845	0.0403	0.7685	0.0840
Isoamylpropionate	0.6054	0.0368	0.6052	-0.0002
Isobutylacetate	0.4278	0.0281	0.4784	0.0506
Isopropylacetate	0.3578	0.0153	0.4412	0.0834
n-amylalcohol	0.3849	0.0339	0.3497	-0.0352
n-heptanol	0.5040	0.0369	0.4398	-0.0642
n-hexanol	0.4374	0.0130	0.3949	-0.0425
n-propanol	0.2493	0.0150	0.3257	0.0764
Octanol	0.5413	0.0471	0.4565	-0.0848
Octylacetate	0.7351	0.0408	0.6769	-0.0582
Propylacetate	0.5703	0.0742	0.4249	-0.1454
n-butanol	0.2910	0.0101	0.3885	0.0975

* Solvents were excluded from fit

Table IVG. Poly (4-hydroxy styrene) results.

Sensor 4-HydroxyPS Solvent name	Experimental Relative change in Resistivity	Experimental Uncertainty	Calculated Relative change in Resistivity	Calculated-Exptl. Difference
2-pentanol	0.0361	0.0056	0.0649	0.0288
3-pentanol	0.0439	0.0066	0.0759	0.0320
Amylacetate	0.0484	0.0142	0.0094	-0.0390
Butylacetate	0.0674	0.0207	0.0457	-0.0217
Decylacetate*	0.0621	0.0102	0.0000	-0.0621
Ethanol	0.8128	0.0514	0.8154	0.0026
Ethylacetate	0.4638	0.0989	0.4540	-0.0098
Hexylacetate	0.0424	0.0152	0.0032	-0.0392
Iso-amylalcohol	0.0476	0.0188	0.0450	-0.0026
Isoamylacetate	0.0488	0.0548	0.0112	-0.0376
Isoamylbenzoate	0.0590	0.0088	0.0004	-0.0586
Isoamylbutyrate	0.0210	0.0065	0.0010	-0.0200
Isoamylcaproate	0.0331	0.0053	0.0001	-0.0330
Isoamylpropionate	0.0306	0.0111	0.0022	-0.0284
Isobutylacetate	0.0338	0.0097	0.0319	-0.0019
Isopropylacetate	0.0520	0.0141	0.1083	0.0563
n-amylalcohol	0.0800	0.0176	0.0444	-0.0356
n-heptanol	0.0145	0.0049	0.0041	-0.0104
n-hexanol	0.0232	0.0033	0.0176	-0.0056
n-propanol	0.3152	0.0215	0.3082	-0.0070
Octanol	0.0120	0.0037	0.0015	-0.0105
Octylacetate	0.0282	0.0167	0.0002	-0.0280
Propylacetate*	0.3872	0.0712	0.1209	-0.2663
n-butanol	0.1103	0.0066	0.0881	-0.0222

*Solvents were excluded from fit.

Table V. Pearson R values and slopes of the correlation plots of predicted against experimental relative change in resistivities for each of seven detectors.

Detector name	Slope	R value	Figure number
Poly(caprolactone)	0.858	0.925	1
Poly(sulfone)	0.932	0.962	2
PMMA	0.678	0.827	3
PEVA	0.888	0.936	4
Poly(ethylene)	0.870	0.933	5
PEO	0.746	0.874	6
4-HydroxyPS	1.018	0.991	7

Table VI. Back prediction of the identity of twenty two solvents based on the minimum RMS differences between the experimental relative change in resistivity and the predicted relative change in resistivity using the best fit coefficients for the permeability relation (Equation 1) using seven detectors.

Test Solvent	**Best match**	**Second Best**	**Third Best**
2-pentanol	**2-pentanol**	n-amylalcohol	iso-amylalcohol
RMS	0.0317	0.0463	0.0471
3-pentanol	2-pentanol	n-butanol	**3-pentanol**
RMS	0.0273	0.0347	0.0512
Amylacetate	Isoamylbutyrate	**Amylacetate**	Isoamylpropionate
RMS	0.0724	0.0777	0.0839
Butylacetate	Propylacetate	Isopropylacetate	**Butylacetate**
RMS	0.0751	0.0827	0.1079
Ethanol	**Ethanol**	n-propanol	2-pentanol
RMS	0.0272	0.1989	0.2920
Ethylacetate	**Ethylacetate**	Propylacetate	Isopropylacetate
RMS	0.0395	0.1627	0.1750
Iso-amylalcohol	n-hexanol	n-heptanol	n-amylalcohol
RMS	0.0194	0.0405	0.0454
Isoamylacetate	Isoamylbutyrate	Amylacetate	**Isoamylacetate**
RMS	0.0598	0.0600	0.0603
Isoamylbenzoate	Octanol	n-heptanol	**Isoamylbenzoate**
RMS	0.0606	0.0737	0.0741
Isoamylbutyrate	Isoamylpropionate	**Isoamylbutyrate**	Isoamylacetate
RMS	0.0637	0.0823	0.1251
Isoamylcaproate	Octylacetate	**Isoamylcaproate**	Isoamylbutyrate
RMS	0.0426	0.0474	0.1029
Isoamylpropionate	**Isoamylpropionate**	Isoamylbutyrate	Isoamylacetate
RMS	0.0327	0.0581	0.1052
Isobutylacetate	**Isobutylacetate**	Isoamylacetate	Butylacetate
RMS	0.0511	0.0513	0.0591
Isopropylacetate	**Isopropylacetate**	Butylacetate	Propylacetate
RMS	0.0684	0.0690	0.0722
n-amylalcohol	n-butanol	3-pentanol	2-pentanol
RMS	0.0290	0.0310	0.0471
n-heptanol	**n-heptanol**	Isoamylbenzoate	Octanol
RMS	0.0311	0.0368	0.0446
n-hexanol	**n-hexanol**	n-butanol	2-pentanol
RMS	0.0429	0.0473	0.0498
n-propanol	**n-propanol**	2-pentanol	n-butanol
RMS	0.0428	0.1094	0.1186
Octanol	**Octanol**	Isoamylbenzoate	n-heptanol
RMS	0.0412	0.0538	0.0632
Octylacetate	**Octylacetate**	Isoamylcaproate	Isoamylbutyrate
RMS	0.0414	0.0771	0.0866
Propylacetate	Ethylacetate	**Propylacetate**	Isopropylacetate
RMS	0.1208	0.1588	0.1667
n-butanol	2-pentanol	**n-butanol**	3-pentanol
RMS	0.0404	0.0597	0.0671

Table VII. Back prediction of the identity of twenty two solvents based on the minimum RMS differences between the experimental relative change in resistivity and the predicted relative change in resistivity using the best fit coefficients for the permeability relation (Equation 1) using six detectors (poly(Caprolactone) excluded).

Test Solvent	Best Match	Second Best	Third Best
2-pentanol	**2-pentanol**	n-amylalcohol	iso-amylalcohol
RMS	0.0342	0.0500	0.0509
3-pentanol	2-pentanol	n-butanol	**3-pentanol**
RMS	0.0244	0.0367	0.0542
Amylacetate	Isoamylbutyrate	**Amylacetate**	Isoamylpropionate
RMS	0.0776	0.0838	0.0891
Butylacetate	Propylacetate	Isopropylacetate	**Butylacetate**
RMS	0.0811	0.0893	0.1166
Ethanol	**Ethanol**	n-propanol	2-pentanol
RMS	0.0294	0.2146	0.3152
Ethylacetate	**Ethylacetate**	Propylacetate	Isopropylacetate
RMS	0.0422	0.1753	0.1883
Iso-amylalcohol	n-hexanol	n-heptanol	n-amylalcohol
RMS	0.0200	0.0438	0.0469
Isoamylacetate	Isoamylbutyrate	Amylacetate	**Isoamylacetate**
RMS	0.0634	0.0648	0.0651
Isoamylbenzoate	Octanol	**Isoamylbenzoate**	n-heptanol
RMS	0.0646	0.0786	0.0789
Isoamylbutyrate	Isoamylpropionate	**Isoamylbutyrate**	Isoamylacetate
RMS	0.0687	0.0887	0.1334
Isoamylcaproate	Octylacetate	**Isoamylcaproate**	Isoamylbutyrate
RMS	0.0427	0.0510	0.1086
Isoamylpropionate	**Isoamylpropionate**	Isoamylbutyrate	Isoamylacetate
RMS	0.0351	0.0627	0.1121
Isobutylacetate	**Isobutylacetate**	Isoamylacetate	Butylacetate
RMS	0.0548	0.0549	0.0638
Isopropylacetate	**Isopropylacetate**	Butylacetate	Propylacetate
RMS	0.0730	0.0741	0.0775
n-amylalcohol	n-butanol	3-pentanol	2-pentanol
RMS	0.0310	0.0335	0.0507
n-heptanol	**n-heptanol**	Isoamylbenzoate	Octanol
RMS	0.0336	0.0394	0.0481
n-hexanol	**n-hexanol**	n-butanol	2-pentanol
RMS	0.0464	0.0509	0.0536
n-propanol	**n-propanol**	2-pentanol	n-butanol
RMS	0.0457	0.1176	0.1265
Octanol	**Octanol**	Isoamylbenzoate	n-heptanol
RMS	0.0445	0.0581	0.0682
Octylacetate	**Octylacetate**	Isoamylcaproate	Isoamylbutyrate
RMS	0.0441	0.0821	0.0925
Propylacetate	Ethylacetate	**Propylacetate**	Isopropylacetate
RMS	0.1276	0.1704	0.1792
n-butanol	2-pentanol	**n-butanol**	3-pentanol
RMS	0.0430	0.0622	0.0712

Table VIII. Back prediction of the identity of twenty two solvents based on the minimum RMS differences between the experimental relative change in resistivity and the predicted relative change in resistivity using the best fit coefficients for the permeability relation (Equation 1) using six detectors (PEVA excluded).

Test Solvent	Best Match	Second Best	Third Best
2-pentanol	**2-pentanol**	n-amylalcohol	iso-amylalcohol
RMS	0.0340	0.0492	0.0501
3-pentanol	2-pentanol	n-butanol	**3-pentanol**
RMS	0.0277	0.0373	0.0550
Amylacetate	**Amylacetate**	Isoamylbutyrate	Isoamylacetate
RMS	0.0680	0.0740	0.0848
Butylacetate	Propylacetate	Isopropylacetate	**Butylacetate**
RMS	0.0809	0.0891	0.1166
Ethanol	**Ethanol**	n-propanol	2-pentanol
RMS	0.0281	0.2146	0.3145
Ethylacetate	**Ethylacetate**	Propylacetate	Isopropylacetate
RMS	0.0402	0.1745	0.1879
iso-amylalcohol	n-hexanol	n-heptanol	n-amylalcohol
RMS	0.0209	0.0436	0.0464
Isoamylacetate	Amylacetate	**Isoamylacetate**	Isoamylbutyrate
RMS	0.0612	0.0629	0.0645
Isoamylbenzoate	Octanol	n-heptanol	**Isoamylbenzoate**
RMS	0.0645	0.0792	0.0794
Isoamylbutyrate	Isoamylpropionate	**Isoamylbutyrate**	Isoamylacetate
RMS	0.0682	0.0881	0.1313
Isoamylcaproate	Octylacetate	**Isoamylcaproate**	Isoamylbutyrate
RMS	0.0441	0.0501	0.1112
Isoamylpropionate	**Isoamylpropionate**	Isoamylbutyrate	Amylacetate
RMS	0.0348	0.0620	0.1092
Isobutylacetate	**Isobutylacetate**	Isoamylacetate	Butylacetate
RMS	0.0532	0.0533	0.0614
Isopropylacetate	Butylacetate	**Isopropylacetate**	Propylacetate
RMS	0.0710	0.0720	0.0761
n-amylalcohol	3-pentanol	n-butanol	2-pentanol
RMS	0.0292	0.0304	0.0509
n-heptanol	**n-heptanol**	Isoamylbenzoate	Octanol
RMS	0.0336	0.0343	0.0481
n-hexanol	**n-hexanol**	n-butanol	2-pentanol
RMS	0.0464	0.0509	0.0537
n-propanol	**n-propanol**	2-pentanol	n-butanol
RMS	0.0448	0.1150	0.1235
Octanol	**Octanol**	Isoamylbenzoate	n-heptanol
RMS	0.0444	0.0553	0.0682
Octylacetate	**Octylacetate**	Isoamylcaproate	Isoamylbutyrate
RMS	0.0430	0.0753	0.0901
Propylacetate	Ethylacetate	**Propylacetate**	Isopropylacetate
RMS	0.1302	0.1716	0.1800
n-butanol	2-pentanol	**n-butanol**	3-pentanol
RMS	0.0430	0.0628	0.0685

Table IX. Back prediction of the identity of twenty two solvents based on the minimum RMS differences between the experimental relative change in resistivity and the predicted relative change in resistivity using the best fit coefficients for the permeability relation (Equation 1) using three detectors (Polysulfone, PEVA and 4-HydroxyPS).

Test Solvent	Best Match	Second Best	Third Best
2-pentanol	**2-pentanol**	n-butanol	n-hexanol
RMS	0.0204	0.0342	0.0452
3-pentanol	n-butanol	**3-pentanol**	2-pentanol
RMS	0.0291	0.0296	0.0336
Amylacetate	Isoamylpropionate	Isoamylacetate	**Amylacetate**
RMS	0.0464	0.0705	0.0734
Butylacetate	Propylacetate	Isopropylacetate	**Butylacetate**
RMS	0.1032	0.1098	0.1543
Ethanol	**Ethanol**	n-propanol	n-butanol
RMS	0.0295	0.2955	0.4244
Ethylacetate	**Ethylacetate**	Propylacetate	Isopropylacetate
RMS	0.0232	0.2231	0.2334
iso-amylalcohol	n-hexanol	n-amylalcohol	**iso-amylalcohol**
RMS	0.0174	0.0262	0.0278
Isoamylacetate	Isoamylbutyrate	Isoamylpropionate	Amylacetate
RMS	0.0285	0.0426	0.0711
Isoamylbenzoate	n-heptanol	Octanol	**Isoamylbenzoate**
RMS	0.0342	0.0401	0.0454
Isoamylbutyrate	**Isoamylbutyrate**	Isoamylpropionate	Octylacetate
RMS	0.0207	0.0421	0.0755
Isoamylcaproate	**Isoamylcaproate**	Octylacetate	Isoamylbenzoate
RMS	0.0241	0.0290	0.0597
Isoamylpropionate	**Isoamylpropionate**	Isoamylbutyrate	Amylacetate
RMS	0.0229	0.0329	0.0647
Isobutylacetate	**Isobutylacetate**	Isoamylacetate	Butylacetate
RMS	0.0310	0.0465	0.0470
Isopropylacetate	**Isopropylacetate**	Butylacetate	Propylacetate
RMS	0.0413	0.0492	0.0501
n-amylalcohol	3-pentanol	n-butanol	2-pentanol
RMS	0.0245	0.0437	0.0573
n-heptanol	n-hexanol	**n-heptanol**	Isoamylbenzoate
RMS	0.0106	0.0294	0.0307
n-hexanol	2-pentanol	n-butanol	3-pentanol
RMS	0.0315	0.0385	0.0466
n-propanol	**n-propanol**	n-butanol	2-pentanol
RMS	0.0318	0.1441	0.1510
Octanol	**Octanol**	n-heptanol	Isoamylbenzoate
RMS	0.0232	0.0445	0.0695
Octylacetate	Isoamylbutyrate	**Octylacetate**	Isoamylbenzoate
RMS	0.0443	0.0505	0.0555
Propylacetate	Ethylacetate	**Propylacetate**	Isopropylacetate
RMS	0.0615	0.1592	0.1687
n-butanol	**n-butanol**	2-pentanol	3-pentanol
RMS	0.0299	0.0427	0.0428

Figure

Correlation of Predicted versus Experimental Relative Resistivities

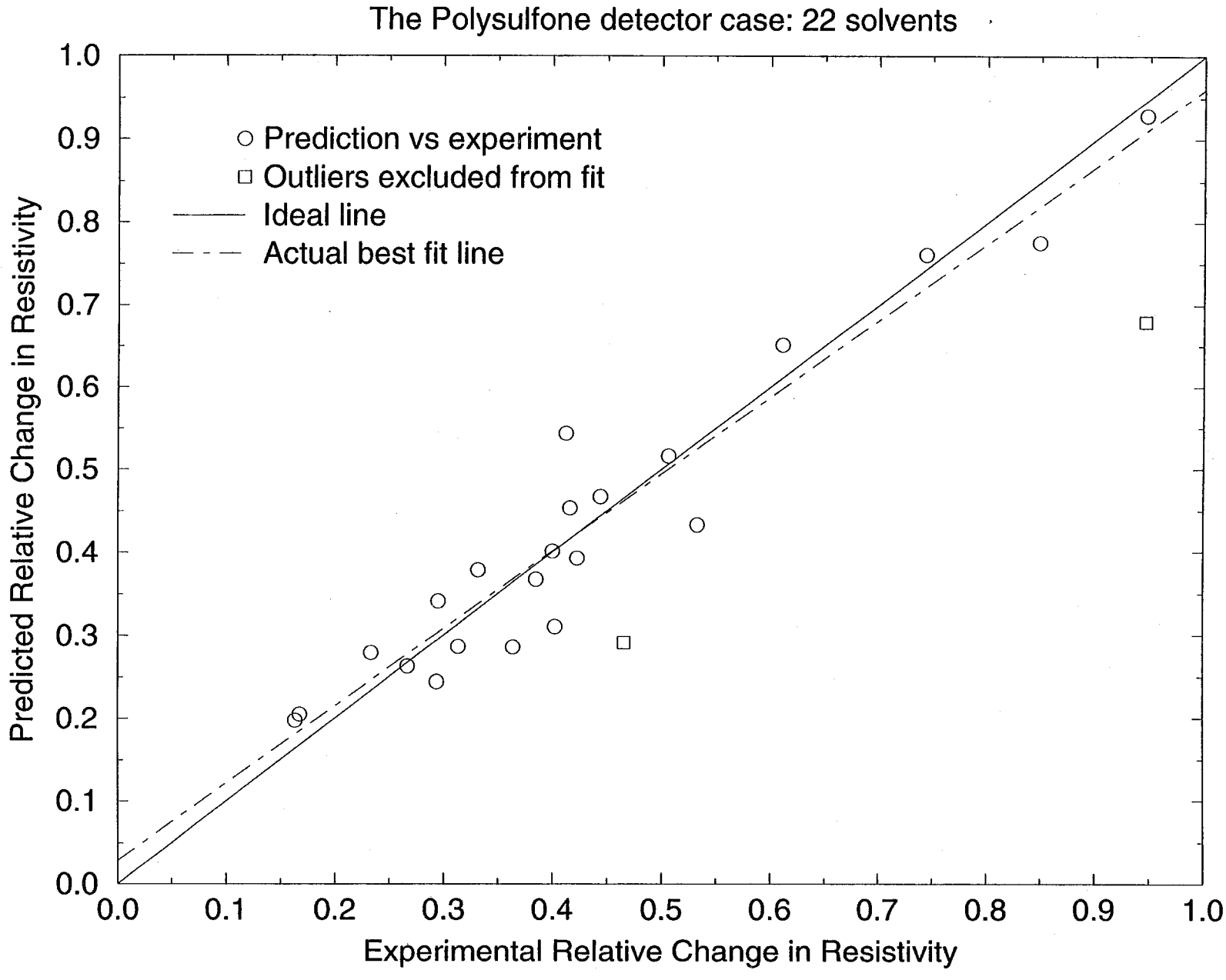

Figure 2

Correlation of Predicted versus Experimental Relative Resistivities

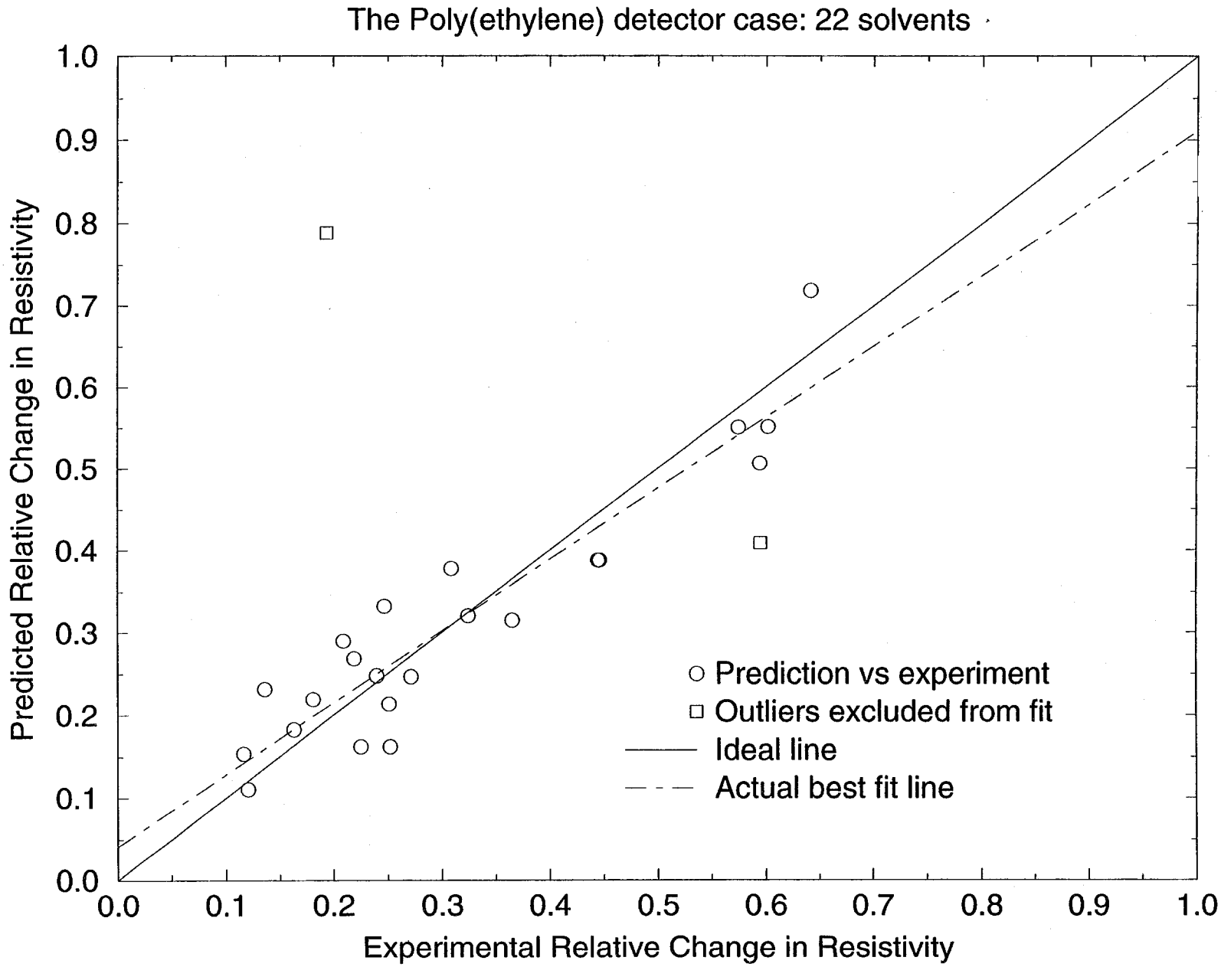

Figure 3

Correlation of Predicted versus Experimental Relative Resistivities

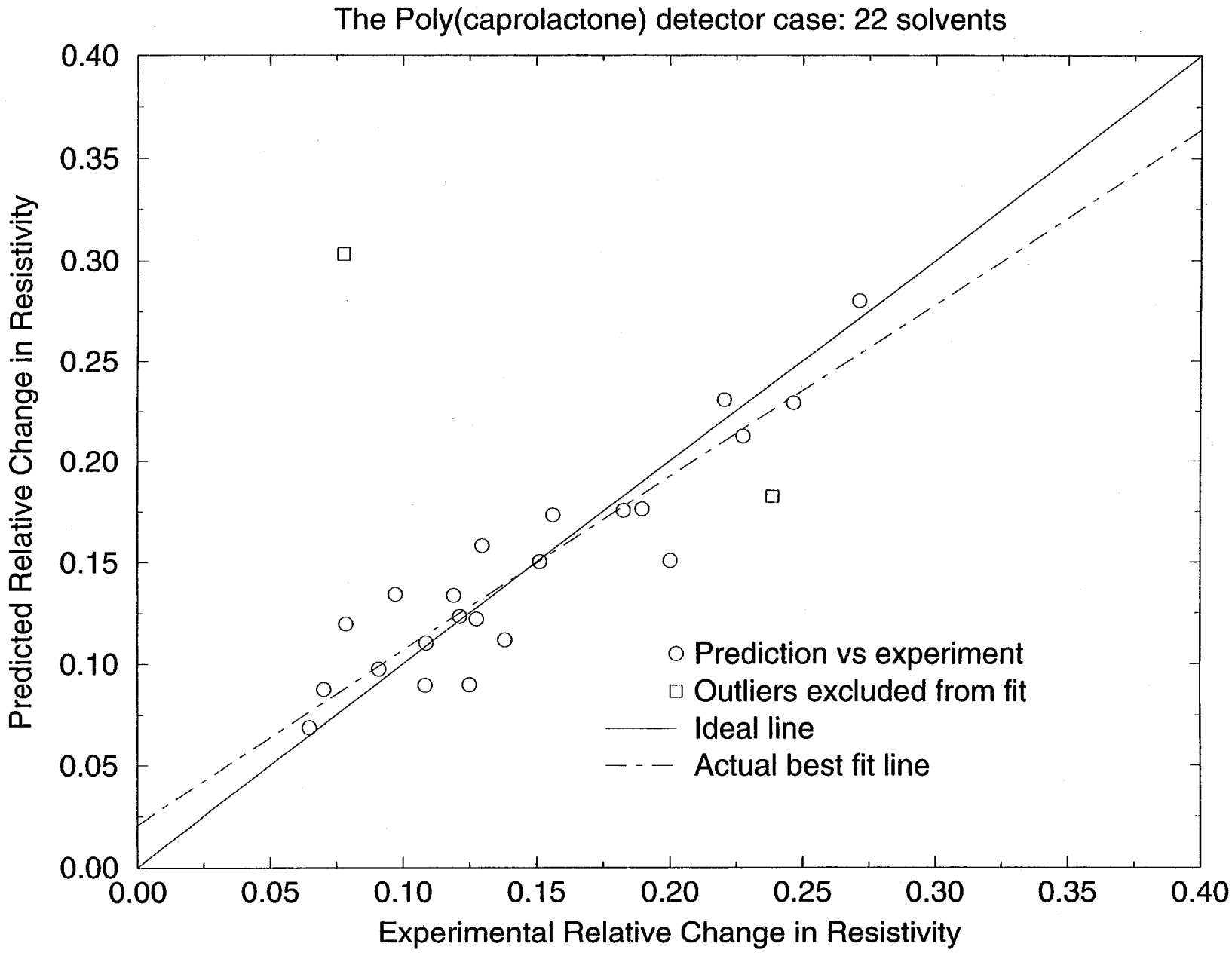

Figure 4

Correlation of Predicted versus Experimental Relative Resistivities

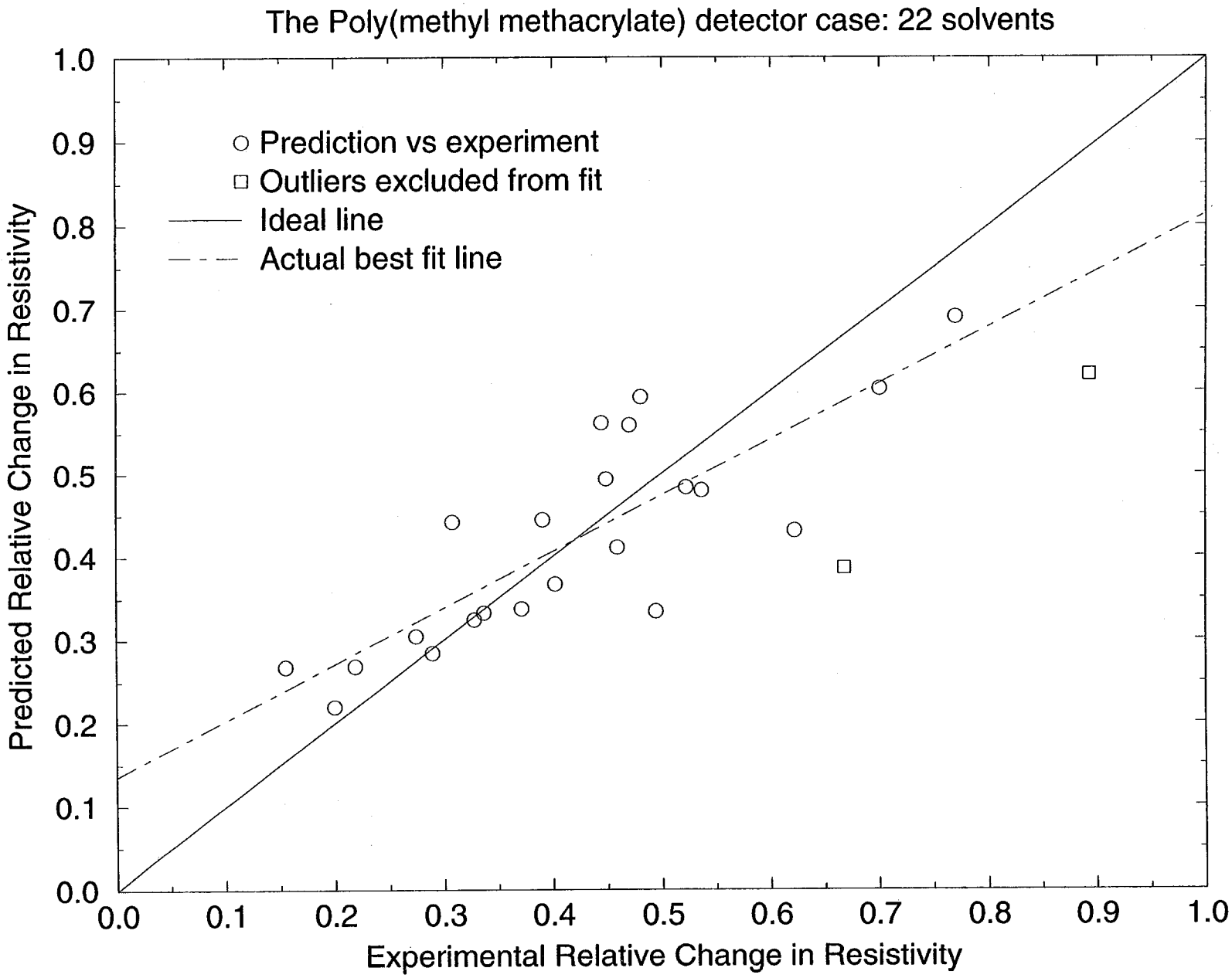

Figure 5

Correlation of Predicted versus Experimental Relative Resistivities

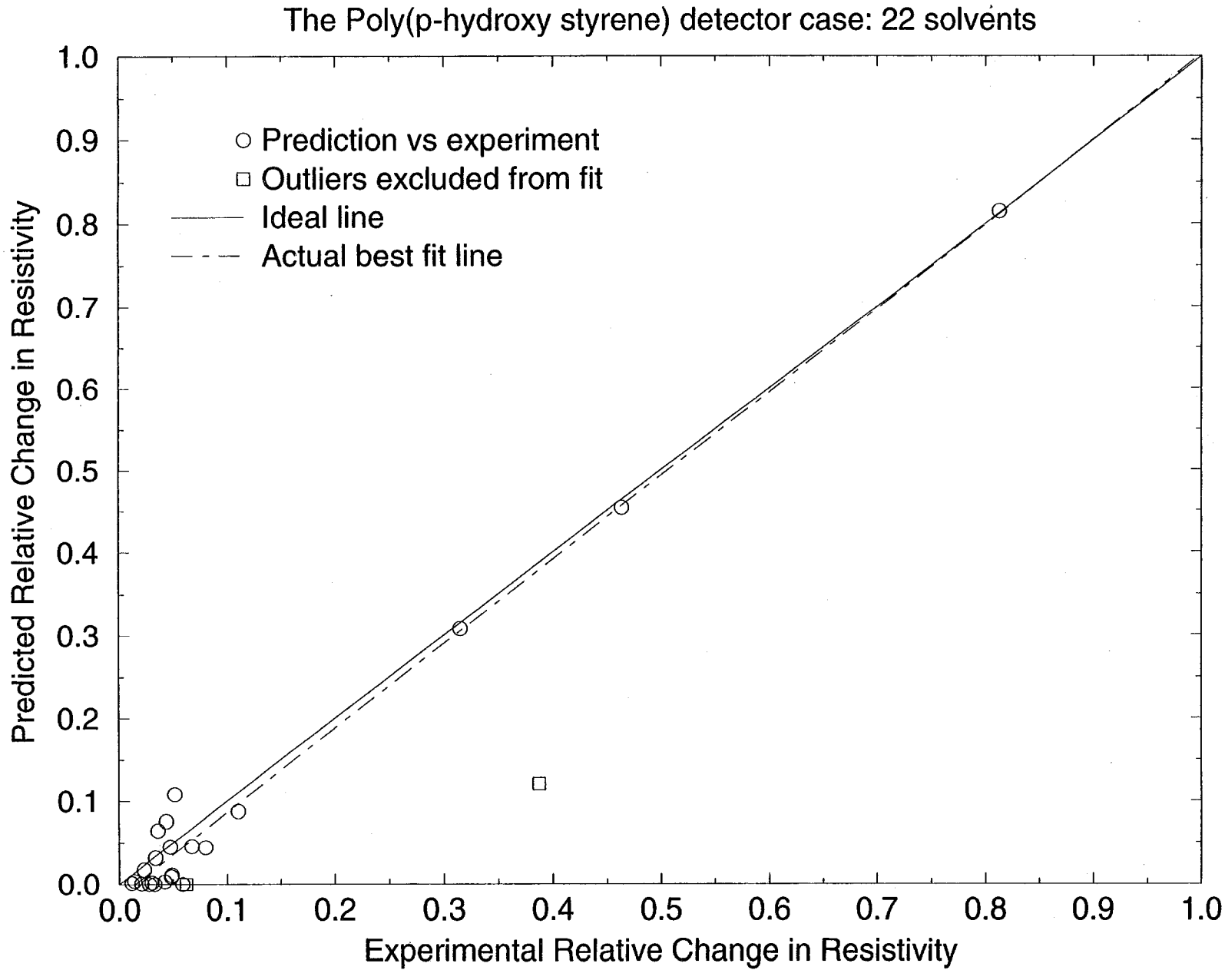

Figure 6

Correlation of Predicted versus Experimental Relative Resistivities

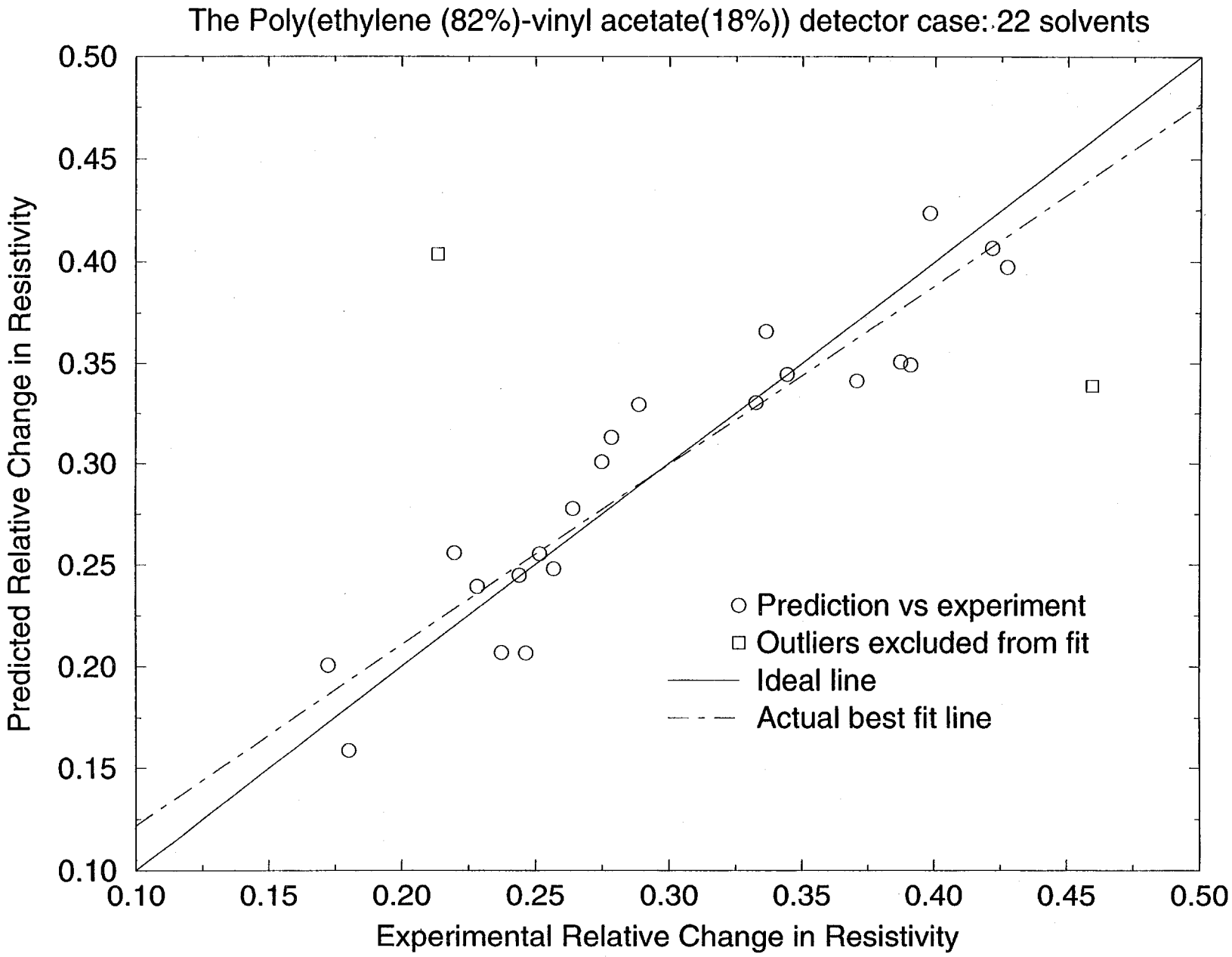

Figure 7

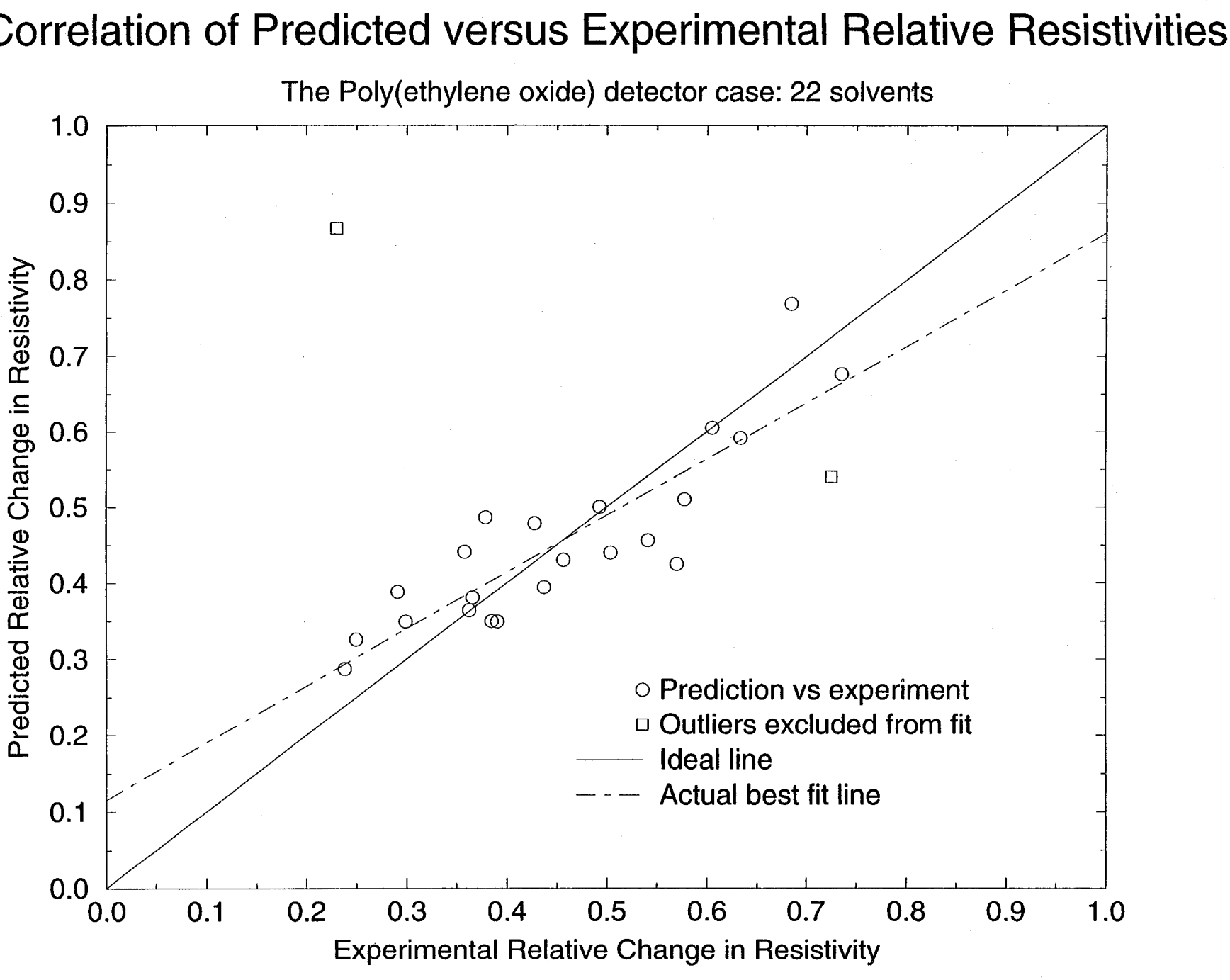
Correlation of Predicted versus Experimental Relative Resistivities
The Poly(ethylene oxide) detector case: 22 solvents
Predicted Relative Change in Resistivity
Experimental Relative Change in Resistivity
0.0
0.1
0.2
0.3
0.4
0.5
0.6
0.7
0.8
0.9
1.0
Prediction vs experiment
Outliers excluded from fit
Ideal line
Actual best fit line

Chapter 4

Abstract

The principle behind the electronic nose project is the prediction of the identity of vapor molecules based on patterns of relative change in resistivity of polymer sensors filled with carbon black upon exposure. A computational method was developed to efficiently calculate the direct energy of interaction between solvent molecules and bulk polymers. The experimentally derived relative change in resistivity in polysulfone for a series of twenty two esters and alcohols was successfully correlated with the electrostatic, hydrogen bonding, and Van der Waals binding energy components as well as the molecular volume through a permeability equation. A particularly good correlation between the relative change in resistivity and the permeability expression was obtained by scaling the interaction energy components by the molecular volume (cal/cc units).

Application of a New Method for the Electronic Nose Project: The Calculation of Interaction Energies of a Molecule with a Polymer with Minimal Host Structure Disruption

Introduction

The process and thermodynamics of sorption of a molecule inside a polymer or protein is of great usefulness for industrial, pharmaceutical and academic purposes. Various researchers have carried out numerous excellent atomistic studies of polymer permeation by small molecules. Suter and co-workers have developed an atomistic scheme for calculating the chemical potential of small molecules in polymer systems using Widom's insertion method and thermodynamic integration methods involving molecular dynamics.[1,2] The solubility of small molecules in polymers depends on the difference in chemical potential between the molecule in the polymer and the molecule in the pure state, which become equal at equilibrium. Other simpler studies involving molecular dynamics of the sorption of ethanol and water mixtures in poly (dimethyl siloxane) membranes have been reported.[3] The diffusion and sorption behavior of carbon dioxide in Bisphenol-A Polycarbonate has been studied at the molecular level as well.[4] However, the calculation of heats of sorption of relatively large molecules using first principles modeling techniques in polymers is of great interest in the "electronic nose" project and therefore, an efficient computational technique was developed to calculate energies of interactions between large molecules and polymers. The initial

results of the nose project clearly proved that there is a direct connection between sensor response to a penetrant, and quantities related to the intrinsic cohesive energy solvent properties. The goal of the second phase of the project is to calculate direct binding energies between polymers and molecules. As a result, a new modeling technique was created to efficiently insert a molecule in any region of a periodic bulk polymer, and relax efficiently the polymer/solute system without any major polymer structure perturbation while uniformly spreading the stresses into the whole system. A preliminary application of this method to the study of energies of interactions between twenty-four solvent molecules and the polysulfone polymer sensor will be presented.

Description of the Procedure

a) The first step in the procedure is to obtain an equilibrated periodic polymer sample through a special modeling procedure described in the previous "electronic nose sensor" chapter. The Dreiding forcefield was used in all calculations.[5] Charges for the polymer and molecule were calculated with the charge equilibration scheme (Qeq).[6] In this study, the initial polymer sample was a nearly cubic periodic box of eight polysulfone chains, with four monomers per chain. The density and volume of the system were 1.264 g/cc and 11551.5 $Å^3$ respectively. The box dimensions were 22.31 Å, 22.57 Å, and 22.96 Å for *a*, *b* and *c* respectively. The cell angles were 88.28°, 91.27°, 89.94° for α, β and γ respectively. The Ewald accuracy in the preliminary equilibration steps

of the polymer-solute system is 0.10 kcal/mol for both the Van der Waals and electrostatic energy calculation for computational expediency. Then the unit cell volume is expanded by a factor of five with respect to the target volume by scaling the *reduced* cell coordinates appropriately. The result is a very low-density system with many voids in which the polymer atoms are spread out uniformly. Then a solvent molecule is placed into a random position in the polymer "mist." A total of twenty seven uniform "reduced" cell positions are defined in the unit cell of the polymer and the "chain end" of the functional group of the molecule is placed into each of these twenty seven random positions, one molecule at a time. It should be noted that the geometry of each of the twenty-seven solvent molecules was obtained from the unit cells of the solvent study described in the previous chapter. Therefore, the molecular geometries for each solvent are random. Then the solvent molecule is relaxed by ten steps of *steepest descent* minimization in the *frozen* polymer, 30 steps of *conjugate gradient* minimization, followed by 250 steps of solvent molecule dynamics at 700 K for further relaxation. Then the potential energy of the molecule is minimized further with *conjugate gradient* for 30 steps.

b) The reduced unit cell coordinates are decreased such that the total volume is four times the target volume. Then the coordinates of the molecule are minimized 30 steps with *conjugate gradient* while keeping the polymer coordinates frozen.

c) Step b) is repeated, except this time the total volume is three times the target volume.

d) Step c) is repeated except this time the total volume is twice the target volume.

e) The reduced unit cell coordinates are decreased such that the total volume is 1.20x the target volume. This time, the potential energy of both the polymer and molecule coordinates are minimized with ten steps of *steepest descent* while maintaining the cell fixed, followed by 40 steps of conjugate gradient minimization.

f) The reduced unit cell coordinates are decreased such that the total volume is 1.15x the target volume. Then the potential energy of the polymer and molecule is minimized for 40 steps with the conjugate gradient minimization method.

g) Step f) is repeated, except the total volume is reduced to 1.10x the target volume.

h) Step g) is repeated, except the total volume is reduced to 1.05x the target volume.

i) The reduced unit cell coordinates are decreased to the target volume (1.00x) and the polymer and solvent are minimized for 40 steps with the conjugate gradient minimization method. Then the system is relaxed by annealing the atoms at 700 K for 750 steps, while holding the unit cell fixed. Then the polymer and molecule are minimized for 100 steps with

the conjugate gradient minimization method. Then the cell coordinates are allowed to relax with 50 steps of minimization with the conjugate gradient minimization method. Then the following sequence of minimization procedures was found to be optimal for effectively relaxing the whole system (including cell coordinates):

1) Thirty steps of minimization using the *smart minimizer* (available in Cerius2).
2) Thirty steps of minimization using the *conjugate gradient* minimizer.
3) Thirty steps of minimization using the *smart minimizer.*
4) Thirty steps of minimization using the *conjugate gradient* minimizer.
5) Thirty steps of minimization using the *smart minimizer.*
6) One hundred steps (Maximum) of minimization using *conjugate gradient* with a Coulomb and Van der Waals accuracy of 0.05 kcal/mol.
7) The interaction energy between the molecule is calculated by evaluating the periodic energy of the whole system with the polymer coordinates fixed, and the accuracy of both Van der Waals and electrostatic Ewald sums is set to 0.0001 kcal/mol. Then the vacuum energy of the solvent molecule is subtracted from the previously calculated total energy to obtain polymer-molecule energy of interaction.

Discussion of the Advantages of the New Procedure over Previous Techniques

The technique described in this paper allows for the efficient introduction of a solute molecule into any bulk system such as a polymer, because the initial step involves a five fold uniform expansion of the polymer volume which creates many vacancies while still conserving the connectivity, topology, and structure of the polymer. A molecule may be introduced much more easily and efficiently into the expanded system than the actual condensed system. The first stage of this procedure allows for a "natural" adjustment of the solvent molecule conformation and position to the original structure of the polymer. In the second relaxation stage, the stress created by the presence of the solvent molecule is gradually diffused into the polymer and the result is a relaxed polymer/solvent system. As an illustration, the structure of the poly (sulfone) polymer is shown in **Figure 1** while the structure of the "relaxed" poly (sulfone)/n-octanol system is shown in **Figure 2.** Note that there are only minor perturbations to the polymer structure after insertion of the n-octanol molecule.

Besides having applications for the study of the interactions of solvent molecules with polymers, this method may easily be applied to drug molecule docking on protein targets, in which most of the protein structure is minimally disturbed. Protein structure reorganization will occur mainly around the drug molecule. This may allow for the discovery and characterization of protein binding sites/pockets.

Application of the New Method towards the Study of the Interaction of Twenty Four Molecules with the Polysulfone Polymer Sensor

The procedure previously described is repeated twenty seven times at "random" positions of the bulk polymer system for each of twenty-four different ester and alcohol molecules. The average of the best 80% of binding energies (not including rejected samples) is shown in Table 1. The energies are broken down into the dispersive, electrostatic and hydrogen bond components with the respective uncertainties as well. The last column gives the number of samples that were eliminated due to bad packing effects such as molecules trapped within polymer rings. The calculated energies of interaction were correlated with the experimental resistivities through the permeability equation given by[7]

$$P=A\exp\left((\Delta H_s/k_BT) - (E_D/k_BT)\right) \quad (1)$$

where A is the exponential prefactor related to entropy, ΔH_s is the heat of sorption of the solute and E_D is the activation energy for diffusion of the molecule in the polymer. In the actual initial correlation reported, the heat of sorption is represented by

$$\Delta H_s/k_BT = C_1E_{Coul.} + C_2E_{VDW} + C_3E_{Hbnd} \quad (2)$$

where $E_{Coul.}$, $E_{VDW.}$ And E_{Hbnd} is the computed interaction energy components of the solute with the polymer shown in Table 1. The values C_1, C_2 and C_3 are parameters that are best fit to match the experimental relative resistivity data and are interpreted as a sum of entropy and $1/k_BT$ contributions to each energy component. Similarly, the activation energy for diffusion is given by

$$E_D/k_BT = C_4V_{solvent} \qquad (3)$$

where $V_{solvent}$ and C_4 are calculated bulk molar volume of the solvent (cc/mol) and an adjustable parameter respectively. In another test, the molecular values of $V_{solvent}$ were computed using a probe (1.4 Å radius) approach in the *Polygraf* software. Gas phase molecular volumes at 300 K were obtained by averaging 20 snapshots over a 20 ps trajectory. The results for the best-fit parameters for the two methods are shown in Table 2. The predicted relative change in resistivity for both models as a function of solvent is given in Table 3. The two solvents highlighted in bold (Table 3) for each fit was excluded when determining the parameters in Table 2. The predicted values of relative change in resistivity for the models using liquid molar volumes and molecular volumes are plotted against the experimental values in **Figure 3** and **Figure 4** respectively. The model based on the liquid molar volume had a root mean square deviation from experiment of the signal prediction of 0.0734, a slight improvement over the model based on the molecular volume, which had a corresponding rms prediction of 0.0777. However, both models, which were based on direct calculations of the energy of interaction between polymer and solute, were slightly inferior over the model based on pure solvent data, which had a corresponding rms prediction of 0.0542. However, the performance of the models using direct energies of interactions should be verified with other sensors in order to have a better comparison with the model using solvent data only.

Introduction and Discussion of Molecular Volume Scaled Polymer-Solute Interactions

The energetics of polymer permeation by a molecule, involve the replacement of a given volume of polymer by a volume of the solute. Let us define the "cohesive energy density of interaction" (CEDI) as the solute-solvent interaction divided by the molar (or molecular) volume of the solute. A possibly useful and approximate measure of the energy difference per unit volume of replacing molecule *a* into polymer *x* versus replacing molecule *b* into polymer *x* is the difference between their cohesive energy density of interaction. Similarly, the heat of sorption per unit volume may be approximately defined by

$$\Delta H_{s\text{-}pervol} = CEDI_a - CEDI_{polx} \quad (4)$$

where $CEDI_a$ is the cohesive energy density of interaction of solvent *a* with bulk polymer *x*, and $CEDI_{polx}$ is the cohesive energy density of interaction of a polymer chain with the bulk polymer **x**.

Therefore, the dispersive, electrostatic and hydrogen bond components of the cohesive energy density of interaction were used instead of the respective actual energies of interaction in the permeability fit to the experimental resistivities. The quantities $E_{Coul.}$, E_{VDW} and E_{Hbnd} in Equation 2 were replaced by $CEDI_{coul}$, $CEDI_{VDW}$ and $CEDI_{Hbnd}$ respectively. The calculated total CEDI's and the three individual components for all 24 solvents based on the liquid (solvent) molar volume and molecular volume are listed in Table 4 and Table 5

respectively. The wide discrepancy between the two calculated CEDIs is due to a large difference between the liquid molar volumes and the calculated probe-based molecular volumes. However, in this particular application, the trends in volumes are what matters and not the absolute values of the volumes. The best fit parameters for the permeability equation using the molar bulk volume and molecular volume are listed in Table 6 and the predicted signals are compared to experiment in Table 7. The predicted values of relative change in resistivity for the models using molar volume and molecular volume are plotted against the experimental values in **Figure 5** and **Figure 6** respectively. The model based on the molar volume had a root mean square deviation from experiment of the signal prediction of 0.0599, slightly worse than the model based on the molecular volume, which had a corresponding rms prediction of 0.0591. The new permeability model based on CEDI was an improvement over the previous model with rms values of 0.0734 and 0.0777 for the molar volume and molecular volume based approaches respectively. However, both CEDI models remained slightly inferior over the model based on pure solvent data, which had a corresponding rms prediction of 0.0542.

Discussion of Results

A good connection or correlation between permeability related quantities and the experimentally calculated polymer sensor change in resistivities was found using atomistically calculated energies of interaction between polymer and solute interactions. The energies of interaction were calculated using an

efficient polymer-molecule packing scheme. A series of four similar correlations between a permeability-like expression and the experimental relative change in resistivity were tested. The first two correlations used the calculated energy of interaction between the molecule and the polymer in the permeability equation. The root mean square deviation between the experimental and predicted signals was 0.0734 and 0.0777 for the molar volume and molecular volume based correlation respectively. Remember, the volume values were used as quantities representing the diffusion term in Equation 3. The last two correlations used a solvent volume normalized energy (CEDI, cohesive energy density of interaction, cal/cc) of interaction between the molecule and the polymer in the permeability equation. The root mean square deviation between the experimental and predicted signals was 0.0599 and 0.0591 for the molar volume and molecular volume based correlation. The results for the CEDI calculation were significantly better than the results based on direct energy of interaction between the polymer and the molecule. In CEDI based calculations, molecules of different sizes are all compared in equal terms in the correlation, and this may allow for the CEDI of the polymer to "fall out" as an empirically determined constant in the correlation. This may be an explanation why the CEDI based correlation works better than the non-normalized energies of interactions.

Conclusions

A method was developed for an efficient sampling of the interactions between a polymer and a solute, which may be readily used as an analytical tool for the electronic nose project. There are several scenarios where the use of direct energies of interaction could yield better results than using the data related to the pure bulk solvents. For example, a solvent may have hydrogen bond acceptors such as acetone, and the polymer may have hydrogen bond donors such as amide groups and direct calculation of energies of interaction would not necessarily correlate with the properties of the pure solvent. Another interesting case would be chiral interactions between a solvent and a polymer, where biological systems are a prime example. Therefore, the usefulness of atomistic modeling in the electronic nose project may prove to be very valuable.

Table 1. Energy of interaction of various solvents with bulk polysulfone. The Van der Waals, electrostatic and hydrogen bond components and the respective uncertainties are also listed as well as the number of rejected samples.

Solvent name	Total Energy Kcal/mol	Sigma Kcal/mol	VDW Kcal/mol	Sigma Kcal/mol	Electrostatic Kcal/mol	Sigma Kcal/mol	Hbond kcal/mol	sigma kcal/mol	number of failures
2-pentanol	-28.84310	2.834	-18.71452	2.576	-7.31878	2.916	-2.80980	1.546	0
3-pentanol	-27.82088	3.083	-18.18283	1.838	-7.19230	2.740	-2.44575	1.607	1
n-amylacetate	-35.84531	3.027	-27.19872	2.732	-8.64660	3.218	0.00000	0.000	2
n-butylacetate	-31.68710	4.321	-24.22418	2.214	-7.46293	4.663	0.00000	0.000	4
n-decylacetate	-49.46453	4.002	-40.84146	1.802	-8.62307	4.184	0.00000	0.000	0
Ethanol	-20.64603	3.441	-9.09059	1.291	-8.40549	2.972	-3.14996	1.398	0
Ethylacetate	-27.32038	4.497	-18.09716	1.597	-9.22321	5.025	0.00000	0.000	1
Hexylacetate	-40.87665	3.022	-30.06995	2.282	-10.80669	3.408	0.00000	0.000	3
iso-amylalcohol	-29.36863	2.955	-18.54943	1.595	-8.43190	2.475	-2.38731	1.667	1
iso-amylacetate	-34.00896	2.832	-25.69441	1.999	-8.31456	3.098	0.00000	0.000	3
Iso-amylbenzoate	-46.76476	3.508	-37.60405	1.856	-9.16073	4.068	0.00000	0.000	3
iso-amylbutyrate	-39.88201	4.332	-31.38348	3.381	-8.49854	4.968	0.00000	0.000	1
Iso-amylcaproate	-47.61572	2.676	-37.49545	2.420	-10.12026	4.072	0.00000	0.000	1
Iso-amylpropionate	-37.29536	4.157	-29.86850	2.000	-7.42687	4.944	0.00000	0.000	4
iso-butylacetate	-32.23245	4.011	-23.47219	1.453	-8.76028	3.746	0.00000	0.000	3
Iso-propylacetate	-30.22997	2.912	-21.02533	1.427	-9.20466	3.221	0.00000	0.000	1
n-amylalcohol	-29.77899	3.291	-18.01479	2.346	-8.72829	3.220	-3.03590	1.337	4
n-heptanol	-35.67196	2.097	-24.64136	1.993	-8.49341	2.217	-2.53719	1.731	2
n-hexanol	-32.20561	3.423	-21.26336	2.216	-8.49790	2.620	-2.44434	1.793	2
n-propanol	-23.39654	2.988	-12.25217	1.904	-8.57233	2.539	-2.57202	1.771	1
n-octanol	-38.79004	4.233	-27.69820	1.579	-8.57129	3.312	-2.52055	1.730	3
n-octylacetate	-44.66194	3.692	-35.22450	2.042	-9.43744	3.535	0.00000	0.000	6
n-propylacetate	-29.59510	3.650	-20.73788	2.129	-8.85724	3.752	0.00000	0.000	4
n-butanol	-26.23133	2.742	-15.45521	1.309	-7.85817	2.522	-2.91795	1.632	0

Table 2. Relative change in resistivity best fit parameters for the permeability model (Equations 1-3) using the solvent molar volume in the first case and the molecular volume in the second case. "RMS fit" refers to the root mean square deviation of experimental versus predicted signals given in Table 3.

	A	C4	C1	C2	C3	RMS
Method	Preexp	Diffusion	Coulomb	Dispersion	Hbond	Fit
Molar Volume	2.717221	-0.049260	0.082304	-0.22116	0.214125	0.0734
Molecular Volume	1.876897	-0.000995	-0.038321	0.03744	0.368258	0.0777

Table 3. Relative change in resistivity predictions for 24 solvents based on the best fit coefficients given in Table 2 for the cases using the solvent molar volume and the molecular volume respectively. Solvent signals in bold were excluded from the fit.

Solvent	**Predicted signal** (Molar Volume)*	**Predicted signal** (Molecular Volume)**	**Experimental** Signal
2-pentanol	0.3889	0.2768	0.3850
3-pentanol	0.3573	0.3225	0.4159
Amylacetate	0.6394	0.5206	0.5065
Butylacetate	0.8554	**0.5923**	0.9463
Decylacetate	0.2184	0.2310	0.1632
Ethanol	0.3926	0.4371	0.2953
Ethylacetate	0.9471	0.8997	0.9467
Hexylacetate	0.4880	0.4780	0.5329
Iso-amylalcohol	0.3745	0.3428	0.3139
Isoamylacetate	0.5054	0.5505	0.4121
Isoamylbenzoate	**0.5312**	0.3093	0.2334
Isoamylbutyrate	0.3494	0.3957	0.3998
Isoamylcaproate	0.2197	0.2974	0.2668
Isoamylpropionate	0.5250	0.4267	0.4438
Isobutylacetate	0.6122	0.6444	0.6114
Isopropylacetate	0.7853	0.7617	0.7440
n-amylalcohol	**0.2674**	**0.2748**	0.4658
n-heptanol	0.2535	0.2264	0.2939
n-hexanol	0.2894	0.2824	0.4025
n-propanol	0.3719	0.4544	0.3320
Octanol	0.2442	0.1914	0.1676
Octylacetate	0.2980	0.3312	0.3639
Propylacetate	0.7583	0.7551	0.8482
n-butanol	0.3010	0.3249	0.4228

Table 4. Total cohesive energy density of interaction (cal/cc) between twenty four solvents and polysulfone as well as the components. The values were calculated using the molar volume of the condensed solvent.

Solvent name	CEDI (Molar Vol.) cal/cc	CEDI, Coulomb cal/cc	CEDI, Dispersive cal/cc	CEDI, Hbond cal/cc
2-pentanol	-291.212	-73.894	-188.950	-28.369
3-pentanol	-277.735	-71.801	-181.519	-24.416
Amylacetate	-261.568	-63.095	-198.473	0.000
Butylacetate	-264.605	-62.320	-202.285	0.000
Decylacetate	-224.701	-39.172	-185.529	0.000
Ethanol	-394.376	-160.560	-173.646	-60.170
Ethylacetate	-313.172	-105.725	-207.447	0.000
Hexylacetate	-269.270	-71.188	-198.082	0.000
iso-amylalcohol	-296.518	-85.132	-187.283	-24.103
Isoamylacetate	-250.780	-61.311	-189.469	0.000
Isoamylbenzoate	-250.535	-49.077	-201.458	0.000
Isoamylbutyrate	-236.910	-50.484	-186.426	0.000
Isoamylcaproate	-235.152	-49.979	-185.173	0.000
Isoamylpropionate	-240.515	-47.895	-192.620	0.000
Isobutylacetate	-266.382	-72.398	-193.983	0.000
Isopropylacetate	-290.064	-88.321	-201.743	0.000
n-amylalcohol	-297.283	-87.134	-179.841	-30.307
n-heptanol	-267.070	-63.589	-184.486	-18.996
n-hexanol	-277.371	-73.188	-183.131	-21.052
n-propanol	-334.815	-122.674	-175.334	-36.807
Octanol	-262.113	-57.918	-187.163	-17.032
Octylacetate	-238.516	-50.401	-188.116	0.000
Propylacetate	-283.972	-84.987	-198.985	0.000
n-butanol	-297.267	-89.053	-175.146	-33.068

Table 5. Total cohesive energy density of interaction (cal/cc) between twenty four solvents and polysulfone as well as the components. The values were calculated using the molecular volume of the solvent.

Solvent name	CEDI, (Molec. Vol) cal/cc	CEDI, Coulomb cal/cc	CEDI, Dispersive cal/cc	CEDI, Hbond cal/cc
2-pentanol	-103.849	-26.351	-67.381	-10.117
3-pentanol	-100.934	-26.094	-65.967	-8.873
Amylacetate	-99.503	-24.002	-75.501	0.000
Butylacetate	-98.351	-23.164	-75.187	0.000
Decylacetate	-91.203	-15.899	-75.304	0.000
Ethanol	-122.267	-49.778	-53.835	-18.654
Ethylacetate	-109.820	-37.075	-72.745	0.000
Hexylacetate	-102.985	-27.226	-75.758	0.000
iso-amylalcohol	-107.965	-30.997	-68.191	-8.776
Isoamylacetate	-96.387	-23.565	-72.822	0.000
Isoamylbenzoate	-103.595	-20.293	-83.302	0.000
Isoamylbutyrate	-93.184	-19.857	-73.327	0.000
Isoamylcaproate	-95.239	-20.242	-74.997	0.000
Isoamylpropionate	-95.160	-18.950	-76.211	0.000
Isobutylacetate	-101.293	-27.530	-73.763	0.000
Isopropylacetate	-106.895	-32.548	-74.347	0.000
n-amylalcohol	-106.251	-31.142	-64.276	-10.832
n-heptanol	-100.980	-24.043	-69.754	-7.182
n-hexanol	-101.671	-26.827	-67.127	-7.717
n-propanol	-113.367	-41.537	-59.367	-12.463
Octanol	-99.188	-21.917	-70.825	-6.445
Octylacetate	-94.947	-20.063	-74.884	0.000
Propylacetate	-103.287	-30.912	-72.375	0.000
n-butanol	-107.897	-32.323	-63.572	-12.002

Table 6. Relative change in resistivity best fit parameters for the permeability model (Equations 1-3) using cohesive energy density of interaction components. The fits were done based on molar volume in the first case and molecular volume in the second case. "RMS fit" refers to the root mean square deviation of experimental versus predicted signals given in Table 7.

Method	A Preexp	C4 Diffusion	C1 Coulomb	C2 Dispersion	C3 Hbond	RMS fit
Molar Volume	1.503751	-0.010621	-0.000991	-0.001741	0.026209	0.0599
Molecular Volume	48.633374	-0.003170	0.008679	0.032003	0.109524	0.0591

Table 7. Relative change in resistivity predictions for 24 solvents based on the best fit coefficients given in Table 6 for the cases using the liquid molar volume and the molecular volume respectively. Solvents signals in bold were excluded from the fits.

Solvent	**Predicted signal** (Molar Volume)*	**Predicted signal** (Molecular Volume)**	**Experimental** Signal
2-pentanol	0.3734	0.34278	0.3850
3-pentanol	0.4031	0.41648	0.4159
amylacetate	0.5276	0.52922	0.5065
butylacetate	**0.6377**	**0.65788**	0.9463
decylacetate	0.2084	0.21909	0.1632
ethanol	0.2827	0.30046	0.2953
ethylacetate	0.9488	0.92782	0.9467
hexylacetate	0.4544	0.42079	0.5329
iso-amylalcohol	0.4210	0.38289	0.3139
isoamylacetate	0.5264	**0.60178**	0.4121
isoamylbenzoate	0.3088	0.26350	0.2334
isoamylbutyrate	0.3659	0.41172	0.3998
isoamylcaproate	0.2539	0.26634	0.2668
isoamylpropionate	0.4248	0.45751	0.4438
isobutylacetate	0.6265	0.67697	0.6114
isopropylacetate	0.7710	0.76645	0.7440
n-amylalcohol	0.3497	0.33136	0.4658
n-heptanol	0.3249	0.30039	0.2939
n-hexanol	0.3732	0.36452	0.4025
n-propanol	0.4181	0.43721	0.3320
octanol	**0.2932**	0.26268	0.1676
octylacetate	0.3002	0.31281	0.3639
propylacetate	0.7648	0.81194	0.8482
n-butanol	0.3669	0.35884	0.4228

Figure 1. Single n-octanol molecule in a relaxed structure of polysulfone.

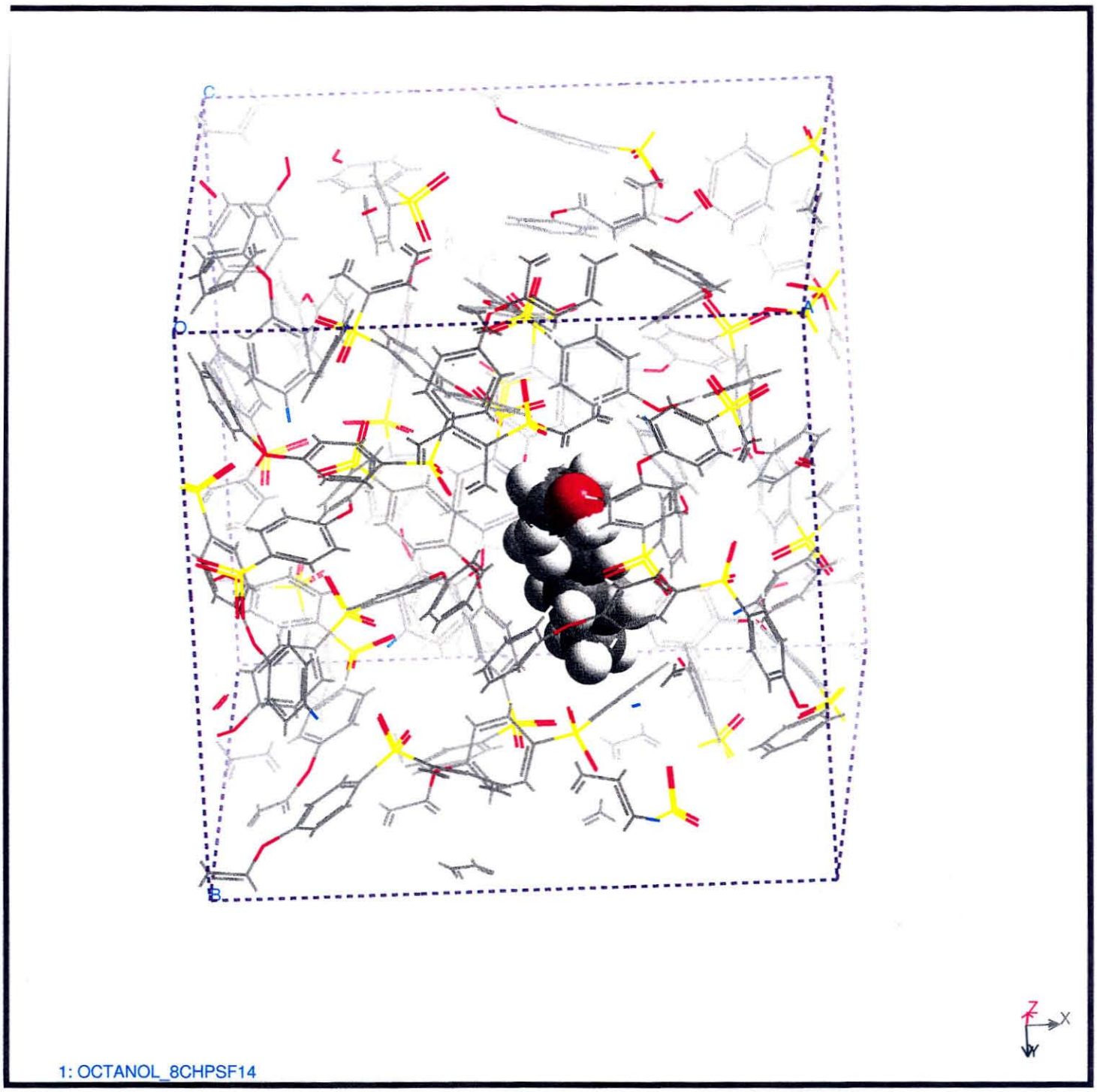

Figure 2. Relaxed polysulfone polymer.

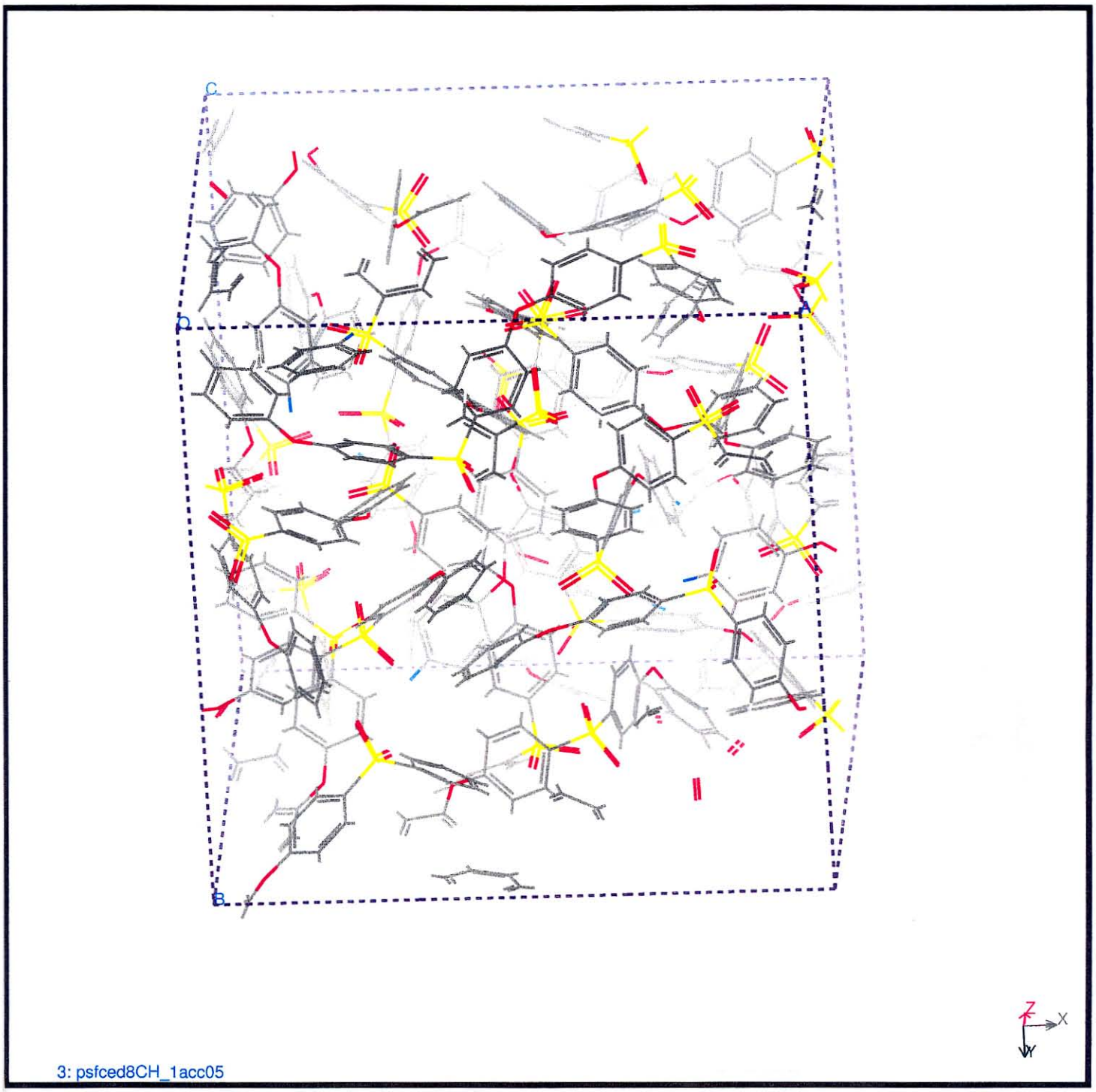

Figure 3

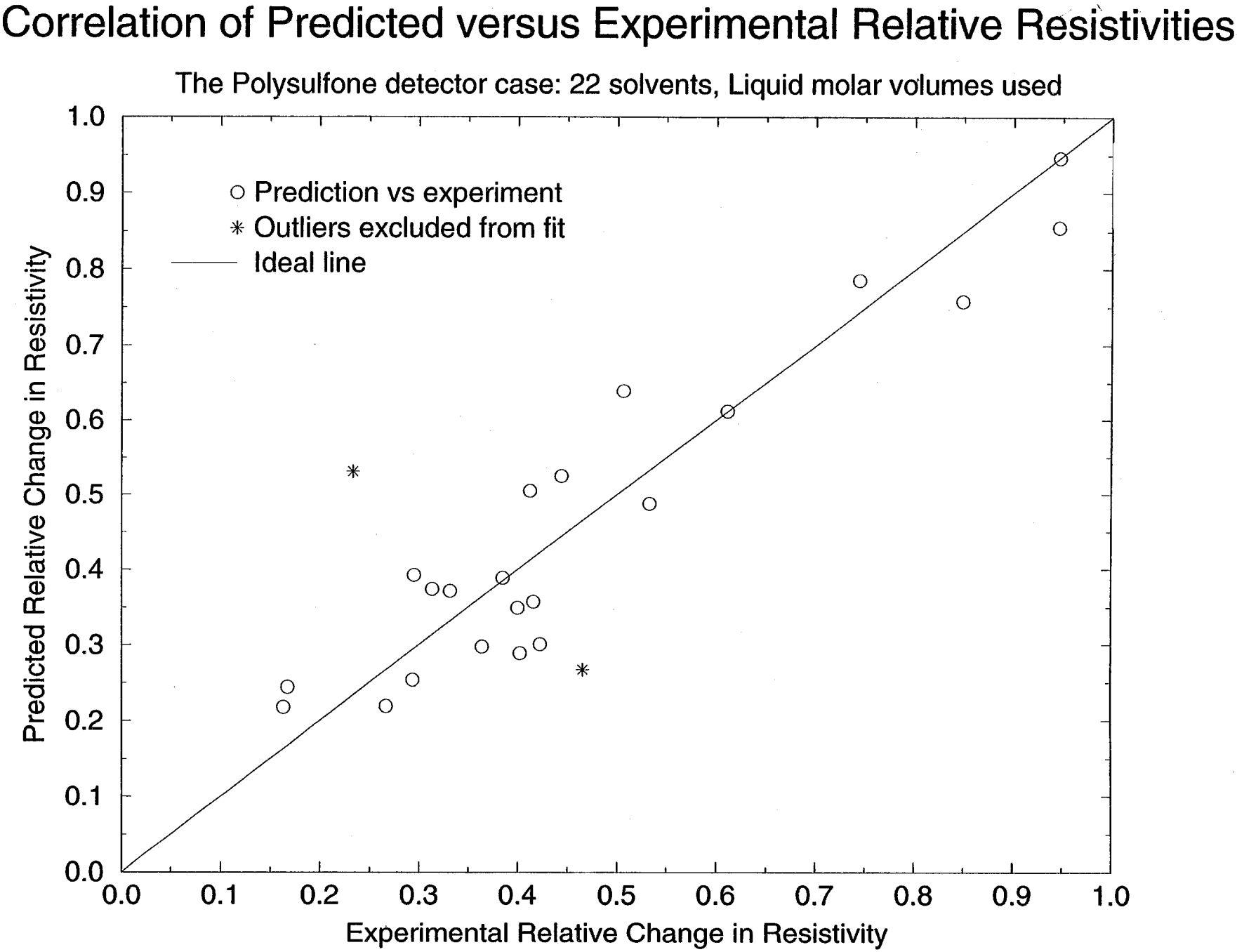
Correlation of Predicted versus Experimental Relative Resistivities
The Polysulfone detector case: 22 solvents, Liquid molar volumes used
Prediction vs experiment
Outliers excluded from fit
Ideal line
Predicted Relative Change in Resistivity
Experimental Relative Change in Resistivity
0.0
0.1
0.2
0.3
0.4
0.5
0.6
0.7
0.8
0.9
1.0

Figure 4

Correlation of Predicted versus Experimental Relative Resistivities

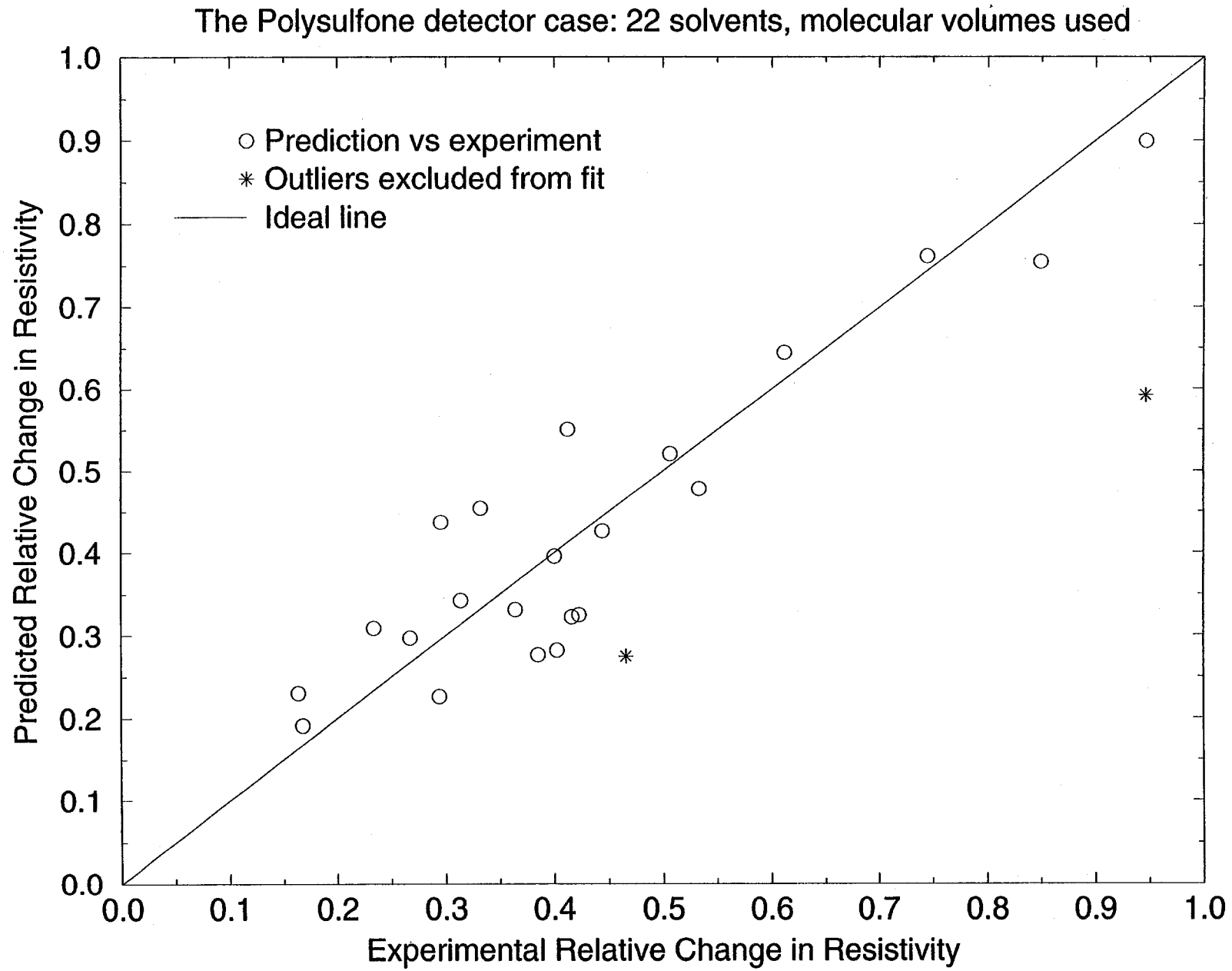

Figure 5

Correlation of Predicted versus Experimental Relative Resistivities

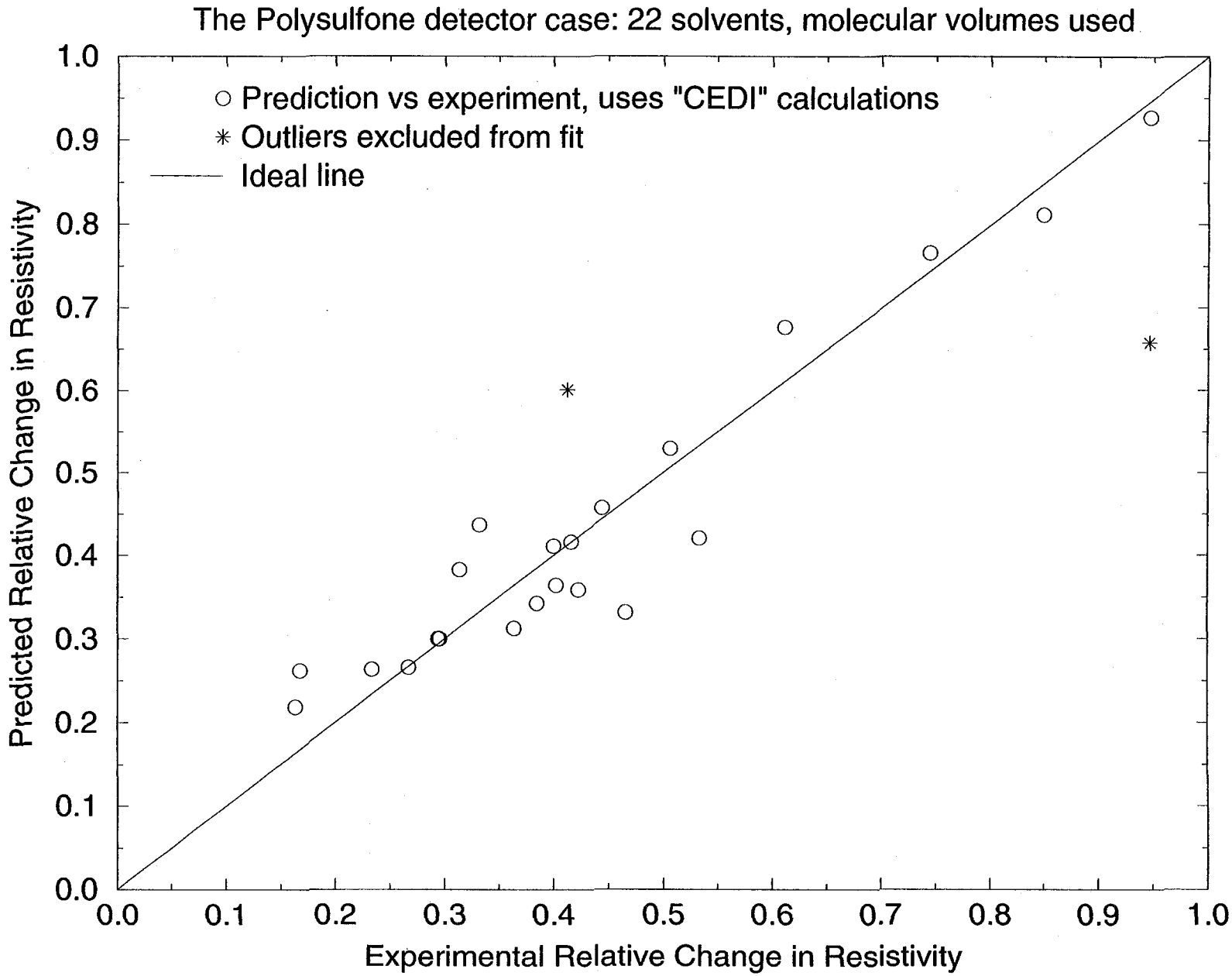

Figure 6

Correlation of Predicted versus Experimental Relative Resistivities

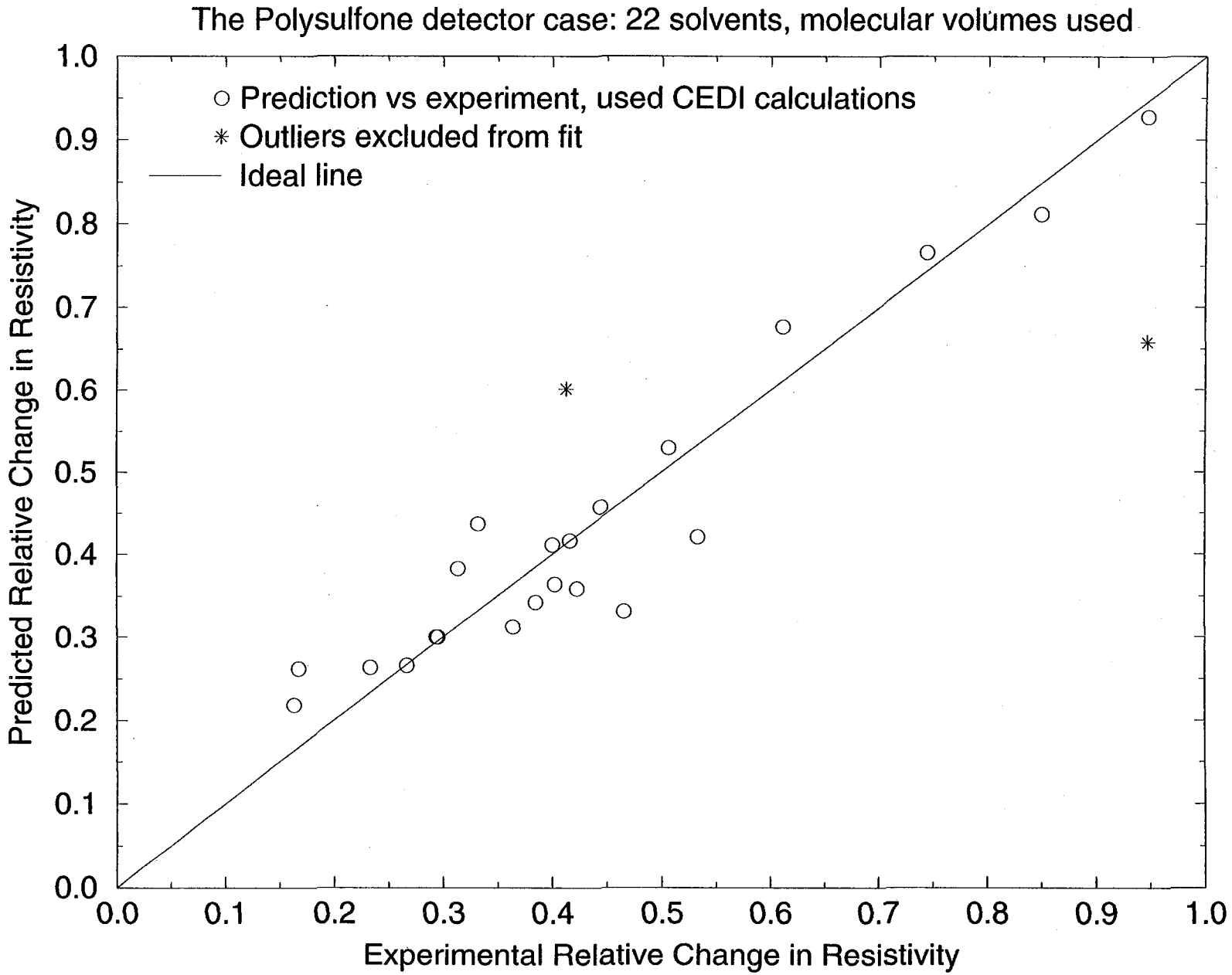

References

1. Knopp, B.; Suter, U. W.; Gusev, A. A.; *Macromolecules*, **30**(20), 6107 (1997)
2. Knopp, B.; Suter; *Macromolecules*, **30**(20), 6114 (1997)
3. Fritz, L.; Hofmann, D; *Polymer*, **38**(5), 1035 (1997)
4. Ralston, A.; Denton, D.; Bicerano, J; Moll, D.; *Computational and Theoretical Polymer Science*, **6**(1-2), 15 (1996)
5. Mayo, S. L.; Olafson, B. D.; Goddard, W. A. III; *Journal of Physical Chemistry*, **94**(26), 8897 (1990)
6. Rappe, A. K.; Goddard, W. A. III; *Journal of Physical Chemistry*, **95**(8), 3358 (1991)
7. Krevelen, D. W. Van; *Properties of Polymers: Their Correlation with Chemical Structure; their Numerical Estimation and Prediction from Group Contributions*, Elsevier Science Publishers, NY (1990), p. 536